Metal Centers in Hydrogenases, Bimetallic Oxidases, and Model Complexes Studied by Advanced X-ray Spectroscopy Techniques and Quantum Chemistry

Dissertation

zur Erlangung des Grades eines

Doktors der Naturwissenschaften (Dr. rer. nat.)

am Fachbereich Physik

der Freien Universität Berlin

vorgelegt von

Ramona Kositzki

Berlin 2018

Freie Universität Berlin

Metal Centers in Hydrogenases, Bimetallic Oxidases, and Model Complexes Studied by Advanced X-ray Spectroscopy Techniques and Quantum Chemistry

Ramona Kositzki

Department of Experimental Physics, Freie Universität Berlin

Erstgutachter: Priv.-Doz. Dr. Michael Haumann

Zweitgutachter: Prof. Dr. Holger Dobbek

Tag der Disputation: 22.05.2019

Pour hermès.

Table of Contents

Abstract **1**

1 Preface **3**
1.1 Motivation and Scope of this Thesis 5

I EXPERIMENTAL BACKGROUND AND THEORETICAL APPROACHES 7

2 X-ray techniques **7**
2.1 XAS 7
2.2 XES 21
2.3 NRVS 26
2.4 TXRF 31

3 Quantum Chemistry Calculations (DFT) **33**
3.1 General aspects of density functional theory 33
3.2 Functional and basis set selection 34
3.3 Geometry optimization and normal mode analysis 35
3.4 Generation of theoretical X-ray spectra 36

Overview of used programs and X-ray facilities **38**

II RESULTS 39

(A) HYDROGENASE ENZYMES AND BIOMIMETIC COMPOUNDS 39
Scientific background 39

4 Electronic and molecular structure relations in diiron compounds mimicking the [FeFe]-hydrogenase active site studied by X-ray spectroscopy and quantum chemistry **49**
4.1 Introduction 49
4.2 Materials and Methods 51
4.3 Results 55
4.4 Discussion 74
Conclusions 76

5 Semisynthetic [FeFe]-hydrogenase generated by *in-vitro* maturation with a synthetic diiron complex **77**
5.1 Introduction 77
5.2 Materials and Methods 78
5.3 Results and Discussion 79
Conclusions 85

6 Lyophilization stabilizes the oxygen-sensitive hydrogenase cofactor **86**
6.1 Introduction 86
6.2 Materials and Methods 86
6.3 Results and Discussion 87
Conclusions 94

(B) BIMETALLIC OXIDASE PROTEINS 95
Scientific background 95

7 Protonation state of MnFe and FeFe cofactors in a ligand binding oxidase revealed by X-ray absorption, emission, and vibrational spectroscopy and QM/MM calculations 105
7.1 Introduction 105
7.2 Materials and Methods 108
7.3 Results 114
7.4 Discussion 137
Conclusions 141

8 R2lox protein – effect of single-point mutations 142
8.1 Introduction 142
8.2 Sample preparation and characterization 146
8.3 Formation of alternative cofactor species in *Gk*R2lox mutants 147
8.4 Assembly mechanism of the heterodimeric Mn/Fe cofactor: Results from TXRF titration series 158
8.5 Discussion 164
Conclusions 166

III SUMMARY AND OUTLOOK 167

IV LIST OF PUBLICATIONS 170
Hydrogenases and Models 170
Oxidases 170
Further publications 171

V REFERENCES 173

VI APPENDIX 187
Zusammenfassung 213
Selbstständigkeitserklärung 214

Abstract

Numerous metal cofactors in proteins are able to catalyze the activation of small molecules such as H_2O, H_2, O_2, and CO_2. Determination of their molecular and electronic properties as well as understanding of their catalytic reaction mechanisms attracts much research interest. In this thesis, two different biological systems based on iron and mixed iron/manganese cofactor sites were predominantly studied. [FeFe]-hydrogenases catalyze reversible hydrogen turnover whereas ligand-binding oxidases activate oxygen. An extensive X-ray absorption and emission spectroscopy and DFT study on a series of synthetic compounds mimicking the diiron site of [FeFe]-hydrogenases was performed. This revealed relations of ligand variation (substitution at terminal ligands and the bridging dithiolate group) to the electronic properties of the diiron complexes. Good agreement between experimental and calculated data was achieved. The study may provide a basis for future improvement of hydrogen forming catalysts. Successful H-cluster formation in HydA1 [FeFe]-hydrogenase (from green algae) reconstituted with synthetic diiron complexes was proven by XAS/XES studies. Comparison of XAS data of freeze-dried and native O_2-sensitive [FeFe]-hydrogenases contributed to establishing lyophilization as a method for preventing O_2-induced H-cluster degradation. Bimetallic cofactor sites in the ligand-binding oxidase *Gk*R2lox (from *Geobacillus kaustophilus*) were investigated by a wide range of synchrotron-based X-ray techniques (XAS, XES, and nuclear resonance vibrational spectroscopy) as well as DFT. This disclosed the molecular structure and electronic configuration including the protonation state of the FeFe and MnFe active sites. The atomic level description of the cofactor structures was significantly improved in combination with XRD data. Site-selective NRVS on ^{57}Fe labelled *Gk*R2lox as well as assignment of vibrational bands with DFT were established. Detailed XAS/TRXF investigations on mutant variants of *Gk*R2lox were performed and revealed the role of amino acid ligands in cofactor metalation and Fe or Mn specificity. Relations between the mechanism of O_2 activation and cofactor structure were provided. Determination of the physiological role of R2lox proteins requires further studies to unravel the interplay of ether cross-linking in the protein scaffold and O_2 activation. The described studies have further established advanced X-ray spectroscopy and quantum chemical methods as a viable tool for characterization of cofactors in enzymes and biomimetic molecules under functional conditions. New insight in the properties of the active sites in hydrogenases and oxidases were obtained. Various contributions to investigations of metal centers in further metalloproteins and synthetic compounds with X-ray methods were made, but are not included in these thesis to keep the focus on binuclear active sites (see own references). The presented results were compiled in several publications, making the developed methodology and scientific findings accessible to a larger community.

1 Preface

Metal cofactors in biological enzymes are responsible for numerous essential and chemically demanding reactions in nature including the activation and conversion of small and thermodynamically stable molecules such as H_2O, H_2, O_2, N_2, CO, CH_4, and NO (see Figure 1-1). Respective reactions are catalyzed with often high turnover rates and selectivity as well as under mild physiological conditions, meaning atmospheric pressure, ambient temperature and neutral pH [111, 145, 199, 264]. Accordingly, the reaction pathways and mechanism of metal-containing enzymes are of global interest, in renewable energy research, medicine and chemistry. Much recent work was devoted to the synthesis of biomimetic molecular models for the biological cofactors aiming at (bioinspired) functional catalysts.[60, 89, 168] Sustainable energy generation will become increasingly important in the future and therefore the development of novel catalysts for example for hydrogen formation as a "green" fuel resource is an important task.

Transitions metals (TM), in particular from the first row of TMs in the periodic table, play an important role in enzymatic systems because of their chemical versatility. They can adopt numerous redox states and coordination geometries.[28] More than 40% of the known proteins are estimated to be metalloproteins containing transition metals such as Mn, Fe, Ni, Cu, as well as Mo. Their functions depend essentially on the identity of the metal ions and the protein environment [28]. Metalloprotein active sites involving iron and manganese are widespread in nature. Iron is the most abundant TM on earth and manganese is also very common. A large number of iron-containing metalloproteins are known, which are involved in oxygen activation, electron transfer, and radical chemistry, for example heme-containing proteins (e.g. hemoglobin, myoglobin, cytochrome), non-heme iron enzymes (e.g. methane monooxygenase, ribonucleotide reductase, hemerythrin), and iron-sulfur cluster containing proteins (e.g. in ferredoxins, nitrogenases, and hydrogenases). Manganese is also involved in many protein systems, most prominently in the oxygen-evolving complex of photosystem II, as well as in manganese-containing superoxide dismutase, catalases, and dioxygenases.

The elucidation of the structure and function of the metal cofactors in enzymes in the course of the (catalytic) reactions leads to a better understanding of the (bio)chemical mechanisms. Deeper insight into the metalloproteins as well as general principles of biocatalysts may be applied for development of improved organometallic systems for modeling of key structural motifs and functional properties of the native cofactors.

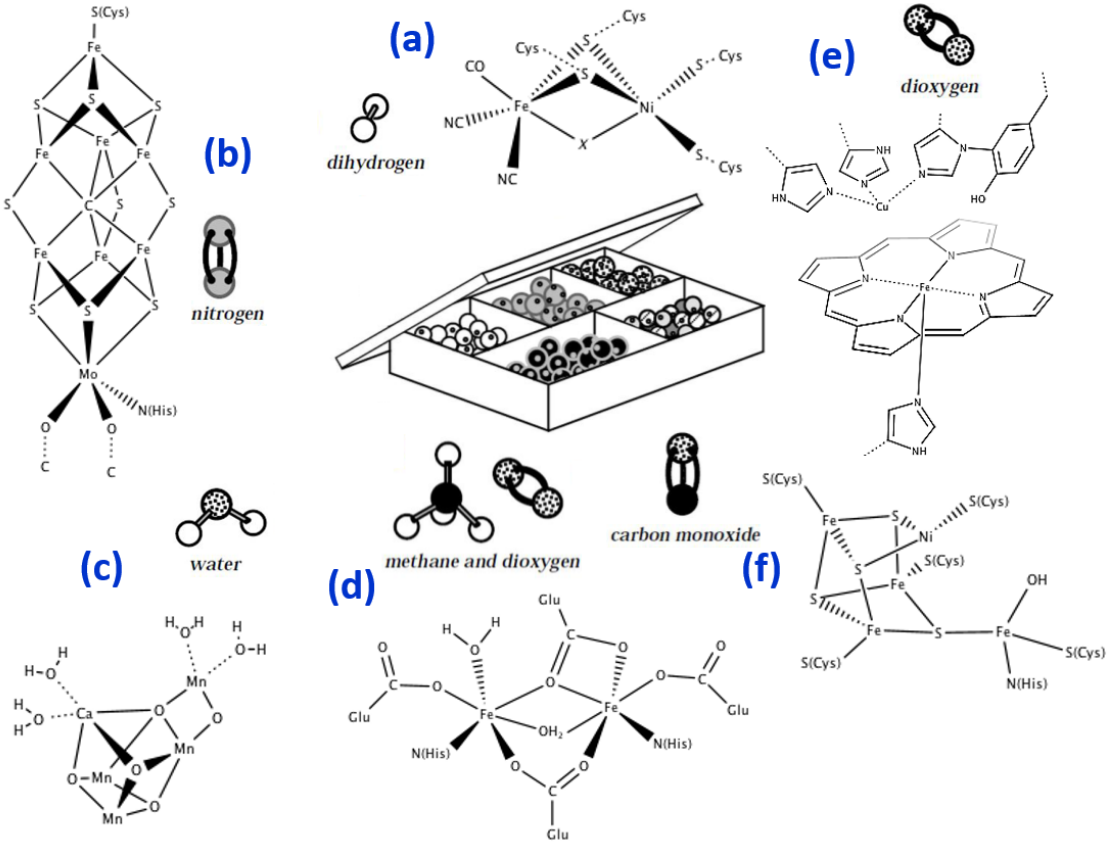

*Figure 1-1: Examples for small molecule activation by metalloenzymes. Illustration of the active sites of (**a**), [NiFe]-hydrogenases, (**b**), iron- and molybdenum-containing nitrogenases, (**c**), the oxygen-evolving complex of photosystem II, (**d**), methane monooxygenases, (**e**), cytochrome c oxidases, (**f**), carbon monoxide dehydrogenase/acetyl CoA synthase.*
Reprinted (adapted) from [264] with permission from The Royal Society of Chemistry.

Protein crystallography (XRD) can be often employed to determine the structure of the metalloproteins but has to rely on protein crystals. Importantly, the integrity of the relevant metals as well as their sensitivity to X-ray radiation is a problem in XRD.[28] X-ray absorption and emission spectroscopy (XAS/XES) is a powerful complementary method to investigate metalloproteins in non-crystalline, solution samples under functional conditions. X-ray spectroscopy methods provide structural and electronic information. High-valent metal active sites can also be examined by using time-revolted energy-sampling approaches [289]. The here employed combination of high-resolution XAS and XES, nuclear resonance vibrational spectroscopy (NRVS) and quantum chemistry calculations on metal centers in biological enzymes and synthetic model compounds provides access to the molecular, electronic and

vibrational properties of the studied metal centers and cofactor species, thereby leading to a more detailed understanding of the restraints that govern the reactivities.

1.1 Motivation and Scope of this Thesis

Determination of the molecular and electronic structure of the metal cofactors in metalloenzymes is a prerequisite for understanding their catalytic reactivity. Synchrotron-based X-ray methods as employed in the presented studies (XAS, XES, NRVS) provide element- and site-specific information on geometric, electronic and vibrational properties of metalloproteins actives sites as well as of biomimetic compounds. The combination of XAS and XES (XAES) facilitates spin-, valence- and site-selective X-ray experiments. The combination of X-ray spectroscopy with quantum chemistry methods (DFT and QM/MM calculations) enables the verification and interpretation of the observed spectroscopic features for quantitative analysis. Two different systems are in focus of this thesis, namely manganese-iron and iron-iron centers in R2-like ligand-binding oxidases (R2lox) and iron-iron centers in hydrogenases, which catalyze either oxygen activation or hydrogen conversion. A systematic study on synthetic model compounds mimicking the diiron site of [FeFe]-hydrogenases was performed to unravel relations between structural and functional features of potential interest for generation of modified hydrogenase enzymes. Furthermore, combination of the X-ray spectroscopic methods with QM calculations facilitates mutual benchmarking of experimental and theoretical parameters for improvement of the applicability of theoretical approach. As an example the cofactor site of a novel heterobimetallic oxidase protein (R2lox) was investigated with a broad range of advanced X-ray techniques to deduce the intrinsic metal specificity and gain insight into the unique two-electron redox chemistry.

This thesis comprises two main Results sections, which summarize the studies on [FeFe]-hydrogenase and biomimetic complex (A) and on oxidase proteins (B).

A Hydrogenase and model compounds.

Chapter 4 presents a study on 18 different synthetic diiron complexes mimicking the [FeFe]-hydrogenase active site using high-resolution X-ray absorption and emission spectroscopy (XAS/XES), supported by density functional theory calculations (DFT).

Chapter 5 shows a comparison of semi-synthetic with native [FeFe]-hydrogenases focusing on accessing of *in-vitro* H-cluster assembly by XAS/XES.

Chapter 6 summarizes XAS results on lyophilized [FeFe]-hydrogenases, which contributes to a procedure for stabilization of the oxygen-sensitive hydrogenase cofactor in potential applications.

B Oxidase proteins.

Chapter 7 comprises a comprehensive investigation on the trivalent homo- and hetero-dinuclear metal cofactors in a ligand-binding oxidase protein (*Gk*R2lox) using XAS/XES as well as nuclear resonance vibrational spectroscopy (NRVS) in combination with DFT calculations.

Chapter 8 contains the results of an extended examination (XAS and TXRF) of *Gk*R2lox with single-point mutations to clarify the function of ligand species in cofactor assembly, metalation, and activity.

During my thesis work, I participated also in investigations on various other metalloproteins and synthetic systems, which has contributed to several publications (see references list). The respective results from my work were not included in this thesis to keep the focus on bimetallic cofactors. For such systems, the application of complementary, advanced X-ray spectroscopy methods in combination with quantum chemistry is outlined.

I Experimental Background and Theoretical Approaches

The experimental methods described below were used to investigate metal cofactors in metalloproteins (ligand-binding oxidases, Chapter 7-8 and hydrogenases, Chapter 5-6) as well as synthetic model compounds (diiron model compounds of the [FeFe]-hydrogenase active site, Chapter 4). The obtained structural and electronic information was compared with the results of quantum chemical approaches (e.g. density functional theory (DFT) calculations) on cofactor model structures.

2 X-ray techniques

This section provides an overview of the in-house and synchrotron-based X-ray spectroscopy methods used in this work. After a brief introduction to the applied methods, an explanation of the experimental setup and data processing and of the information that can be obtained from the experimental spectra is provided.

2.1 XAS

X-ray absorption spectroscopy (XAS) is a well-established and powerful technique to characterize structural and electronic properties of metals in biological materials and in inorganic compounds. For example, XAS can be used "stand alone" or in combination with other techniques to decipher relations between structure and function of metalloprotein active sites. There are a number of monographs [29, 261], book chapters (see e.g. [15, 188]) as well as review articles [175, 285] on XAS available. Furthermore, various online resources with XAS tutorials are available, e.g. from the International X-ray Absorption Spectroscopy Society (http://xafs.org).

The method is based on the absorption of X-rays by the materials under investigation. Analysis of the spectra originating from core level electron excitation (e.g. 1s) provides information about the chemical properties and environment of the element of interest. A major advantage of the method is its absolute element specificity. Because each element has a specific 1s electron binding energy, XAS facilitates analysis of only one element of interest, for example investigation of structural properties of a particular species, selectively in mixed-metal compounds or multinuclear metal sites in proteins. XAS is sensitive to the metal oxidation state

as well as the metal-ligand coordination and provides information on coordination number (number of metal ligands) and interatomic distance (bond length) as well as on atoms in higher coordination spheres. Further advantages are that XAS is not limited to ordered samples (crystals), i.e. samples in all aggregate states (e.g. powder/solids, liquid samples, crystals, gas, frozen solution samples) can be analyzed. XAS is applicable to low concentration samples, which is particularly important for biological systems. Samples can be studied in a wide temperature range and a specific spin state or isotope labeling is not required. However, several limitations apply because XAS is an averaging method, i.e. the scattering signal is the average of all sites of the same element and their surroundings. Therefore, usually an average oxidation state of multinuclear sites is determined. The technique in most cases requires high-intensity X-rays from synchrotron sources. The distinction between neighboring elements in the periodic table by XAS is difficult (e.g. discrimination of nitrogen and oxygen or sulfur and chloride). In general, for metalloprotein systems the available structural information is limited to atoms within a radius ~6 Å around the absorber (higher distances are accessible for well-ordered materials).

Theory of XAS

When matter absorbs light (e.g. X-rays) the incident primary beam with intensity I_0 (and energy $E = hv$) will be attenuated according to the Lambert-Beer law and the absorption coefficient $\mu(E)$ gives the probability of the absorption:

$$\mu(E)x = ln\left(\frac{I_0}{I}\right) \tag{1}$$

Where I represents the transmitted intensity, I_0 the initial intensity, x the sample thickness and $\mu(E)$ is the energy dependent, linear X-ray absorption coefficient. The parameter μ shows a strong dependence on both X-ray photon-energy E and atomic number Z [175]:

$$\mu \approx \frac{\rho Z^4}{AE^3} \tag{2}$$

Where ρ is the sample density and A is the atomic mass.

Figure 2-1A shows the X-ray absorption as a function of energy exemplary for the region 1-100 keV including K-edges of the elements manganese, iron and K- and L-edges of molybdenum. In general, the absorbance decreases continuously with increasing X-ray energy due to the E^{-3} dependence. At certain energies, an abrupt increase of the absorption probability

can be observed. This sharp rise in the spectra, the so-called absorption edge, occurs when the core electron absorbs energy equal to or higher than its binding energy, which is characteristic for the absorbing element. As the core electron binding energy increases with increasing atomic number *Z*, correspondingly higher excitation energies are obtained. The large energy differences between the absorption edges are due to the dependence of the edge energy on the atomic number ($E(edge) \sim Z^2$) [175], which facilitates element-specific studies (e.g. K-edge energy for Mn: 6539 eV; Fe: 7112 eV, Mo: 19999.5 eV). The annotation of edge absorption refers to the principal quantum number, i.e. depending on the shell where the excited electron

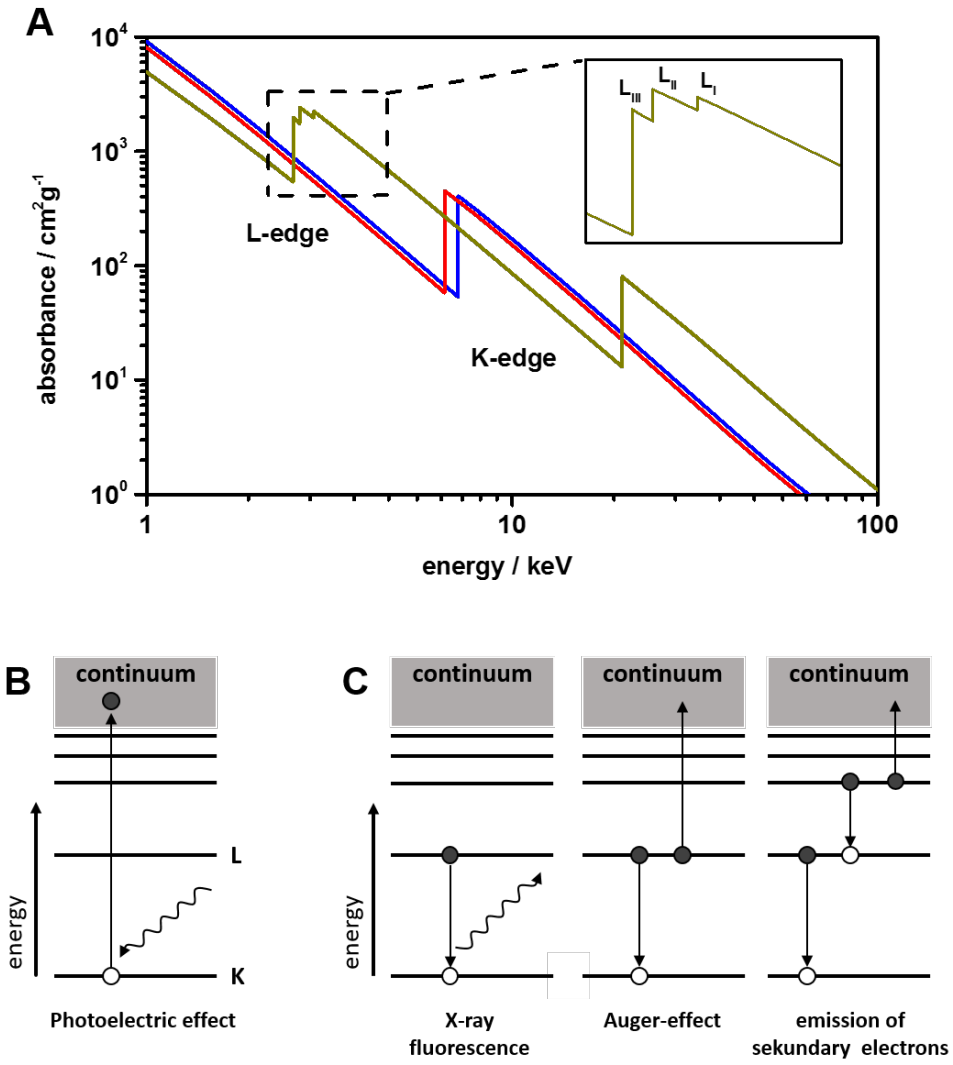

Figure 2-1: Illustration of X-ray absorption.
*(**A**) X-ray absorption spectra for the elements manganese (red; Z=25), iron (blue, Z=26) and molybdenum (dark yellow, Z=42). Shown are the K and L edge, i.e. transitions corresponding to the excitation of an electron from 1s or 2p levels, respectively. Inset, details of L transitions for molybdenum. Schematic illustration of (**B**) photo-electric effect and (**C**) possible relaxation processes. The excited state can relax by either X-ray fluorescence (left), the Auger-effect (middle) or the emission of a second electron (right). Data of the mass attenuation coefficient, μ/ρ, as a function of photon energy from https://physics.nist.gov/PhysRefData/XrayMassCoef/tab3.html.*

originates from, e.g. the K-absorption edge reflects the excitation of a 1s core electron, the L-absorption edge reflects the excitation of a 2s electron (L_I) or electrons from 2p orbitals (L_{II}, L_{III}). Investigations of metals in bioinorganic samples are often carried out at the K-edge instead of the corresponding lower-energy L-edge, since experiments at L-edges require high-vacuum techniques for most elements and X-ray related sample damage is much less severe for K-edge spectroscopy.

After the absorption process (Figure 2-1B) the atom in the excited state will relax within a few femtoseconds by filling the electron hole in the core orbital by different relaxation pathways. Figure 2-1C illustrates possible radiative and non-radiative relaxation mechanisms, (i) the emission of fluorescence radiation, (ii) the generation of Auger-electrons and (iii) the emission of secondary electrons. Which process is preferred depends mainly on the atomic number *Z* and the energy level, e.g. in the hard X-ray regime (>2 keV) X-ray fluorescence is the dominating relaxation process, whereas at lower energies and for low *Z*-elements the Auger emission occurs favorably. X-ray fluorescence occurs when an electron from a higher shell fills the core hole. The fluorescence energies are element specific and can distinguish e.g. between Kα- (relaxation of 2p electrons into the core-hole) and Kβ-fluorescence (relaxation of 3p electrons) emission. The X-ray fluorescence is directly proportional to the absorption probability of an incident photon by a core electron.

XAS spectrum

Figure 2-2 illustrates X-ray absorption (XAS, right) and emission spectra (XES, left) of an iron-containing protein sample. The energy diagrams in the inset represent the corresponding absorption and emission transition processes at the K-edge.

A core level electron of the absorber (e.g. an iron 1s electron) can be excited (i) to higher unoccupied levels (resonant excitation) or (ii) into the continuum (non-resonant excitation, photoelectron generation) when the energy of the incident X-ray photon is sufficiently high. The **XAS spectrum** (Figure 2-2, right) can be divided into three regimes, which provide complementary information regarding the absorbing element as well as its neighboring atoms or ligands. The X-ray Absorption Near Edge Structure (**XANES**) spanning the energy region around the absorption edge follows the weak so-called **pre-edge region**. The Extended X-ray Absorption Fine Structure (**EXAFS**), starting ~50 eV above the edge, shows modulation of the absorption due to backscattering processes. If the energy of the incident X-rays is too low to excite electrons of the absorber, this results in a structureless absorption background. Whereas

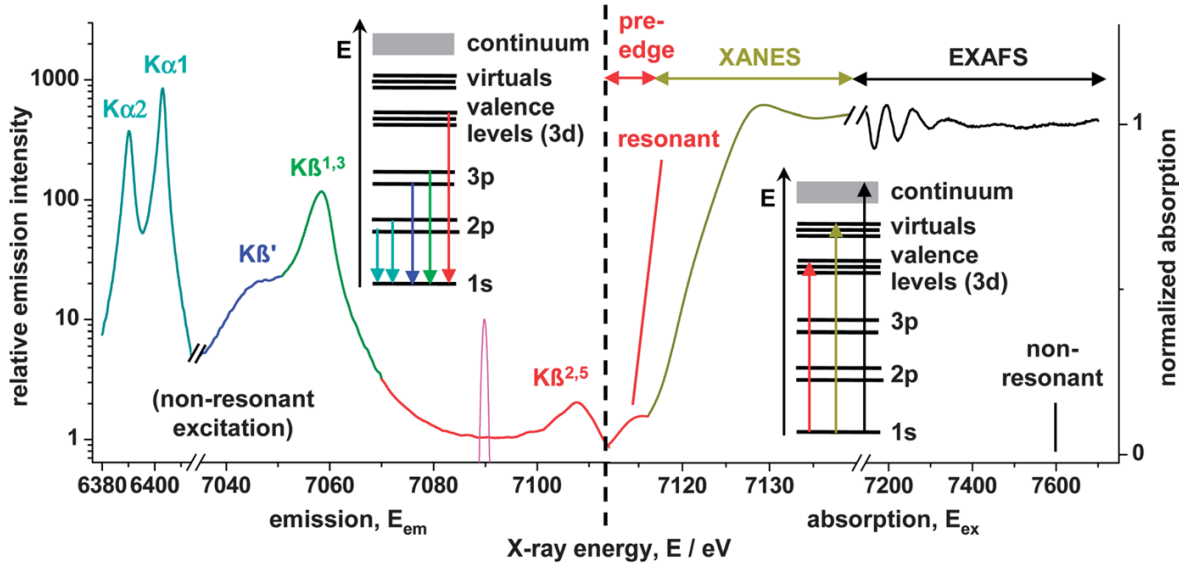

*Figure 2-2: Schematic representation of X-ray absorption (**right**) and emission (**left**; note the logarithmic y-axis) spectra of iron in a protein sample on a common energy scale. Reproduced from [133] with permission from The Royal Society of Chemistry.*

the spectrum around the absorption edge (pre-edge and XANES) is sensitive to electronic and geometric properties of the absorber (e.g. oxidation state and local symmetry) the analysis of the EXAFS oscillations provides geometric information on the surrounding atoms, such as absorber-ligand distances as well as coordination numbers and chemical nature of neighboring atoms. A more detailed description of the individual XAS regions is given below.

(i) The **pre-edge absorption** (resonant core-to-valence excitation, ctv) provides information on the site symmetry as well as the oxidation state and spin state of the absorber [279]. This feature stems from transitions into unoccupied valence states and the analysis of their energies and intensities enables determination of electronic properties (redox and spin state, molecular orbital (MO) configuration) of metal centers in proteins and inorganic compounds. For first-row transition metals, the 1s core electron can be excited into 3d valence states for open-shell elements (for example Zn contains a fully occupied 3d shell and no pre-edge feature is observed at the K-edge)[233]. With respect to the selection rules for photoelectric absorption (dipole $\Delta l \pm 1$; spin $\Delta s = 0$) [287], this quadrupole-allowed but dipole-forbidden 1s⟶3d excitation results in a weak pre-edge feature. However, the intensity can increase due to mixing of 4p and 3d metal orbitals arising by deviation from ideal octahedral symmetry at the absorber, i.e. distortion of centrosymmetry [279]. In general, the larger the distortion of the local geometry, the stronger the 3d-4p-mixing and thus the pre-edge feature will be [279]. The oxidation state of the metal site affects the pre-edge energy position, in that generally a higher oxidation state

of the metal results in a higher pre-edge energy for compounds with similar ligand systems. Furthermore, the analysis of the energy splitting of pre-edge features enables estimation of the d-level degeneracy. Density functional theory (DFT) can be used to calculate theoretical ctv XAS spectra (see Chapter 3), which is essential for in-depth interpretation of experimental pre-edge data.

(ii) The analysis of the energy of the sharp rise in absorption, the so-called absorption edge (**XANES**), can provide information regarding the oxidation state of the absorber atom, whereas the edge shape and amplitude is sensitive to the number and chemical identity of ligands. For first-row transition metals, the K-edge absorptions result mainly from dipole-allowed 1s → 4p excitations ($\Delta l = \pm 1$). The edge energy is proportional to the metal oxidation state and can be evaluated by different approaches (see section on data processing). In general, an increasing oxidation state of the absorber leads to an increasing edge energy [188, 285], i.e. for metals with similar ligation environment, an increase of ~1-4 eV per oxidation state occurs [126]. It should be noted, however, that other factors such as the spin state [159] or different ligand environments (see Chapter 4) also affect the K-edge energy. Simulation of the edge shape is sophisticated and therefore the analysis is often carried out in a more qualitative way by comparison to reference spectra of known model compounds.

(iii) The fine structure above the edge (**EXAFS** oscillation) provides information about chemical element, number and distance of neighboring atoms and in certain cases also information about bond angles [126]. The sinusoidal, damped oscillation of the absorption $\mu(E)$

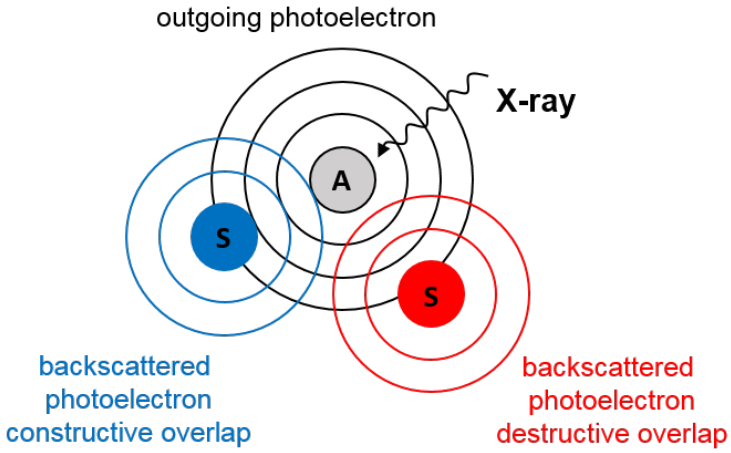

Figure 2-3: Scheme of single X-ray backscattering for two atoms (S) around the absorber (A). The backscattered photoelectron waves can interfere constructively (blue) or destructively (red). Constructive interference results in a local maximum and destructive interference in a local minimum in the EXAFS oscillation.

is caused by the neighboring atoms, i.e. if no surrounding atoms are present, no oscillation is observed (e.g. for noble gases)[225]. The EXAFS oscillations can be explained with scattering theory. The generated photoelectron, resulting from the absorption of an X-ray photon by the 1s core-electron and excitation into the continuum, can be represented by a spherical outgoing electron wave with a wavelength λ proportional to $(E-E_0)^{-1/2}$. The energy of the photoelectron is the difference between incoming X-ray photon energy (E) and binding energy of the excited core electron (E_0). When the emitted wave hits a neighboring atom, the wave is backscattered. The fine structure is then created by interference of the outgoing and backscattered photoelectron waves, resulting either in constructive or destructive interference (depending on the wavelength λ and thus on the energy of the photoelectron) and thereby causes the absorption modulation.

The EXAFS function $\chi(E)$ (i.e. the modulation of the X-ray absorption coefficient $\mu(E)$) can be calculated using Eq. 3. It is the difference between the total X-ray absorption coefficient $\mu(E)$ (measured) and the absorption coefficient of the isolated atom μ_0, normalized to the absorption edge $\Delta\mu_0$.

$$\chi(E) = \frac{\mu(E) - \mu_0(E)}{\Delta\mu_0(E)} \tag{3}$$

For correlating the modulation of $\chi(E)$ with molecular structural parameters, the EXAFS-function is converted to a wavelength-dependent function $\chi(k)$ using Eq. 4, where the photoelectron wave-vector k is inversely proportional to the de Broglie wavelength λ of the photoelectron wave and has the dimension of reverse distance ($\hbar$ = Planck constant, h/2π).

$$k = \frac{2\pi}{\lambda} = \frac{\sqrt{2m_e}}{\hbar}\sqrt{(E - E_0)} \approx 0.5\sqrt{(E - E_0)} \tag{4}$$

E_0 is the energy of the absorption edge or rather the binding energy of the photoelectron with mass m_e (the so-called threshold energy for excitation of the core electron, apparent Fermi energy). The EXAFS formula for single scattering processes represents the oscillation as the sum of the individual scattering paths, Eqs. 5 and 6.

$$\chi_{total}(k) = \sum_i \chi_i(k) \tag{5}$$

$$\chi(k) = \sum_{i}^{n} \frac{S_0^2(k) N_i}{k {R_i}^2} f_i(\mathrm{k}) \exp\left(-\frac{2R_i}{\lambda(k)}\right) \exp\left(-2\sigma_i^2 k^2\right) \sin(2kR_i + \Phi_{0i}(k)) \quad (6)$$

Equation 6 consists of two parts describing the amplitude and frequency of the oscillation. The amplitude term contains the coordination number *N* of the i-th shell, the distance *R* between absorber and backscatterer (of the i-th shell), the backscattering amplitude function *f(k)* (depending on the type of backscatterer) as well as additional amplitude damping terms. (i) The amplitude reduction factor S_0^2, which considers that both single and multiple excitation of electrons can occur at the absorbing atom, (ii) the first exponential term with the mean free path of the photoelectron takes into account inelastic losses in the scattering process due to the fact that both photoelectron and core-hole have finite lifetimes, and (iii) the second exponential term containing the Debye-Waller factor σ^2 reflecting thermal and static disorder in the system. The frequency of the oscillation is represented by the sine function depending on distance *R* between absorber and backscatterer and the phase shift Φ_i.

The following effects on the EXAFS signal are observed due to variation of the parameters in the EXAFS formula [261, 287]: (a) The amplitude increases linearly with the coordination number *N* for a given distance. (b) Increasing the interatomic distance *R* leads to reduction of the amplitude by $1/R^2$ and simultaneous increase of the frequency. (c) The type of backscatterer affects the amplitude envelope. Increasing the atomic number leads to increased scattering amplitudes and the maximum of the amplitude shifts to higher *k* values. (d) Reduction of the structural disorder σ^2, for example by lowering the temperature, diminishes thermal vibrations so that only static disorder contributes, which causes diminished damping of the oscillation. (e) The choice of the energy range for the measurement and thus the k-range influences the distance resolution according to $\Delta R = \pi/2\Delta k$. The EXAFS for simple scattering processes contains only paths from the absorber to the scatterer and directly back to the absorber. The excited X-ray photoelectron may also be scattered by two or more neighboring atoms so that multiple-scattering paths contribute to the EXAFS. The combination of XAS with high-resolution X-ray emission spectroscopy (XES) provides access to site-selective chemical information by exploiting different spin- and oxidation states of the same atom type in a given sample (further details in section 2.2).

Experimental setup

Figure 2-4 illustrates a typical setup for XAS experiments (e.g. at beamlines KMC-1, KMC-3; SAMBA; SuperXAS): a monochromatic X-ray beam hits a sample and the incoming and transmitted X-rays intensities as well as the intensity of X-ray fluorescence are recorded. It follows a brief description of the individual components of XAS setups.

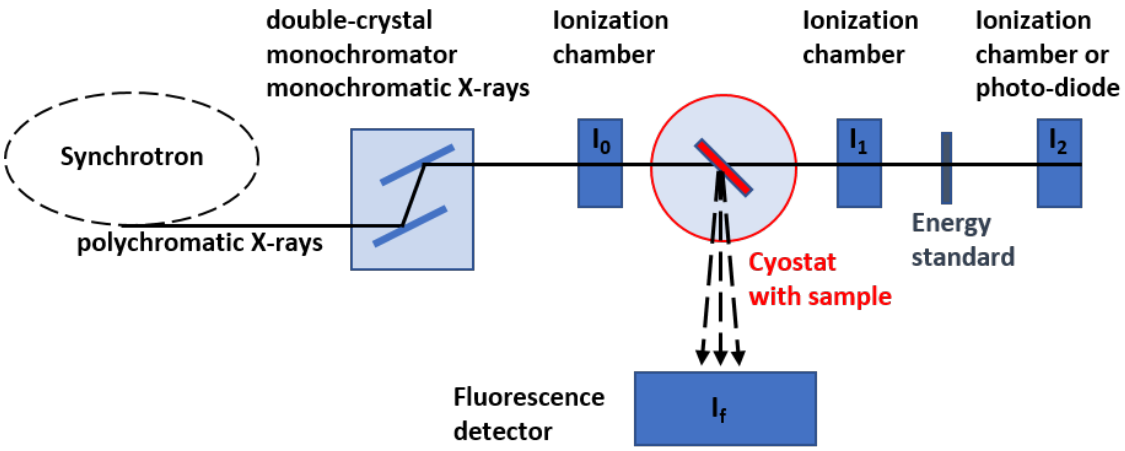

Figure 2-4: Scheme of the experimental setup for standard X-ray absorption spectroscopy.

Synchrotron radiation sources provide polychromatic linear polarized X-ray beams with very high intensities, high stability and small divergence. The generated "white beam" is monochromatized by a double crystal monochromator and focused and size adjusted by additional mirrors and slits. Common are Si[111] monochromators. A higher resolution can be achieved with Si[220] or Si[311] monochromators, but with loss of photon flux. The intensity of the incident as well as transmitted X-ray beam is measured with ionization chambers (IC). While the first IC (I_0) measures the intensity of the incoming beam, the second and third chambers (I_1, I_2) are used to measure the beam intensities after interacting with the sample and with the energy standard used for energy calibration. For calibration of the energy axis an energy standard with known absorption edge energy (e.g. metal foil) is measured simultaneously with the sample. The sample itself is often located in a liquid He-cooled cryostat in a heat-exchange gas (He) environment (e.g. at 20 K).

Concentrated samples (e.g. powders) can typically be measured in transmission mode, and the absorption is calculated from the logarithmic ratio of transmitted (I_1) and incoming (I_0) X-ray intensity (Eq. 7).

$$\mu(E) = -log\left(\frac{I_1}{I_0}\right) \quad (7)$$

Biomolecules are typically measured in fluorescence mode, because the concentration of the absorbing atoms is usually low. The fluorescence detector (usually a multi-element energy resolving solid-state detector with Ge or Si crystals as X-ray absorbers) is placed perpendicular to the incoming beam and in the horizontal plane to minimize elastic scattering and maximize the fluorescence signal, i.e. the sample is rotated 45° with respect to the incident beam and the emitted fluorescence is detected at an angle of 90°, see Figure 2-4. Additionally, a filter foil ("Z-1" filter) may be placed between sample and detector to attenuate elastic scattering contributions from the incident beam. The fluorescence intensity (I_f) is directly proportional to the X-ray absorption coefficient (Eq. 8).

$$\mu(E) \sim \frac{I_F}{I_0} \quad (8)$$

Data processing

Figure 2-5 shows the general steps of the extraction of EXAFS oscillations from experimental X-ray absorption spectra. The data processing procedure is illustrated by the example of an Fe-foil measured in transmission mode. Data processing was performed with in-house software. The data for fluorescence as well as transmission measurements were treated in the same way. The transmission (I_1) or fluorescence (I_F) signals were converted to $\mu(E)$ using Eq. 9 or 10, respectively.

$$\mu(E) = -ln\left(\frac{I_1}{I_0}\right) \quad (9)$$

$$\mu(E) = \frac{I_F}{I_0} \quad (10)$$

After detector dead-time correction and energy calibration, several spectra were averaged to yield the final spectrum of the sample. Energy calibration was carried out by using the absorption of an energy standard (e.g. metal foil), see Figure 2-4. The first maximum in the derivative of the reference spectrum was fitted with a Gaussian function plus first order polynomial and shifted to the reference energy (e.g. for Fe-foil, 7112 eV). Subsequently, the background of the averaged spectrum $\mu(E)$ was subtracted by a linear fit in a range before the edge. In the next step the spectrum was normalized by dividing through a polynomial function

(2^{nd} or 3^{rd} order) in the EXAFS region. The resulting normalized spectrum $\mu(E)$ represents the absorption of one X-ray photon per metal ion and can be used for XANES analysis.

The extraction of the EXAFS oscillations ($\chi(E)$ spectrum) included fitting the range after the absorption edge with a polynomial spline function (number of knots 3-5) and dividing the spectrum by the spline function. The spline function represents the background absorption of an atom without neighbors. The selected threshold energy E_0 of the absorption edge was subtracted from the energy axis. The resulting energy scale (E-E_0) was converted into wave vector (k) scale (Eq. 4) and the $\chi(k)$ spectrum was reduced to ~100-150 data points equidistant in k-space. The oscillation was weighted with k^3, to compensate the damping of $\chi(k)$ with increasing k. This results in about uniform oscillation amplitudes over the entire k-range. The Fourier transform (FT) from $\chi(k)$ into R-space enables visualization of the absorber-backscatter interactions, i.e. the structural information from EXAFS becomes directly accessible. The maxima in the FT correspond to coordination shells of neighboring ligands at certain distance from absorber. The peak position refers to the mean distance R (note that the reduced distance is ~0.4 Å smaller than the real distance [252]) and the peak amplitude is related to the coordination number N and the Debye-Waller-factor σ^2.

EXAFS simulations were performed with the in-house software SimXLite (developed by Dr. Petko Chernev). The program FEFF [207, 208] was used to calculate phase-functions for EXAFS fitting. The parameters N_i, R_i, σ_i and S_0^2 from the EXAFS equation (Eq. 6) were fitted to the data in k-space using the calculated phase-functions. The fit quality was evaluated by the filtered R-factor representing relative deviations between experimental and simulated spectra after Fourier-filtering in a given R-range. EXAFS analysis provides ligand-absorber distances with an accuracy of ~0.02 Å, a value much better than that determined by protein XRD. The error in coordination numbers is relatively higher (~20%) due to strong correlation between N and σ.

Figure 2-6 shows the data processing steps for XANES (A) and pre-edge (B) spectra for the example of an iron-containing compound $[Fe_2(\mu\text{-adt})(CN)_2(CO)_4]^{2-}$ (adt, azadithiolate; structure see Chapter 4). The measured fluorescence spectra are dead-time corrected, energy calibrated and normalized to I_0 (Eg. 10). Like the EXAFS data processing the averaged XANES spectra are background subtracted (by a straight line) and normalized by dividing by a polynomial function (1^{nd} or 2^{rd} order, depending on the measured energy range). The pre-edge features are subtracted from the normalized XANES spectrum or the separately measured pre-edge spectrum by a polynomial background.

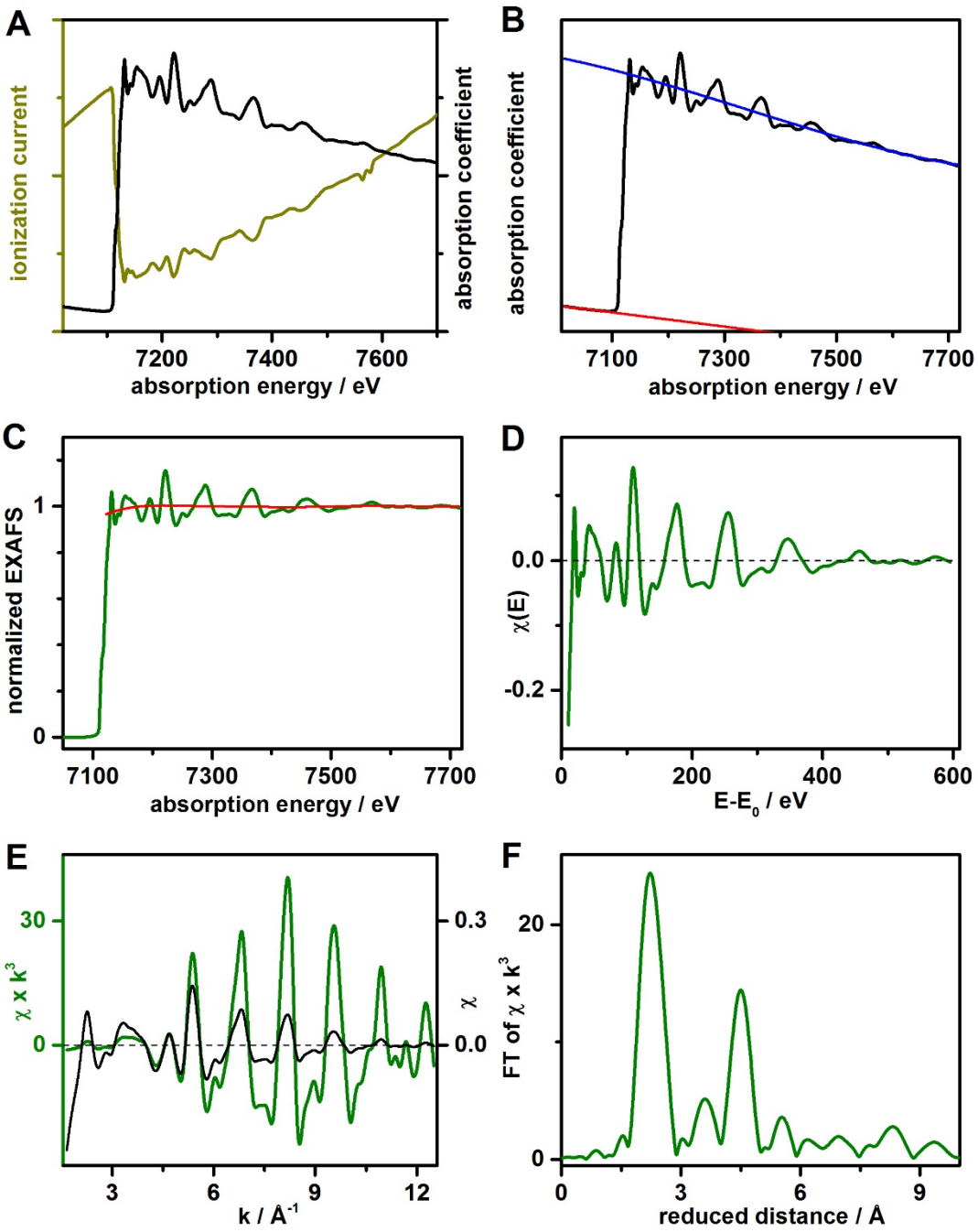

Figure 2-5: EXAFS data evaluation.
*(**A**) Raw X-ray absorption spectrum for Fe foil, transmission signal (black) and absorption signal (dark yellow). (**B**) X-ray absorption μ(E), background (red line) and polynomial (blue line) for normalization. (**C**) Normalized spectrum μ(E) (green) and post-edge background (red line) (**D**) χ(E) spectrum. Note the (E-E$_0$) energy axis. (**E**) Transformation of the energy scale to a vector scale leads to the EXAFS spectrum χ(k) (black) and k-weighted k^{3}χ(k) EXAFS (green). (**F**) Fourier transform of the k^3-weighted spectrum.*

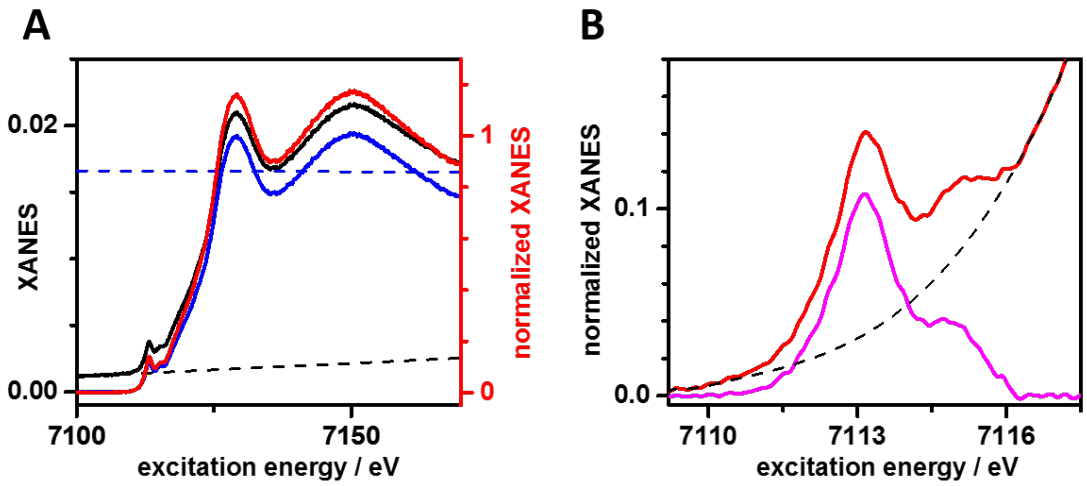

*Figure 2-6: Data processing for (**A**) XANES and (**B**) pre-edge spectra for an iron-containing compound. (**A**) Final XANES spectrum (red) after subtracting of a straight line (black dashes) from the raw data (black), followed by division by a polynomial function (blue dashes) results in the normalized spectrum (blue). (**B**) Final pre-edge spectrum (pink) after subtracting of a polynomial background (black dashes) from the normalized XANES (red).*

In general, there are three different ways to determine the K-edge energy: (i) the inflection-point method, (ii) the half-height method and (iii) the integral method [49]. In the first method the edge energy is considered to be equal to the first zero-crossing point of the second derivative of $\mu(E)$ in the XANES [163]. The second method utilizes the edge half-height, i.e. the edge energy corresponds to a normalized μ-value of 0.5. This approach was used here. In the last method, the edge energy is determined by the mean energy value in a selected edge region [49]. The correlation between formal oxidation state and edge energy determined by the different methods was studied in reference [49] for various manganese compounds, which revealed that the integral method and the half-height method provide an approximately linear relation between metal oxidation state and K-edge energy, while the inflection-point method is not suitable for reliable edge energy determination.

For concentrated samples, it is necessary to correct the fluorescence-detected XAS spectra for the so-called self-absorption effect. Uncorrected data may lead to erroneous XANES peak heights and attenuated amplitudes of EXAFS oscillations leading to too low coordination numbers. As a rule-of-thumb, if the sample absorbs more than 20%, a correction of the fluorescence (*Fluo*) data using transmission data (*Abs*) is required (Eqs. 11 and 12, k and A are fit parameters) to obtain the corrected fluorescence signal ($Fluo_{corr}$).

$$Fluo = A\,(1 - \exp\,(-k\,Abs)) \tag{11}$$

$$Fluo_{corr} = \frac{-ln\,(1-(-Fluo/A))}{k} \tag{12}$$

Figure 2-7 illustrates the self-absorption correction for the example of a concentrated powder sample of a nickel complex. The nickel compound absorbs more than 50% of the incident X-rays (see Figure 2-7A) and therefore, the resulting fluorescence spectrum (Figure 2-7B) must be corrected (Figure 2-7C).

Further details of data processing are given in the Material and Methods sections of the respective Results Chapters.

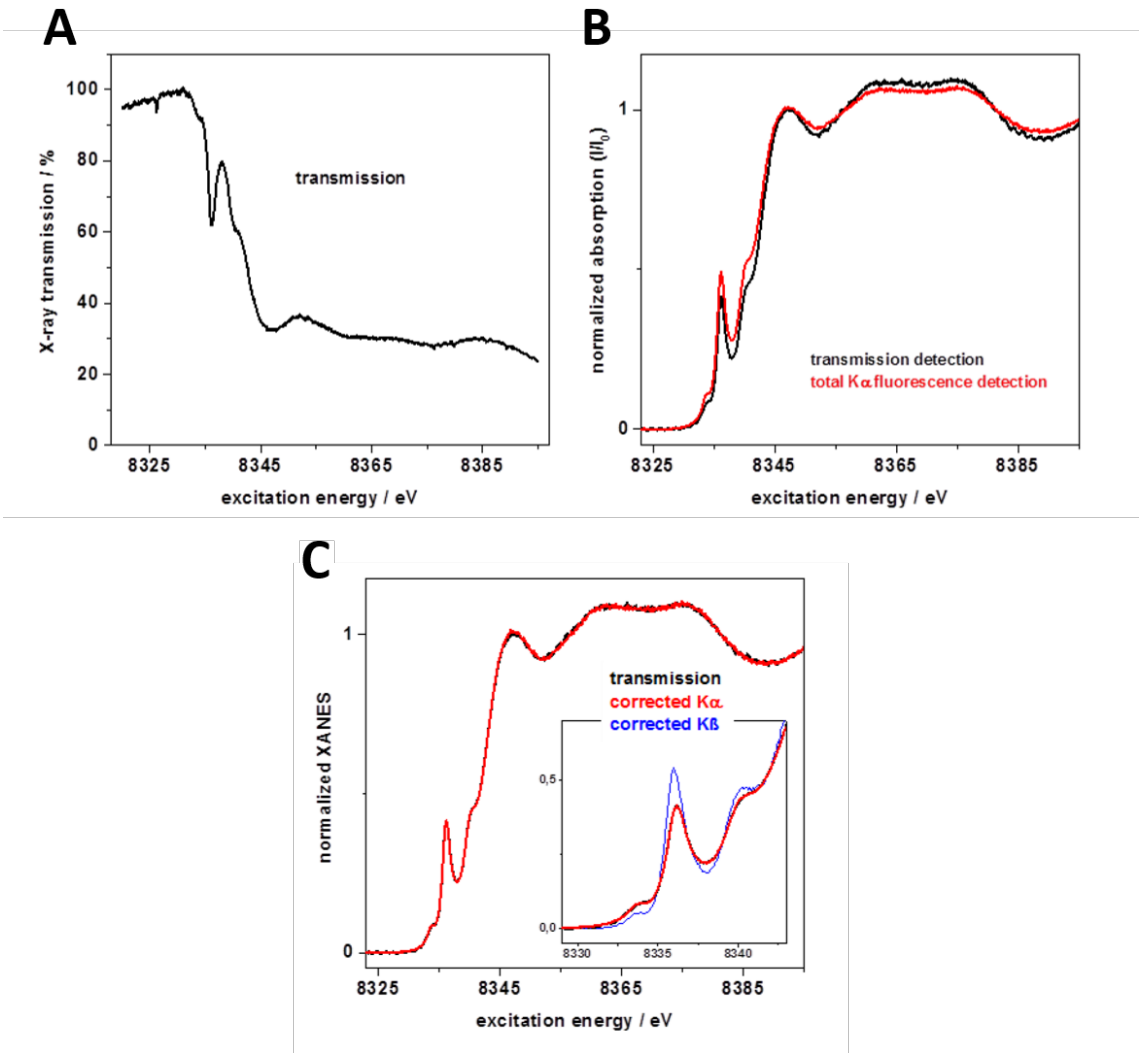

*Figure 2-7: Self-absorption correction for fluorescence-detected XAS spectra of a concentrated powder sample of a nickel complex. (**A**) Raw transmission-detected K-edge spectrum (black). (**B**) The normalized transmission-detected (black) and the uncorrected total Kα-fluorescence (red) spectrum. (**C**) The normalized corrected Kα- (red) and Kβ-detected (blue) spectrum and transmission-detected (black) spectrum, (inset: pre-edge region). Reproduced from [192] with permission from The Royal Society of Chemistry.*

2.2 XES

X-ray fluorescence emission arises as a consequence of the absorption of an X-ray photon by a core level electron and thus can be considered as a second-order optical process [18]. In the fluorescence process the electron vacancy of a low lying orbital is filled with a valence electron, which is accompanied by the emission of an X-ray photon. X-ray emission spectroscopy (XES) measures these emitted fluorescence X-ray photons. When the emission event results from refilling a 1s core hole (K shell), the emerging emission lines are called K fluorescence emission lines. Basically, XES can be divided into (i) non-resonant and (ii) resonant XES. In the first case, the core electron is excited into the continuum by an incident X-ray photon whereas in the second case the core electron is excited into higher unoccupied levels (see also Chapter XAS).

X-ray emission spectra of metalloenzymes and transition metal compounds provide information about metal oxidation and spin state [76], as well as ligand environment [20] and can be considered as a complementary method to XAS. While XAS provides insights in the unoccupied molecular orbitals (MOs), X-ray emission spectroscopy (XES) probes the occupied MOs (see energy diagrams in Figure 2-2 representing these processes at the K-edge). XES exhibits the same advantages as XAS, e.g. it is element-specific and applicable to all aggregate and spin states. Limitations of this technique include the obligatory use of a synchrotron light source and especially, for measurement of the weak high energy features (i.e. Kβ satellite lines) due to the relatively low intensity in this region, the requirement for reasonable sample concentration and, in some cases, even advanced measurement techniques.

XES spectrum

In addition to the XAS-spectrum (right), the emission spectra (XES, left) of an iron-containing protein sample is shown in Figure 2-2. The plot on the same energy scale clarifies the direct correlation between spectral regions. The energy diagrams in the inset represent the corresponding absorption and emission transition processes at the K-edge. The XES spectrum can be divided into three different regions. (i) The strong K-shell fluorescence line, Kα is followed by (ii) up to an order of magnitude weaker Kβ main-lines and (iii) the even weaker Kβ satellite lines, the so-called valence-to-core (vtc) emission.

(i) Origin of Kα emission is refilling of the created core hole by a 2p→1s transition resulting in a doublet line (Kα1+2) due to the 2p spin-orbit coupling. These lines show a moderate sensitivity to the metal spin state [278].

(ii) The **Kß main-lines** results from 3p→1s transitions, i.e. occur when 3p electrons refill the 1s vacancy. Due to the 3p-3d exchange interaction this transition contains two features, the main $K\beta_{1,3}$ line and a weaker Kβ' line at lower energy. The occurrence of a Kβ' feature and the splitting between both features ($K\beta_{1,3}$ and Kβ') becomes larger (i.e. the $K\beta_{1,3}$ shifts to higher energies, e.g. compare high-spin and low-spin Mn(III) compounds [187] or Fe(III)/Fe(II) compounds [137]) with increasing valence spin (i.e. with increasing number of unpaired electrons) and thus greater 3p-3d exchange coupling [76]. Hence, the overall Kβ main-line shape can be used as a marker for the local metal spin state [137]. Both shape and energy of the $K\beta_{1,3}$ line are sensitive to the spin and oxidation state and can also be affected by ligation changes (e.g. ligand types, number and geometry of the ligands, metal-ligand bond covalency) [35, 76, 133, 137, 140, 196, 289]. Furthermore, the strong dependence of the main-line features on metal spin and valence state can be exploited for advanced site-selective XAS measurements in multinuclear metal compounds (see below).

(iii) At the tail of the Kβ main-line the **Kβ satellite lines** occur resulting from refilling the 1s core hole with a valence electron (for example 3d→1s decay). The valence-to-core (vtc) transitions originate from molecular orbitals with metal valance character along with dominant ligand character and can split into two features, denoted Kβ'' and $K\beta_{2,5}$, regarding transitions from ligand ns or np to the metal 1s orbital. These features, which are more than three orders of magnitude weaker than the Kα line, are highly sensitive to the ligand environment including ligand identity, number of ligands, and protonation state changes, as well as metal oxidation and spin state. The energy of the Kβ'' peak relative to the $K\beta_{2,5}$ provides information about the ligand identity, enabling distinction between ligands with similar atomic numbers (e.g. nitrogen and oxygen), which it not possible in EXAFS [20, 76, 137, 194]. The intensities of the Kβ'' transitions can be used to estimate the number of ligands and their bond lengths [20, 76, 290]. In general, shorter metal-ligand bonds lead to a more intense vtc features [138]. The Kβ satellite line can also provide information regarding the ligand protonation state, e.g. for investigation of protonation of metal-bridging ligands [136, 137]. Protonation tends to reduce both the energy and the intensity of the vtc features [136, 195], resulting in changes in Kβ'' (shift to lower energy) and small variations in $K\beta_{2,5}$. Furthermore, the energy of the $K\beta_{2,5}$ transition is sensitive to the oxidation state [20, 137, 290] and the intensity is sensitive to the metal spin state [137]. Vtc XES spectra can be combined and analyzed with quantum chemical calculations, e.g. ground-state DFT calculations are used for interpretation of intensities and energies of experimental Kβ satellite line features [137] (for further details, see Chapter 3).

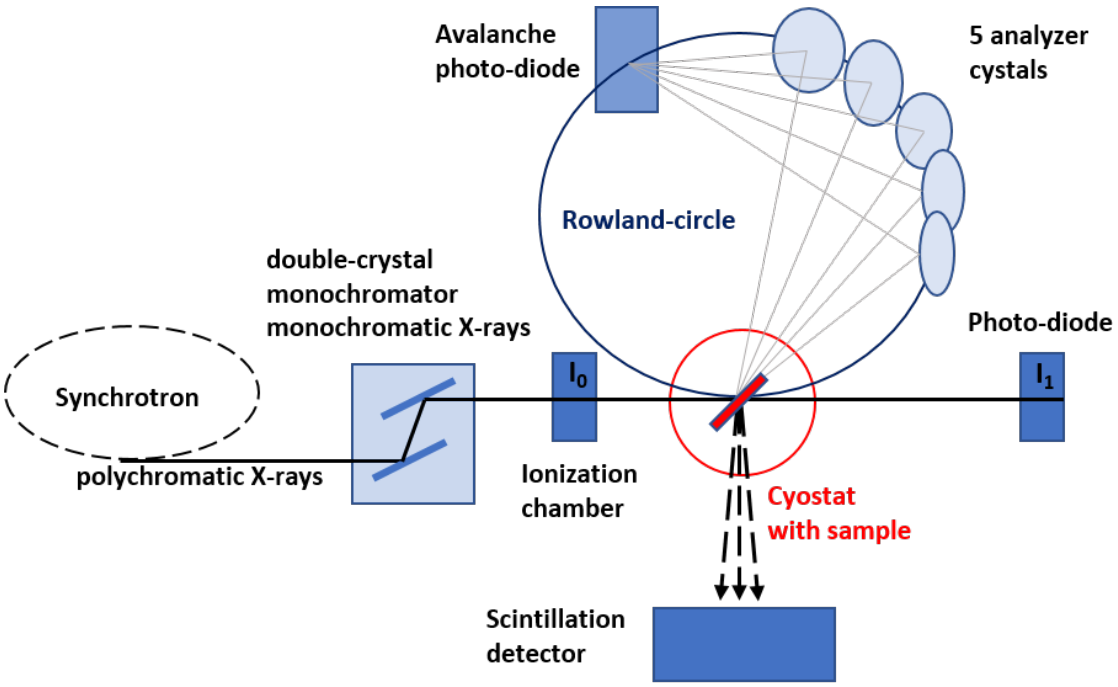

Figure 2-8: Scheme of the experimental setup for high-resolution XES/XAS measurements at the ID26 at ESRF. The double-crystal monochromator is used to select the energy of the incident X-ray and the analyzer crystals choose the energy of the fluorescence emission spectrum [76].

Figure 2-8 illustrates the setup for combined high-resolution XAS and XES experiments at the beamline ID26 (ESRF). An Si[311] double crystal monochromator is used to select the excitation energy (with 0.2 eV energy bandwidth). The intensity of the incident X-ray beam is measured with an ionization chamber before it hits the sample. The sample is oriented with an angle of 45° relative to the incident beam and held in a liquid-helium cryostat. The transmitted X-ray beam is detected by a photodiode. A vertical-plane Rowland-type spectrometer with analyzer crystals (e.g. five Ge[620] single crystals for Fe K-edge measurements) and an avalanche photodiode (APD) detector are used to achieve high energy-resolution emission detection (energy resolutions around 1 eV). Sample, analyzer crystals as well as the detector are arranged in the Rowland-circle geometry (diameter of 1 m) [195]. For collection of Kβ emission spectra, the energy is scanned (by simultaneously changing the Bragg angles of all analyzer crystals [18]) over the main- or satellite line region with a constant energy step size (e.g. 0.35 eV) [138]. Measuring the weak Kβ satellite lines of samples which suffer rapid X-ray photoreduction requires an advanced measurement approach, the so-called time resolved energy-sampling technique (see Chapter 7 and ref. [289]). The setup at ID26 allows also the

measurement of conventional K-edge absorption spectra (XANES and EXAFS), where the total X-ray fluorescence (mostly Kα emission) is monitored with a large-area scintillation fluorescence detector (located around 1 m from the sample). Energy calibration (monochromator and emission spectrometer) is assured by using the absorption of a corresponding powder sample (e.g. $KMnO_4$) or metal foil (Fe-foil) with known energy and the elastic scattering peak as references [35, 133].

For data evaluation, the separately measured Kβ main-line and satellite line emission counts were divided by I_0 and averaged. The spectra were measured with overlapping energy ranges for normalization (see Figure 2-9A inset). For this, the satellite line spectra were scaled to the tail of the main-line. Form the resulting Kβ emission spectra a small offset level (background correction) was removed before normalizing to unity area in the entire Kβ region (not shown). Figure 2-9B shows the raw, the background corrected (blue line) as well as isolated Fe valence-to-core emission spectra. For the extraction of the Kβ satellite line features (Figure 2-9B; pink line) the contribution from the high-energy tail of the $K\beta_{1,3}$ fluorescence was removed by using a background curve (Figure 2-9B, blue dashed line) [35]. The energy of the $K\beta_{1,3}$ emission line can be estimated from the calculation of the first moment M in a selected energy window by Eq. 13 [289]:

$$M = \frac{\sum[E_i \times I(E_i)]}{\sum[I(E_i)]} \tag{13}$$

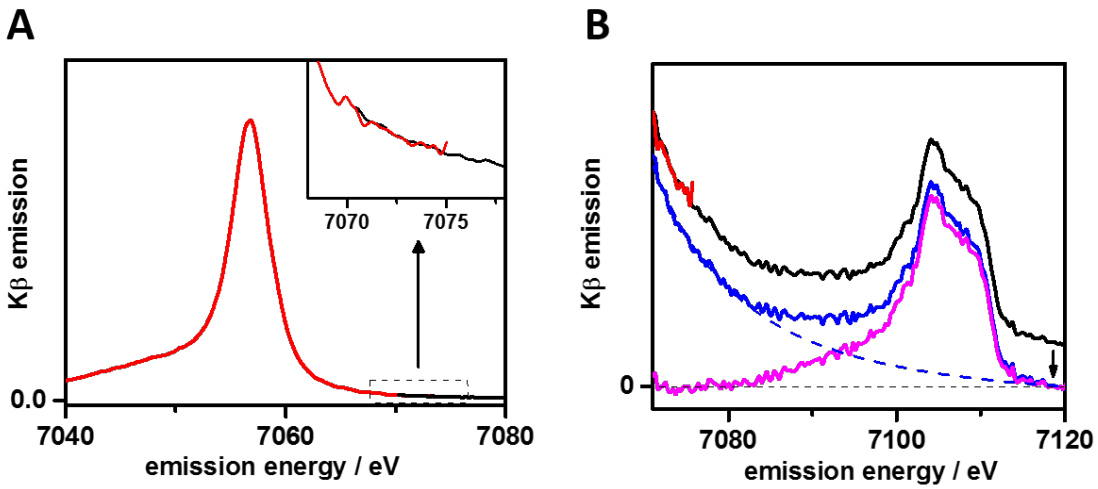

*Figure 2-9: Data processing for Kβ emission spectra for an iron-containing compound. (**A**) Experimental Kβ main-line (red) and satellite line (black) emission spectra collected with overlapping spectral ranges (see inset). (**B**) Satellite line emission spectra before (black) and after (blue) removal of an offset level. Extracted vtc emission spectra (pink).*

Combined high-resolution XAS and narrow-band detection XES:

The combination of high-resolution XAS and narrow-band detection XES offers the possibility of site-selective spectroscopic discrimination of metal sites in multinuclear compounds with respect to their different spin states, oxidation states, or coordination environment [35]. As previously shown, the emission energies in high-resolution Kβ main-line emission spectra correlate with both the oxidation state and the spin state of the metal center. Because the $K\beta_{1,3}$ and Kβ' features correspond to different spin orientations, by XAS detection using the $K\beta_{1,3}$ or Kβ' emission, spin-selective K-edge absorption spectra including pre-edge features can be obtained, e.g. distinction between low- and high-spin iron sites of the two subsites of the H-cluster in the hydrogenase protein [35], see also Chapter 5. An example of site-selective XAS measurements in mixed-valence compounds can be found in ref [77]. Valence-selective EXAFS measurements for Prussian blue, which contains two irons in different oxidation and spin state (high-spin Fe(III) and low-spin Fe(II)) were performed by using the chemical sensitivity of the $K\beta_{1,3}$ main-line, i.e. low and high energy $K\beta_{1,3}$ emission detected EXAFS spectra. Another example for site-selective XAS are Kβ-detected pre-edge measurements on asymmetric diiron model compounds [138], where both iron sites contain the same spin and oxidation state but a different coordination environment.

2.3 NRVS

Nuclear Resonance Vibrational Spectroscopy (NRVS; also termed nuclear inelastic scattering, NIS) is a synchrotron-based technique, which is related to Mössbauer and Raman spectroscopy and can be regarded as a combination of nuclear resonance of ^{57}Fe (classical Mössbauer effect) and detection of phonons (molecular vibrations, similar to Raman).[220] In NRVS, excitation or annihilation of phonons coincident with excitation of the nucleus are observed. Thus, the measured absorption spectrum shows vibrational sidebands in addition to the recoilless resonance.[221]

The NRVS method provides exclusively vibrational modes involving displacement of the Mössbauer-active nucleus (usually ^{57}Fe) [220] and thus offers for example information about metal-ligand vibrations at active sites in iron-containing metalloproteins. Besides the often used ^{57}Fe NRVS spectroscopy other Mössbauer isotopes such as ^{83}Kr or ^{119}Sn can be investigated, e.g. by synchrontron Mössbauer spectroscopy [4, 221, 272]. NRVS is a difficult technique for proteins, because of low count rates, and only a handful of publications about NRVS experiments on Fe-containing proteins are available ([75, 123, 130, 132, 157, 160, 221]). Another benefit of this method, in addition to its strict element specificity, is the applicability to all oxidation and ligation states [291]. Although NRVS resembles Raman spectroscopy, it is not restricted to the optical selection rules of conventional vibrational methods such as Raman and infrared (IR) spectroscopy. Thus, NRVS can be used as a complementary technique providing access to all vibrational modes including the ^{57}Fe nucleus.

There are only few synchrotron radiation sources with beamlines facilitating NRVS experiments, including the beamlines ID18 at ESRF in France and P01 at PETRA III in Germany, as well as beamlines at Spring-8 in Japan and at sources in the United States [272]. Usually, special operation modes of the storage ring are required for nuclear resonance measurements, i.e. time spacing of bunches should be as long as the lifetime of the resonant nucleus ($\tau = 141$ *ns* for ^{57}Fe) [255]. For ^{57}Fe-NRVS experiments at ID18, the 16-bunch mode with a time window of 176 ns between 16 adjacent bunches of the same size (see Figure 2.11C) or the hybrid mode are suitable of NRVS. Due to the low natural abundance of ^{57}Fe (2.14%), enrichment of samples with the isotope mostly is necessary, especially for bioinorganic samples. Isotope-enriched metalloprotein samples can be prepared, e.g. by ^{57}Fe enrichment during protein reconstitution [272, 291]. Due to site-specific labeling, an analysis of site-selective vibrational information in materials with multiple iron sites [221] is also

possible.[160]. Detailed descriptions of the NRVS method (underlying physics as well as experimental details) and application examples can be found in refs. [4, 184, 217, 220, 255, 272, 291].

Theory and NRVS spectrum

Figure 2-10 illustrates the energy level scheme for the ^{57}Fe nucleus, where the nuclear excited states have the spin quantum numbers *I=1/2* and *I=3/2*. Absorption of a 14.413 keV photon leads to excitation of the nuclear ground-state. The nuclear excited state decays mostly via excitation of a 1s electron to the continuum followed by core hole refill and emission of a Fe K-fluorescence photon (~6.4 keV).[291] The lifetime of the Kα fluorescence therefore reflects the lifetime of the nuclear excited state (for ^{57}Fe, $\tau = 141$ *ns*). The relatively long lifetime allows separation of the prompt elastic scattering signal from the NRVS signal in a time-resolved fluorescence detection scheme (i.e. recording the Kα fluorescence with ~1 ns time resolution and starting at ca 10 ns after the X-ray pulse) after each exciting synchrotron bunch.[291] By tuning the energy of the incident X-ray photons around the nuclear resonance transition energy in the range of ~100 meV the ^{57}Fe nucleus is excited with or without simultaneous excitation (Stokes) or deexcitation (anti-Stokes) of molecular vibrational modes (i.e. phonon creation or annihilation) [255, 256].

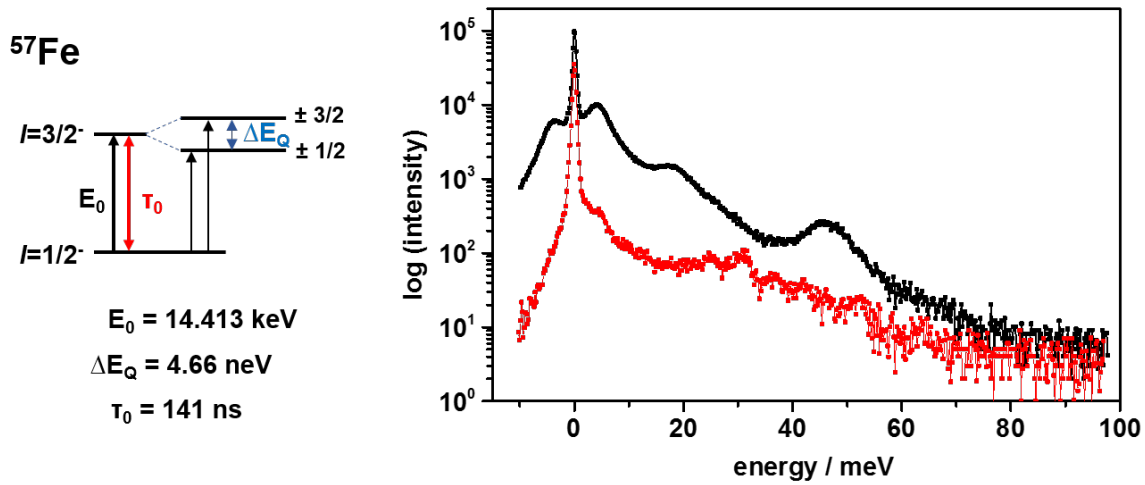

*Figure 2-10: **Left**, energy level scheme for ^{57}Fe. The nuclear excited state of ^{57}Fe with an excitation energy E_0 = 14.413 keV has a relatively long lifetime (τ_0 =141 ns) and a very narrow energy width (ΔE_Q = 4.66 neV). **Right**, as an example, the measured NRVS spectrum of a ^{57}Fe containing inorganic compound ($FeCl_2$, solved in H_2O (black)) and a ^{57}Fe-recontrituted protein sample (GkR2lox- FeFe (red)).*

Figure 2-10 shows the measured NRVS spectrum for a ^{57}Fe enriched inorganic and bioinorganic sample. The spectrum consists of three regimes, the anti-Stokes region (negative energies, E < 0), the resonance peak around E = 0 and the Stokes region (positive energies, E > 0). The resonance peak is due to the recoilless absorption of the ^{57}Fe nucleus at the nuclear transition energy of E_0 = 14.413 keV. The features in the positive and negative energy regions indicate vibrational modes with contributions from the ^{57}Fe nucleus [220].

Experimental setup and data processing

Figure 2-11A illustrates the experimental setup for NRVS at the undulator beamline ID18 at the ESRF. "White" X-rays are generated by an undulator and the pulsed beam is monochromatized in two steps by a heat-load monochromator (HHL) and a high-resolution monochromator (HRM) before it passes through the ionization chamber (which monitors the

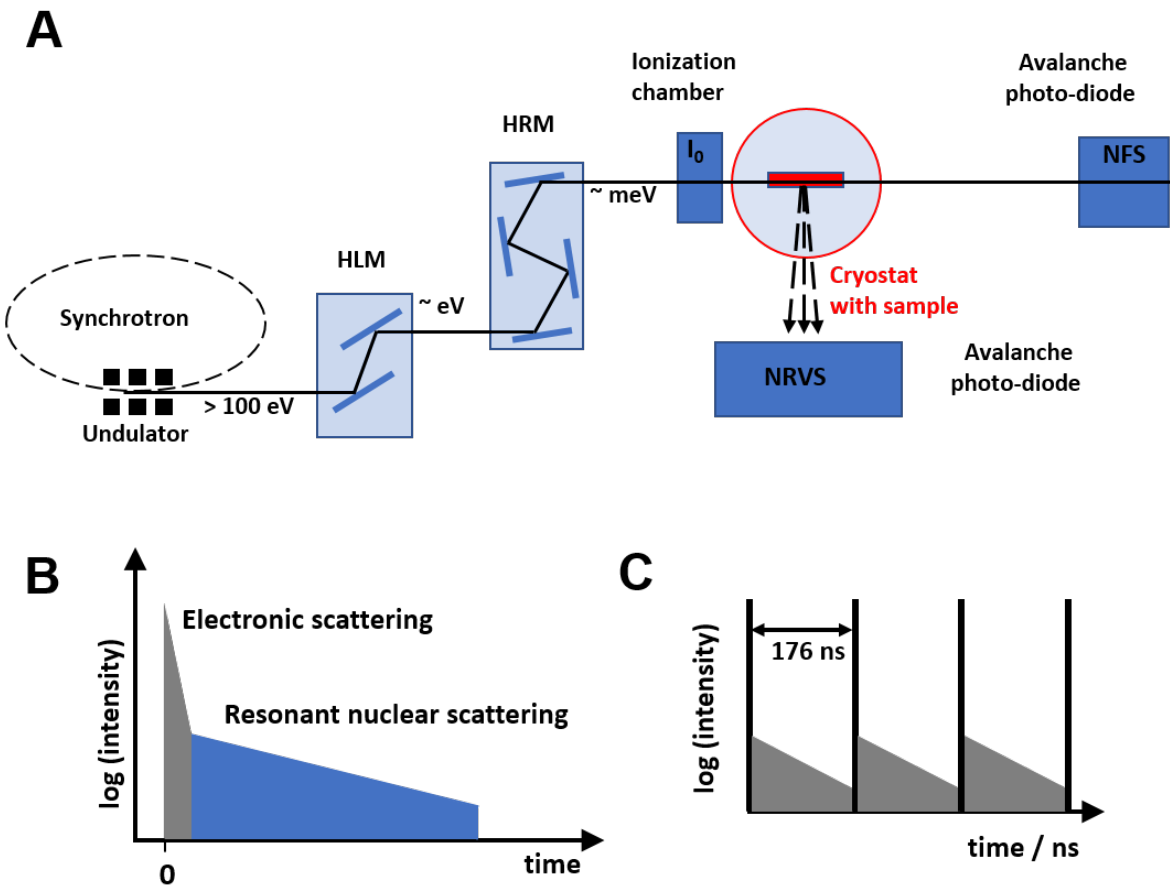

*Figure 2-11: (**A**) Scheme of the experimental setup for NRVS measurements at the ID18 at ESRF. Description of the individual components is in the text. (**B**) Illustration of scattered intensity versus time after excitation of a resonant nucleus by synchrotron radiation pulse. The prompt scattering from electrons (~100 MHz) is followed by the delayed fluorescence signals from the nuclear resonance absorption (~100 Hz). (**C**) Illustration of 16-bunch SR operation mode at the ESRF. (Note the logarithmic y-axis in B and C.)*

intensity of incident beam) and hits the sample. The sample was located in a cold-finger cryostat. The HHL reduces the energy bandwidth from the white beam to a few eV. The HRM is used to tune the energy of the X-ray beam over a range where the probability for excitation or annihilation of vibrations is relatively high (e.g. within ±100 meV off the 14.4 keV resonance of ^{57}Fe) [255]. The energy resolution of the HRM was ~0.75 meV (FWHM). The X-ray fluorescence was monitored with an avalanche photodiode (APD) positioned at ~1 mm to the sample at 90 ° relative to the incident X-ray beam (NRVS detector) [272]. A second APD was located in forward direction and at ~2 m to the sample and monitored the nuclear forward scattering signal (NFS detector) [291]. Proper timing and detection electronics facilitated separation of prompt and delayed fluorescence emission [291] (Figure 2.11B). See refs. [255, 272] for detailed description.

NRVS data were analyzed with the software package available at the beamline ID18. The software requires as input (i) data files corresponding to the samples and the monochromator resolution function and (ii) the sample temperature. Figures 2-12A - D illustrate NRVS data evolution for $FeCl_2$ solution samples. The spectra were recorded between -10 meV to 90 meV in 0.2 meV steps and normalized to incident beam intensity. To improve the signal-to-noise ratio, multiple scans of the same sample are averaged (Figure 2-12A). The experimental NRVS spectrum is dominated by the elastic scattering line at E = E_0. This feature reflects the HRM energy resolution function (Figure 2-12B) [291]. It was removed using an instrumental function monitored with the NFS detector by subtraction from the raw spectrum. Subsequently, the pDOS (partial vibrational density of states) is calculated from the spectrum (Figure 2-12C, see [37, 38] for the theoretical background of pDOS calculation). The pDOS spectrum (Figure 2-12D) provides information on vibrational frequencies (1 meV = 8.07 cm^{-1}) and amplitudes, i.e. the observed peaks can be assigned to molecular vibrational modes of the material [185]. The vibrational modes from the NRVS experiment can be compared with calculated modes, e.g. from DFT calculations [221]. The sample temperature (for individual spectra) was calculated using the ratio of anti-Stokes (n_-) to Stokes (n_+) intensities of NRVS spectra in a certain energy range (ΔE) according to Eq. 14 (T, temperature; k_B, Boltzmann constant).[255] Figure 2-12E shows an example of temperature determination.

$$T = \frac{\Delta E}{ln\left(\frac{n_+}{n_-}\right) k_B} \qquad (14)$$

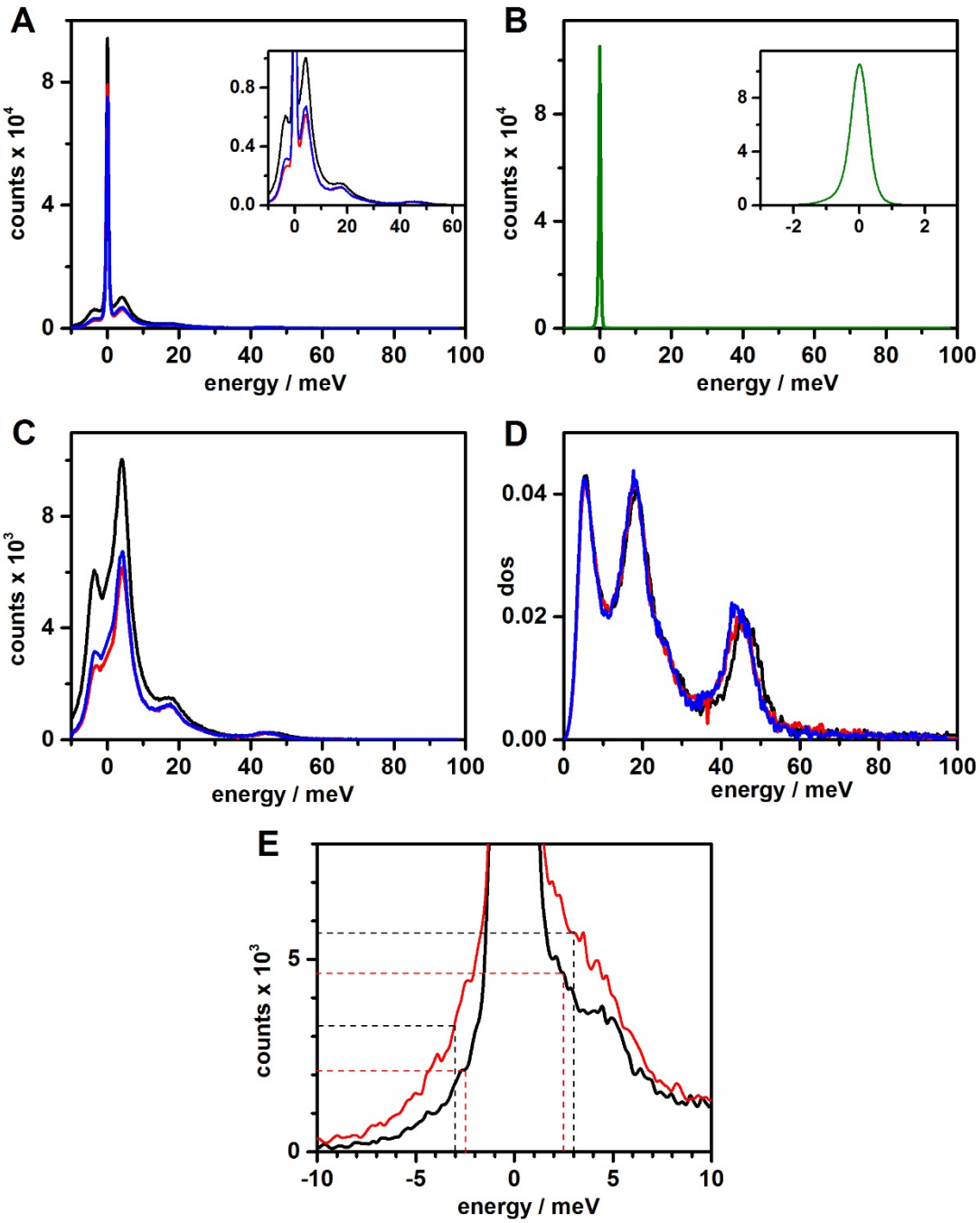

*Figure 2-12: (**A-D**) NRVS data processing. Shown are data for 0.5M $^{57}FeCl_2$ dissolved in 100% H_2O (black), D_2O (red) and $^{18}OH_2$ (blue). (**A**) Four scans each were averaged to obtain the respective raw spectra. (**B**) Energy resolution function of the HRM (green). (**C**) Spectra after subtraction of the elastic peak. (**D**) pDOS spectra of the respective samples. (**E**) Determination of sample temperature exemplified for two ^{57}Fe-reconstituted protein samples.*

2.4 TXRF

Total reflection X-ray fluorescence analysis (TXRF) is an established analytical technique to determine the content of metals or other elements in a sample [116, 117, 283]. It relies on quantification of X-ray emission lines. The TRXF measurements in this thesis were performed with the S2 PICOFOX spectrometer[1] from Bruker. Figure 2-13 shows the basis components of a TXRF spectrometer.

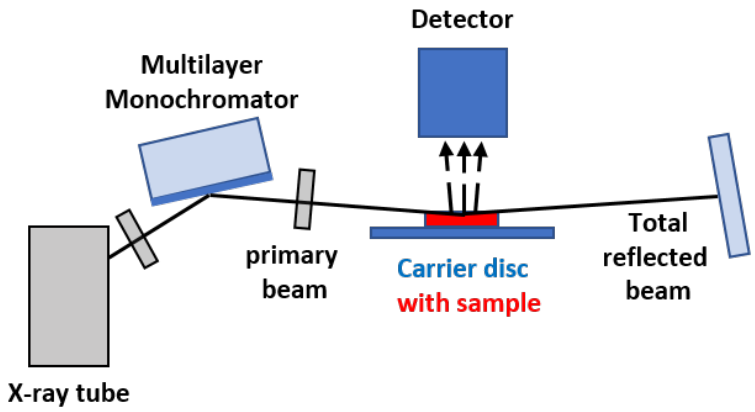

Figure 2-13: Scheme of a TXRF spectrometer. Here, the PICOFOX instrument from Bruker was used.

Data analysis

Figure 2-14A illustrates the TXRF-spectrum of a clean quartz glass carrier. In addition to the peak of the scattered molybdenum primary radiation (from the Mo X-ray tube), the K-fluorescence line of silicon from the quartz glass and a peak of argon arising from the fluorescence of Ar in air appear in the spectrum. As an example, a TRXF spectrum of a ligand-binding oxidase protein sample with a manganese/iron cofactor including an internal standard (Ga) is shown in Figure 2-14B. TXRF provides quantitative analysis of elements in the sample. To calculate the concentration of the elements in the sample the addition of an internal standard with a known concentration is necessary. For first-row transition metal containing protein samples, a gallium solution was used as internal standard. If the protein concentration is known, one can estimate the stoichiometric ratios of metals present in metalloenzymes. For statistical data processing, several sample solutions of the same sample (with or without internal standard)

[1] https://www.bruker.com/de/products/x-ray-diffraction-and-elemental-analysis/micro-xrf-and-txrf/s2-picofox/overview.html

are prepared and at least two sample carriers were loaded with the same solution. Finally, the measured concentrations are averaged for all sample replicates.

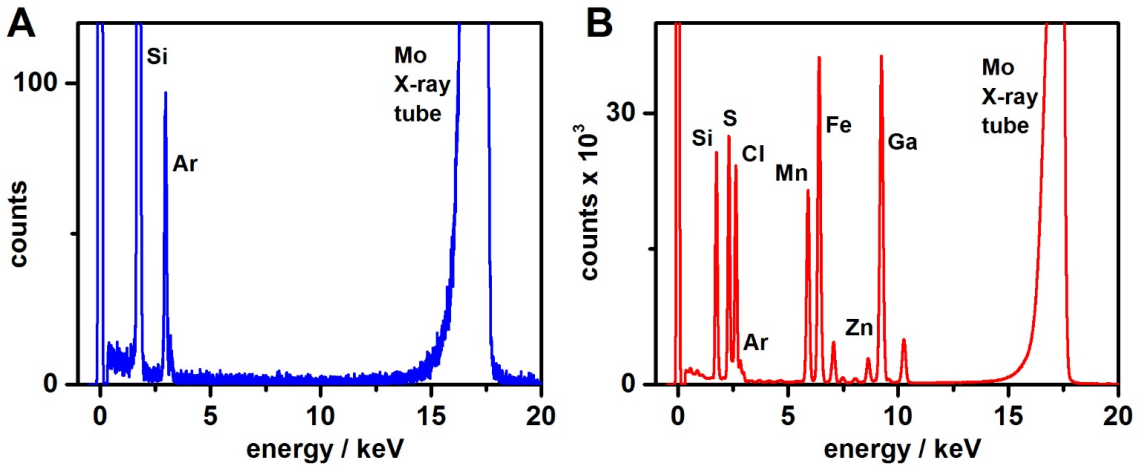

*Figure 2-14: (**A**) Spectrum of a clean TXRF sample carrier (e.g. quartz glass carrier). (**B**) Spectrum of a protein sample with a manganese/iron cofactor and a protein concentration of ~3 mM.*

3 Quantum Chemistry Calculations (DFT)

3.1 General aspects of density functional theory

Density functional theory (DFT) is a well-established method to calculate molecular properties (e.g. geometries, energies, and spectroscopic parameters). There are a number of monographs [119], several book chapters (see e.g. [43, 103, 104]) as well as review articles [173, 182] on DFT available. The theoretical basis of DFT is given by the theorems of Hohenberg and Kohn (presented in 1964, [100]). The first (existence theorem) states that the electronic ground-state energy and all other physical properties of a system can be determined entirely by the electron density ρ. The second theorem (variations theorem) proves that the electron density is subject to the variation principle, i.e. the ground-state energy can be determined variationally and the correct electron density of the ground-state minimizes the total energy of the system ($E[\rho] \geq E_0^{exact}$).

A general expression of the (total) energy of a system (in terms of its density) within the Born-Oppenheimer approximation (BON) is given by Eq. 15, where T is the kinetic energy, E_{ee} the electron-electron interaction and E_{ne} the attraction between the nuclei and electrons. In analogy to the Hartree-Fock (HF) theory, E_{ee} can divided into a coulomb (J) and an exchange (K) part.

$$E[\rho] = T[\rho] + E_{ee}[\rho] + E_{ne}[\rho] \tag{15}$$

$$E[\rho] = T[\rho] + J[\rho] + K[\rho] + E_{ne}[\rho] \tag{16}$$

The idea of the Kohn-Sham formalism (1965, [120]) is to employ n 1-electron calculations with non-interacting electrons instead of one calculation of an n-electron system with interacting electrons. Consequently, the electron-electron interaction has to be included into the calculations by exchange-correlation parameters affecting the model electron density. Thus the kinetic energy can be divided into two parts, yielding an exactly calculated (for the non-interacting electron gas) and a small unknown term. Accordingly, the DFT energy can be expressed as:

$$E_{DFT}[\rho] = T_{nw}[\rho] + E_{ne}[\rho] + J[\rho] + E_{XC}[\rho] \tag{17}$$

Where T_{nw} is the kinetic energy of a non-interacting system and E_{xc} the exchange-correlation energy.

The major limitation of DFT is the unknown exact formula for the exchange-correlation functional, i.e. if the exchange-correlation functional would be known exactly, the exact ground-state energy could be calculated using the DFT approach. The great benefit of using the electron density instead of the wave function for the theoretical calculation is the fact that the number of variables depends only on three parameters (i.e. the spatial coordinates of the three dimensions) instead of *n*-variables.

3.2 Functional and basis set selection

As mentioned above, the exact expression of the exchange-correlation term is unknown. Therefore the chosen approximation of the exchange-correlation functional determines the "quality" of the DFT calculations. $E_{XC}[\rho]$ can be divided into an exchange part ($E_X[\rho]$) and a correlation part ($E_C[\rho]$). In general, each exchange functional can be combined with any of the correlation functionals [119]. There exist many methods, e.g. local (spin) density approximation (LDA and LSDA), generalized gradient approximation (GGA), hybrid methods and further functionals (so-called meta-GGA functionals or double hybrid functionals).

In this thesis two different types of exchange-correlation functionals were used for DFT calculations, one GGA (BP86) and two hybrid functionals (B3LYP, TPSSh). In the Gradient Corrected or Generalized Gradient Approximation (GGA), the exchange and correlation functional also depend on the gradient of the electron density and thus considers the local density as a non-uniform electron gas, which leads to an improvement compared to the LSDA approach. The used **BP86** functional includes the Becke exchange (1988) and the Perdew correlation (1986) functional [13, 189]. Calculations with this functional yield good results for geometries and vibrational frequencies in short computing times. It has been shown, that the inclusion of exact Hartree Fock (HF) exchange can improve the calculated results [104] at the expense of longer computing times. The Hybrid functional (or hyper-GGA method) is composed of DFT exchange-correlation with exact HF exchange. The **B3LYP** functional, which is one of the most popular functionals in chemistry for calculating molecular structures, energies as well as electronic properties, is a three parameter functional and the experimentally determined coefficients are $a_0 = 0.20$, $a_x = 0.72$ and $a_c = 0.81$ [14].

$$E_{XC}^{B3LYP} = (1 - a_0)E_X^{LSDA} + a_0E_X^{HF} + a_X\Delta E_X^{B88} + a_CE_C^{LYP} + (1 - a_C)E_C^{VWN}$$

TPSSh, is a so-called hybrid meta-GGA on the basis of the TPSS functional, which was augmented with ~10% exact HF exchange [104, 105], which is lower than the 20% exact HF exchange used in B3LYP.

In general, each molecular orbital (MO) can be described using linear combination of basis functions χ (BF), i.e. the basis set (BS). Ideal basic functions should reflect the shape of atomic orbital (AO) and, on the other hand, their use should be time efficient. Therefore often Gaussian-type orbitals (GTO) are used as BF instead of the more precise but more demanding Slater-type orbitals (STO). The accuracy of the calculated results depends not only on the used functional, but also on the chosen basis sets. In this thesis, the triple-zeta valence plus polarization (**TZVP**) basis set of Ahlrichs et al. [219] was mostly used in the DFT calculations. TZVP is a split-valence BS composed of a minimal basis set for the inner shell and three BFs for the valence orbitals. It contains a polarization function, which adds orbitals with higher angular momentum for each atom (except hydrogen).

3.3 Geometry optimization and normal mode analysis

DFT calculations are typically used for geometry optimization of the examined system, i.e. searching of global or local minima on the potential energy surface (PES) and these stationary points represent equilibrium geometries of the molecules. Gradient optimization techniques use the first (and partly also the second) derivative of the energy in relation to the coordinates. In general, the optimizing process begins with a starting geometry and after several optimization cycles, the iterative procedure ends when the optimization converges (convergence criteria, e.g. change in energy or geometry between two cycles is below a threshold). While short and strong metal-ligand bonds can be accurately predicted, weaker metal-ligand bonds are typically overestimated in length. The achieved optimized structures of small molecules or structures are usually in good agreement with results from XRD or EXAFS.

After the geometry optimization, a calculation of the vibration frequencies is typically performed to characterize the stationary point, i.e. if the solution represents a minimum or a saddle point. The normal mode analysis is performed by determining the second derivative of the energy with respect to the Cartesian coordinates (Hessian matrix). If the analysis reveals an imaginary frequency, i.e. a negative frequency (i=0, 1 or >1), the true minimum was not reached. Importantly, the calculated vibrational frequencies can be used to simulate IR, Raman as well as NRVS spectra [173, 182].

3.4 Generation of theoretical X-ray spectra

Both the pre-edge absorption features (core-to-valence) and the satellite Kβ emission spectra (valence-to-core) can be calculated with quantum chemistry methods based on DFT. Whereas the ctv features result from transitions that arise due to excitation of a 1s level core electron into unoccupied metal orbitals (3d or low-lying virtual orbitals), the vtc features are caused by electronic decay of valence electrons (ligand s- or p-character) to the 1s core hole. For interpretation of energies and intensities of the experimental ctv and vtc spectra, it is necessary to understand the electronic structure of the material under investigation. Combination of advanced X-ray spectroscopy with DFT calculations facilitates correlation of the spectroscopic features on the one hand and of electronic and molecular structures on the other hand, providing electronic excitation/decay transition energies and probabilities, valence level configurations, as well as ligand type, metal spin and oxidation state, protonation states, and metal-ligand bond lengths.

Spin-unrestricted single-point DFT calculations based on crystal or geometry-optimized structure coordinates were carried out to compute the X-ray emission or absorption spectra. For further analysis and comparison to experimental data, the calculated ctv or vtc stick spectra were broadened by Lorentzian or Gaussian line shapes and shifted in energy (see Figure 3-1). The used shift of the energy axis (e.g. ~182.5 eV) depends on the used theory level (i.e. it is different for varying functional and basis set combinations). The intensity of the calculated spectra reflects the sum of electronic dipole, magnetic dipole and electronic quadrupole contributions, the dipole transitions being the major contribution (> 95% of the total intensity) [195]. The calculations provide MO energies and metal/ligand characters, giving access to a thorough understanding of the resulting spectra, i.e. a chemical interpretation of the underlying electronic state. Additionally, for a more quantitative analysis, experimental as well as theoretical vtc and ctv spectra can be simulated by the sum of several (e.g.) Gaussian functions to derive the main peak amplitudes and energies of the spectral features (see Chapter 4). Generally, we observed that the experimental ctv and vtc spectra can be reasonably simulated by DFT with a suitable functional/basis set combination (see for example [137] and Chapter 4). In conclusion, comparison between experimental XAS/XES data and calculated ctv and vtc spectra from DFT facilitates benchmarking of correlations between molecular structures and electronic configurations.

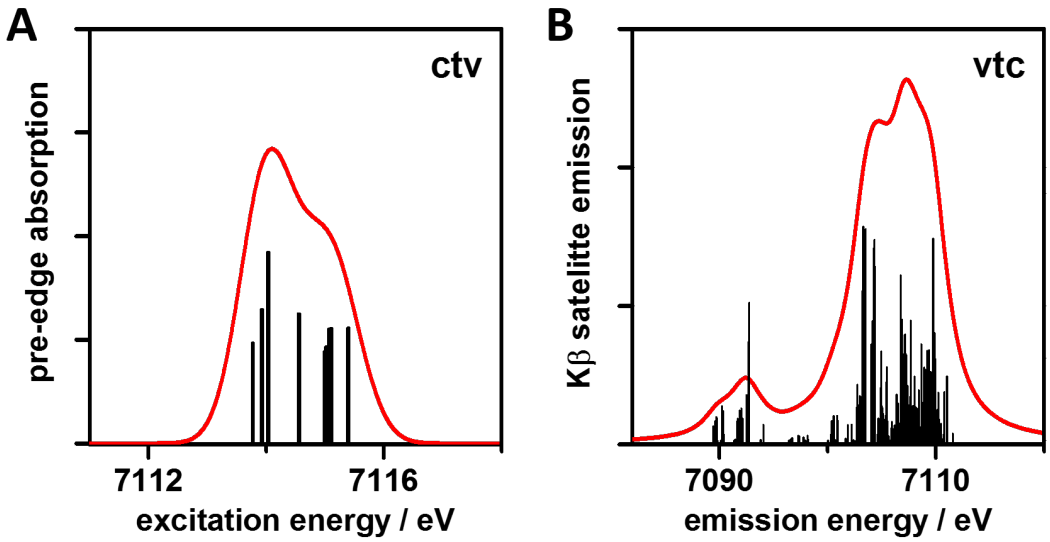

*Figure 3-1: (**A**) ctv and (**B**) vtc stick spectra (black) from DFT calculation. Red, spectra after Gaussian (ctv) and Lorentzian (vtc) broadening and energy shifting of stick spectra for an oxidase protein.*

Theoretical NRVS/pDOS spectra were calculated using NISspec [185] based on vibrational frequencies derived from normal mode analysis of relaxed molecular structures. Lorentzian broadening of calculated vibrational modes in the pDOS data was applied for comparison with experimental NRVS spectra (see Figure 3-2). For a more quantitative analysis of the NRVS spectra, individual metal-ligand vibrations were assigned based on the calculations.

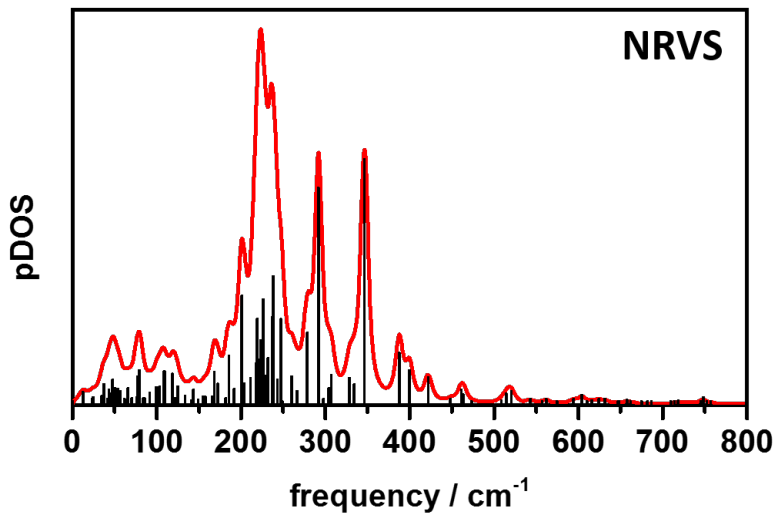

Figure 3-2: Calculated NRVS spectra from DFT calculation. Red, pDOS spectra after Lorentzian broadening of stick spectra (black) for an oxidase protein.

Examples of Gaussian09 input files for geometry optimization and frequency analysis and ORCA input files for spectral calculations are given in the Appendix (see Appendix Chapter 7). Further details of DFT calculations are given in the Material and Methods sections of the respective Results Chapters.

Overview of used programs and X-ray facilities

For the XAS, XES and NRVS measurements, beamlines of different synchrotron facilities in Europe were visited. Standard XAS measurements were performed at the SAMBA beamline of the SOLEIL (Paris, France), SuperXAS beamline of the Swiss Light Source (Paul Scherrer Institute, Villigen, Switzerland) and the beamlines KMC-1 and KMC-3 at BESSY (Helmholtz-Zentrum für Materialien und Energie, Berlin, Germany). High-resolution XAS and XES measurements were carried out at the beamline ID26 of the European Synchrotron Radiation Facility (ESRF, Grenoble, France). The NRVS measurements were done at the beamline ID18 at the ESRF.

All quantum chemical calculations presented in this thesis were carried out on the Soroban, Sheldon, and Yoshi computer clusters of the Freie Universität Berlin. Geometry optimizations and normal mode analysis were performed with GAUSSIAN09 [73]. The core-to-valence region of the XAS spectra and the valence-to-core region of the XES spectra were calculated with the ORCA quantum chemistry program [174] using different theory levels (varying functional and basis set combination, solvation model, and broken-symmetry approach as described in the respective Chapters). Theoretical NRVS/pDOS spectra were obtained from the NISspec program [185].

II Results

(A) Hydrogenase enzymes and biomimetic compounds

Scientific background

Hydrogenases are metalloenzymes which catalyze the formation of dihydrogen and the reverse reaction, the cleavage of H_2 into electrons and protons:

$$2H^+ + 2e^- \rightleftharpoons H_2 \quad . \tag{18}$$

They are widespread in nature and occur in archaea, prokaryotes and some eukaryotes (e.g. fungi and green algae). Numerous review articles regarding the classification, maturation and function of hydrogenases have been published in the last 20 years (see for example the "Hydrogen" special issue in *Chemical Reviews* in 2007 and refs. [148, 172, 191]). These enzymes contain transition metal cofactors and are classified according to the metal ion composition of their active sites as [NiFe]-, [FeFe]- and [Fe]-hydrogenases (Figure A-1). A common feature of [NiFe]-and [FeFe]-hydrogenases is the unusual ligation of the iron atoms of the sulfur-bridged bimetallic center by CO and CN^- ligands. Both enzymes contain also at least one iron-sulfur [FeS] cluster. In [Fe]-hydrogenases, which contain only a mono-iron active site coordinated by a bidentate guanylylpyridinol, one cysteine sulfur and two CO ligands, the FeS clusters are absent and they need a second substrate (methylentetrahydromethanopterin) to activate hydrogen. This third class is only occurring in methanogenic archaea.

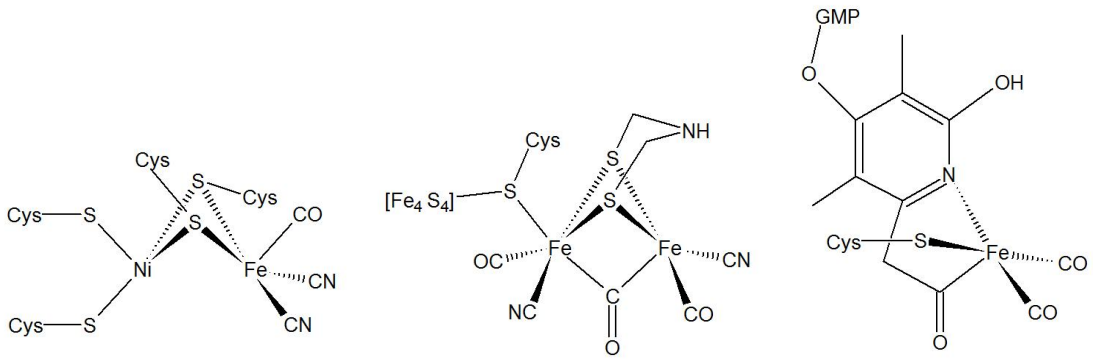

Figure A-1: Chemical structures of the active sites of the three classes of hydrogenases. ***Left****, [NiFe]-hydrogenase;* ***middle****, [FeFe]-hydrogenase;* ***right****, [Fe]-hydrogenase (Cys = cysteine; GMP = guanosinemonophosphate).*

Hydrogenases usually can catalyze both the H_2-uptake and the H_2-formation reaction, i.e. they are bidirectional depending on the physiological context in the cell. In general, [FeFe]-hydrogenases are more active in H_2 formation and [NiFe]-hydrogenases are more active in H_2 oxidation. Some [FeFe]-hydrogenases can generate up to ~10^4 molecules of H_2 per second at room temperature [32, 148, 254]. This capacity qualifies the [FeFe]-hydrogenase for renewable energy applications. Determination of their structure and function as well as understanding of their enzymatic reaction may contribute significantly to the design of "artificial hydrogenases", which may lead to novel non-platinum hydrogen conversion catalysts [65].

In contrast to [NiFe]-hydrogenases, which are reversibly inhibited by O_2 or even oxygen-tolerant, [FeFe]-hydrogenases are very oxygen-sensitive and their catalytic activity is irreversibly inhibited when the enzymes are exposed to O_2 [134, 253]. Detailed analysis of the O_2-inhibition of the active site of HydA1 from *Chlamydomonas reinhardtii* algae was done in 2011 by Lambertz et al. [134]. Their results from X-ray absorption spectroscopy at the Fe K-edge revealed a three phase mechanism of "H-cluster degradation". The first step is the initial binding of a superoxide (O_2^-) ligand at the distal iron of the [2Fe] subsite of the active site [134, 160, 250, 258]. It is assumed that O_2^- protonation is necessary to form reactive oxygen species (ROS), which induce the structural decomposition, as visible in crystal structures [258]. Recently, Mebs et al. have shown that the protonation can be prevented by interruption of the proton pathway to the active site by mutation of the amino acid Cys169 to alanine (C169A) and therefore the bound superoxide ligand can be stabilized which prevents the formation of mobile ROS [160]. Noth et al. have shown that the depletion of adjacent water molecules by lyophilization of the [FeFe]-hydrogenase can be used to stabilize the oxygen-sensitive hydrogenase cofactor (see Chapter 6) [180].

The crystal structures of the periplasmic [FeFe]-hydrogenase from the bacterium *Desulfovibrio desulfurian*s (*Dd*) and the cytoplasmic [FeFe]-hydrogenase from the bacterium *Clostridium pasterianum* (*CpI*) were provided in the late 1990`s [178, 183, 190] and revealed the structure of the cofactor of these enzyme, a unique six-iron complex denoted as H-cluster. Besides the H-cluster the enzymes host additional redox cofactors, the enzyme from *Dd* contains two [4Fe4S] clusters and the enzyme from *Ca* contains three [4Fe4S] clusters and one [2Fe2S] cluster (Fig. A-2). XAS and XRD (X-Ray Diffraction) studies on HydA1 [FeFe]-hydrogenase from *Chlamydomonas reinhardtii* (*Cr*) shows that the overall organization of the green-algae H-cluster is similar to that of bacteria [133, 252]. However, in contrast to the bacterial [FeFe]-hydrogenases, *Cr*HydA1 contains no additional FeS clusters (Fig. A-2). The crystal structures

of the H-cluster of different [FeFe]-hydrogenases are ambiguous in some aspects. They differ in the nature of the bridgehead atom as well as in the ligands of the diiron subunit. This ambiguity is probably due to resolution limitations and redox state heterogeneity [133]. Spectroscopic methods (e.g. EPR (Electron Paramagnetic Resonance), FTIR (Fourier-transform infrared spectroscopy), XAS) have revealed a wealth of details of the H-cluster (see for example refs. [133, 148, 149, 238, 241, 252, 254]).

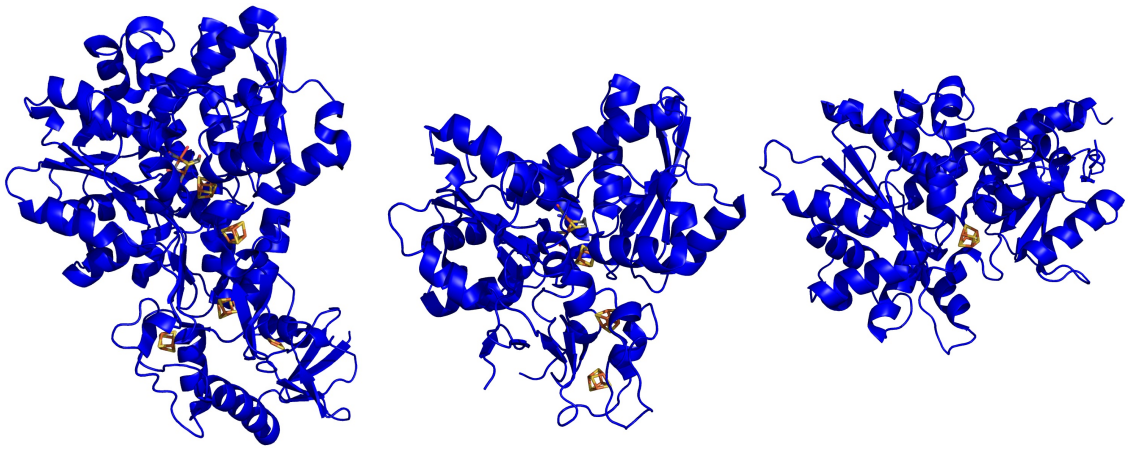

Figure A-2: Crystal structures of three different [FeFe]-hydrogenases. ***Left*** *and* ***middle****, bacterial [FeFe]-hydrogenases from Clostridium pasterianum (CpI, PDB entry 3C8Y, ref. [183]) and Desulfovibrio desulfuricans (Dd, PDB entry 1HFE, ref. [178]);* ***right****, apo-form of HydA1 from the green alga Chlamydomonas reinhardtii (Cr, PDB entry 3LX4, ref. [169]).*

The H-cluster (Figure A-3) consists of a [4Fe4S] cubane cluster and a unique diiron subsite [2Fe]. Both units are connected via a thiolate group of a cysteine residue. Both iron atoms (distal, Fe_d and proximal, Fe_p, relative to the cubane cluster) in the [2Fe] complex show coordination by CO and CN^- ligands, keeping the two Fe atoms in low-spin states, and they are connected via an azadithiolate (adt: $(SCH_2)_2NH$) bridge [61, 176, 241]. Furthermore, the distal iron atom contains an open coordination site in the resting state, (H_{ox}), and it is generally accepted that substrates and reversible inhibitors (e.g. CO) can bind here. It is assumed that the bridgehead group of the dithiolate bridge (-NH) participates in the proton transfer chain between the catalytic site at the distal iron ion (Fe_d) and the solvent [281]. The H-cluster is embedded in a protein framework through a hydrogen-bond network of amino acid and water molecules, e.g. by H-bonding or electrostatic interactions with the diatomic ligands (CO and CN^-) as well as with the adt amine group of the [2Fe] subsite [118, 148, 281]. The polypeptide environment provides a ligand sphere that could probably affect the electrochemical properties of the H-cluster and play an important role for the catalytic process. Moreover, the polypeptide

structure ensures specific pathways for the entry and exit of the substrates and of the products [281]. For example, FTIR and EPR studies on [FeFe]-hydrogenases with site-direct mutagenized amino acids located in the vicinity of the H-cluster have shown that mutation of these highly conserved residues results in a damaged H-cluster or highly diminished catalytic activity [118]. This illustrates the role of conserved amino acids for both the structural integrity and reactivity of the H-cluster [118, 148, 191, 281].

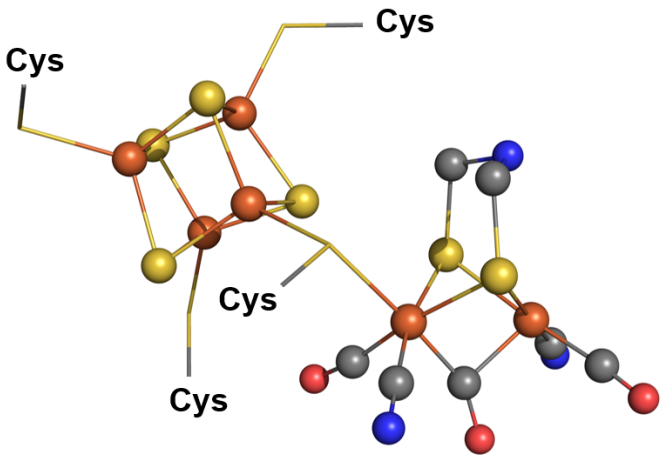

Figure A-3: Crystal structure of the oxidized H-cluster for the semisynthetic bacterial [FeFe]-hydrogenase CpI_{adt} (PDB entry 4XDC, 1.63 Å resolution, ref. [64]). Color code: C, grey; O, red; N, blue; S, yellow; Fe, orange (Cys = cysteine). Protons are omitted for clarity.

*Cr*HydA1 from green algae *Chlamydomonas reinhardtii* containing only the H-cluster and no accessory FeS clusters is the smallest known [FeFe]-hydrogenase in nature (molecular weight = 48 kDa) [254]. Overexpression in *Escherichia coli* results in inactive apo-protein which contains only the [4Fe4S] cubane cluster assembled by the iron-sulfur cluster housekeeping machinery [180]. The *in-vivo* biosynthesis of the [2Fe] subunit of the H-cluster of the [FeFe]-hydrogenases requires hydrogenase-specific maturation enzymes, namely HydE, HydF and HydG [169, 197]. So far, a crystal structure of *Cr*HydA1 containing the entire H-cluster is not available.

In the last years alternative methods for (*in-vitro*) maturation were reported (Fig. A-4). Berggren at al. have shown that synthetic mimics of the [2Fe] subunit can be transferred to apo-HydA1 by previous incorporation in the maturation enzyme HydF [17]. The chemically synthesized [2Fe] subsite analogues are very similar to the native [2Fe] site and vary only in composition of their bridging dithiolate ligand (-CH_2, -NH or -O as bridgehead group) and in an additional CO ligand. Determination of hydrogenase activity revealed that significant H_2

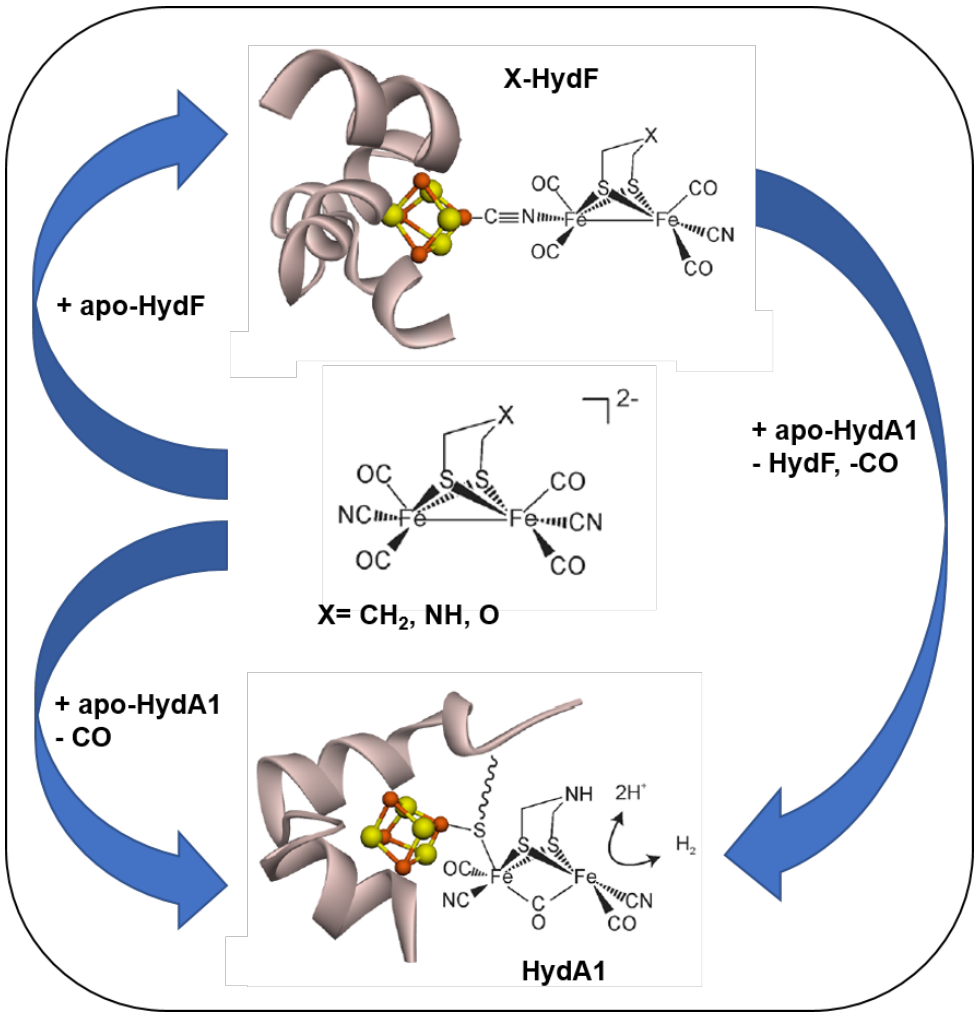

Figure A-4: In-vitro maturation of the H-cluster of [FeFe]-hydrogenase. Top: maturation mechanism via incorporation of an [2Fe] active site mimic into maturase protein HydF (ref. [17]). Bottom: direct maturation by a synthetic [2Fe] mimic (ref. [63]). Reprinted (adapted) with permission from ref. [148]. Copyright (2014) American Chemical Society.

evolution can only be detected when apo-HydA1 was *in-vitro* maturated by the HydF hybrid protein containing the $[2Fe]_{adt}$ complex. The hydrogenase activity of this artificially maturated HydA1 is at least as high as that of the *in-vivo* maturated enzyme [17]. In contrast, when HydF hybrid species containing the synthetic mimics $[2Fe]_{pdt}$ or $[2Fe]_{odt}$ (pdt: $S_2(CH_2)_2CH_2$); odt: $S_2(CH_2)_2O$) were used, the maturated HydA1 enzymes showed no activity. Esselborn et al. have reported an artificial maturation of the active H-cluster with an inorganic [2Fe] subsite mimic [63]. They demonstrated that HydA1 can also be *in-vitro* maturated by a synthetic [2Fe] mimic in the absence of the maturases. The incubation of inactive apo-HydA1 (heterologously produced in *E.coli*) with a solution of the $[2Fe]_{adt}$ mimic resulted in fully active protein. FTIR and EPR studies have shown that the *in-vitro* maturated H-cluster is identical to the native H-

cluster [63]. The integration of the $[2Fe]_{pdt}$ mimic into the apo-HydA1 results in an inactive protein, although FTIR demonstrated the presence of the [2Fe] site in the protein [63].

The integration of the $[2Fe]_{adt}$ mimic in the apo-protein of the bacterial [FeFe]-hydrogenase *Cp*I from *Clostridium pasteurianum* resulting in the active semisynthetic enzyme *Cp*I_{adt} was also reported by Esselborn et al. [63]. Analysis of possible structural changes of the apo-protein as well as the active enzyme due to the integration of the [2Fe] complex is feasible by the recently reported crystal structures [64]. The H_2 formation activity of the semisynthetic *Cp*I_{adt} and of the native *Cp*I are comparable [63, 118] and comparison of the crystal structures reveals identical conformations [64]. A comparison of the crystal structures of the active and the inactive (*in-vitro* maturation with $[2Fe]_{pdt}$, $[2Fe]_{odt}$ or $[2Fe]_{sdt}$ (sdt: $S_2(CH_2)_2S$)) enzymes show that the [2Fe] subunit as well as their protein environment remains unchanged. This suggested that chemical properties of the central bridgehead atom of the bridging dithiolate ligand (μ-$(SCH_2)_2X$; X = CH_2, NH, O or S) are important for H_2 evolution activity. Finally, the amine group seems to be the most efficient base for proton exchange in the catalytic cycle. Additionally, Noth at al. have shown that the "H-cluster manipulation" is not limited to the diiron subsite and can be applied also to the [4Fe4S] cubane site so that *in-vitro* syntheses of the entire H-cluster is possible [179]. For example, the *in-vitro* maturated $HydA1_{adt}$ with a selenium-substituted [4Fe4Se] cluster maintains full catalytic activity [179]. Synthesis of the H-cluster with ^{57}Fe containing precursors (e.g. $^{57}FeCl_2$ solution or ^{57}Fe(adt)) and thus resulting selective ^{57}Fe labeling of the H-cluster enables NRVS experiments on the cofactor [160]. In conclusion, the *in-vitro* reconstitution of both cofactor subunits in HydA1 as well as in bacterial enzymes starting from synthetic [2Fe] mimics and inorganic [4Fe4S] precursors are feasible [160], which facilitates site-selective spectroscopic studies on the H-cluster.

*Cr*HydA1 from *Chlamydomonas reinhardtii* can be considered as "minimal unit" of biological hydrogen turnover [44]. The fact that this [FeFe]-hydrogenase contains only the H-cluster makes it very suitable for spectroscopic studies, in particular for the analysis of the active site structure and its O_2-inhibition mechanism [133] as well as for the catalytic mechanism of H_2 formation. EXAFS analysis can reveal the general H-cluster structure [252] and site- and spin-selective X-ray absorption and emission experiments provide access to the electronic structures of the two subsites, [2Fe] and [4Fe4S], due to their different iron spin states [35, 133]. Additionally, the artificial synthesis of HydA1 provides access to site-selective labelling e.g. with ^{57}Fe for NRVS (Nuclear Resonance Vibrational Spectroscopy) experiments [160, 186, 209]. Thereby, site-selective analysis of the vibrational modes is feasible due to ^{57}Fe labeling

at [2Fe], [4Fe4S] or the entire H-cluster. Advanced investigation of the CO/CN^- stretching vibrations of the [2Fe] subunit by FTIR is possible by the treatment with labelling gases, e.g. the stepwise or selective isotope editing with ^{13}CO [161, 230, 231]. The combination of *in-vitro* maturation and advanced spectroscopic methods with theoretical studies provides access to selective ligation changes and redox reactions at the two subunits of the H-cluster.

In addition to the oxidized H-cluster (H_{ox}), containing a mixed-valence [2Fe] subsite with a bridging CO ligand and an oxidized [4Fe4S] cluster, several redox states of the H-cluster (including H_{hyd}, H_{red}, H_{red}', H_{sred}, and H_{trans}) were identified by various spectroscopic methods (see for example refs. [3, 160, 161, 171, 186, 230, 248]). The relevance of some of these redox intermediates in the catalytic cycle is still under debate. This is exemplified in Figure A-5, which shows three proposed catalytic cycles of [FeFe]-hydrogenases with different intermediates [94, 170, 209].

The catalytic cycle by Reijerse et al. (Figure A-5A) is based on earlier proposals by the Lubitz group [3, 248] and includes putative hydride species [209]. It is assumed that the hydride species is the catalytic state prior the H_2 formation [186] and contains a reduced cubane cluster and an oxidized diiron site with a hydride terminally bound to Fe_d ($[4Fe4S]^+$-Fe(II)Fe(II)$[H^-]$). Winkler et al. have shown that the transient hydride state can be accumulated in the catalytic cycle using different methods [282] which allows its spectroscopic investigation e.g. by NRVS and FTIR [186, 209]. For example, an interruption of the proton-transfer pathway due to site-directed mutation enhances the H_{hyd} concentration (e.g. C169S mutant of *Cr*HydA1). Also the exchange of the native azadithiolate ligand by artificial modification with $[2Fe]_{odt}$ or $[2Fe]_{pdt}$ complexes lead to an H_{hyd} enrichment.

The earlier proposed mechanism by Adamska et al. (Lubitz group) [3, 148] contains besides the "active oxidized state" H_{ox} ($[4Fe4S]^{2+}$-Fe(I)Fe(II)) and the "active reduced state" H_{red} ($[4Fe4S]^{2+}$-Fe(I)Fe(I)) a "super-reduced state" H_{sred}, which is one electron reduced from H_{red} at the [4Fe4S] cubane cluster ($[4Fe4S]^+$-Fe(I)Fe(I)). These authors suggested that only in the two-electron reduced state the bridging CO ligand shifts to a terminal position at Fe_d, whereas in the H_{red} state the H-cluster presumably comprises a semi-bridging CO ligand. Adamska et al. proposed that the H_{sred} state is the starting point for proton reduction. Furthermore, this state seems to be stabilized as a resting state only in algal [FeFe]-hydrogenases (*Cr*HydA1) where accessory [FeS] clusters are absent. It was assumed that the protonated H_{sred} state can form a hydride which is bound (terminally) to Fe_d of the diiron site. The reaction of the hydride with a proton provided by the adt ligand yields molecular hydrogen and restores the H_{ox} state. Further

investigations (FTIR) resulted in an extension of this mechanism by including proton coupled electronic rearrangements between H-cluster states [248], for example the one-electron reduced state H_{red} occurs in an unprotonated and a protonated form. Whereas one species (H_{red}) contains a reduced [4Fe4S] cluster, the other species ($H_{red}H^+$) harbors an extra electron at the [2Fe] subunit. The conversion between both states includes electron transfer from the cubane subunit to the diiron site. Accordingly, Sommer et al. (Lubitz group) suggested an extension in the first steps of the proposed catalytic cycle ($H_{ox} + e^- \rightarrow H_{red} + H^+ \rightarrow H_{red}H^+ + e^- \rightarrow H_{sred}H^+$).

The mechanism of Mulder et al. (Fig. A-5B) resembles the previously presented catalytic cycle (Fig. A-5A). Whereas mostly similar states are proposed during H_{hyd} formation in both cycles, the last step is different. Mulder et al. assume that the protonation of H_{hyd} leads to H_2 formation in a formal diferrous diiron site coupled to a reduced [4Fe4S] cluster ($[4Fe4S]^+$-Fe(II)Fe(II)[H_2]) and the release of H_2 finally regains the Hox state.[170]

The groups of Happe, Haumann and Stripp promote an alternative catalytic cycle of the [FeFe]-hydrogenases (Fig. A-5C) [94, 160, 229, 230]. The key point of this mechanism is the conversion of H_{ox} into $H_{red'}$ by binding of a regulatory proton at the sulfur atom of one of the terminal cysteine ligands of the reduced [4Fe4S] cluster [229] (H_{red}'; $H^+[4Fe4S]^+$-Fe(I)Fe(II)), prior to the subsequent protonation and reduction of the diiron site ($H_{ox} + e^- + H^+ \rightarrow H_{red}' + e^- + H^+ \rightarrow H_{hyd}$). Recent experimental and computational investigations by Mebs et al. [160] support the structure of H_{hyd} (two-electron reduced species with a μCO ligand, an apical hydride at the distal iron, and protonated [4Fe4S] cluster) [160, 161]. Accordingly, during the conversion between the catalytic states, H_{ox}, H_{red}' and H_{hyd}, the geometry of the diiron site remains similar with a bridging CO ligand, whereas H_{red} and H_{sred} contain a terminal CO ligand at the diiron site and a bridging hydride [161]. The ligand rotation seems to be incompatible with the large turnover rates of [FeFe]-hydrogenases and presumably exclude H_{red} and H_{sred} as catalytic intermediates [161]. The protonation, which accompanies the reduction of the [4Fe4S] cluster prevents premature reduction and μH binding at the catalytic diiron site [94, 230] and stabilizes a conservative H-cluster geometry. Finally, the presence of a protonated [4Fe4S] cluster seems to be relevant for the formation of H_{red}' and H_{hyd} and therefore likely is important for fast hydrogen turnover.

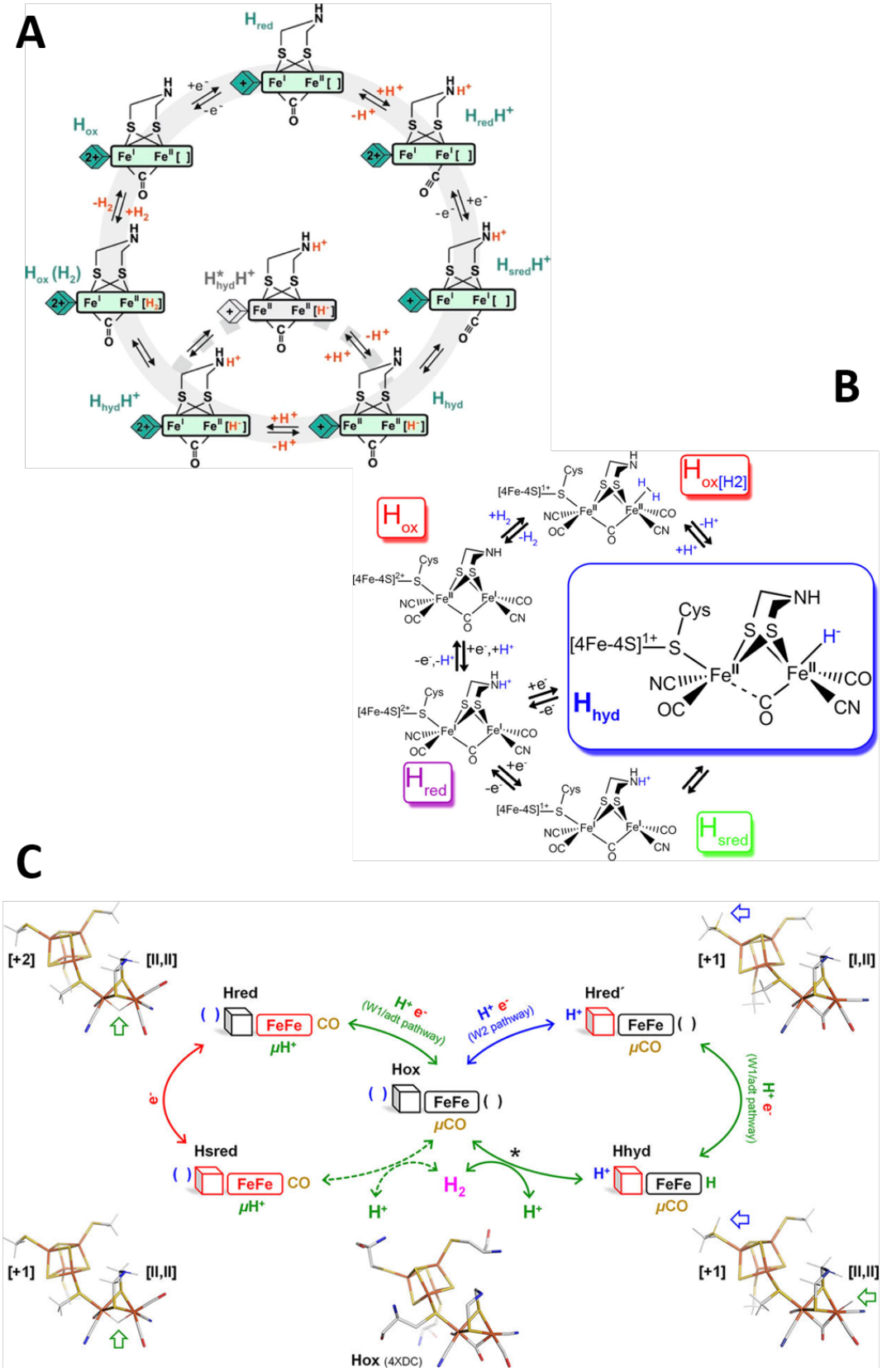

*Figure A-5: Proposed catalytic cycle of hydrogen turnover, (**A**) of Reijerse et al. (2017) (Reprinted with permission from ref [209]. Copyright (2017) American Chemical Society), (**B**) of Mulder et al. (2017) (Reprinted with permission from ref [170]. Copyright (2017) American Chemical Society), (**C**) of Haumann and Stripp (2018) (Reprinted with permission from ref [94]. Copyright (2018) American Chemical Society).*

In-depth understanding of the catalytic cycle of [FeFe]-hydrogenases may help to improve "artificial hydrogenases", which may be used in bio-hydrogen production and biofuel cell technology. Over the last decades, chemists have produced numerous (> 300) biomimetic complexes of the H-cluster and many publications regarding the synthesis and characterization of [FeFe] model systems have appeared (see for example refs. [45, 47, 61, 65, 79, 223, 242, 260]). Even full H-cluster models were reported.[259] Although a large number of model complexes have been synthesized, which mimic the essential structural features of the native [2Fe] subsite, they show mostly too low hydrogen turnover rates and stabilities to be suitable for technical applications [69, 139]. Therefore, further investigations focusing on structure-function relations of the biomimetic complexes are required to gain insight into the limiting factors for H_2 conversion.

In this work, synthetic diiron site models and [FeFe]-hydrogenase proteins were studied by X-ray techniques in combination with quantum chemistry methods. **Chapter 4** is focused on model compounds for the [FeFe]-hydrogenase active site and **Chapters 5 and 6** present investigations on the native HydA1 [FeFe]-hydrogenase protein and on semi-synthetic as well as lyophilized [FeFe]-hydrogenases.

4 Electronic and molecular structure relations in diiron compounds mimicking the [FeFe]-hydrogenase active site studied by X-ray spectroscopy and quantum chemistry

This chapter has been published in:
R. Kositzki, S. Mebs, N. Schuth, N. Leidel, L. Schwartz, M. Karnahl, F. Wittkamp, D. Daunke, A. Grohmann, U.-P. Apfel, F. Gloaguen, S. Ott, and M. Haumann, *Dalton Trans.* **2017**, *46*, 12544-57 https://doi.org/10.1039/c7dt02720f [124][2]

Reproduced with permission from The Royal Society of Chemistry.

4.1 Introduction

Hydrogen (H_2) is a promising fuel for a future economy based on sustainable energy sources.[10, 27, 210] Efficient proton reduction catalysts based on cheap and earth-abundant transition metals would represent a step forward towards the ubiquitous use of H_2.[8, 9, 45, 201] The most efficient H_2 conversion catalysts in nature are the [FeFe]-hydrogenases, which possess an iron cofactor (H-cluster).[148, 191, 254] The H-cluster consists of a [4Fe4S] cubane linked to a diiron unit, the latter being the active site of H_2 turnover. Its two iron ions bind carbon monoxide (CO) and cyanide (CN^-) ligands, as well as a dithiolate bridge containing a pendant amine base (Fig. 4-1).[64, 177, 190, 241] The strong-field CO/CN^- ligands bias the iron ions towards the low-spin state and they likely shuttle between Fe(I) and Fe(II) in the reaction cycle.[56, 193] The specific roles of the diatomic ligands, the dithiolate bridge, and the cofactor geometry in the catalytic reactions are not fully understood so far.

Synthetic chemistry has produced a wealth of model compounds of the diiron unit with the aim to create functional [FeFe]-hydrogenase mimics.[6, 8, 21, 46, 47, 65, 78, 79, 95, 143, 153, 200, 223, 242, 257, 260, 263, 273] At least 300 diiron complexes have been reported, which reproduce essential features of the natural cofactor, such as diatomic ligand binding, open coordination sites, and metal-bridging groups. Selective ligand exchange has been explored for

[2] RK, SM, NS, NL, LS, MK, FW, DD performed research; RK, SM, MH analyzed data; RK made DFT calculations; RK, AG, UPA, FG, SO, MH designed research; RK, MH wrote the paper

example to vary the basicity and geometry of the two iron sites, and to stabilize vacancies for substrate interactions. Characterization of diiron compounds with bound hydride, as well as studies on redox chemistry, protonation reactions, and oxygen sensitivity, limiting the applicability of synthetic and natural systems, [134, 258] are a further research focus.[11, 12, 35, 66, 70, 71, 79, 140, 147, 158, 170, 202, 223, 226, 274-276] A better understanding of the protonation of diiron systems is important as many compounds tend to form an unreactive Fe-Fe bridging hydride, from which H_2 formation often requires considerable overpotentials.[7, 88, 135, 234, 247, 284] A diiron compound working fully reversibly and close to the thermodynamic limit, like the natural system, has not yet been obtained. More rigorous analysis of the effects of ligand variations and geometry changes on the atomic-level physical properties of the compounds may help to improve this situation. In this study, 18 diiron compounds were analyzed, which show varying terminal ligands and substitutions at the bridging dithiolate molecule, as well as symmetry alterations.

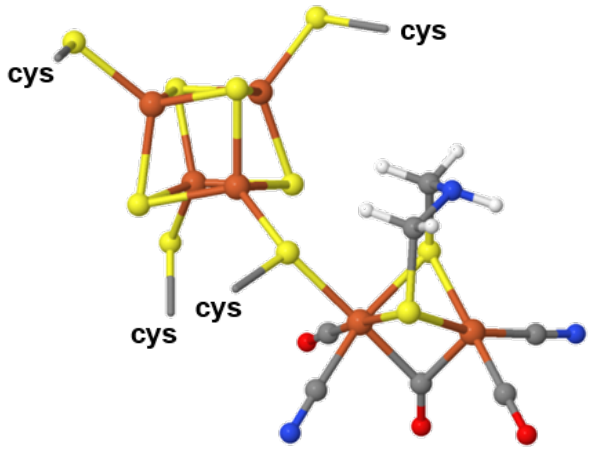

Figure 4-1: Hydrogen-converting cofactor in [FeFe]-hydrogenase. The shown crystal structure (PDB entry 4XDC, ref. [64]) is for the oxidized H-cluster in a bacterial enzyme. Color code: C, grey; O, red; N, blue; S, yellow; Fe, orange; cys denotes cysteine amino acids of the protein.

Advanced X-ray absorption and emission spectroscopy techniques (XAS, XES) in concert with quantum chemical computations provide access to electronic features of metal complexes.[19, 53, 54, 70, 74, 76, 90, 115, 195, 236, 265, 270] However, a combination of these methods has relatively rarely been applied to [FeFe]-hydrogenase mimics.[35, 39, 87, 127, 138-140, 147, 286] The K-edge absorption reflects the redox state and transitions into unoccupied molecular orbitals. The pre-edge absorption is due to resonant 1s core electron excitation into unoccupied orbitals (core-to-valence transitions, ctv) with selection-rule weighted transition probabilities.

The ctv provides information on the energy distribution of unoccupied valance levels. The Kβ main-line emission stems from radiative decay of 3p electrons to the 1s hole. Line splitting into the $K\beta_{1,3}$ and Kβ´ features due to 3p/3d-spin exchange coupling renders it sensitive to the metal spin state. The $K\beta_{2,5}$ and Kβ´´ features of the Kβ satellite emission are due to valence electron decay to the core hole (valence-to-core transitions, vtc) and probe occupied valence levels. The use of XAS/XES and crystal structures to benchmark density functional theory (DFT) results of spectral simulations is expected to provide detailed relations between structural and electronic features.

Here, we present a systematic study on an extended series of diiron compounds of increasing complexity using XAS/XES and DFT. Fe K-edge absorption variations were related to geometry changes at the Fe(I) centers, for which Kβ main-line emission spectra revealed the low-spin state. Good agreement of experimental and calculated pre-edge absorption (ctv) and Kß satellite emission (vtc) spectra was obtained, revealing correlations between molecular and electronic parameters. Variation of the dithiolate bridge mainly affects the Fe-Fe distance, while an asymmetric donor substitution decreases the metal charge and enhances the valence delocalization. Cyanide ligation, like in the natural paragon, effectively alters most electronic properties of the diiron core.

4.2 Materials and Methods

4.2.1 Synthesis of compounds and sample preparation

Compounds **1-18** were synthesized as described earlier (see Fig. 4-2 and Table 4-1 for references). Powder (microcrystalline) material of compounds **1-18** was homogeneously diluted by grinding with boron nitride (1:10 to 1:20) in an anaerobic chamber. The resulting samples were loaded into Kapton-covered acrylic-glass holders for XAS/XES and immediately frozen in liquid nitrogen.

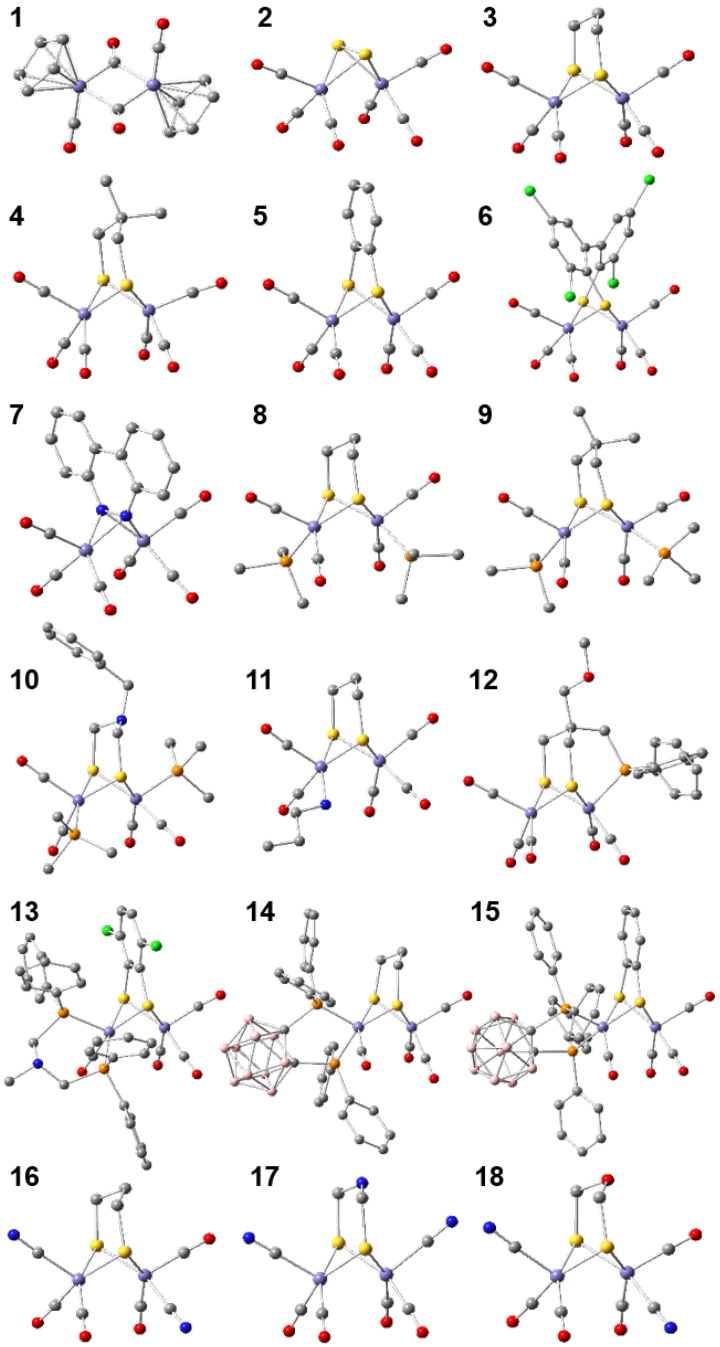

*Figure 4-2: Crystal structures of diiron compounds **1-18**. Color code: B, light-brown; C, grey; O, red; N, blue; P, orange; S, yellow; Cl, green; Fe, violet. Compound annotations: $Fe_2(\mu\text{-}CO)_2(Cp)_2(CO)_2$ (Cp = cyclopentadienyl, C_5H_5), **1**[166]; $Fe_2(\mu\text{-}S_2)(CO)_6$, **2**[62]; $Fe_2(\mu\text{-pdt})(CO)_6$ (pdt = 1,3-propanedithiolate, $(SCH_2)_2CH_2$), **3**[151]; $Fe_2(\mu\text{-dmpdt})(CO)_6$ (dmpdt = 2,2-dimethyl-pdt, $(SCH_2)_2C(CH_3)_2$), **4**[245]; $Fe_2(\mu\text{-bdt})(CO)_6$ (bdt = benzene-1,2-dithiolate, $S_2C_6H_4$), **5**[31, 228]; $Fe_2(\mu\text{-}Cl_4bpdt)(CO)_6$ (Cl_4bpdt = tetrachloro-biphenyl-2,2'-dithiolate, $S_2(C_6Cl_2H_2)_2$), **6**[34]; $Fe_2(\mu\text{-bc})(CO)_6$ (bc = benzo[c]cinnoline, $N_2(C_6H_4)_2$), **7**[59]; $Fe_2(\mu\text{-pdt})(CO)_4(PMe_3)_2$ (Me = CH_3), **8**[292]; $Fe_2(\mu\text{-dmpdt})(CO)_4(PMe_3)_2$, **9**[244]; $Fe_2(\mu\text{-}(SCH_2)_2N(CH_2Ph))(CO)_4(PMe_3)_2$ (Ph = C_6H_5), **10**[226]; $Fe_2(\mu\text{-pdt})(CO)_5(H_2NPr)$ (Pr = C_3H_7), **11**[227]; $Fe_2(\mu\text{-dmpdt-OMe})(CO)_5(PPh_2)$, **12**[52], $Fe_2(\mu\text{-}Cl_2bdt)(CO)_4(Ph_2PCH_2CH_3CH_2PPh_2)$, **13**[67]; $Fe_2(\mu\text{-pdt})(CO)_4(BC)$ (BC = 1,2-bisdiphenyl-phosphine-1,2-o-carborane, $C_2B_{10}H_{10}$), **14**[112]; $Fe_2(\mu\text{-bdt})(CO)_4(BC)$, **15**[112]; $[Fe_2(\mu\text{-pdt})(CN)_2(CO)_4]^{2-}$, **16**[224]; $[Fe_2(\mu\text{-adt})(CN)_2(CO)_4]^{2-}$ (adt = azadithiolate, $(SCH_2)_2NH$), **17**[142]; $[Fe_2(\mu\text{-odt})(CN)_2(CO)_4]^{2-}$ (odt = oxodithiolate, $(SCH_2)_2O$), **18**[249]. Protons were omitted for clarity. See Fig. A4-1 for schematic drawings of the compound structures.*

Table 4-1: Structural parameters of diiron compounds.

compound[a]	number of CO ligands	Fe-Fe distance [Å]	mean Fe-ligand bond length [Å]	CSD[b] code	reference
1	4	2.54	2.03	CYPFEC03	[166]
2	6	2.56	1.97	FOKCOX01	[62]
3	6	2.51	1.98	CAZMAR	[151]
4	6	2.49	1.99	VOFGUT	[245]
5	6	2.48	1.98	SIHXIQ	[31, 228]
6	6	2.51	1.99	ERAMEQ	[34]
7	6	2.51	1.83	BCINFE	[59]
8	4	2.55	2.05	VOQCUZ	[292]
9	4	2.57	2.05	NONFAY	[244]
10	4	2.55	2.05	UCAYUT	[226]
11	5	2.55	2.00	XEPZEY	[175, 227]
12	5	2.52	2.02	n.a.	[52]
13	4	2.53	2.07	CUTSAM	[67]
14	4	2.54	2.06	CEBBAO	[112]
15	4	2.50	2.06	CEBBES	[112]
16	4	2.52	1.99	WOLROE	[224]
17	4	2.51	2.00	YOBSEN	[142]
18	4	2.52	1.99	n.a.	[191, 249]

[a]All compounds contain a formal Fe(I)Fe(I) core; [b]CSD = Cambridge Structural Database;[86] n.a., not available in the CSD.

4.2.2 X-ray absorption and emission spectroscopy

XAS/XES spectra at the Fe K-edge were collected at the triple-undulator beamline ID26 at the European Synchrotron Radiation Facility (ESRF, Grenoble, France).[35, 133, 140, 159, 286] Samples were held at 20 K in a liquid-He cryostat (Cryovac). The excitation energy was set by a Si[311] double-crystal monochromator (energy bandwidth ~0.2 eV). The spot size on the

samples was shaped by slits to ca. 0.2 mm (in vertical) and 0.3-0.5 mm (in horizontal). Fe K-edge absorption spectra were collected using the rapid scan mode of ID26 (scan duration ~5 s). The total (Kα) X-ray fluorescence was monitored with a scintillation detector shielded by 10 μm Mn foil against scattered X-rays. Fluorescence-detected K-edge spectra were corrected for minor flattening effects using the simultaneously measured transmission spectra.[192] A vertical-plane Rowland-circle spectrometer and an avalanche photodiode (APD) detector were used for monitoring of the non-resonantly (7600 eV) excited Kβ X-ray fluorescence. An energy bandwidth of ~1.0 eV at the Fe Kβ fluorescence lines was achieved using the Ge[620] Bragg reflections of 5 spherically-bent Ge wafers (R = 1000 mm). The energy axis of the monochromator was calibrated at an accuracy of ±0.1 eV using the K-edge spectrum of a Fe metal foil (fitted reference energy of 7112 eV in the first derivative spectrum). The energy axis of the emission spectrometer was calibrated at an accuracy of ±0.1 eV using a Gaussian fit to the elastic scattering peak of the energy-calibrated excitation beam. Kβ main-line spectra were collected using spectrometer step-scanning (scan duration ~5 s, energy steps of 0.3 eV). About five spectra from separate sample spots were averaged for signal-to-noise ratio improvement and then normalized to unity area in a 7035-7075 eV range. Kβ satellite line emission spectra were collected using the previously described approach (energy step size 0.3 eV, 5 s data acquisition per sample spot, 5-7 data sets averaged).[123, 289] A rapid shutter blocked the incident X-rays during emission spectrometer movements. XAS/XES data were processed and evaluated using our earlier described procedures and in-house software.[35, 49, 133, 140, 159, 286] Pre-edge absorption spectra (ctv) were derived by polynomial background subtraction from normalized XANES spectra using in-house software. Kβ satellite emission spectra (vtc) were derived by subtraction of a smooth background accounting for the high-energy tail of the $K\beta_{1,3}$ line and normalization to unity area within 7075-7120 eV. Fits using 2 (ctv) or 6 (vtc) Gaussian functions with a variable full-width-at-half-maximum (FWHM) for the ctv spectra (same FWHM for the 2 peaks) or a fixed FWHM of 3.5 eV for the vtc spectra provided energies and intensities of experimental ctv and vtc peak features.

4.2.3 DFT calculations

Calculations were carried out on the Soroban computer cluster of the Freie Universität Berlin. Spin-unrestricted single-point DFT calculations on the crystal structures were carried out using the BP86/TZVPP functional/basis set combination [13, 189, 219] as implemented in the ORCA program [174] to derive ctv and vtc stick spectra (i.e. transition intensities and energies) and MO energies, as well as MO metal/ligand characters of the compounds.[35, 159, 192] For the

two low-spin Fe(I) centers in all complexes, a total spin (S) of zero (multiplicity, M = 2S + 1 = 1) was favored by the lowest single-point energy of the structure in all cases. CM5 charges were calculated on the basis of geometry-optimized structures (BP86/TZVP, COSMO solvation model, ε = 4) using the Gaussian09 program [73]. Molecular orbitals were visualized with Gview.[73] For comparison with experimental spectra, calculated ctv sticks (in a range from the LUMO to ~3 eV) were shifted 181.9 eV on the energy axis, broadened by Gaussians (FWHM 0.8 eV), and resulting spectra were scaled (x165); calculated vtc sticks (in a range from ~7080 eV to the HOMO) were shifted by 181.3 eV on the energy axis, broadened by Lorentzians (FWHM 2.0 eV), and resulting spectra were scaled (x60). Calculated ctv spectra were fitted with 2 Gaussians (variable FWHM) and calculated vtc spectra were fitted with 6 Gaussians (FWHM 2.5 eV) as the experimental spectra to derive energies/intensities of ctv/vtc peaks.

4.3 Results

4.3.1 Structure of diiron compounds

The crystal structures of the diiron compounds are depicted in Figs. 4-2 and A4-1 (given in the Appendix). Selected metrical parameters are given in Tables 4-1 and A4-1 (given in the Appendix). All compounds have a formal Fe(I)Fe(I) valence and exhibit increasing complexity, ranging from symmetric structures with all-carbonyl terminal iron ligation and no, small, or increasingly bulky bridging dithiolate or diamino groups (**1**-**7**), over structures with terminal ligand substitutions (e.g. by phosphine or cyanide) and small dithiolate groups (**8**-**11**, **16**-**18**), to asymmetric structures with diverse and bulky dithiolate groups and/or terminal groups such as a bisphosphine-carborane ligand (**12**-**15**). Despite the pronounced structure variations, the Fe-Fe distance deviated by maximally about ±0.05 Å from the mean value of 2.53 Å. Similarly, only moderate deviations (±0.12 Å) from the average iron-ligand bond length (~2.01 Å) were observed, although a larger bond-lengths spread was realized in the compounds with a more heterogeneous ligand environment. All complexes have 5-coordinated iron sites (except **1** with four ligands) carrying one to three CO and two μS ligands (except **7** with two μN ligands), as well as a variety of further ligand species (Fig. 4-2).

4.3.2 K-edge XAS and Kβ XES

XANES spectra at the Fe K-edge of the diiron compounds are shown in Fig. 4-3A. The spectra revealed pronounced shape variations due to changes in energy of unoccupied levels. The K-edge energy varied by almost 5 eV (~7120-7125 eV). Compounds **8-10** and **12-15** carrying phosphine or bisphosphine-carborane ligands at both Fe ions or only at one Fe ion showed lowest K-edge energies. **5-7** bearing phenyl or aryl groups at the dithiolate or diamino bridge showed highest energies. Compounds **16-18** binding CN^- ligands and **1** had intermediate energies. The edge energy of ferrous iron-oxide (i.e. Fe(II)O) was lower than that of the Fe(I)Fe(I) compounds. Kβ main-line emission spectra are shown in Fig. 4-3B. The spectra appeared very similar for all compounds, showing a prominent $K\beta_{1,3}$ feature at ~7057 eV and a negligible Kβ' feature at ~7045 eV. The small Kβ' feature in comparison to the larger Kβ′ feature for high-spin Fe(II) in FeO indicates that the iron ions in all diiron complexes were in the low-spin state.[35, 140, 159, 196, 278] The $K\beta_{1,3}$ line energy varied by less than 0.3 eV. The complexes carrying, e.g., phenyl or CN^- groups (**5-7**, **16-18**) had lower $K\beta_{1,3}$ energies whereas the complexes with, e.g., phosphine or bisphosphine-carborane groups (**8-12**, **14**, **15**) had higher $K\beta_{1,3}$ energies. For an increase of the iron oxidation state by one unit in a comparable coordination environment, a shift of the K-edge by 2-3 eV to higher energies and a ~0.6 eV higher $K\beta_{1,3}$ energy is anticipated.[55, 127, 133, 159, 218, 279] Therefore, the absolute K-edge energies and the variable energy changes between the compounds likely were dominated by the variations in the ligation environment of the diiron compounds, rather than being determined by changes in the iron redox state. Presumably, the altered coordination geometries at the iron centers affected the energy distribution of unoccupied levels. Rather similar $K\beta_{1,3}$ energies also imply that the apparent iron oxidation state varied only slightly in the compounds and that the line energy changes mostly reflect the structural changes.[159, 196, 289]

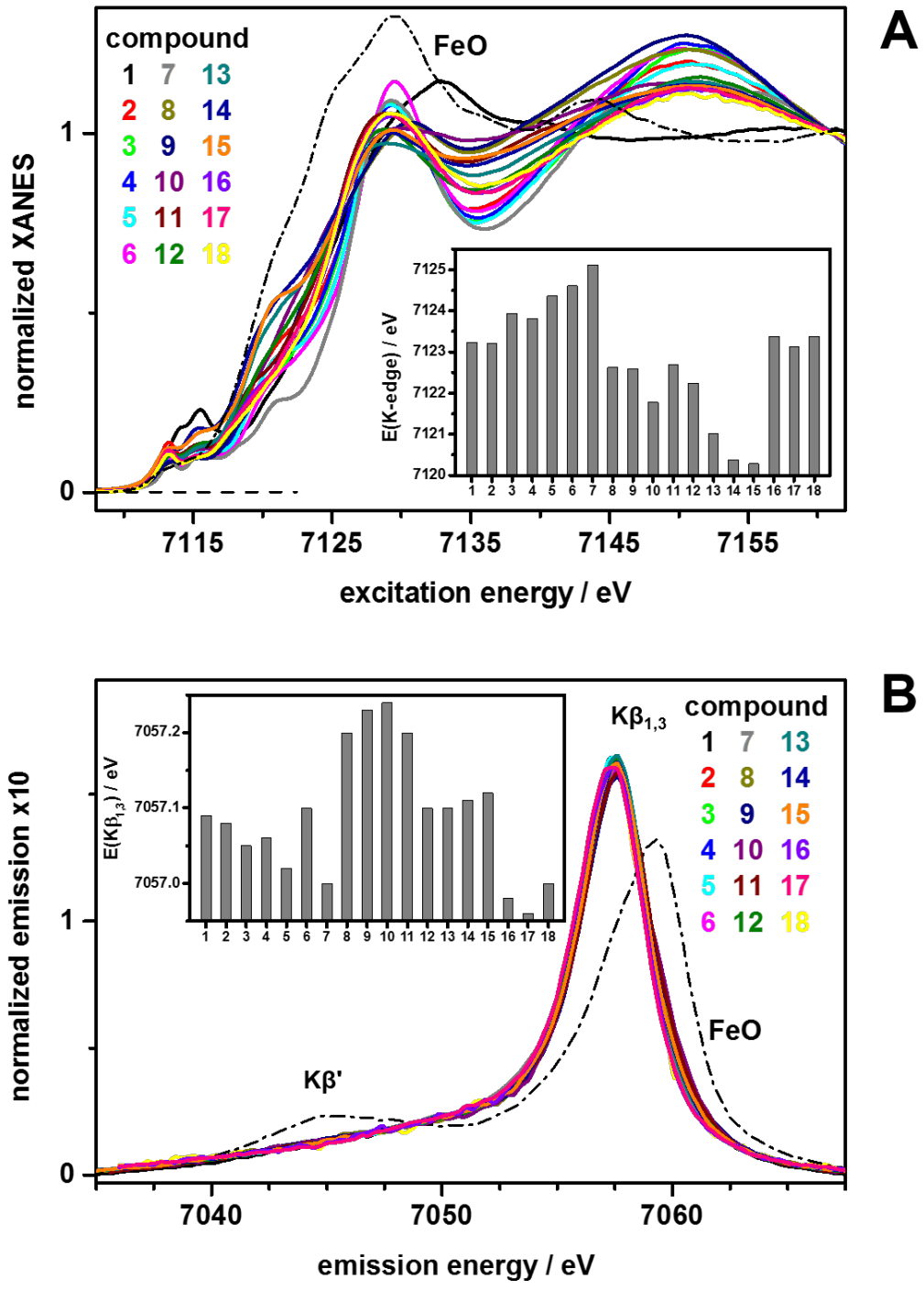

*Figure 4-3: Fe K-edge absorption and Kβ main-line emission spectra of **1-18**. (**A**) XANES spectra (inset, K-edge energies; see Fig. A4-2 for magnified pre-edge features). (**B**) Kβ main-line emission spectra (inset, $K\beta_{1,3}$ energies). Table 4-2 lists K-edge and $K\beta_{1,3}$ energy values. Spectra of Fe(II)O shown in (A) and (B) for comparison.*

Table 4-2: K-edge and Kβ$_{1,3}$ line energies.[a]

compound	E(K$_{edge}$) [eV]	E(Kβ$_{1,3}$) [eV]
1	7123.2	7057.09
2	7123.2	7057.08
3	7123.9	7057.05
4	7123.8	7057.06
5	7124.4	7057.02
6	7124.6	7057.10
7	7125.1	7057.00
8	7122.6	7057.20
9	7122.6	7057.23
10	7121.8	7057.24
11	7122.7	7057.20
12	7122.2	7057.10
13	7121.0	7057.10
14	7120.4	7057.11
15	7120.3	7057.12
16	7123.4	7056.98
17	7123.1	7056.96
18	7123.4	7057.00

[a]*Data correspond to spectra in Fig. 4-3A,B and to data in the insets. The K-edge energy (at 50% level) error is ~0.1 eV, the Kβ$_{1,3}$ line energy error from 1st-moment calculation is ~0.05 eV.*

4.3.3 Pre-edge absorption and Kβ satellite emission

Core-to-valence X-ray absorption spectra (ctv) and valence-to-core emission spectra (vtc) are shown in Figs. 4-4, -5, and Figs. A4-2, -3 (given in the Appendix). The ctv spectra revealed two apparent peak features with moderate intensity, band width, and energy variations (Fig. 4-4A). In the vtc spectra, six apparent emission peak features were discernable, which vary in energy and shape (Fig. 4-5A). DFT calculations on the crystal structures yielded theoretical ctv and vtc spectra (Figs. 4-4B and -5B) that fairly well reproduce the differences between the experimental ctv and vtc spectra. Notably, very similar ctv/vtc spectra were calculated for geometry-optimized structures (Figs. A4-4 - 6, Table A4-1, given in the Appendix). Dissection of the characters of target molecular orbitals (MOs) for electronic excitation underlying the ctv spectra revealed that peak 1 is dominated by transitions into MOs with mostly Fe and weak ligand character whereas peak 2 reflects transitions into MOs with mainly CO ligand character

and minor Fe contributions (Fig. 4-6). Dissection of the characters of source MOs for electronic decay underlying the vtc spectra revealed that peak 6 is dominated by MOs with mainly Fe character, peaks 1, 2, and 5 show major contributions from MOs mostly located at the bridging (dithiolate) groups and non-CO terminal ligands, while peaks 3 and 4 reflect transitions from CO-centered MOs (Fig. 4-6).

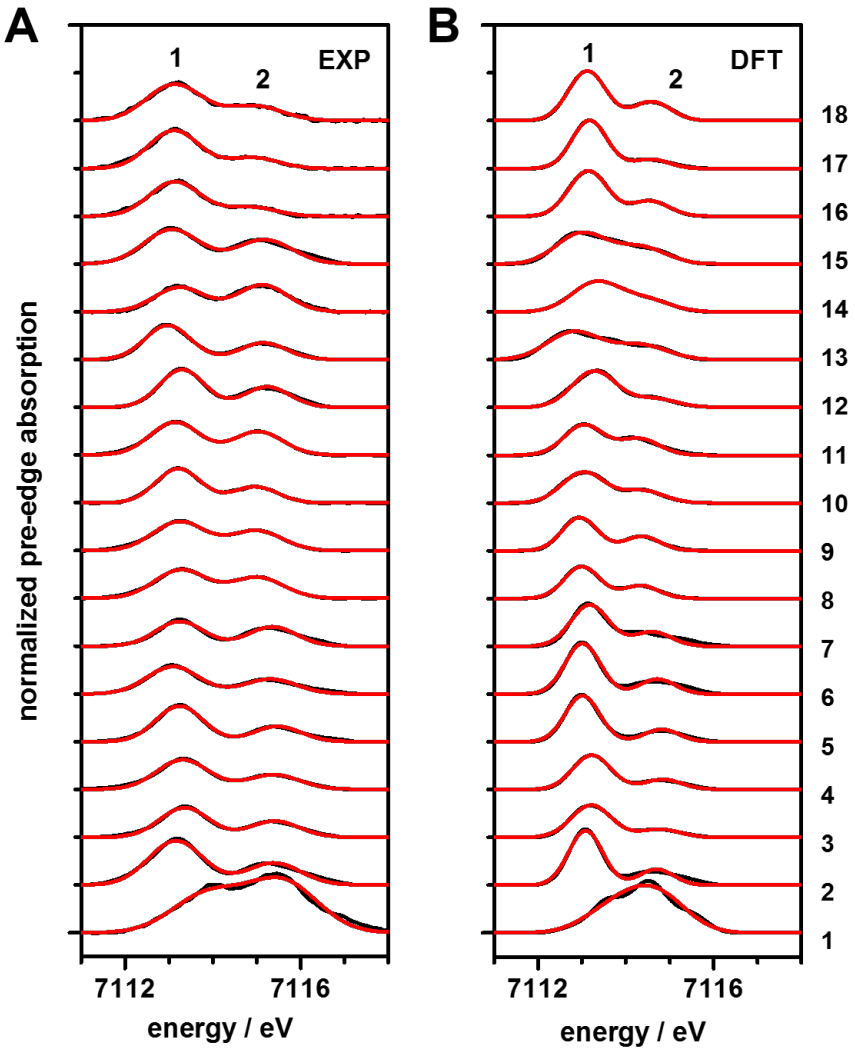

*Figure 4-4: Experimental and calculated Fe pre-edge absorption spectra of **1-18**. (**A**) Experimental ctv spectra derived after background subtraction from XANES data in Figs. 4-3A and A4-2. (**B**) ctv spectra from DFT on crystal structures after Gaussian broadening of stick spectra. (A and B): spectra of compounds indicated on the right; black lines, experimental data; red lines, fit curves with two Gaussians accounting for ctv peaks labeled 1 and 2 (top). Characters of target MOs for ctv electronic excitation transitions in (B) are shown in Fig. 4-6.*

For a more quantitative analysis, experimental and calculated ctv and vtc spectra were fitted with two or six Gaussian functions, which accounted for the visibly discernable spectral features (Figs. 4-4A, B and -5A, B). Correlations between the respective energies of all ctv/vtc peaks are shown in Fig. 4-7 (see Table 4-3 for correlations of individual ctv/vtc peaks). For the ctv spectra (Fig. 4-7A), the experimental and calculated energies of the two peaks agreed within margins of less than about ±0.2 eV for a mean energy difference of ~2 eV between the two peaks. The correlation line slope revealed ~25 % underestimation of the peak energy splitting,

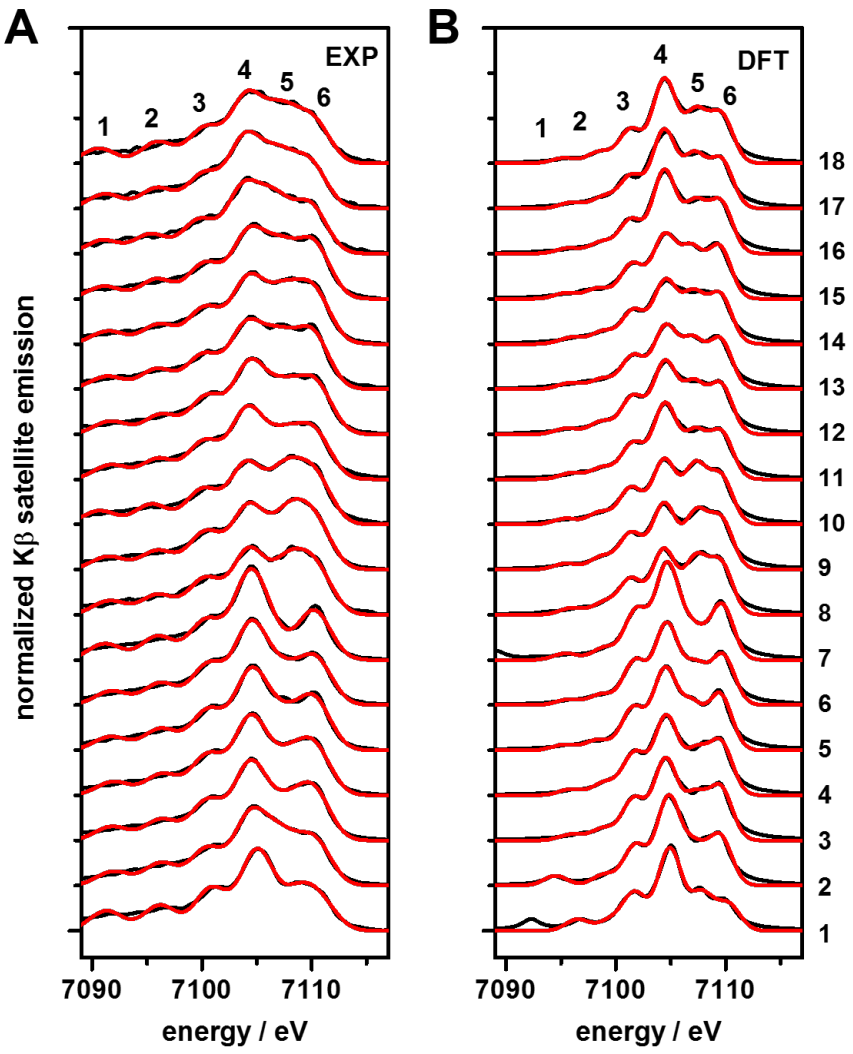

*Figure 4-5: Experimental and calculated Fe Kβ satellite emission spectra of **1-18**. (**A**) Experimental vtc spectra derived after subtraction of the background due to the high-energy tail of the $K\beta_{1,3}$ line (Figs. 4-3B, A4-3). (**B**) Calculated vtc spectra from DFT on crystal structures after Lorentzian broadening of stick spectra. (A and B): spectra of compounds indicated on the right; black lines, experimental data; red lines, fit curves with six Gaussians accounting for vtc peak features labeled 1-6 (top). Characters of source MOs for vtc electronic decay transitions in (B) are shown in Fig. 4-6.*

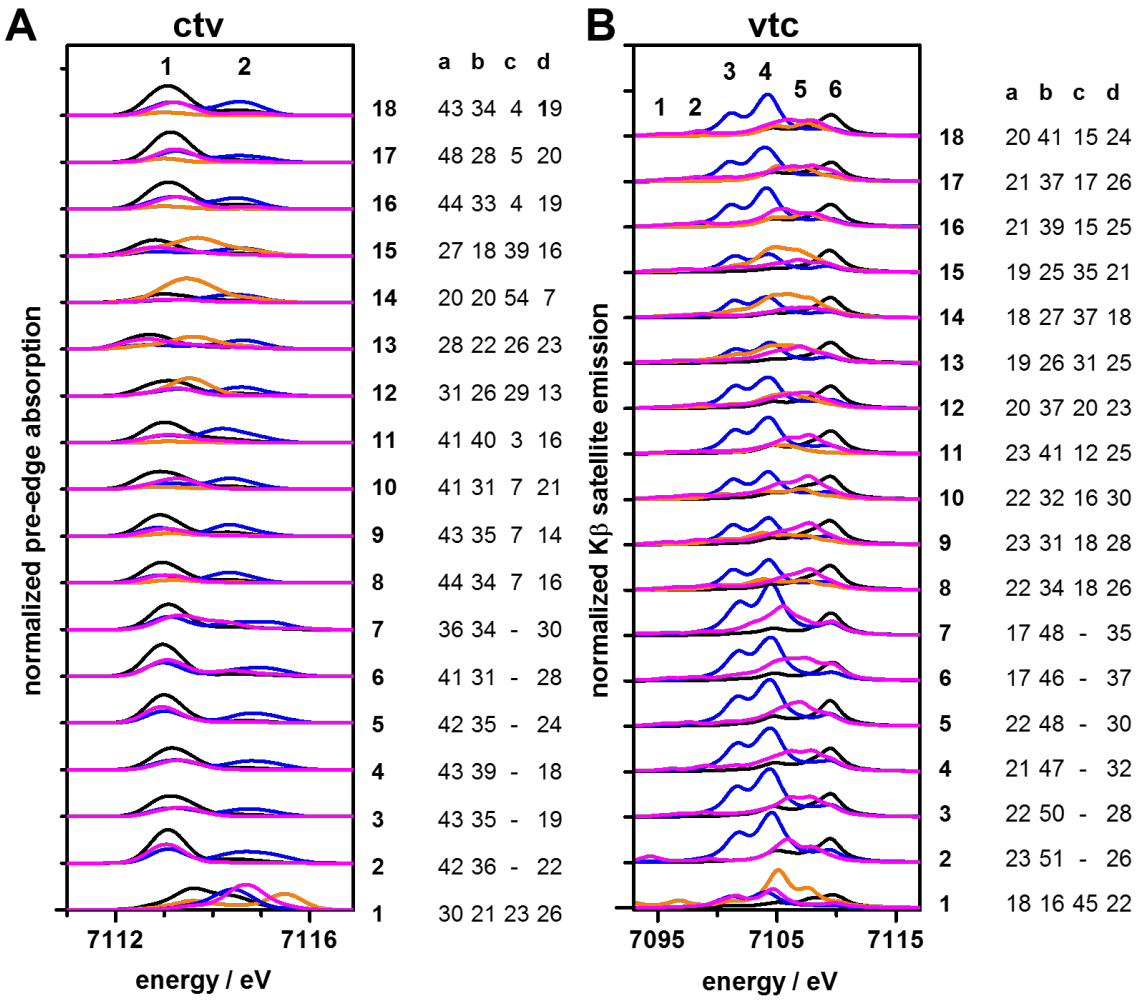

*Figure 4-6: Iron and ligand contributions to ctv and vtc spectra from DFT. (**A**) Characters of target MOs for ctv electronic excitation transitions in Fig. 4-4B. (**B**) Characters of target MOs for vtc electronic decay transitions in Fig. 4-5B. Color code in A and B: Fe, black; terminal CO ligands, blue; other terminal ligands, orange; bridging ligands, magenta. Numbers on the right in (A) and (B) denote: 1st column, diiron compound; and 2nd to 5th column (a, b, c, d), rounded contribution of the spectra of Fe, terminal CO ligands, other terminal ligands, and bridging ligands to the envelope spectrum (see Figs. 4-4 and -5) in percent. Spectra were vertically shifted for comparison. Numbers above the top spectrum in (A) and (B) correspond to discernable peak features (2 in ctv and 6 in vtc spectra) in the envelope spectra.*

as previously observed for the chosen theory level.[35, 133, 138-140] This energy deviation is mostly attributable to the use of the general gradient approximation in the BP86 functional lacking Hartree-Fock exchange energy admixture,[152, 251] but may contain contributions due to the use of only two ctv peaks in the analysis, as visible in the experimental ctv spectra. The peak intensities matched within about ±30 % (reflecting, e.g., limited accuracy of background

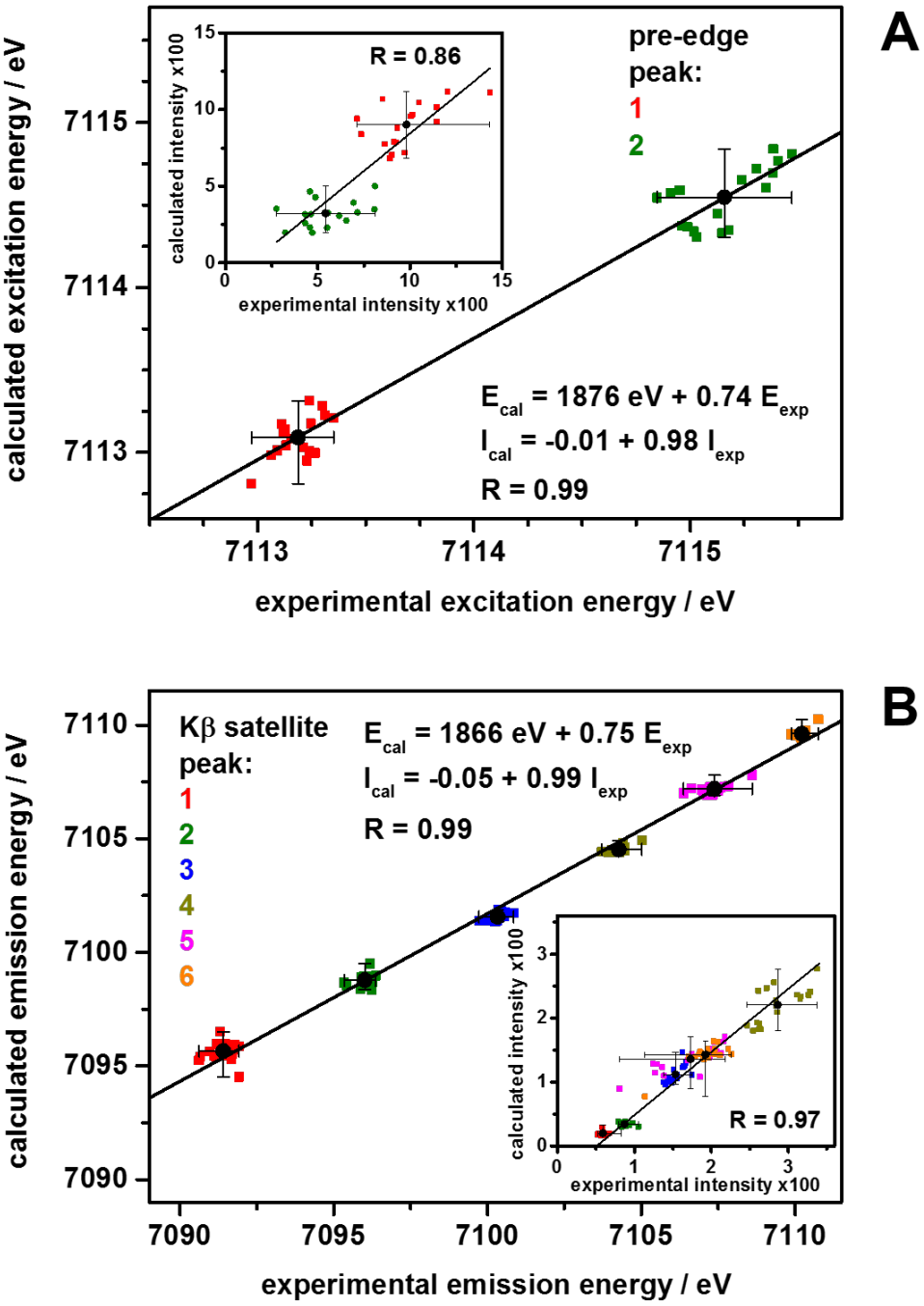

*Figure 4-7: Correlation of ctv and vtc transitions from experiment and DFT. (**A**) ctv energies (intensities in the inset). (**B**) vtc energies (intensities in the inset) corresponding to Gaussian fit functions in Fig. 4-4A,B (A) and Fig. 4-5A,B (B). (A and B): black symbols and bars, mean values and full parameter ranges; straight lines, linear regressions with indicated parameters. Mean experimental ctv/vtc energy (relative intensity) errors are about ±0.1 eV (±10%). For correlations of energies/intensities of individual ctv/vtc peaks see Table 4-3.*

subtraction from experimental data), but the correlation line slope was close to the ideal value of 1. The latter finding supported that the use of two peaks in the simulations was sufficient to reproduce the major spectral changes. For the vtc spectra (Fig. 4-7B), reasonable correlation between experimental and calculated energies for the six peaks within margins of less than ±0.5 eV for a mean energy difference of peaks 1 and 6 of ~20 eV and similar underestimation of energy differences were observed. Peak intensities matched within ±30% and the correlation line slope was close to 1. Relatively small energy and intensity changes in the ctv spectra implied that ligand exchange has a moderate effect on the energies of unoccupied valence MOs, as well as on the excitation transition probabilities. Larger changes in the vtc spectra suggested more pronounced differences in the energies of the occupied valence MOs and, in particular, varying decay contributions from MOs centered at the different ligands. MOs dominating the ctv/vtc transitions are exemplified for a symmetric and an asymmetric compound (**3** and **15**) in Fig. 4-8.

Table 4-3: Fit parameters for calculated vs. experimental ctv and vtc energies and intensities.[a]

spectra	peak	energy			intensity		
		offset [eV]	slope	R	offset [r.u.]	slope	R
ctv	1	1452	0.80	0.61	0.05	0.45	0.56
	2	2697	0.63	0.68	0.02	0.22	0.39
vtc	1	4901	0.31	0.37	-0.01	0.45	0.70
	2	5069	0.29	0.31	0.05	-0.17	0.44
	3	4211	0.41	0.64	0.03	0.93	0.73
	4	4363	0.39	0.74	0.02	0.71	0.71
	5	4964	0.30	0.74	0.06	0.44	0.84
	6	2619	0.63	0.70	0.02	0.61	0.83

[a]*Values correspond to linear fits (E/I_{cal} = offset + slope x E/I_{exp}) of plots of DFT-calculated vs. experimental (Figs. 4-4 and -5) data points for energies and intensities of individual ctv and vtc peaks in Fig. 4-7. Note R-values (shaded).*

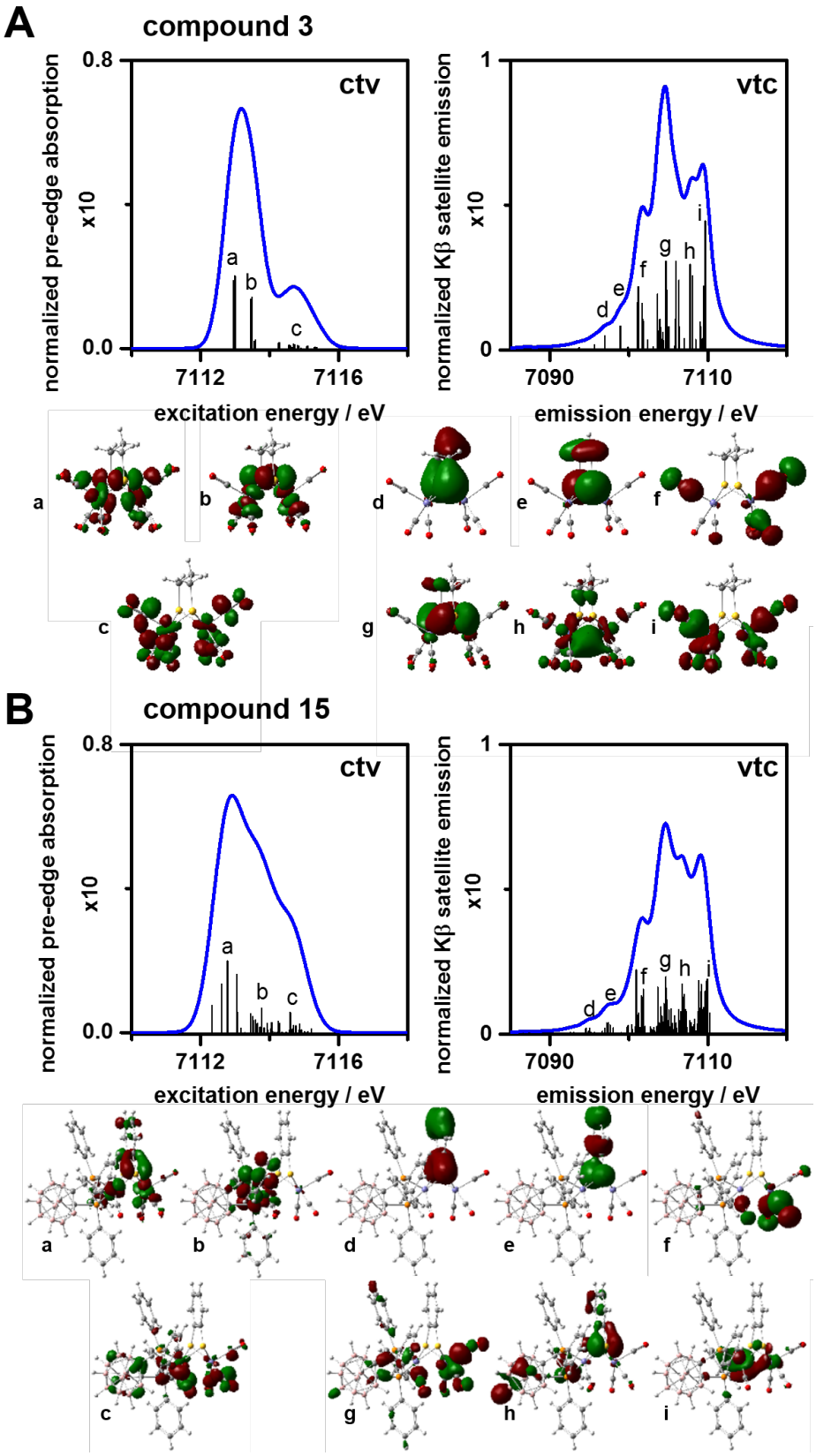

*Figure 4-8: Molecular orbitals involved in ctv and vtc transitions. Shown are ctv **(left)** and vtc **(right)** stick spectra from DFT, spectra after Gaussian (ctv) or Lorentzian (vtc) broadening of stick spectra, and corresponding selected target MOs for ctv excitation (labeled a-c) and source MOs for vtc decay (labeled d-i) for compound **3** **(A)** and compound **15** **(B)**.*

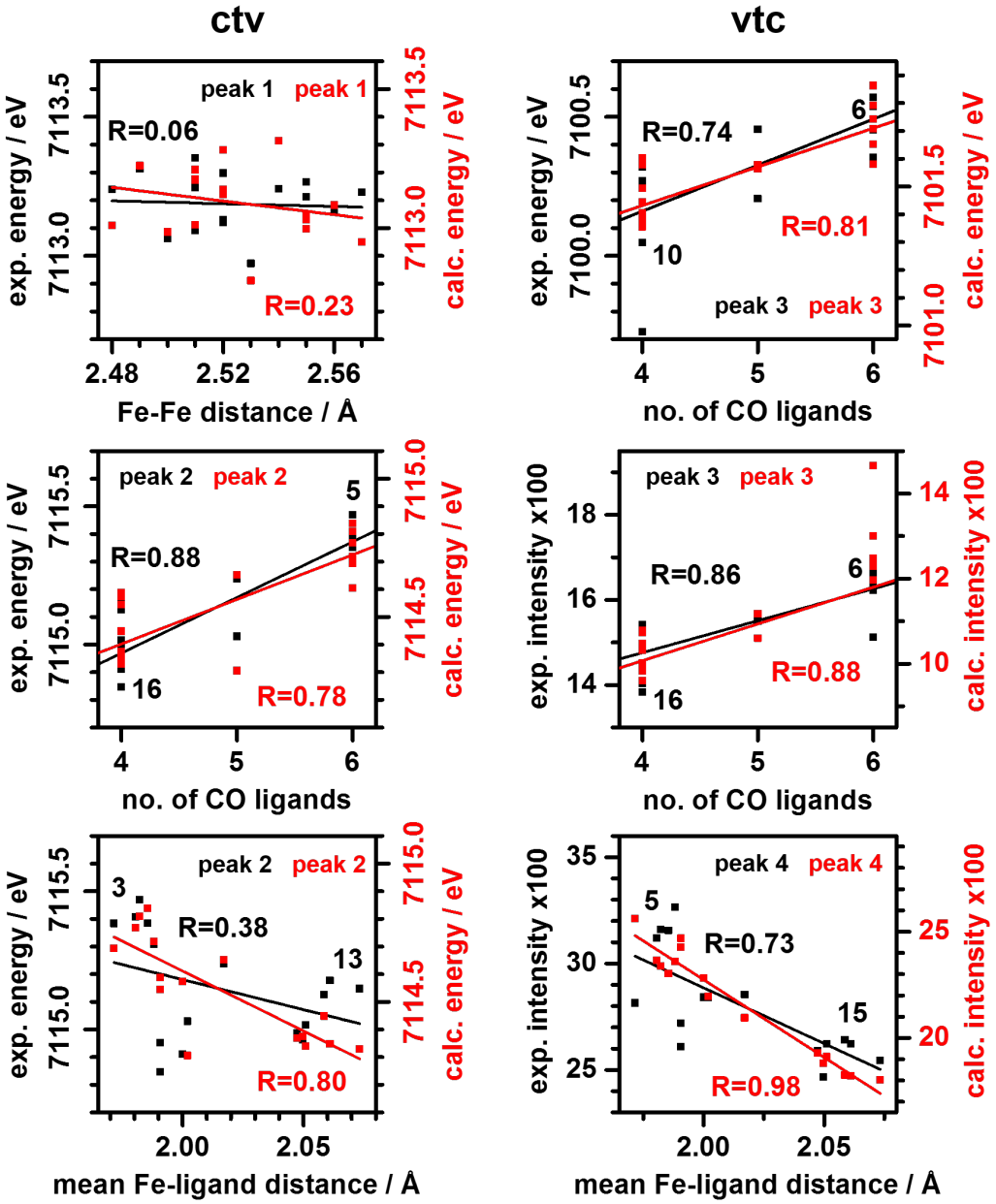

*Figure 4-9: Correlation of structural features and ctv/vtc spectra for **1-18**. Data from experiment (exp., black symbols and lines, left y-axis) and DFT (calc., red symbols and lines, right y-axis) and linear fits (lines). Energies and intensities of ctv (**left panels**) and vtc (**right panels**) peaks correspond to data in Fig. 4-7. Selected compounds with parameter values at the extremes are indicated. Data for **1** and **7** were omitted from the analysis.*

Consistent behavior in correlation plots of experimental or calculated ctv and vtc peak energies and amplitudes versus structural parameters of the diiron compounds emerged (Fig. 4-9). Linear fits, which were used as an approximation to the experimental and computational data, revealed similar slopes and R values for both sets of data (compare black and red lines in Fig. 4-9).

Notably, the use of the mean Fe-ligand distance, which levels out the increased bond length spread in the more asymmetric compounds to some extent, may be the reason for a relatively weak correlation to the energies of the ctv peak features. These findings showed that the trends in the experimental data were reasonably reproduced by the computational approach. The energy of ctv peak 1 was unrelated to the Fe-Fe distance, which means that small differences in metal-metal bond strength do not systematically affect the energies of unoccupied valence MOs. An energy increase by ~0.5 eV of ctv peak 2 implies a shift of unoccupied MOs with dominant CO character to higher energies for an increase of the number of CO ligands from four to six (as in **16** vs. **5**). An overall energy decrease by ~0.5 eV of ctv peak 2 for a ~0.1 Å increase of the mean metal-ligand distance was compatible with the data and presumably reflects increasing contributions of non-CO ligands to unoccupied MOs (e.g. in **8**-**18**). The energy increase by ~0.5 eV and intensity increase by ~15% of vtc peak 3 for a change of the number of CO ligands from four to six is due to enhanced decay contributions from CO-centered MOs. A decrease by ~20% of the intensity of ctv peak 4 for a mean metal-ligand bond elongation by ~0.1 Å is consistent with diminished decay probabilities from respective ligand-centered occupied MOs.

4.3.4 Charge distribution

DFT was used to calculate CM5 charges on the iron ions and the ligands (Fig. 4-10). The mean summed charge on the iron centers was ~0.7. A smaller charge on iron for **8**-**10** and **13**-**18**, a larger charge for **2**-**6** and **11**-**12**, and maximal charges for **1** with bridging CO ligands and for **7** with a diamino bridge were found. Both iron ions were about equally charged, except for compounds **13**-**15** with an asymmetric ligation sphere at the two iron centers, which showed asymmetric charging due to less positive charge at Fe1 binding a bisphosphine-carborane, and increased charge on Fe2. Compounds **11**-**12**, which hold a nitrogen or phosphine ligand only at one iron center, had less positive charge on Fe2. Significant negative charge on the terminal CO ligands was enhanced in **16**-**18** by the CN^- ligands. The other terminal ligands including the phosphine groups carried significant positive charge in **8**-**15**. Almost one negative charge was located on the CN^- ligands in **16**-**18**. The bridging CO ligands in **1**, the diamino bridge in **7**, and the dithiolate bridges in **16**-**18** showed enhanced negative charge, while smaller negative charge was calculated for the bridging ligands of the other compounds. The phosphine or CN^- ligands in **8**-**10** and **16**-**18** thus result in a slight apparent reduction of iron, while asymmetric ligation leads to an unequal charge distribution on the metal centers.

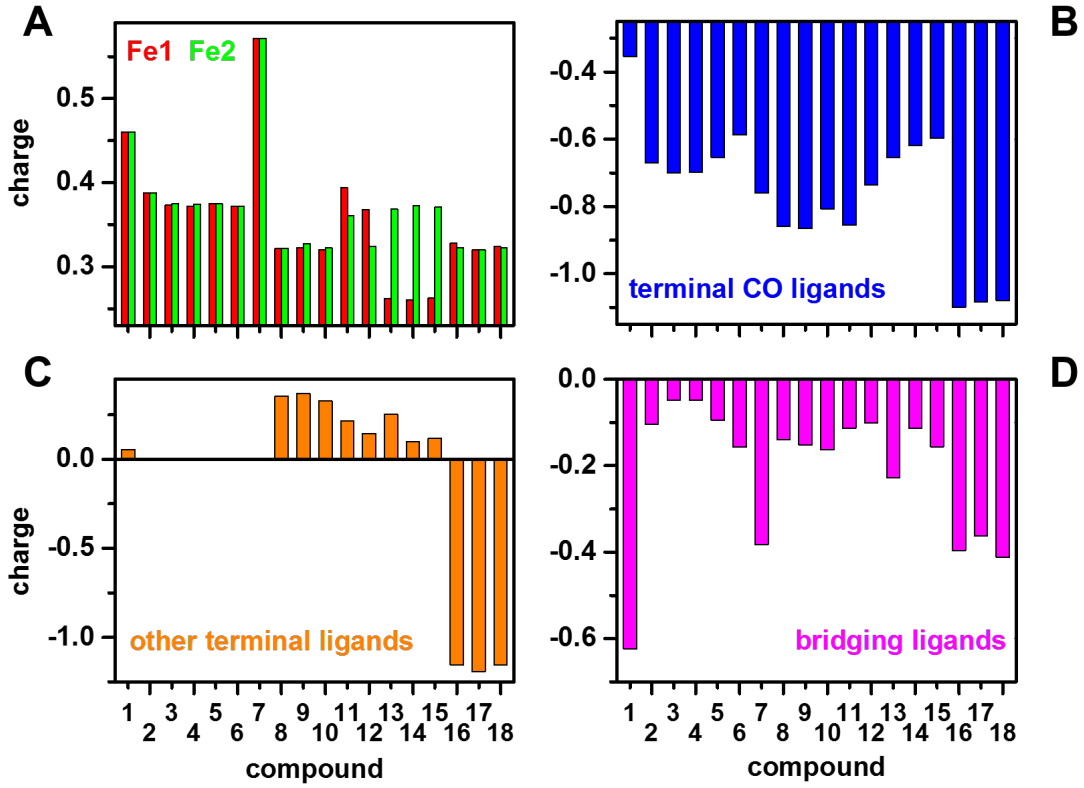

*Figure 4-10: Charge distribution in **1-18** from DFT. CM5 charges are for relaxed structures (Figs. A4-4, -5). (**A**) Fe1 and Fe2 charges (left or right iron ions in Fig. 4-2). (**B**) Summed charge of terminal CO ligands. (**C**) Summed charge of bridging ligands. (**D**) Summed charge of remaining ligands.*

4.3.5 Valence level configuration

Calculated HOMOs and LUMOs are shown in Fig. 4-11. In most cases, the HOMO was dominated by iron contributions (>50%). In the symmetric compounds with mostly CO ligands, extensive HOMO delocalization over both iron ions was observed whereas increasingly asymmetric ligation caused localization on Fe1 or Fe2. The LUMO in most cases was also dominated by iron and delocalized over both centers in the more symmetric complexes, while it was increasingly localized at Fe1 or Fe2 and showed larger ligand contributions in the asymmetric complexes (**13-15**). We estimated experimental LUMO and HOMO energies from the lowest- or highest-energy inflection points of the ctv or vtc spectra (i.e. from the respective zero-crossing points in the 2nd-derivative spectra, Fig. 4-12). The experimental and calculated LUMO – HOMO energy differences (ΔE) varied by ~0.7 eV for a calculated mean ΔE ~2.3 eV. The ~1 eV smaller experimental mean ΔE may reflect systematic underestimation by the experimental estimation approach (see above), overestimation by DFT (possibly in part due to

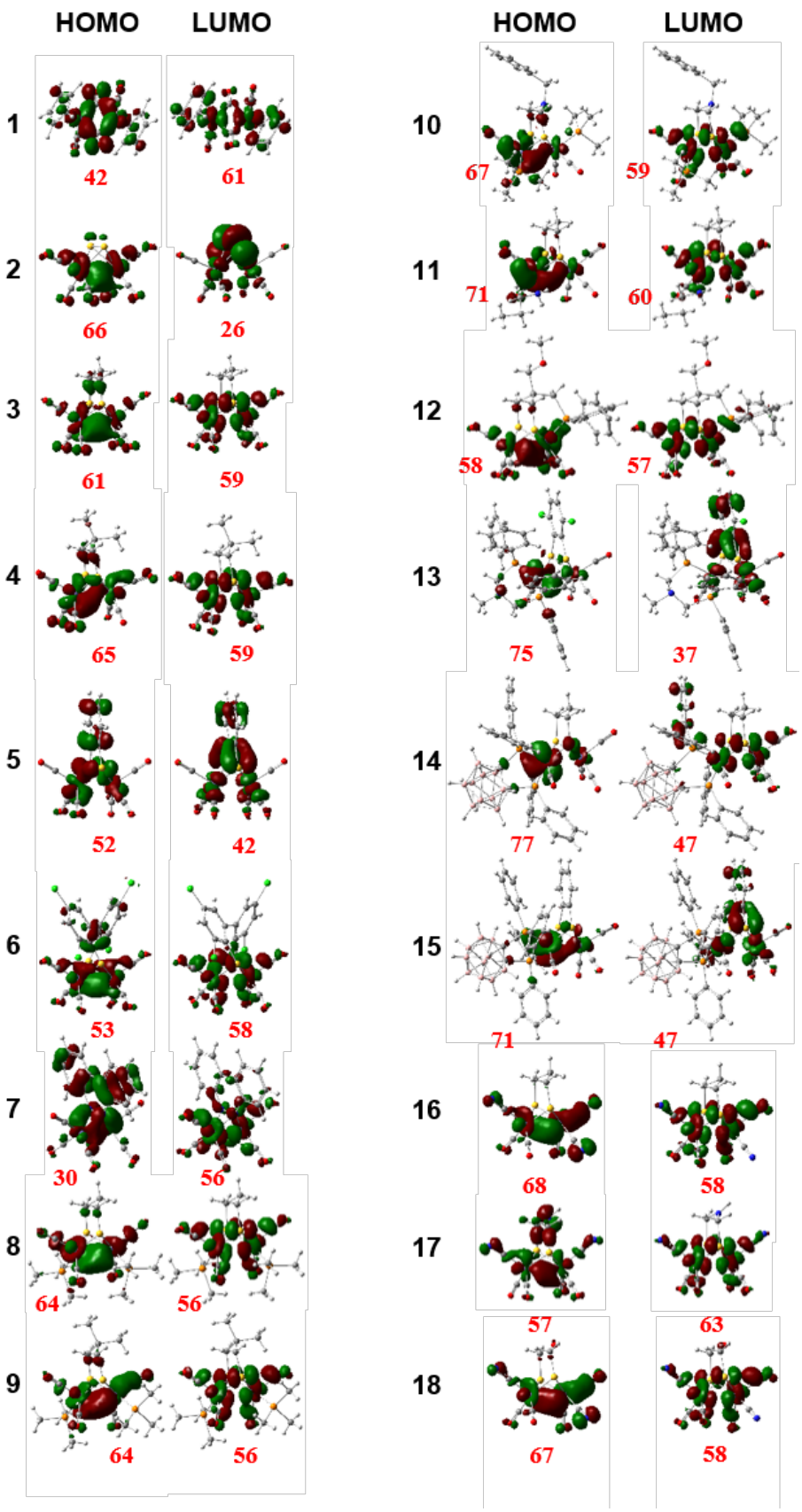

*Figure 4-11: HOMO and LUMO for **1-18**. Red numbers, total Fe contribution (in %) to MOs (α and β spin MOs are at the same energy and therefore identical for the structures with a total spin of zero due to anti-ferromagnetic coupling of the two Fe(I) ions).*

small contributions of core hole potential differences in the XAS and XES calculations to the frontier MO energy differences), or a combination of both effects (Fig. 4-13). The correlation between calculated and experimental ΔE values was relatively weak. It became accessible only due to the use of a comparably large number of compounds in the analysis. The calculated HOMO energy varied between about -4 eV (in **18**) and -6 eV (in **2**) and the LUMO energy varied between -2 eV (in **18**) and -4 eV (in **2**), revealing that the more symmetric compounds had relatively lower HOMO/LUMO energies (Table 4-4).

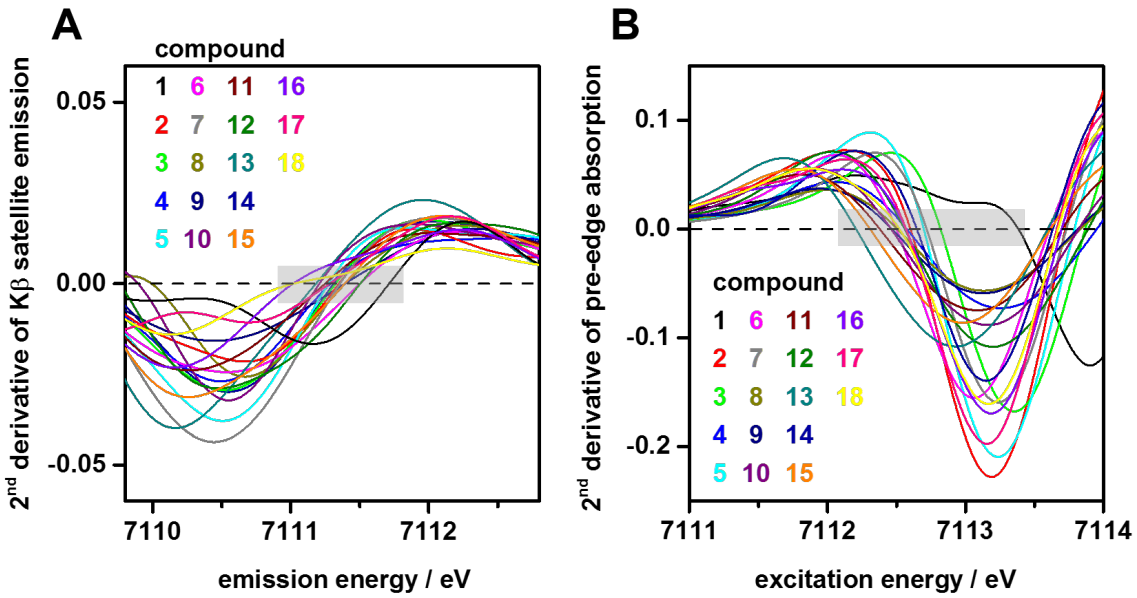

*Figure 4-12: Second derivative spectra of experimental vtc and ctv spectra of **1-18**. (**A**) $K\beta_{2,5}$ emission spectra (vtc). (**B**) Pre-edge absorption spectra (ctv). Apparent relative HOMO or LUMO energies and respective energy gaps were derived from the spectra by determination of the zero crossing point at highest (vtc) or lowest (ctv) energy (marked by the dashed line and grey-shaded rectangle in A and B). The vtc and ctv spectra (Figs. A4-2 and -3, given in the Appendix) were smoothed by adjacent averaging over 3 data points and 1st and 2nd derivative spectra were calculated using cubic spline smoothing over 10 (vtc) or 5 (ctv) data points to yield the shown spectra.*

From the DFT data, 20 unoccupied or occupied MOs of Fe1 and Fe2 with predominantly Fe(d) character were identified (Fig. 4-14). They were delocalized over Fe1 and Fe2 in the most symmetric compounds and showed increasing localization for increasing ligation asymmetry. Moderate changes (<0.5 eV) in mean relative energies (about 2 eV and -1 eV) of unoccupied and occupied Fe(d) MOs were observed (Fig. 4-14). Although all compounds have 5-coordinated iron ions (except **1** with four ligands), the d-level degeneracy was closer to that of

octahedral species with a clear separation of 3 t_{2g} and 2 e_g levels, suggesting significant Fe-Fe bonding. Calculated LUMO – HOMO energy differences (ΔE) and energy ranges (corresponding to the apparent d-level degeneracy), total Fe(d) characters, and specific contributions from Fe1/Fe2 to the MOs are summarized in Table 4-4. Smallest or largest ΔE values were found for the most asymmetric (**13**, **15**) or symmetric complexes, regardless of CO to CN^- ligand exchange (i.e. in **3** vs. **17**). The energy range varied by ~1.2 eV and ~0.6 eV (except for complex **1**) for occupied or unoccupied Fe(d) levels. In particular the most asymmetric compounds with bulky ligands (**12-15**) showed decreased Fe(d) degeneracy. The Fe-character of occupied/unoccupied MOs varied within ~52-66/32-54% with larger contributions for very symmetric compounds. Similar specific Fe1/Fe2 characters of Fe(d) MOs were observed in the more symmetric compounds (**1-9**, **16-18**) whereas Fe1/Fe2 characters deviated by up to ~10% in the more asymmetric compounds (**10-15**).

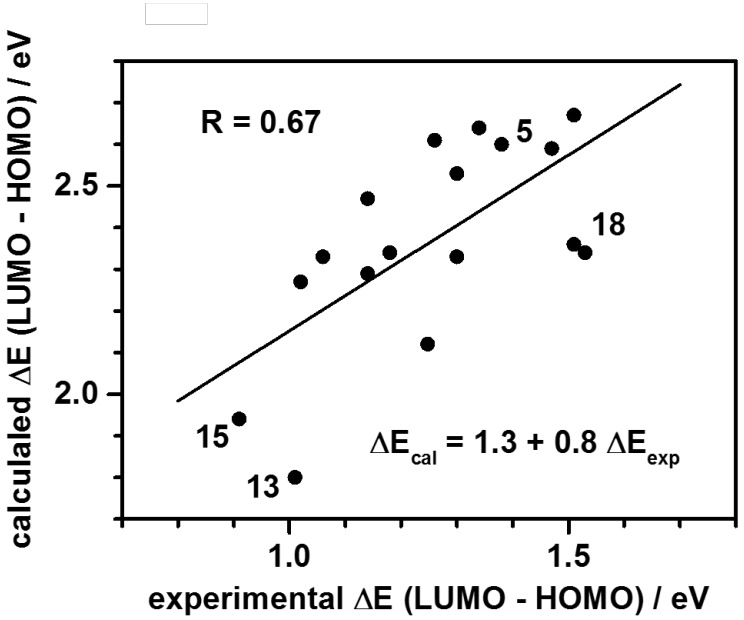

*Figure 4-13: Frontier MO energy differences in **1-18**. Calculated vs. experimental LUMO – HOMO energy differences, solid circles; linear regression, line (for details see the text).*

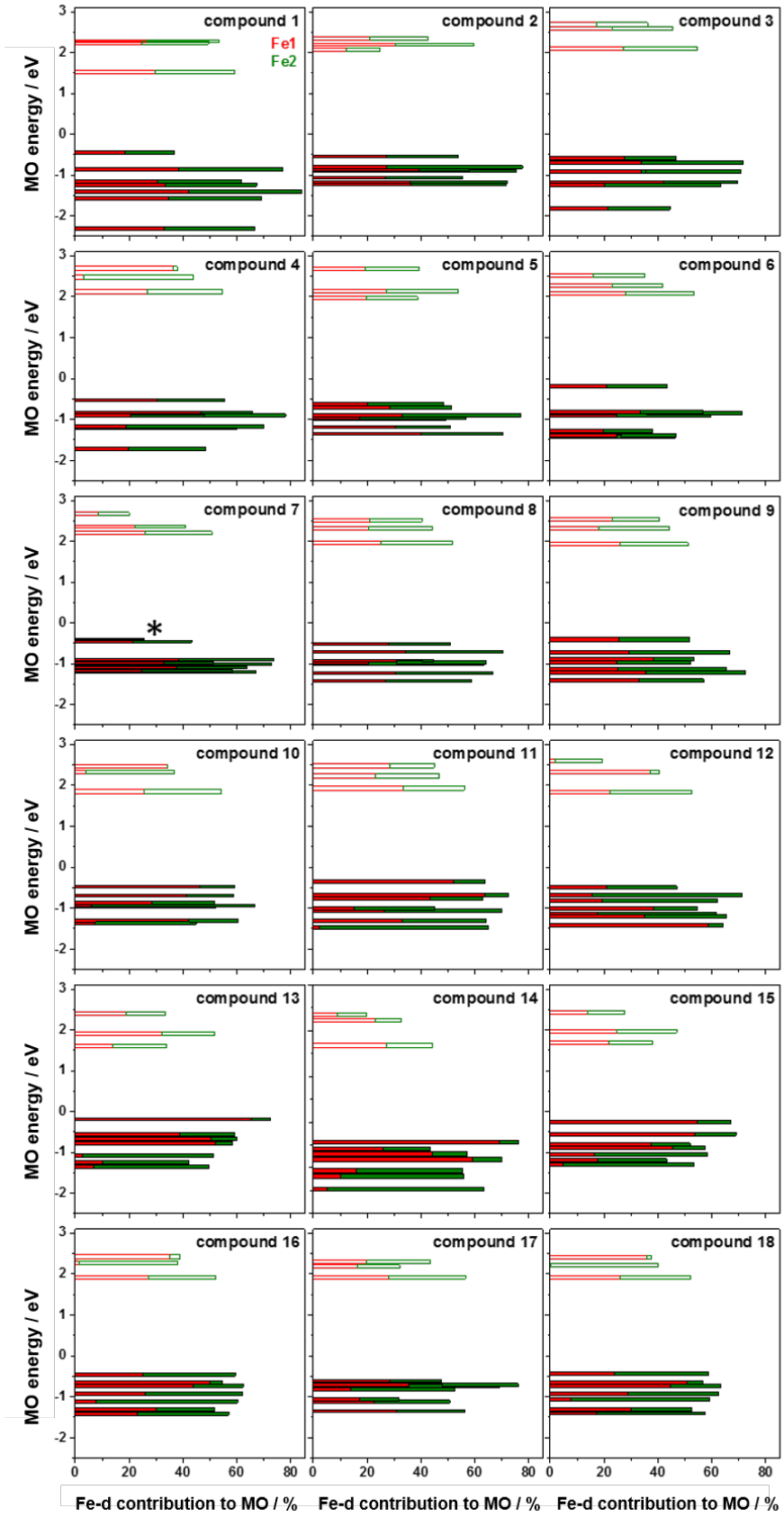

*Figure 4-14: Fe(d) character and energy of valence MOs. Bars show the Fe(d) character contribution of Fe1 (red) and Fe2 (green) to the 10 valence MOs (open bars, unoccupied MOs; solid bars, double occupied MOs; *the black solid bar for 7 shows the HOMO). The mean energy of the MOs for each compound was set to zero.*

*Table 4-4: Valence level energies and characters of **1-18** from DFT calculations.*

compound	energy [eV]		ΔE [eV][a]	energy range [eV][b]		Fe character [%][c]		Fe(d) character [%][d]	
	LUMO	HOMO		occ. MOs	unocc. MOs	occ. MOs	unocc. MOs	Fe1	Fe2
1	-2.84	-4.81	1.97	1.87	0.75	65.9	53.9	50.0	50.0
2	-3.62	-6.23	2.61	0.68	0.30	66.2	42.3	54.2	53.4
3	-3.23	-5.90	2.67	1.23	0.59	61.9	45.5	54.1	55.1
4	-3.24	-5.88	2.64	1.19	0.57	62.2	45.5	68.7	68.2
5	-3.45	-6.04	2.59	0.72	0.71	57.6	43.9	56.1	56.1
6	-3.73	-6.00	2.27	1.24	0.44	51.8	43.4	55.1	52.5
7	-3.26	-5.86	2.60	0.74	0.46	61.4	37.2	56.2	55.0
8	-2.20	-4.68	2.47	0.90	0.57	59.8	45.4	59.1	56.1
9	-2.19	-4.52	2.33	1.01	0.61	59.8	45.3	57.5	56.1
10	-2.19	-4.52	2.33	0.89	0.62	56.2	41.7	82.7	72.3
11	-2.66	-4.96	2.29	1.10	0.55	63.3	49.2	70.0	62.6
12	-2.71	-5.04	2.34	0.92	0.75	60.9	37.5	70.4	73.4
13	-2.91	-4.70	1.80	1.17	0.79	56.1	39.6	78.3	71.6
14	-2.88	-4.99	2.12	1.03	0.67	60.1	32.2	76.5	67.7
15	-3.05	-4.99	1.94	1.06	0.74	57.2	37.5	73.8	63.5
16	-1.80	-4.15	2.36	0.96	0.52	58.1	43.0	72.5	71.8
17	-1.81	-4.34	2.53	0.74	0.36	54.8	44.0	56.5	56.3
18	-1.70	-4.03	2.34	0.97	0.50	58.5	43.3	72.6	73.8

[a]LUMO – HOMO energy differences, [b]energy difference between highest- and lowest-energy occupied (occ, 7 MOs) or unoccupied (unocc, 3 MOs) orbitals with predominant Fe(d) character, [c]mean Fe contribution to occ. or unocc. MOs, [d]mean Fe(d) contribution from Fe1 or Fe2 (left or right iron ion in Fig. 4-2) to Fe-character of the 10 MOs. Energies, Fe characters, and Fe1/Fe2 contributions for the 10 individual MOs shown in Fig. 4-14.

4.3.6 Structural and electronic parameter relations

Detailed comparison of experimental and calculated parameters related to iron properties such as Fe-Fe distance and Fe charge, valence level energies (HOMO/LUMO, vtc/ctv, and $K\beta_{1,3}$/K-edge energies), and Fe(d) degeneracy/localization (Tables 4-1, -2, and A4-2; Fig. 4-15) allowed us to identify four main groups within the 16 compounds bearing a dithiolate bridge (**3-6**, **8-12**, **13-15**, **16-18**), revealing four primary effects in response to ligand exchange vs. **2**. For the hexacarbonyl compounds **3-6**, increasingly complex dithiolate bridge decorations mainly result in a shortening of the Fe-Fe distance in comparison to **2**. For compounds **8-12**, CO to phosphine exchange mainly leads to a decrease of the charge on iron compared to the previous group. For

compounds **13**-**15**, CO to bisphosphine-carborane group exchange at one iron center diminishes the degeneracy (i.e. increases the energy differences) and localization of Fe(d) character valence levels vs. **2**. For compounds **16**-**18**, CO to CN^- exchange at both iron centers has the most pronounced effect on the diiron core and, in particular, is increasing the HOMO/LUMO energies. Compound **17** with a nitrogen bridgehead atom shows the strongest deviation of the four properties.

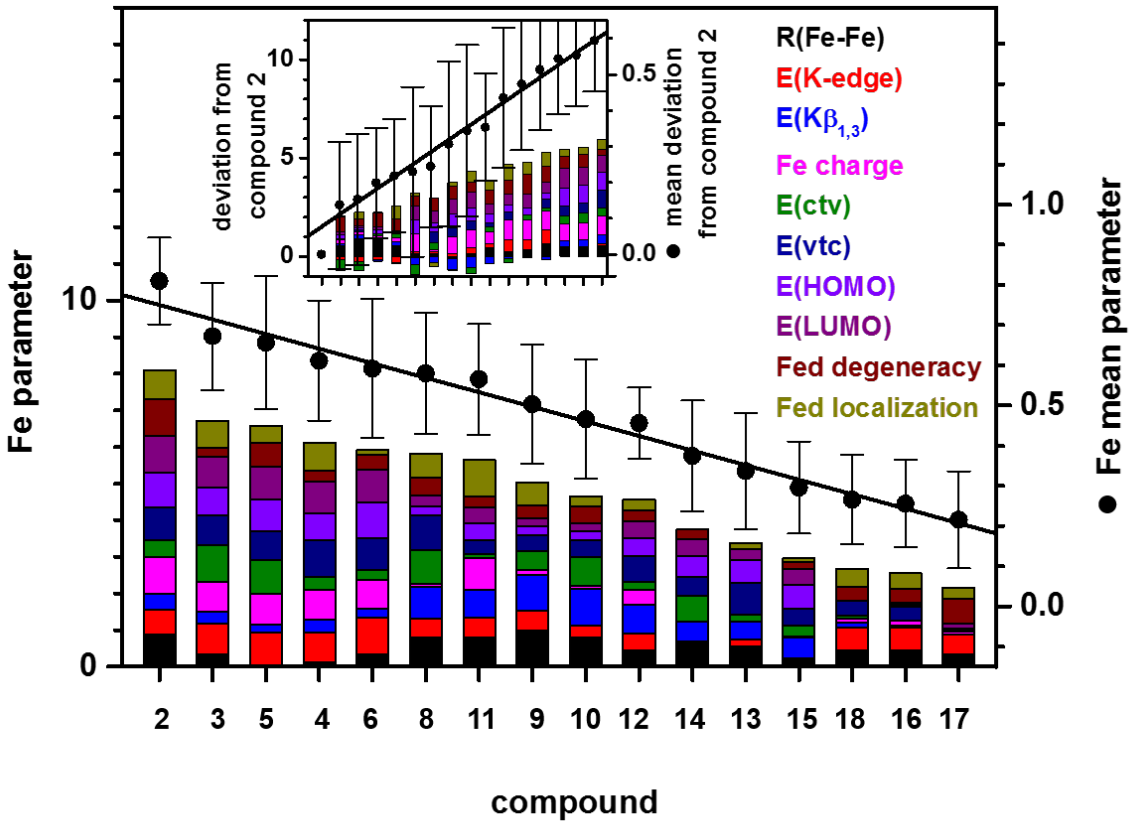

Figure 4-15: Relation of normalized structural and electronic parameters. For the 16 compounds with a dithiolate bridge, the ranges of the experimental and calculated parameters related to the properties of iron, i.e. the Fe-Fe distance and Fe charge, energy of valence levels (occupied MOs: HOMO, vtc, and $K\beta^{1,3}$ energies; unoccupied MOs: LUMO, ctv, and K-edge energies), and Fe(d) level degeneracy and localization, were normalized between 0-1 (Table A4-2) and normalized values were averaged so that a mean apparent Fe parameter was derived. Main panel: indicated individual normalized parameters (coloured bars, left y-axis) and mean Fe parameter ($\Sigma p_i^{norm}/10$, solid circles, right y-axis). Inset: deviations of individual parameters for compounds 3-18 from the respective values of compound 2 (coloured bars, left y-axis) and mean Fe parameter deviations (solid circles, right y-axis). Error bars show standard deviations, regression lines guide the eye, ctv and vtc energies correspond to mean energies of 2 or 6 peak features in the experimental spectra (Figs. 4-4A and -5A), Fe(d) degeneracy and localization refers to the mean energy ranges of, or to the mean Fe(d) contribution to unoccupied and occupied MOs (Table 4-4). Note the ordering of compounds on the x-axis.

4.4 Discussion

We report a systematic XAS/XES and DFT study on a broad series of diiron-dithiolate model compounds of the [FeFe]-hydrogenase active site. This approach has further established the sensitivity of K-edge and pre-edge (ctv) absorption spectra and of Kβ main-line and satellite line (vtc) emission spectra for spin state determination and detection of electronic changes in response to ligation variations at the low-spin Fe(I)Fe(I) centers. The DFT level of theory (BP86/TZVPP) yielded reasonable agreement of experimental and calculated parameters, thereby providing electronic excitation/decay transitions, charge distributions, and valence level configurations. Taking into account the relatively small energy and intensity changes of the ctv and vtc features among the compounds, revealing of correlations between the structural and electronic features has only become feasible due to the use of a large and homogeneous series of diiron compounds in the analysis. Mutual benchmarking of experimental and theoretical XAS/XES data is versatile for prediction and verification of effects of ligation changes on structural, electronic, and spectroscopic properties of diiron compounds in the solid state, as well as in solution, to monitor rotational isomers, redox changes, and protonation events.[35, 133, 139]

Our data show that four main effects on the diiron core, namely alteration of the Fe-Fe bond length, iron charge, valence level degeneracy/localization, and frontier MO energies, can be preferentially related to changes involving either the dithiolate bridge or the terminal ligands (Fig. 4-16). Derivatization of the dithiolate bridge, as, for example, in **5**, which has an electron-withdrawing benzene-1,2-dithiolate bridge, vs. **3** having a 1,3-propanedithiolate bridge, shortens the Fe-Fe distance, i.e. alters the Fe-Fe bond strength, as the main effect. Related changes in metal-metal bonding electron density could be decisive for biasing protonation to this bond or to alternative sites, thereby affecting the probability of bridging hydride formation.[11, 70, 71, 79, 139, 147] Substitution of CO by more potent electron donors (e.g. phosphine ligands) decreased the charge on iron vs. the parent hexacarbonyl compounds, as expected, which may decrease the required potential for metal-centered redox reactions.[79] Asymmetric ligand exchange, including electron-donating bisphosphine-carborane groups, caused charge differences at the two iron centers, enhanced valence level delocalization, and HOMO-LUMO gap narrowing, which may facilitate localized redox reactions at less negative potentials to yield mixed-valence species.[109, 110, 112, 181, 211, 243, 277, 286] Such diiron site species are important in the catalytic cycle of [FeFe]-hydrogenases. CN^- vs. CO exchange at both iron centers altered most diiron core properties significantly, decreasing the metal

charge, favoring valence delocalization, and increasing frontier MO energies (for example in **16** vs. **3**). For this exchange, which conserves the overall geometry of compounds **16-18** in comparison to **2** with six carbonyl ligands, the combined effects on the diiron core are expected to alter both redox and protonation properties.[142, 151, 155, 202, 249] These considerations may provide further rationales for the synthesis of related diiron compounds as well as for experimental and computational evaluation of their features.

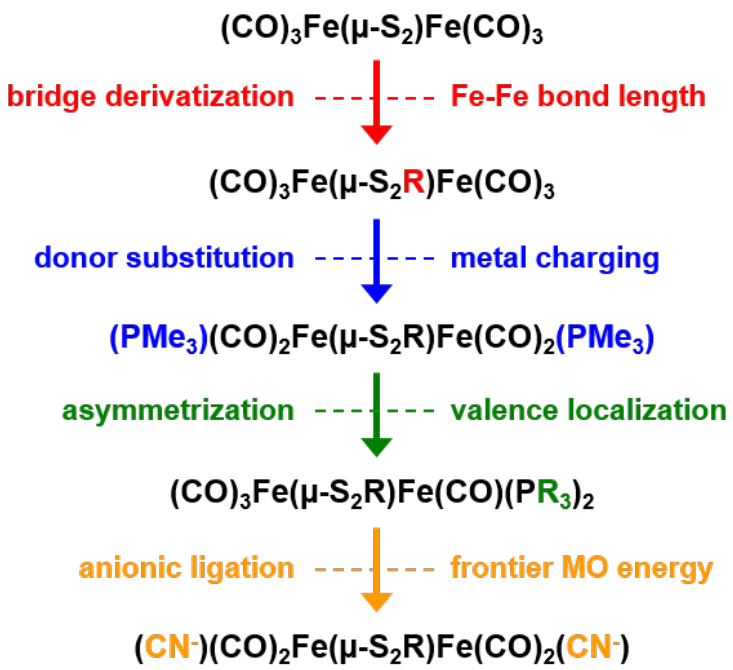

*Figure 4-16: Effects on the diiron core caused by different ligand variations. Indicated alterations in the coordination sphere (**left**) of one or both iron centers (**middle**) lead to indicated main changes at the Fe(I) centers (**right**). The scheme summarizes our central findings, for further details see text and Information in the Appendix.*

The diiron site in [FeFe]-hydrogenases shows one terminal CO and one CN^- ligand at each iron center, bridging CO and azadithiolate groups, and asymmetric metal coordination (see Fig. 4-1). Apo-protein can be converted to the functional enzyme upon binding of **17** to the pre-assembled cubane, release of one CO, and CO rotation into the bridging position.[2, 17, 63, 64, 75, 89, 231] Compound **17** thereby becomes a superior H_2 conversion catalyst, but reconstitution of [FeFe]-hydrogenases with other diiron compounds (e.g. **16**, **18**) has so far not yielded comparable catalytic activity.[1, 17, 64, 162, 235] The low activities, at least in part, reflect perturbed proton conduction to the active site for exchange of the bridgehead amine.[281] CN^- binding and asymmetric metal sites in the native enzyme resemble the

properties of, e.g., **13**-**15** and **16**-**18**, so that similar effects on the diiron core may be expected. Investigations on [FeFe]-hydrogenases have indeed revealed stabilization of mixed-valence diiron species, biasing of surplus electrons to the diiron or cubane moiety, protonation at the Fe-Fe bond or at the apical vacancy upon reduction due to rotational mobility of diatomic ligands, and decreased frontier MO energy differences compared to diiron compounds.[3, 35, 72, 133, 146, 170, 239, 240] A combination of asymmetric metal ligation by anionic, protonable, and electron-delocalizing groups is presumably beneficial for the design of improved diiron hydrogen-conversion catalysts.

Conclusions

The diiron subsite of the H-cluster of [FeFe]-hydrogenases is coordinated by amino acid and inorganic ligands. Over the last decades, chemists have synthesized numerous model compounds that mimic the structural features of the active cofactor in these hydrogen-forming enzymes. The aim of this study was to correlate spectroscopic and structural features to determine the electronic configuration of the models compounds. An unprecedented large series (18) of synthetic diiron compounds with varying terminal ligands, substitutions at the bridging dithiolate group, and symmetry alterations were investigated by X-ray absorption and emission spectroscopy in combination with density functional theory. Generally good agreement between experimental and calculated spectroscopic data was achieved. The main effects on the diiron site (metal-metal bond strength, metal charge, valence level degeneracy/localization, and frontier MO energies) could be assigned to the alteration of the dithiolate bridge or the variation of the terminal ligands. Whereas the length of the iron-iron bond is mainly affected by the dithiolate bridge, the metal charge can be changed by the number of electron donating terminal ligands. Asymmetric organization of the ligands has an effect of the valence level localization. Negatively charged ligands such as cyanide altered all relevant properties as well as the frontier molecular orbital energies of the diiron core. The results of this study were published in Kositzki et al., *Dalton Trans.* **2017**, *46*, 12544-57 [124]. Mutual benchmarking of experimental and theoretical parameters provides guidelines to verify the electronic properties of synthetic diiron mimics of the [FeFe]-hydrogenase active site and may be useful for development of improved diiron catalysts for hydrogen conversion in the future.

.

5 Semisynthetic [FeFe]-hydrogenase generated by *in-vitro* maturation with a synthetic diiron complex

Results reported in this chapter have contributed to following paper:
P. Chernev. C. Lambertz, A. Brünje, N. Leidel, K.G.V. Sigfridsson, R. Kositzki, C.-H. Hsieh, S. Yao, R. Schiwon, M. Driess, C. Limberg, T. Happe, and M. Haumann, **Hydride Binding to the Active Site of [FeFe]-Hydrogenase**, *Inorg Chem*, **2014**, 53, 12164-77
https://doi.org/10.1021/ic502047q [35]

5.1 Introduction

In-vitro maturation of HydA1 [FeFe]-hydrogenase apo-protein with the chemically synthetized $[2Fe]_{adt}$ complex, which closely resembles the [2Fe] subunit of the H-cluster, results in active protein (holo-HydA1). Comparison of the specific H_2 evolution efficiencies revealed similar activity for HydA1 spontaneously activated by $[2Fe]_{adt}$ and for *in-vivo* maturated HydA1. So far, mainly FTIR and EPR spectroscopy were used to analyze the electronic structure of the semi-artificial H-cluster [63, 235]. The treatment of apo-HydA1 with $[2Fe]_{pdt}$, a synthetic mimic which differs from the natural [2Fe] cofactor analogue $[2Fe]_{adt}$ in the central bridgehead group of its dithiolate ligand ($-CH_2$ instead of -NH) results in inactive protein (less than one percent of H_2 evolution activity compared to adt enzyme) [235], but the FTIR spectrum shows that $[2Fe]_{pdt}$ is incorporated in the cofactor. Why hydrogen is formed exclusively after integration of the $[2Fe]_{adt}$ complex needs to be understood. The chemical properties of the dithiolate bridge seems to be important for enzyme activity while steric effects presumably have a minor influence [64].

Investigation of the structural and electronic parameters of the H-cluster variants by high-resolution X-ray absorption and emission spectroscopy (XAS/XES) methods was caried out for three different [FeFe]-hydrogenase holo-proteins, which were *in-vitro* maturated with $[2Fe]_{adt}$, $[2Fe]_{pdt}$ or $[2Fe]_{odt}$, respectively. Discrimination of the two sub-clusters of the H-cluster can be achieved by the use of site-selective XAS/XES due to the different spin states (low-spin at the diiron site and high-spin at the [4Fe4S] cluster) of their iron ions [35, 133]. This advanced technique allows site-selective determination of electronic and molecular properties of the two cofactor sub-complexes.

5.2 Materials and Methods

5.2.1 Protein samples

HydA1 protein samples for X-ray absorption and emission spectroscopy were prepared by Annika Brünje from our collaboration partner (group of T. Happe in Bochum, Germany). Inactive *C. reinhardtii* [FeFe]-hydrogenase protein (apo-HydA1) was derived by protein overexpression in *E. coli* in the absence of the three maturation enzymes HydE, -F, -G. *In-vitro* maturation of apo-protein to yield the different holo-proteins was achieved by treatment with chemically synthesized $[2Fe]_x$ complexes (x = adt, pdt, odt) as described earlier [63]. HydA1 apo and holo-protein samples were concentrated to 1-2 mM and NaDT was added. Then, the as-isolated solution samples were injected under anaerobic conditions into Kapton-covered XAS sample holders and stored in liquid nitrogen until use at the synchrotron. As reference samples, solutions of the parent $[2Fe]_x$ compounds with concentrations of 3-9 mM were used.

5.2.2 TXRF

The iron content of the HydA1 apo-protein and the three holo-HydA1 preparations was quantified by TXRF analysis on a PicoFox spectrometer (Bruker) after the XAS measurements using a gallium metal standard (Sigma; 5 µl protein sample was mixed with 5 µl Ga solution at 50 mg l^{-1}) and the respective HydA1 protein concentration (in the range of 1.1-2.0 mM) in the determination.

5.2.3 X-ray spectroscopy

X-ray absorption and emission spectroscopy at the Fe K-edge was performed at the undulator beamline ID26 of the European Synchrotron Radiation Facility (ESRF, Grenoble, France) as described in Chapter 4 and in ref. [35]. For normalization, the Kβ main-line (Kβ' and $K\beta_{1,3}$) and satellite line ($K\beta_{2,5}$) emission spectra were collected with overlapping spectral ranges. The resulting Kβ emission line spectra were normalized to unity area in the energy range 7035-7120 eV after setting the average amplitude of the last 10 high-energy points to zero. For the Kβ main-line region 3-8 spectra from separate sample spots and for the Kβ satellite line region 7-18 spectra from separate sample spots were averaged. Conventional Fe K-edge absorption spectra (XANES) were measured using the rapid scan mode of ID26 (scan duration 15 s) and total-fluorescence detection with a scintillation detector. Up to 80-120 XAS rapid-scans (five scans per sample spot) were averaged for the protein samples. Taking into account the X-ray

photoreduction of the solution samples of the diiron compounds, only first scans were used and 29-37 XAS rapid-scans (15 s) on separate sample spots were averaged. Site-selective XANES spectra were measured using Kβ' (7045 eV) or $K\beta_{1,3}$ (7058 eV) emission detection. For monitoring the Kβ-detected XANES a vertical-plane Rowland-circle spectrometer with an avalanche photodiode (APD) detector was used.

5.3 Results and Discussion

5.3.1 Metal content quantification with TXRF

Table 5-1 shows the iron contents in HydA1 apo- and holo-protein samples determined by TXRF analysis. The results confirm the expected iron contents of the samples. The apo-protein contains 4 ± 1 irons, the holo-proteins on average 6 ± 1 irons. The increase of ~2 Fe suggest the quantitative binding of the [2Fe] unit to the cubane cluster. In the protein maturated with the $[2Fe]_{odt}$ complex, the iron content is somewhat lower compared to the other samples. It could be assumed that in this case the [2Fe] complex binds less well and/or is partially removed during the protein purification step.

Table 5-1: Metal and protein concentrations and relative amounts of iron in HydA1 samples.

HydA1	concentration [mM]		Fe/protein
	protein	iron	
apo	1.98	8.5 ± 1.9	4.3 ± 1.0
holo (with $[2Fe]_{adt}$)	1.19	7.0 ± 0.5	5.9 ± 0.4
holo (with $[2Fe]_{pdt}$)	1.13	6.8 ± 0.5	6.0 ± 0.5
holo (with $[2Fe]_{odt}$)	1.21	6.1 ± 0.3	5.0 ± 0.2

Metal concentrations were determined by TXRF (mean of each 2 determinations for three (holo-protein) or four (apo-portein) preparations, ±standard deviation).

5.3.2 XES on HydA1 proteins

Figure 5-1A shows the Fe Kβ emission spectra of the apo-protein as well as the as-isolated holo-protein samples. The Kβ main-line as well as the satellite line emission spectra of the holo-

proteins are very similar in shape and amplitude but differ considerably from the apo-protein. The ligand environment of the iron atoms in all samples is therefore very similar. This suggests that all three [2Fe] cofactor analogues bind quantitatively to the [4Fe4S] cluster in the *in-vitro* maturation as it was also suggested by FTIR experiments [17, 235]. Hydrogen turnover activity, however, was only demonstrated for the $[2Fe]_{adt}$ maturated HydA1 [17, 63, 148]. These differences in activity may thus not be due to the direct iron-ligand environment but predominantly to the dithiolate ligand. The spectra of the three [2Fe] complexes (powder samples) are shown in Chapter 4 (model compounds, Fig. 4-3). As expected, no significant differences in shape and amplitude is observed, since the C / O / N atom in the bridgehead does not contribute significantly to the emission spectra. Fig. 5-1B shows a comparison of Kβ emission spectra of apo-protein, the $[2Fe]_{adt}$ complex, and the corresponding HydA1 holo-protein. The pronounced differences can be explained by the stoichiometric binding of the two sub-complexes in the protein and possibly also by different binding of the CO ligands to the [2Fe] unit (all terminal in the $[2Fe]_{adt}$ complex, but terminal and bridging in the [2Fe] subsite of the holo-protein [35]). The Kβ' feature at ~7045 eV is correlated with the number of unpaired 3d electrons and thus gives an indication of the spin state. While it is negligible for the diiron complex revealing its low-spin state (no unpaired spins) this feature is strongly increased for the high-spin iron containing [4Fe4S] cubane cluster. In the spectrum of the $[2Fe]_{adt}$ complex the maximum of the $K\beta_{1,3}$ feature is at lower energy compared to the apo-protein due to the influence of the CO/CN-ligands as well as the lower mean oxidation state (Table 5-2). It is suggested that in tendency, the energy of the $K\beta_{1,3}$ maximum increases with increasing mean Fe-ligand bond length as well as decreasing average field strength of the ligands according to the spectrochemical series [138]. The Kβ main-line (Kβ' and $K\beta_{1,3}$) spectrum for the holo-protein is intermediate between the $[2Fe]_{adt}$ complex and apo-protein regarding its Kβ' intensity and $K\beta_{1,3}$ energy. An overall shape closer to the apo-protein shows dominance of the cubane subsite in the H-cluster. Both subunits of the H-cluster contribute stoichiometrically to the $K\beta_{2,5}$ satellite emission line spectra (inset of Fig. 5-1B). Whereas the features at low energy are similar to $[2Fe]_{adt}$, the high-energy features are comparable to the apo-protein. The pronounced higher $K\beta_{2,5}$ emission intensity at lower energies for the [2Fe] compound is due to the additional CO ligand (decay from MOs with mainly CO character, see also the analysis of vtc emission for model compounds in Chapter 4). Accordingly, for the holo-protein, the [4Fe4S] cubane cluster contributes predominantly at higher energies whereas the diiron subunit contributes also at lower energies.

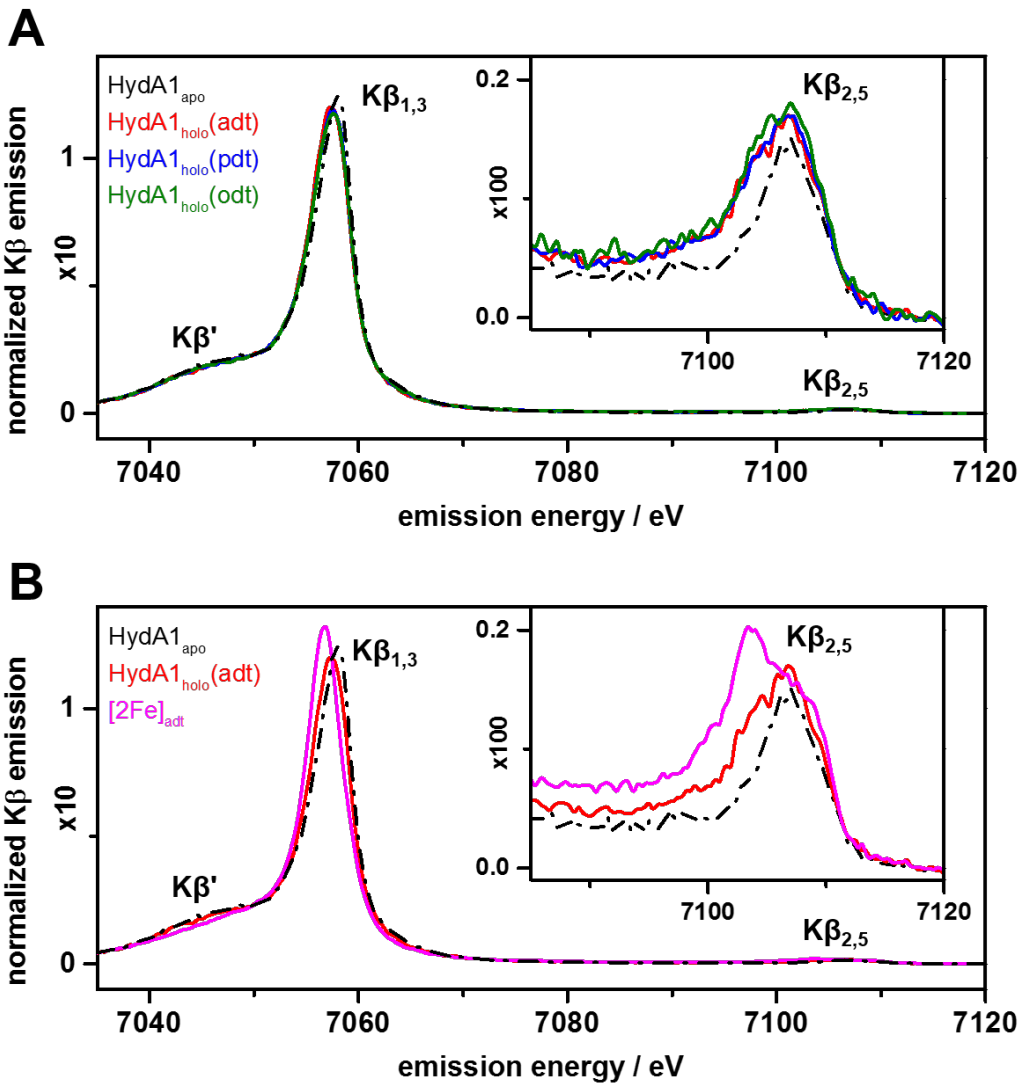

*Figure 5-1: Fe Kβ emission spectra of HydA1 samples and FeFe model compound (inset, Kβ satellite emission spectra). (**A**), spectra of apo-HydA1 protein and three different holo-proteins. (**B**), comparison of HydA1 apo-protein, with $[2Fe]_{adt}$ maturated holo-protein and the synthetic $[2Fe]_{adt}$ complex.*

Table 5-2: Fe $K\beta_{1,3}$ line energies.

	E (Fe-$K\beta_{1,3}$) [eV]
$HydA1_{apo}$	7057.1
$HydA1_{holo}$ (adt)	7056.9
$HydA1_{holo}$ (pdt)	7057.0
$HydA1_{holo}$ (odt)	7057.0
$[2Fe]_{adt}$	7056.7

Fe $K\beta_{1,3}$ line energies, from first moment calculations [163] over 7052-7062 eV (error ~ 0.05 eV). Data correspond to spectra in Fig. 5-1.

In summary, XES data shows the quantitative binding of the diiron unit to the apo-HydA1 protein. Furthermore, the comparison of the Kβ satellite emission spectra between the [2Fe] compound and the holo-HydA1 protein reveals different CO ligation, i.e. $[2Fe]_{adt}$ contains one additional CO ligand versus the H-cluster in holo-HydA1. It can be concluded that during H-cluster formation one CO ligand is released and thereby a bridging CO is formed.

5.3.3 XAS on HydA1 proteins

XANES spectra at the Fe K-edge of as-isolated holo-protein samples as well as the apo-protein, which were measured using detection of the total X-ray fluorescence, are shown in Figure 5-2A. Like in the XES spectra, the XANES spectra of the holo-proteins with three different dithiolates are very similar in edge shape and energy (Table 5-3). The XANES spectra of the three different synthetic diiron compounds are also very similar (see Chapter 4, Fig. 4-3). This confirms the almost quantitative binding of the diiron complex to the apo-protein and the very similar oxidation state and ligand environment of the iron atoms in the three reconstituted HydA1 samples.

Pronounced differences in the XANES spectra between apo-protein, the $[2Fe]_{adt}$ complex, and the holo-protein (Fig. 5-2B) are mainly due to the different coordination geometry of the respective iron centers and the chemical nature of their ligands. The XANES of apo-protein shows a typical shape for FeS clusters, whereas a higher edge energy and a distinctive primary maximum at ~7129 eV is observed for the diiron compounds. For the holo-protein the K-edge shape and energy reflect the dominance of the [4Fe4S] cubane cluster, e.g. the small primary maximum reveals a predominant coordination of Fe by sulfur ligands [252].

The respective pre-edge absorption features are emphasized in the inset of Figure 5-2A and B. The core-to-valence spectra reveal for the $[2Fe]_{adt}$ two distinct peak features at slightly higher excitation energies compared to the apo- as well as holo-proteins for which one main peak feature is discernible at roughly the same energy. As described in Chapter 4, XAS data and DFT calculations on different low-spin diiron compounds revealed that the second peak reflects transitions into MOs with mainly CO ligand character. The first peak is dominated by transitions into MOs with mostly Fe-d and weak ligand character [124].

The collection of XAS spectra for two different emission energies allows a site-selective analysis due to the spin selectivity of the Fe Kβ emission. The emission energies were selected in a way that either the high-spin or the low-spin iron species predominantly contributed to the spectra. The $K\beta_{1,3}$-detected XANES is dominated by the high-spin iron ions in the apo-protein

and the Kβ'-detected XANES is dominated by the low-spin iron ions in the diiron model complex. Consequently, $K\beta_{1,3}$ detection (7058 eV) probes selectively the high-spin irons and Kβ' emission detection (7045 eV) probes selectively the low-spin irons of the H-cluster of HydA1 [35, 133].

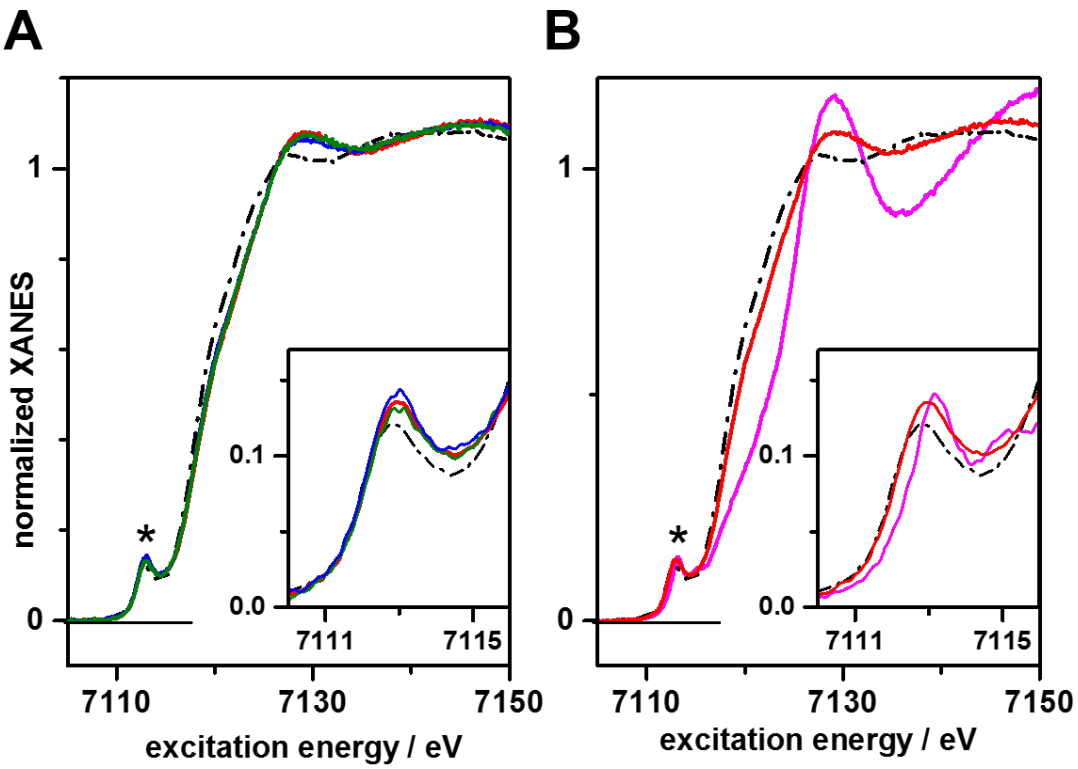

*Figure 5-2: XANES spectra at the Fe K-edge of HydA1 samples and the FeFe model compound (inset, pre-edge absorption spectra, marked as asterisk in XANES spectra). (**A**) spectra of apo-HydA1 protein and three different holo-proteins. (**B**) comparison of HydA1 apo-protein, with $[2Fe]_{adt}$ maturated holo-protein and the synthetic $[2Fe]_{adt}$ complex. The color code is the same as in Figure 5-1.*

Table 5-3: Fe K-edge energies.

	E (Fe-edge) [eV]
$HydA1_{apo}$	7118.7
$HydA1_{holo}$ (adt)	7119.3
$HydA1_{holo}$ (pdt)	7119.2
$HydA1_{holo}$ (odt)	7119.3
$[2Fe]_{adt}$	7122.4

Fe K-edge energies (± 0.1 eV) were derived at 50% level of the normalized XANES spectra in Fig. 5-2.

Figure 5-3 shows narrow-band Kβ-detected Fe K-edge spectra of the apo-protein, $[2Fe]_{pdt}$ complex and the adt holo-protein. Whereas for the main K-edge shape and energy only slight changes occur, prominent energy and intensity variations are visible in the pre-edge region. For Kβ' emission detection the pre-edge feature is almost absent for the apo-protein, which contains only high-spin iron ions. The Kβ' emission is explained by the interaction between unpaired metal 3d spins and the spin of the decaying 3p electron with the same flavor [35]. For resonant excitation (pre-edge, 1s → 3d), no excitation of a 1s electron with an α-spin can occur in high-spin Fe(II) and Fe(III) complexes and thus no coupling between unpaired 3d spins with decaying 3p electrons. For the low-spin diiron complex the feature increased expectedly compared to the $K\beta_{1,3}$ emission detection. The holo-protein containing low-spin and high-spin iron shows a decrease of the pre-edge features in comparison to Kβ' to $K\beta_{1,3}$ emission detection, which is in agreement with a stoichiometric contribution of the sub-complexes.

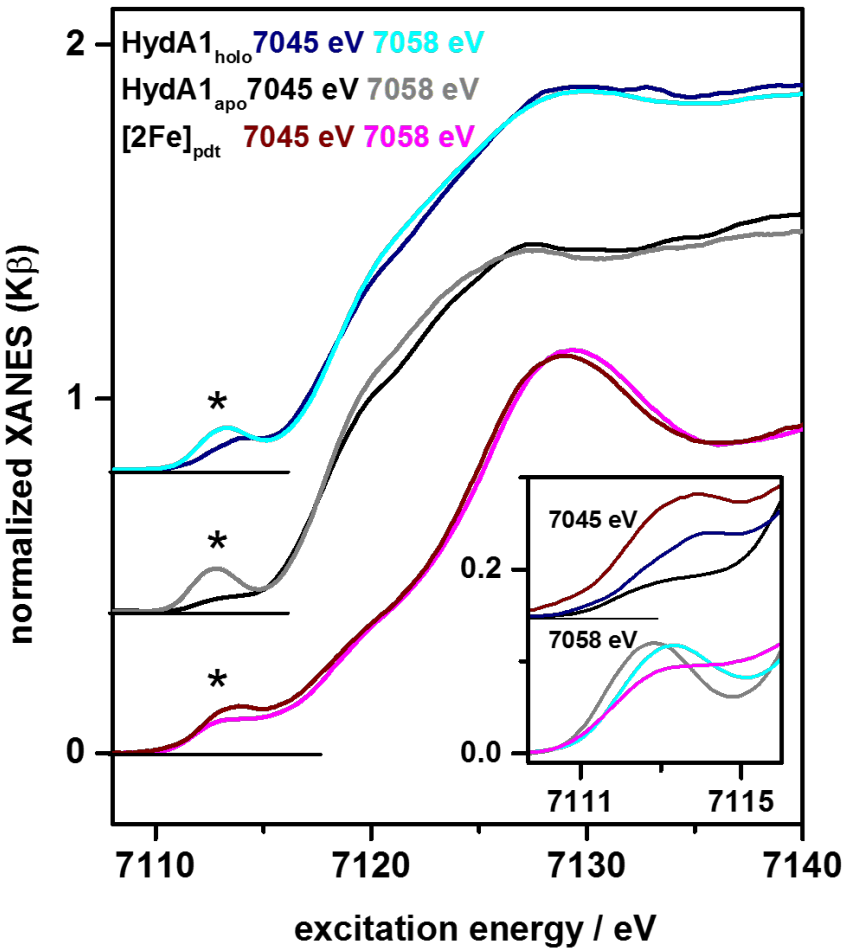

Figure 5-3: Smoothed Kβ-detected Fe K-edge spectra of the apo-HydA1 protein ($HydA1_{apo}$), holo-HydA1 protein ($HydA1_{holo}$), and of a synthetic diiron model compound ($[2Fe]_{pdt}$). The inset shows the Fe pre-edge absorption (asterisk) for $K\beta_{1,3}$ emission detection (7058 eV) and for Kβ' emission detection (7045 eV). Spectra are partly vertically shifted for comparison.

Conclusions

XAS/XES at the Fe K-edge was used to compare the properties of the H-cluster derived from *in-vitro* maturation with adt, pdt or odt diiron compounds. Comparison to earlier published data shows that the Kβ main- and satellite emission spectra as well as the Fe K-edge absorption spectra of the *in-vitro* matured HydA1 proteins are very similar to the spectra obtained for the native *in-vivo* maturated enzyme [35, 133]. This confirms successful H-cluster formation by reconstitution of HydA1 apo-protein with the synthetic diiron complexes. TXRF analysis, showing the expected four iron atoms in apo-protein and on average two additional iron atoms in the *in-vitro* matured HydA1 samples, further strengthens this motion.

The Kβ emission spectra as well as the Kα-detected XANES spectra of the HydA1 proteins show that the H-cluster subsites contribute stoichiometrically to the spectra, i.e. they represent the stoichiometric sum of the individual contributions of all six iron atoms in the H-cluster [35]. Comparison of apo-protein, holo-protein and respective synthetic [2Fe] model compounds reveals that the $K\beta_{2,5}$ feature around ~7104 eV as well as the pre-edge absorption at highest energies is an indicator for CO ligation changes at the [2Fe] subsite. The $K\beta_{2,5}$ spectrum at lowest energies is primarily influenced by changes at the μS bridges in the [4Fe4S] cubane which e.g. occur during redox changes. The combination of high-resolution X-ray absorption and emission spectroscopy thus provides a sensitive tool to monitor CO coordination and redox changes at the H-cluster [35, 133]. In addition, spin selectivity of the Kβ' and $K\beta_{1,3}$ spectral regions for resonant excitation into the pre-edge facilities discrimination between both subsites of the H-cluster with regard to their low-spin and high-spin iron species and thus an individual monitoring of their redox reactions and ligation changes.

Variation of the dithiolate bridge (C / O / N atom in the bridgehead) does not significantly alter the X-ray absorption and emission spectra of both the [2Fe] model compounds and the respective HydA1 holo-proteins. It has been suggested that the secondary amine acts as a base for proton exchange in the catalytic cycle [148]. The Brønsted base function of the adt-NH group as well as its conformational flexibility likely is important for proton binding and transfer to the active site prior to H_2 formation and therefore fundamental for the high catalytic activity of [FeFe]-hydrogenases [235]. Replacement of the amine by an oxygen atom or a CH_2-group may lead to a loss of hydrogen bonding interactions to the surrounding amino acids which probably is important in the hydrogen conversion reaction [118, 281].

6 Lyophilization stabilizes the oxygen-sensitive hydrogenase cofactor

Results reported in this chapter have been published in part in:
J. Noth, R. Kositzki, K. Klein, M. Winkler, M. Haumann, and T. Happe, **Lyophilization protects [FeFe]-hydrogenases against O_2-induced H-cluster degradation**, *Scientific Reports*, **2015**, *5*, 13978 https://doi.org/10.1038/srep13978 [180]

6.1 Introduction

[FeFe]-hydrogenases catalyze efficiently the reversible formation of molecular hydrogen (H_2) and are therefore promising tools for renewable energy applications. Unfortunately, the high sensitivity towards molecular oxygen (O_2) is a drawback for use of [FeFe]-hydrogenases in biotechnological H_2 production. Irreversible O_2-induced H-cluster degradation occurs even during exposure to traces of O_2 for seconds. Freeze-drying (lyophilization) can be used to stabilize the oxygen-sensitive hydrogenase cofactor and thus may facilitate the utilization of the enzymes as sustainable catalysts in biotechnological applications. The integrity of the H-cluster in lyophilized HydA1 [FeFe]-hydrogenase from the green alga *Chlamydomonas reinhardtii* was analyzed by X-ray absorption spectroscopy. XANES and EXAFS spectra reveal an intact H-cluster in lyophilized HydA1 proteins before and after exposure to dry pure O_2 gas. Only exposition to air at ambient humidity causes an irreversible degradation of the H-cluster. Determination of H_2-evolution shows that full activity is regained after rehydration of previously lyophilized hydrogenase enzyme.

6.2 Materials and Methods

6.2.1 Protein samples

Lyophilized HydA1 protein samples were prepared by Dr. Jens Noth from the group of T. Happe (Bochum, Germany). *E. coli* expressed apo-HydA1 (generated in the absence of the three maturases HydE, -F, -G) was *in-vitro* maturated with the chemically synthetized $[2Fe]_{adt}$ complex ($[Fe_2(\mu\text{-adt})(CN)_2(CO)_4]^{2-}$, adt = $(SCH_2)_2NH$) and purified as previous described [63]. Apo- and holo-HydA1 samples were concentrated to 2.2 mM. NaDT was added and ~30 µl of

these samples was injected anaerobically into Kapton-covered XAS sample holders. For lyophilization (freeze-drying) the protein samples were frozen in a round-bottom flask filled with liquid nitrogen and put into the freeze-dryer for 24 h as described in ref. [180]. For O_2-exposure part of the samples were then aerated with dry 100% O_2 gas for 15 min. After flushing for 5 min with argon the samples were storaged at -80°C and subsequently in liquid nitrogen. One lyophilized holo-protein sample was additionally kept at ambient humidity in air for one day prior to the XAS experiments.

6.2.2 X-ray absorption spectroscopy

XAS experiments at the Fe K-edge was carried out at beamline KMC-1 at BESSY (Helmholtz Center Berlin, Germany) with the storage ring operated in top-up mode (250 mA). A standard setup for XAS [49] (Si[111] double-crystal monochromator, liquid-helium cryostat (Oxford) for holding the samples at 20 K, 13-element energy-resolving Ge detector (Canberra)) was used for Fe X-ray fluorescence detection (shielded by 10 μM Mn foil against scattered X-rays). The spot size on the sample was set by slits to about 5 (horizontal) x 0.5 (vertical) mm^2. Up to 4 single-spot XAS spectra with scan durations of ~30 min per sample were collected. Dead-time corrected XAS spectra were averaged, normalized, and EXAFS oscillations were extracted (E_0 = 7112 eV) as previously described [49]. The absorption spectrum of a Fe foil was measured in parallel and its first inflection point at 7112 eV was used for energy calibration [133, 140]. XANES spectra were processed using in-house software. Fourier-transforms (FT) were calculated (using cos-windows extending over 10% at both k-range ends) and least-squares fit analysis of unfiltered EXAFS spectra were carried out using in-house software [49] and phase functions calculated with FEFF7 (S_0^2 = 0.9; E_0 was refined to about 7115 ± 2 eV in the EXAFS fits).

6.3 Results and Discussion

6.3.1 H_2-evolution activities and O_2-tolerance of lyophilized HydA1 proteins in the apo and holo maturation state

Measurements of H_2-production rates employing the sodium-dithionite driven methyl-viologen-reduction assey were carried out by Dr. J. Noth. Lyophilized HydA1 hydrogenase samples show an activity close to 100% after rehydration. To determinate the activity of the apo

protein, these samples were maturated *in-vitro* using an at least 10-fold excess of the synthetic diiron complex $2Fe_{adt}$. The comparison of lyophilized HydA1 hydrogenase samples with non-lyophilized control samples reveals that HydA1 [FeFe]-hydrogenase can be lyophilized without any loss of catalytic activity.

O_2-tolerance of lyophilized HydA1 was tested by Dr. Jens Noth. H_2-production rates were measured for lyophilized samples (apo and holo enzyme state) after exposing to 100% dry O_2 gas (up to 24 h at RT) or after keeping them in air at ambient humidity for one day and compared with solution samples of non-lyophilized HydA1. The results reveal that lyophilized samples are completely unaffected by O_2 (24 h, 100%) while HydA1 in solution lost the entire activity after 15 min under 2.5% O_2. However, for lyophilized HydA1 after exposed to ambient air for 24 h a complete deactivation was observed. Analysis of the O_2-inhibition at different levels of humidity indicated decreasing O_2-tolerance with increasing humidity. The humidity most probably leads to partial rehydration explaining the loss of O_2-tolerance. Notably, freeze-dried apo-enzyme loses its competence for being *in-vitro* maturated to active holo-enzyme when exposed to O_2 under humid conditions. This suggests that even the [4Fe4S] cluster alone is attacked by O_2 in solution.

6.3.2 XAS on lyophilized HydA1 proteins

XAS was carried out to determine molecular structure (iron-iron distance and iron-ligand bond lengths) and redox state of the H-cluster sub-complexes in apo-HydA1 and holo-HydA1 proteins. The five lyophilized protein samples (see M&M; denoted as apo-O_2, +O_2; holo-O_2, +O_2, +O_2 +H_2O) were compared with results from former HydA1 studies: (1) apo-HydA1 protein overexpressed in *Escherichia coli* (*Ec*) in the absence of the three maturases HydE, -F, -G and therefore containing only the [4Fe4S] unit of the H-cluster, which was prepared anaerobically and studied in anoxic buffer solution (Chapter 5.1). (2) holo-HydA1 protein containing the complete H-cluster, ([4Fe4S]-[2Fe]), which was prepared anaerobically after overexpression in *Clostridium acetobutylicum* (*Ca*) in the presence of HydE, -F, -G [35, 133] or obtained by *in-vitro* reconstitution of apo-HydA1 from *Ec* with a synthetic [2Fe] analogue ($2Fe_{adt}$) and studied in anoxic solution (Chapter 5.1). (3) Holo-HydA1 protein from *Ca* in solution, which was exposed to O_2 [134].

Figure 6-1 shows the XANES spectra and Table 6-1 the K-edge energies of the eight different HydA1 protein samples. The XANES spectra of apo-HydA1 in solution, after lyophilization, and after extended O_2-exposure of the lyophilized protein are almost indistinguishable and

similar to previously obtained apo-HydA1 spectra [133]. This implies a similar iron oxidation state and coordination environment in an intact [4Fe4S] cluster under these conditions (Fig. 6-1, a). Accordantly, the structure of the [4Fe4S] cluster is practically not affected by lyophilization. Additionally, the XANES results reveal that the "lyophilized" [4Fe4S] cluster is resistant against oxidative degradation. The XANES spectra of the lyophilized apo-protein differ significantly from the corresponding holo-protein sample (Fig. 6-1, b). This indicates quantitative binding of the [2Fe] unit to the cubane cluster in the lyophilized *in-vitro* $2Fe_{adt}$ reconstituted holo-protein. The XANES spectra of the three anaerobic holo-HydA1 preparations (Fig. 6-1, c) are very similar with nearly identical K-edge energies (~7119.5 eV) and also closely resembled previously reported spectra [35, 133]. After O_2-exposure, the XANES of holo-HydA1 in solution (*Ca*) is drastically altered, i.e. the edge energy and primary maximum is increased, reflecting symmetrization of the iron coordination environment, whereas the spectra of the O_2-exposed lyophilized sample shows only small changes compared to the anaerobic holo-HydA1 preparations (Fig. 6-1, d). The slightly increased edge energy and maximum amplitude suggested limited oxygen binding and iron oxidation. This suggests that the O_2-induced H-cluster degradation, as shown for samples in solution [134], is prevented in the lyophilized sample. However, after exposure to air at ambient humidity, the XANES of lyophilized holo-HydA1 is also drastically altered, reflecting symmetrization of the iron

Table 6-1: Fe K-edge energies.

HydA1:		E (Fe-edge) [eV]
apo (*Ec*, sol)	$-O_2$	7118.9
apo (*Ec*, lyo)	$-O_2$	7118.7
	$+O_2$	7118.8
holo (*Ca*, sol)	$-O_2$	7119.5
	$+O_2$	7120.6
holo (*Ec*, adt, sol)	$-O_2$	7119.4
holo (*Ec*, adt, lyo)	$-O_2$	7119.5
	$+O_2$	7119.7
	$+O_2 + H_2O$	7122.0

Fe K-edge energies (± 0.1 eV) were derived at 50% level of the normalized XANES spectra in Fig. 6-1.

coordination environment as shown for the holo-HydA1 in solution (*Ca*) (Fig. 6-1, d). This shows that the O_2-induced H-cluster degradation in lyophilized samples requires previous rehydration.

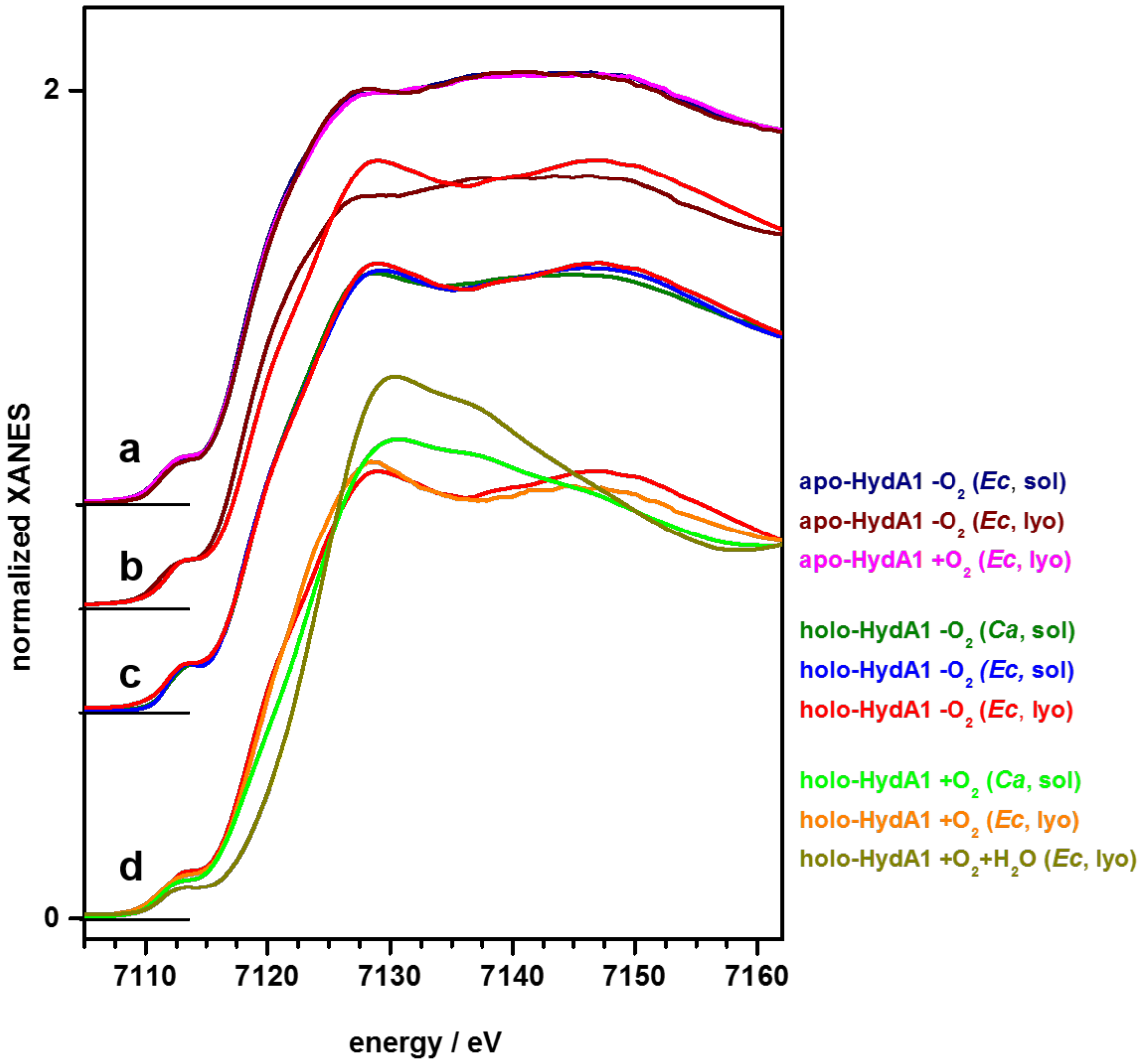

Figure 6-1: XANES spectra of [FeFe]-hydrogenase samples. The spectra were vertically shifted for comparison. Ca and Ec, protein expressed in C. acetobutylicum (with HydE, -F, -G) or E. coli (without HydE, -F, -G); sol and lyo, protein in solution or lyophilized.

EXAFS analysis was carried out to determine the interatomic distances in the H-cluster (Fig. 6-2). The EXAFS spectra of solution and lyophilized apo-HydA1 both are well described assuming an intact [4Fe4S] cubane cluster with the typical four Fe-S bonds (~2.3 Å) and three Fe-Fe distances (~2.7 Å) per Fe ion (Table 6-2). The Fe-S bond lengths are slightly (~0.02 Å)

shorter whereas the Fe-Fe distance is alike in the lyophilized protein. The ~30% smaller Debye-Waller parameter ($2\sigma^2$) of the Fe-Fe distances in the lyophilized protein explains the increased amplitude of the second Fourier-transform (FT) peak of the EXAFS spectrum due to the Fe-Fe distances (Fig. 6-2, a). This may reflect reduced configurational flexibility of the cysteine ligands to [4Fe4S] in the lyophilized protein. The same structural parameters are observed after

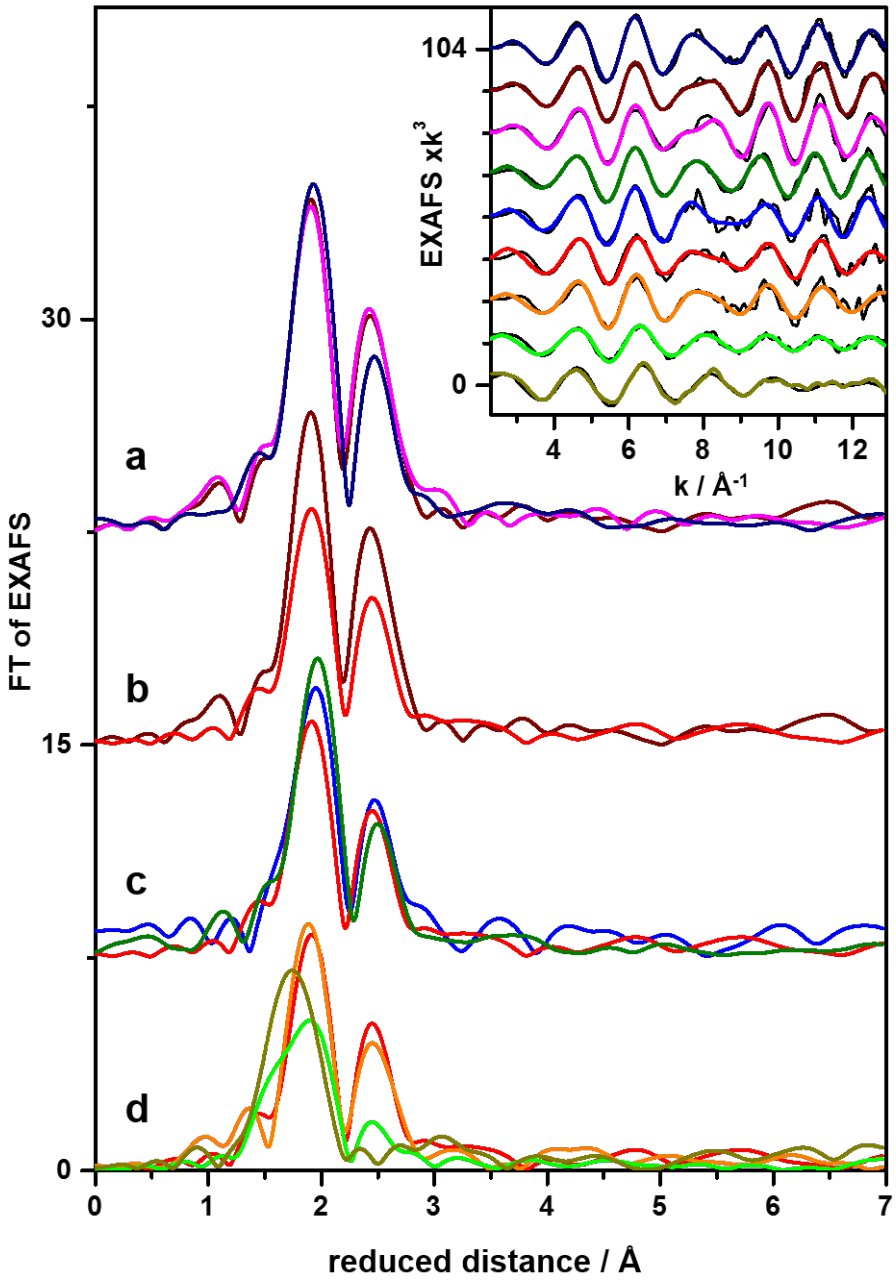

Figure 6-2: Fourier-transforms (FTs of experimental data) of EXAFS spectra in the inset (black lines, experimental data; colored lines, simulation with parameters in Table 6-2). The color code is the same as in Fig. 6-1. The spectra were vertically displaced for comparison.

O_2-exposure of lyophilized apo-HydA1 (Table 6-2). This means that [4Fe4S] did not react with oxygen and supports that freeze-drying of apo-HydA1 prevents the O_2-induced degradation.

Simulation of the EXAFS of holo-HydA1 from *Ca* in solution, containing mainly the reduced H-cluster [35, 133], reveal similar iron-ligand bond lengths and Fe-Fe distances as previously reported [44, 134, 252, 253] (Table 6-2). The Fe-Fe distance in [2Fe] (~2.5 Å) could be distinguished from the Fe-Fe distances in [4Fe4S] (~2.7 Å) and Fe-C(=O/N) bonds in [2Fe] (~1.8 Å, dominated by the shorter Fe-CO bonds) are detectable, next to Fe-S bonds (~2.3 Å). The EXAFS spectra of the $2Fe_{adt}$ reconstituted holo-HydA1 protein in solution as well as in the lyophilized state are well simulated assuming that a complete H-cluster is quantitatively present also in these proteins (Fig. 6-2, c; Table 6-2). The slightly shorter Fe-S bonds, ~0.02-0.04 Å longer Fe-Fe distance in [2Fe], and smaller $2\sigma^2$-value of the thus more homogeneous Fe-Fe distances in [4Fe4S] may suggest that the H-cluster is more poised towards the oxidized state in the $2Fe_{adt}$ reconstituted holo-HydA1 possibly containing a mixed-valence Fe(I)Fe(II) state of [2Fe] [3, 35, 238]. This indicates that a complete and intact H-cluster is also preserved in the lyophilized holo-HydA1 protein. However, the ~0.1 Å longer Fe-C(=O/N) bond length and the longest Fe-Fe distance in the diiron unit (Table 6-2) may suggest that a surplus ligand is bound to the Fe ions of [2Fe] in the lyophilized protein.

After ~15 min O_2-exposure of lyophilized holo-HydA1 only minor structural changes are observed at the H-cluster. The EXAFS spectrum is still compatible with an intact H-cluster (Fig. 6-2, d). However, the shortening of the Fe-C(=O/N) bonds and of the Fe-Fe distances in [4Fe4S] and further elongation of the FeFe distance in [2Fe] (Table 6-2), as well as the slightly increased K-edge energy and amplitude (Fig. 6-1, d) compared to lyophilized anoxic holo-HydA1 can be interpreted by one-electron oxidation of the H-cluster and binding of an oxygen species to [2Fe], as observed in a crystal structure of bacterial [FeFe]-hydrogenase [190] and suggested by previous XAS measurements on short-time O_2-exposed holo-HydA1 from *Ca* [134]. Apparently, the further O_2-induced H-cluster degradation as observed for solution protein is prevented in lyophilized holo-HydA1 (Fig. 6-2, d). Simulation of the EXAFS spectra of O_2-exposured holo-HydA1 from *Ca* in solution reveals clearly increased numbers and longer bond lengths of the shortest iron-ligand interactions, decreased numbers of Fe-S bonds, an increased Fe-Fe distance in [2Fe], and about halved numbers of Fe-Fe distances of ~2.7 Å. This is in agreement with an increased iron oxidation level (increased initial K-edge energy, Table 6-1) and considerable replacement of Fe-S by Fe-O bonds due to significant oxidative degradation of the [4Fe4S] unit under retention of the integrity of the (more oxidized) [2Fe]

unit, as previously suggested [134, 253]. However, after exposure of lyophilized holo-HydA1 to air at ambient humidity, the EXAFS analysis (Fig. 6-2, d) revealed pronounced structural changes indicating an O_2-induced H-cluster degradation similar to that in O_2-exposed holo-HydA1 in solution (Table 6-2).

Table 6-2: EXAFS simulation parameters of HydA1 proteins.

		N [per Fe ion] / R [Å] / $2\sigma^2$ x10^3 [Å^2]					R_F
HydA1:		Fe-C(O)	Fe-S	Fe-Fe, [2Fe]	Fe-Fe, [4Fe4S]	Fe···O/N	[%]
apo							
(*Ec*, sol)	-O_2	-	4 / 2.30 / 6	-	3 / 2.72 / 14	-	9.8
(*Ec*, lyo)	-O_2	-	4 / 2.28 / 7	-	3 / 2.73 / 10	-	9.0
	+O_2	-	4 / 2.28 / 7	-	3 / 2.73 / 10	-	12.2
holo							
(*Ca*, sol)	-O_2	1 / 1.79 / 5$^{\#}$	3.5 / 2.32 / 8	0.5 / 2.51 / 2$^{\#}$	2 / 2.72 / 10	1 / 2.86 / 5$^{\#}$	11.5
	+O_2	1.89* / 2.03 / 5$^{\#}$	1.77* / 2.27 / 8$^{\&}$	0.5 / 2.55 / 2$^{\#}$	1.32* / 2.70 / 10$^{\&}$	1 / 2.90 / 5$^{\#}$	11.4
(*Ec*, adt, sol)	-O_2	1 / 1.81 / 5$^{\#}$	3.5 / 2.31 / 9	0.5 / 2.53 / 2$^{\#}$	2 / 2.72 / 5	1 / 2.85 / 5$^{\#}$	15.4
(*Ec*, adt, lyo)	-O_2	1 / 1.91 / 5$^{\#}$	3.5 / 2.27 / 10	0.5 / 2.55 / 2$^{\#}$	2 / 2.72 / 7	1 / 3.00 / 5$^{\#}$	12.5
	+O_2	1 / 1.87 / 5$^{\#}$	3.5 / 2.26 / 9	0.5 / 2.58 / 2$^{\#}$	2 / 2.71 / 10	1 / 3.05 / 5$^{\#}$	14.4
		0.82* / 1.86 / 5$^{\#}$	3.65* / 2.26 / 10$^{\&}$	0.5 / 2.57 / 2$^{\#}$	1.87* / 2.71 / 7$^{\&}$	1 / 3.07 / 5$^{\#}$	14.7

*N, coordination number; R, interatomic distance; $2\sigma^2$, Debye-Waller parameter; R_F, fit error sum [49] calculated for reduced distances of 1-3 Å. Data correspond to EXAFS spectra in Fig. 6-2. Fit restraints: N-values were fixed to the given numbers in the fits representing the expected coordination numbers for the [4Fe4S] cluster in apo-HydA1 or the approximate N-values for a complete H-cluster in holo-HydA1 [133, 134], *except for N-values that were allowed to vary in the fits; $^{\&}$the same $2\sigma^2$-values were used for respective fits of spectra plus or minus O_2; $^{\#}2\sigma^2$ values that were fixed in the simulations. Ca and Ec, protein expressed in C. acetobutylicum (with HydE, -F, -G) or E. coli (without HydE, -F, -G); sol and lyo, protein in solution or lyophilized; adt, Ec apo-HydA1 reconstituted with the $2Fe_{adt}$ complex [17, 63].*

Conclusions

Freeze-dried [FeFe]-hydrogenase samples were investigated by X-ray absorption spectroscopy in order to characterize O_2-induced H-cluster degradation. Lyophilization of protein samples is advantageous for XAS measurements. In contrast to solution samples, higher X-ray fluorescence signal intensities can be achieved with similar protein contents. Moreover, the scattering background is drastically diminished due to the absence of water. Consequently, data quality increases for shorter measurement times when using lyophilized samples.

The XANES and EXAFS data of lyophilized apo- and holo-HydA1 proteins show that the [4Fe4S] cluster as well as the entire H-cluster are unchanged before and after exposure to oxygen and similar to the corresponding [FeFe]-hydrogenase samples studied in anoxic solution. However, when the lyophilized samples were exposure to ambient humidity air, H-cluster degradation was observed. It can be concluded that freeze-drying converts the extremely oxygen-sensitive [FeFe] hydrogenases into enzymes which are fully resistant against O_2-induced H-cluster degradation. This method may be useful to overcome the limitations for biotechnical applications of [FeFe] hydrogenases as a catalyst for H_2 fuel generation.

(B) Bimetallic oxidase proteins

Scientific background

Proteins of the ferritin-like superfamily containing a dimetal-carboxylate cofactor (DMC) perform various important functions, including iron storage (ferritin and bacterioferritins) and multi-electron redox chemistry such as methane and dioxygen activation [97]. These functions have led to much interest of the chemical industry in the proteins, for example with regard to oxidation of organic molecules with molecular oxygen. The characteristic feature within this protein group is a metal-coordinating 4-helix bundle with a unique topology (Figure B-1A).[97] Dimetal sites coordinated by four carboxylate groups and two histidine residues are in the center of the structures (see Figure B-1). Well-known representatives of the ferritin-like superfamily are the R2 proteins of ribonucleotide reductase (RNR) class I enzymes and the bacterial multicomponent monooxygenases (BMMs). Both proteins contain similar active site structures and reduce molecular oxygen. Their high-valent cofactor states (i.e. oxidized states) catalyze different redox reactions (1- or 2-electron oxidations). While most DMC proteins carry a diiron site, now also proteins have become known with a dimanganese or a heterodinuclear manganese/iron cofactor, which perform similarly versatile chemistry.[96] The four carboxylate ligands of the diiron site in BMMs as well as the heterodinuclear cluster in R2c

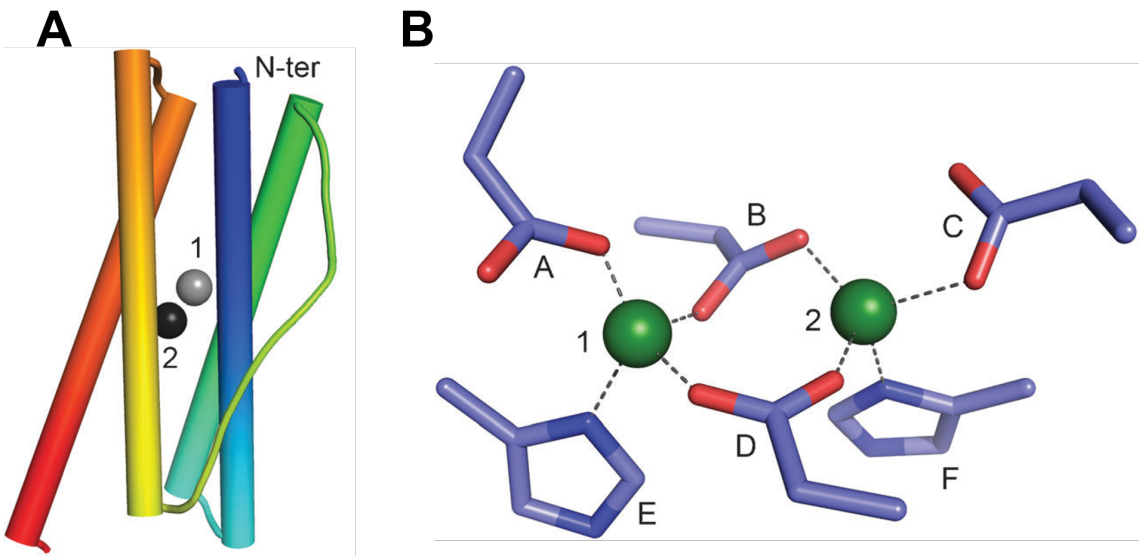

*Figure B-1: (**A**) Architecture of the characteristic 4-helix bundle with distinctive topology in the proteins of the ferritin-like superfamily (site 1, N-terminal metal-binding site, gray sphere; site 2, C-terminal metal-binding site, black sphere). (**B**) Illustration of the dimetal-carboxylate cofactor coordinated by four carboxylate groups (A-D) and two histidine residues (E, F). Reproduced from [97] with permission from The Royal Society of Chemistry.*

(class Ic R2 proteins) are glutamate residues. The homodinuclear clusters in class Ia and Ib R2 proteins contain three glutamate residues and one aspartate (at the N-terminal metal-binding site). The carboxylate coordination modif varies between mono- and bidentate bridging or terminal ligation, which facilitates changes in coordination geometry during the reaction with molecular oxygen (so-called carboxylate shifts) [85].

Bacterial multicomponent monooxygenases (BMM) perform the O_2-dependent hydroxylation of hydrocarbons, for example the oxidation of methane to methanol by the soluble methane monooxygenase (MMO) (Figure B-2). The 2-electron substrate oxidation sequence includes a di-μ-oxo bridged Fe(IV)Fe(IV)-intermediate of the diiron cofactor.

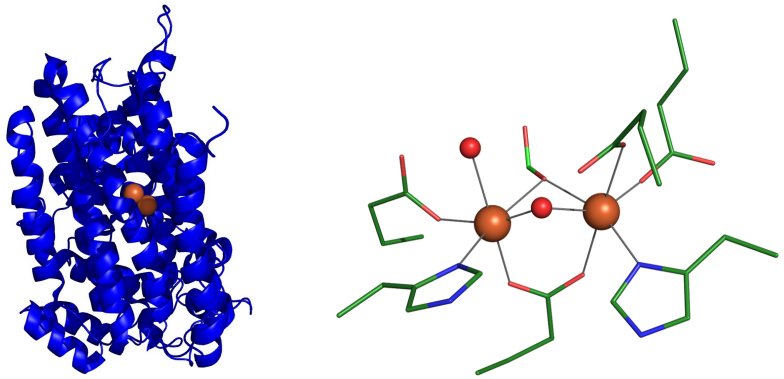

*Figure B-2: Crystal structure (**left**) and cofactor (**right**) of the oxidized resting state of the methane monooxygenase (MMOH) from Methylococcus capsulates (Mc, PDB entry 1FZ1, ref. [280]). Color code: green, carbon atoms, red, oxygen atoms and blue, nitrogen atoms. Iron atom positions are shown as orange spheres, and water/oxo/hydroxo ligands as red spheres. Images were generated using PyMOL.*

$$NADH + CH_4 + O_2 + H^+ \xrightarrow{\text{Methan-Monooxygenase}} NAD^+ + CH_3OH + H_2O \qquad (19)$$

Ribonucleotide reductases (RNR) modify deoxyribonucleotides, which are used in DNA synthesis. The principal reaction starts with the generation of a free thiyl radical (from a conserved cysteine residue at the active site) which initiates the reduction of the C2'-OH bond of the corresponding ribonucleotides.

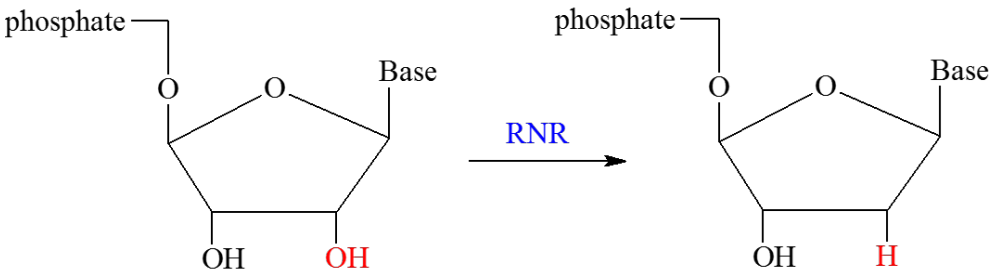

(20)

All RNR proteins employ metal centers and organic radicals in the substrate reactions. Based on the different initial radical states for generating the thiyl radical at the active site and the cofactor types as well as oxygen requirements, three main classes of RNR proteins are distinguished (class I, II, III).[121] The best-known and most-studied **Class I** RNR (e.g. from *E. coli*) contains a dimetal-oxygen cluster and depends solely on O_2 for activation. In **Class II** (e.g. from *Lactobacillus lehmannii*) the thiyl radical can be generated by reaction with a cobalt containing cobalamin cofactor (vitamin B_{12}) under anaerobic as well as aerobic conditions. **Class III** RNRs (e.g. *bacteriophage T4*) are only active in anaerobic environment and harbor a

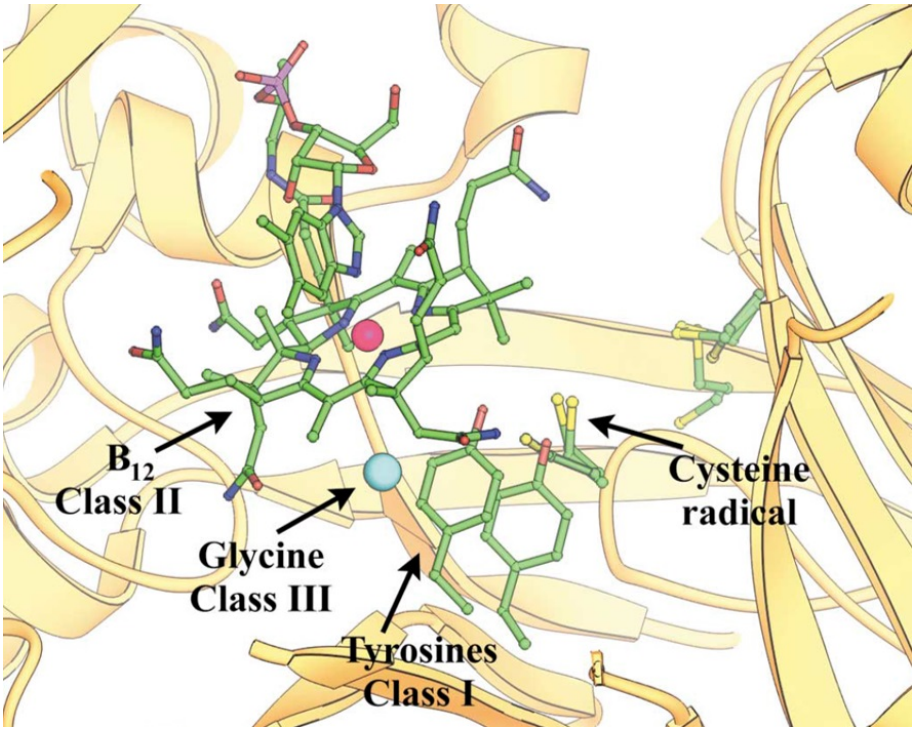

Figure B-3: Indication of the different radical generation systems and transfer pathways in the three classes of RNR, based on superposition of the indicated cysteine radical of the substrate binding active sites. Shown are for class I the last tyrosines, for class II the B_{12}-derivative adenosylcobalamin (magenta sphere: cobalt), and the glycyl radical site for class III (cyan sphere). Reproduced with permission from [246]. Copyright (2002) Springer Nature.

[4Fe4S] cluster coupled to S-adenosylmethionine (SAM) which generates a glycyl radical. Whereas in class II the radical is an amino acid close to the active site, the stable radicals of class I and III are generated on a separate protein subunit and transferred to the active site by proton-coupled electron transfer (PCET) via conversed hydrogen bonded amino acid residues (radical transfer pathway). There are many organisms that contain several different RNRs.[41]

Class I RNR proteins comprise two different subunits (R1(or α) and R2(or β)) in a $R1_2R2_2$ tetramer. The large R1 subunit contains the substrate binding active site and the small R2 subunit harbors the dimetal cofactor. As mentioned above, the R2 subunit of class I RNR belongs to the ferritin-like protein family. The metal cofactor (FeFe, MnMn or MnFe) is coordinated by two histidine and four carboxylate residues. Class I can be further divided in four subclasses (**Ia, Ib, Ic, Id**) based on the nature of the dimetal cluster of the R2 subunit. In general, all subclasses are structurally homologous and contain almost identical metal coordination sites.[41]

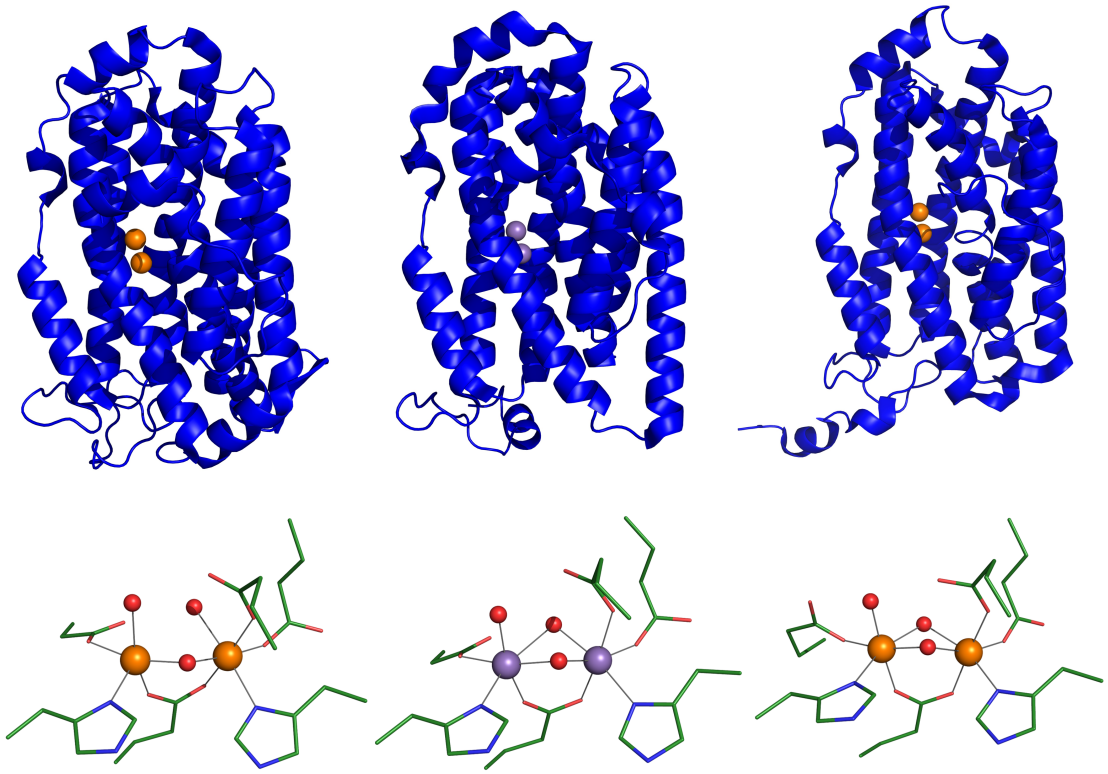

*Figure B-4: Crystal structures (**top**) and cofactors (**bottom**) in the oxidized resting state of three different subclasses of class I RNR R2 subunit. **Left**, class Ia from Escherichia coli (Ec, PDB entry 1MXR, ref. [98]); **middle**, class Ib from Corynebacterium ammoniagenes (Ca, PDB entry 3MJO, ref. [42]); and **right**, class Ic from Chlamydia trachomatis (Ct, PDB entry 1SSY, ref. [99], for R2c in the oxidized state only a structure with an diiron cluster is available). For the color code see Figure B-2. Mn and Fe are shown as purple and orange spheres, respectively.*

The R2 protein of RNR **class Ia** and **Ib** contain a diiron or dimanganese center to produce a stable tyrosyl radical, which is essential for the enzymatic activity.[96] The homodimeric metal centers have identical metal-binding residues (see Figure B-4) and during the reaction of their reduced form with O_2, a radical is generated on a nearby (~5-6 Å) tyrosine residue. The reaction proceeds via a series of intermediate states (see ref. [121] and Figure B-7). In class Ia, decay of the key intermediate "X", which consists of an oxo bridged mixed valent diiron site (Fe(IV)Fe(III)), leads to the active μ-oxo bridged diiron cofactor and the tyrosyl radical. However, in the class Ib R2 proteins with a di-manganese center, an additional protein (NrdI) is essential to form an active cofactor.[97]

In R2 protein of **class Ic** (R2c), the radical forming tyrosine residue is replaced by a redox-inert phenylalanine [99]. Furthermore, the protein contains a heterodinuclear Mn/Fe cofactor and the aspartate ligand to metal in position 1 is replaced by a glutamate [96]. It is assumed that in class Ic the radical equivalent is stored at the metal site.[96] Avoidance of the tyrosyl radical makes this R2 subunit more resistant to radical scavengers [97] such as nitrogen oxide (NO). Whereas in class Ia and Ib the active state of the cofactor is $M(III)_2$-$Y^{\bullet}$ (M = Mn or Fe; $Y^{\bullet}$ = tyrosyl radical), the protein radical in class Ic is generated through the mixed valent Mn(IV)Fe(III) metal cluster. In the recently proposed subclass **Id**, the R2 protein contains a dimanganese cofactor and it is assumed that the radical equivalent is stored in a high-valent Mn(IV)Mn(III) metal cluster [215].

Recently, a new group of R2-like proteins containing a heterodinuclear cofactor was discovered. Two **ligand-binding oxidase** (LBO) proteins from *Mycobacterium tuberculosis* (*Mt*) [5] (Figure B-5) and *Geobacillus kaustophilus* (*Gk*) [84] (see Chapter 7, Fig. 7-1) have been characterized. Crystallographic studies revealed structural similarity between the cofactor of these LBO proteins and the R2 protein of RNR class Ic (Figure B-6). However, the R2lox proteins harbor a long-chain fatty acid ligand. This unusual ligand, which co-purifies with the protein, coordinates both metal ions and is located in a hydrophobic channel leading from the metal cofactor to the protein surface.[84] The cofactor in the ligand-binding oxidases can be of diiron or heterobimetallic type, but aerobic reconstitution with manganese and iron leads preferentially to Mn binding at site 1 [5, 84]. A comprehensive analysis of differences and similarities in the protein sequence and especially in key sequence positions in standard R2 (R2a), R2c, and R2lox proteins can be found in ref. [96].

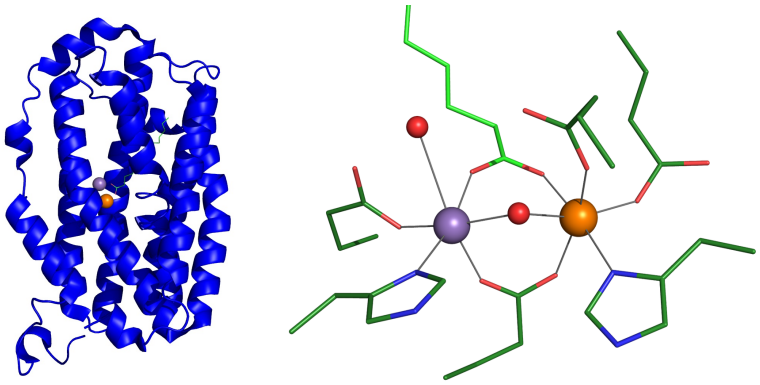

*Figure B-5: Crystal structure (**left**) and metal cofactor (**right**) in the oxidized resting state of the R2-like ligand-binding oxidase protein from Mycobacterium tuberculosis (Mt, PDB entry 3EE4, ref. [5]). For the color code see Figure B-2. Mn and Fe are shown as purple and orange spheres, respectively. Carbon atoms of the fatty acid ligand are colored in light green.*

The physiological function of R2lox proteins is still unknown but it is clear that it is not an RNR R2 component [5, 96]. Interestingly, the cofactor catalyzes formation of an ether cross-link between nearby tyrosine and valine residues in the protein scaffold. In contrast to the R2c protein performing 1-electron-reactions, the metal cofactor of R2lox proteins is capable of catalyzing a two-electron oxidation and therefore is functionally more similar to BMM [96]. While R2c contains a MnFe cluster with two oxygen bridges (μ-oxo/μ-hydroxo) in the oxidized state, in R2lox the metal ions are bridged by a single oxygen bridge (μ-hydroxo) and the fatty acid ligand provides the second bridging motif (Figure B-6). Both proteins can also assemble a [FeFe] cofactor, but R2c with diiron site shows little [141] or no catalytic activity [131]. Furthermore, Griese et al. recently found that the cross-link formation in the R2lox proteins is more efficient with a manganese/iron site [81].

Figure B-7 illustrates the different reaction cycles (oxygen activation and catalysis of one- or two-electron reactions) in the R2a protein versus R2c and R2lox. As mentioned above, the oxygen activation (reduction and cleavage) by the reduced diiron cofactor in R2a proteins occurs via two intermediates containing a μ-peroxo bridged cofactor and a high-valent Fe(IV)Fe(III) site (Intermediate "X"), respectively. Finally, the stable active state of the protein consists of a μ-oxo bridged trivalent diiron cofactor and a tyrosyl radical. In the proteins containing a heterodinuclear cofactor, the catalytic cycle includes high-valent Mn(IV)Fe(IV) species (only observed in R2c) and one- or two-electron reduction of this intermediate leads to the resting μ-oxo, μ-hydroxo bridged Mn(IV)Fe(III) cofactor in R2c or μ-hydroxo bridged Mn(III)Fe(III) cluster in R2lox, respectively.

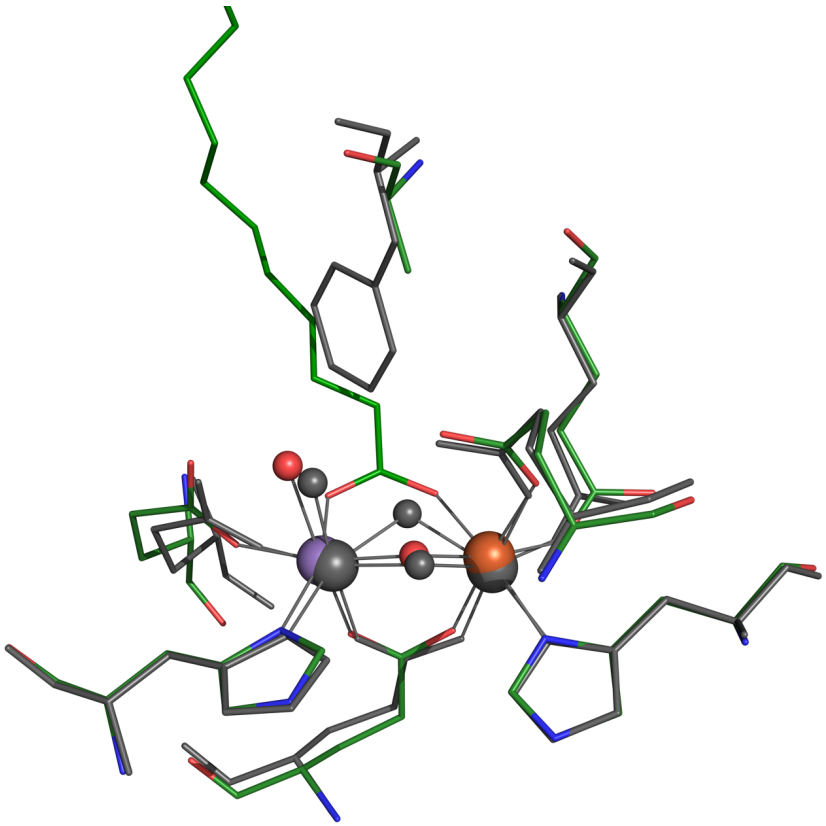

Figure B-6: Superposition of crystal structures of Chlamydia trachomatis R2c (gray, PDB entry 1SYY, ref. [99]) and Geobacillus kaustophilus R2lox in the oxidized state (colored, PDB entry 4HR0, ref. [84]). Color code GkR2lox: green, carbon atoms of metal-coordinating residues as well as of the fatty acid ligand; red, oxygen atoms and blue, nitrogen atoms of metal-coordinating residues. Fe and Mn are shown as orange and purple spheres, respectively, and water/ hydroxo/ oxo ligands as red spheres. Metal-ligand bonds are indicated by grey lines.

Recently, Miller et al. suggested based on time-resolved optical and EPR spectroscopy that reaction of the heterodinuclear Mn/Fe cofactor in R2lox includes further intermediates.[164] During reaction of the two electron reduced metal sites with molecular oxygen the first intermediate is formed containing a μ-peroxo cofactor species (like in R2a). Decay of this intermediate leads to a high-valent species, for which two possible structures were assumed, either a "diamond core" structure with Mn(IV)Fe(IV) (like in R2c [156]) or a μ^2-peroxo species with trivalent metal sites.[164]

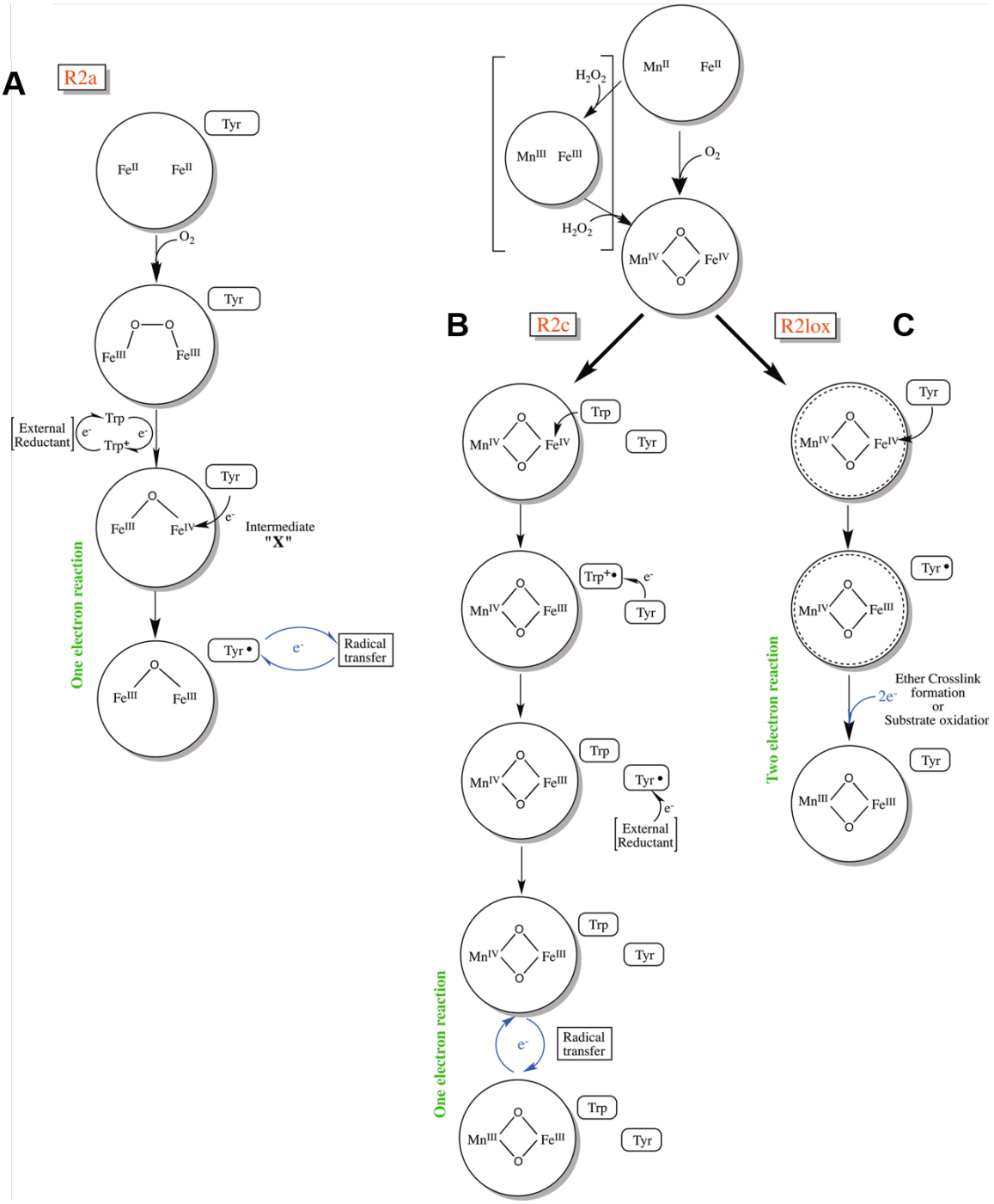

*Figure B-7: Comparison of the cofactor activation (oxygen activation and reaction mechanism) of (**A**) R2a, (**B**) R2c, and (**C**) R2lox. Reproduced from [85].*

R2c and R2lox proteins can also assemble a diiron cofactor besides of the heterodinuclear site. Which cofactor assembly is preferred and how a distinction between Fe and Mn in the different active site positions is achieved, was studied here. The cofactor assembly may depend on the availability of metal species as well as on their concentration and on the metal specificity of the two binding positions.

Both proteins prefer the formation of a Mn/Fe cofactor but via different assembly pathways [85, 131]. Generally, the assembly of the cofactor in these proteins comprises two discrete steps: labile binding of Mn(II) and Fe(II) ions to the protein scaffold followed by metal stabilization in the oxidized active cofactor due to reaction with molecular oxygen.[85] Kutin and al. have analyzed the assembly process in both proteins [131] and the proposed metal binding behavior is depicted in Figure B-8. The authors suggested that Mn(II) binds to the apo-protein at different steps during the reconstitution. While in R2c Mn(II) binds first and can also bind in both sites (in the absence of Fe(II)), the cofactor assembly in R2lox is initiated with the binding of Fe(II) to site 2. The different metal-binding preferences lead to site-specific metal loading with Mn in site 1 in the mixed-metal cofactor in R2lox. The heterodinuclear cofactor in R2c can be formed by subsequent displacement of Mn(II) by Fe(II) at one site (preferentially at position 2) of the inactive dimanganese cofactor and activation by molecular oxygen. In addition, in both proteins excess of Mn(II) promotes the formation of a heterobimetallic cofactor [131].

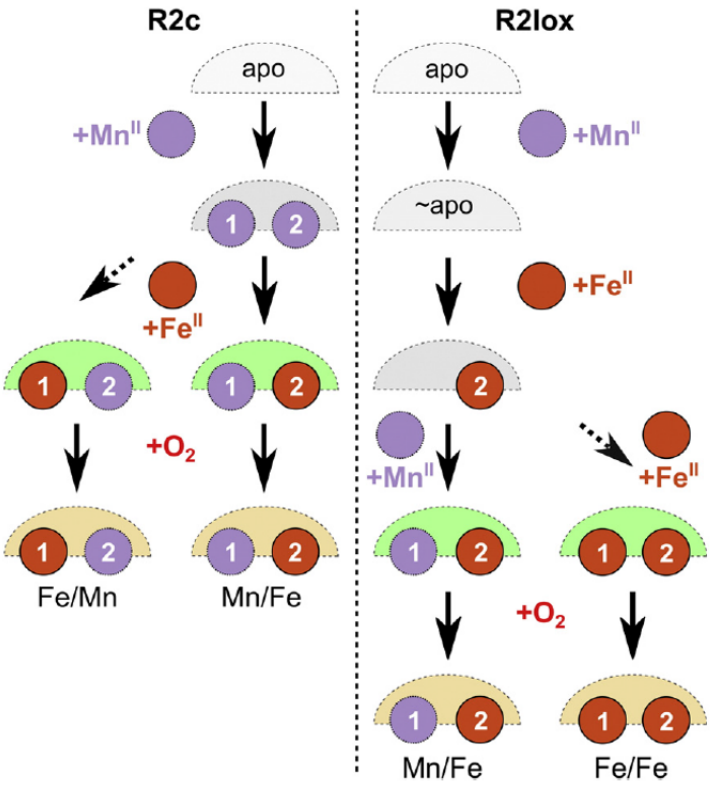

Figure B-8: Proposed model for cofactor assembly in R2c and R2lox. Reproduced with permission from [131]. Copyright (2016) Elsevier.

X-ray crystallography data of R2c and R2lox in the oxidized state reveal the intrinsic problem of rapid X-ray photoreduction (XPR), i.e. X-ray irradiation induced reduction of high-valent metal ions (see Chapter 7 and refs. [83, 141, 237]). Analysis of crystal structures of RNR R2 as well as R2lox proteins by bond-valence-sum (BVS) calculations revealed a mean metal oxidation state of less than 2.5 (average ~2) [83, 141] instead of the expected trivalent metal states. Furthermore, Sigfridsson at al. showed that the metal-metal distances in R2 crystal structures are similar to the XPR-induced (II,II) states.[237] Similar observations were made for the *Gk*R2lox protein.[83] It can be concluded that crystal data of the initially oxidized proteins mostly contain photoreduced (II,II or III,II) cofactors. Thus, the structures of high-valent states of the cofactor, which are important in the reaction cycle, are not accessible with conventional XRD. High-resolution XAS/XES can be performed to obtain structural and electronical information, which is required to understand the mechanism of oxygen activation and catalysis in the DMC enzymes.

In this work, R2lox proteins were studied by advanced X-ray techniques. We focused on the MnFe and FeFe cofactors in a ligand-binding oxidase from the bacterium *Geobacillus kaustophilus* (*Gk*lox). **Chapter 7** comprises studies on R2lox wild-type protein and **Chapter 8** reports characterization of R2lox variants (single point mutations in the R2lox scaffold).

7 Protonation state of MnFe and FeFe cofactors in a ligand binding oxidase revealed by X-ray absorption, emission, and vibrational spectroscopy and QM/MM calculations

This chapter has been published in:
R. Kositzki, S. Mebs, J. Marx, J. J. Griese, N. Schuth, M. Högbom, V. Schünemann, and M..Haumann, *Inorg Chem* **2016**, 55, 9869-85 https://doi.org/10.1021/acs.inorgchem.6b01752 [123][3]

7.1 Introduction

Enzymes with a so-called dimetal-carboxylate cofactor (DMC) form the superfamily of ferritin-like proteins [96, 150, 262] and catalyze reactions among the top challenges in chemistry. Prototypical DMC proteins are class I ribonucleotide reductases (R2 subunit), methane-monooxygenases, and ligand-binding oxidases.[26, 41, 85, 97, 122] The classical DMC comprises two iron ions (FeFe), which are ligated each by a histidine residue and by metal-bridging and terminal carboxylate groups of glutamate or aspartate amino acids as well as non-protein oxygen species. In the last years, a variety of enzymes has been described, which instead contain a hetero-dinuclear manganese-iron (MnFe) or even a MnMn cofactor.[5, 25, 99, 107] X-ray crystallography (XRD) has revealed similar global protein and cofactor site structures in R2-like enzymes irrespective of metalation.[83] In particular the MnFe enzymes have attracted much attention because of observed or suggested reactivity differences compared to their FeFe pendants.[24, 26, 41, 83, 85, 106, 108] However, the factors governing metalation of DMC proteins are still not established.

The assembly of DMC cofactors generally starts with binding of two divalent metal ions to the apo-protein, which are subsequently oxidized by molecular oxygen (O_2) to form a metal(IV)$_2$

[3] RK, SM, NS, performed research; RK, SM, MHa analyzed data; RK and SM made DFT calculations; SM and JM made QM/MM calculations; J.J.G. made protein preparation and performed XRD; RK, MH, VS, MHa designed research; RK, MHa wrote the paper

species, followed either by one- or two-electron reactions.[125] In the classical R2 proteins, oxidation of a neighboring tyrosine residue and injection of an electron from an external donor leads to a Fe(III)Fe(III) site and a stable tyrosine radical.[16] Unusual two-electron chemistry has been proposed to occur in a recently described R2-like ligand-binding oxidase from *Geobacillus kaustophilus* (R2lox).[84] In this enzyme, O_2-induced DMC assembly is followed by formation of an ether cross-link between tyrosine and valine residues close to the active site.[83, 84] XRD and spectroscopy have shown that FeFe, MnFe, and MnMn cofactors can be assembled in R2lox *in-vitro* (Fig. 7-1).[83, 131] Only the FeFe and MnFe sites, however, are active in O_2 reduction and cross-link formation, as possibly related to cofactor protonation and/or redox potential differences,[204, 213] resulting in stable Mn(III)Fe(III) or Fe(III)Fe(III) species.[83, 84]

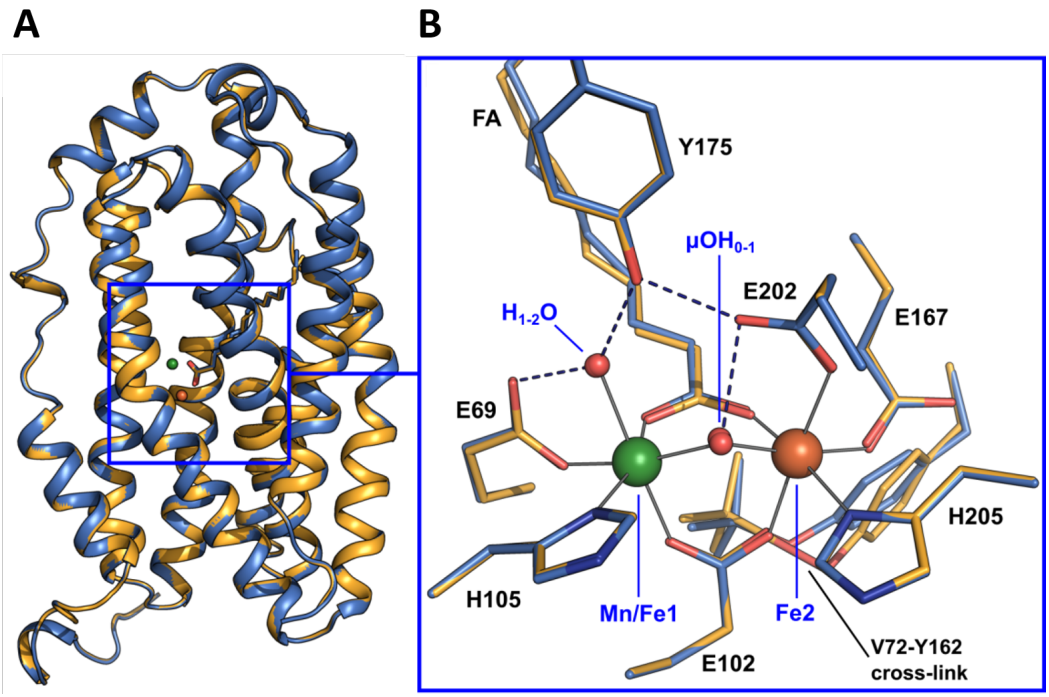

*Figure 7-1: Crystal structures of R2lox protein in the oxidized resting state. (**A**) Superposition of structures containing a MnFe (yellow, PDB entry 4XB9) or FeFe (light-blue, PDB entry 4DCS) cofactor. (**B**) Close-up of the superimposed dimetal cofactor sites (yellow, Mn1Fe2; light-blue, Fe1Fe2) with amino acid, fatty acid (FA), and oxygen (red) ligands marked. Tyr175 is a member of a potential hydrogen-bonding network (dashed lines). A cross-link between Tyr162 and Val72 has been by observed by XRD and mass spectrometry in FeFe- and MnFe-bound protein (refs. [83, 84]).*

The R2lox cofactors differ from the DMC sites in R2 proteins (Fig. 7-1). The two metal ions are bridged by a bidentate carboxylate group of an extended molecule, which was modelled as palmitic acid in the crystal structures (Fig. 7-1). A mixture of long-chain fatty acids (FA) co-purifies with the protein produced in *E. coli* and they presumably occupy the binding site of the

(so far unknown) substrate of the enzyme.[83, 84] Metal binding to R2lox is highly site-specific, as during aerobic apo-protein reconstitution in the presence of both metals, Fe binds preferentially (though not exclusively) to site 2 and Mn to site 1.[84, 131] Both metal ions are bound in (approximately) octahedral geometry, but display different ligation patterns. One coordination site at each metal ion is occupied by the bidentate FA carboxylate and one each by a histidine, whereas glutamate carboxylates occupy three coordination sites on Fe2, but only two on Mn/Fe1. The fifth ligand at Mn/Fe1 is a terminal oxygen species. A further metal-bridging oxygen species provides the sixth ligand to both metal ions in oxidized R2lox.[83, 84] Both oxygen ligands may be derived from O_2 after four-electron reduction by the metal ions and cleavage during cofactor assembly, followed by two-electron metal reduction upon cross-link formation.[84] The oxygen species could correspond to terminal water (H_2O) or hydroxyl (OH^-) and bridging hydroxyl (μOH^-) or oxo (μO^{2-}) groups. EPR studies have favoured a $H_2O/\mu OH$ state of the paramagnetic Mn(III)Fe(III) cofactor in R2lox, but the Fe(III)Fe(III) cofactor is EPR-invisible.[232] Determination of cofactor protonation states in both cofactors is required for understanding the O_2 and cross-link formation chemistry.[212, 213]

We used advanced X-ray spectroscopy techniques, X-ray absorption (XAS) and emission (XES) spectroscopy and nuclear resonance vibrational spectroscopy (NRVS, also called nuclear inelastic scattering, NIS),[90] to site-selectively probe the molecular and electronic configurations, ligand protonation states, and vibrational properties of the Mn(III) and Fe(III) ions in the MnFe and FeFe cofactors in R2lox. XANES spectra at the Mn and Fe K-edges were used to determine metal oxidation states.[206] Metal-ligand bond lengths and metal-metal distances were derived from EXAFS analysis [49] and compared to XRD structures. Rapid X-ray photoreduction (XPR) kinetics of the metal ions, which lead to divalent metal species in XRD structures of DMC proteins,[83, 141, 237] were related to relative redox potentials. Kβ main-line emission spectra due to radiative 3p→1s electronic decay, which are split by 3p/3d spin polarization interactions into $K\beta_{1,3}$ and Kβ' line features,[54, 76, 159, 196] were used for metal spin state determination. The pre-edge absorption feature in the XANES reflects resonant electronic excitation of 1s electrons into unoccupied valence molecular orbitals (MOs) with, e.g., metal-d character (core-to-valence transitions, ctv).[58, 133, 139, 279] The Kβ satellite line emission ($K\beta_{2,5}$ and Kβ'' features) probes the reverse process, radiative electronic decay to the core hole from occupied valence MOs with, e.g., ligand character (valence-to-core transitions, vtc).[137, 159, 194, 286] Collection of ctv and vtc spectra by rapid-scan/time-resolved approaches [91, 92, 289] provided benchmark data for quantum chemical calculations.

NRVS is a relatively recent X-ray technique.[37, 167, 220, 255, 272] It relies on excitation of the ^{57}Fe Mössbauer nuclear resonance (~14.4 keV) and monitoring of the delayed iron X-ray fluorescence (~6.5 keV) following core electron excitation during the decay of the nuclear excited state ($\tau \approx 141$ ns). NRVS probes vibrational side bands, which are excited while scanning the incident energy with a high-resolution monochromator (FWHM of 0.75 meV = 6 cm^{-1}) over the Stokes spectral region above the resonance energy. NRVS, at variance with, e.g., Raman spectroscopy, exclusively probes normal modes with displacement contributions from the ^{57}Fe ion in the MnFe and FeFe cofactors reconstituted with the isotope so that the protein is practically invisible. Nuclear forward scattering (NFS) monitors interference patterns in the time domain due to coherent scattering in forward direction relative to the incident beam from the I = 3/2 and I = 1/2 nuclear excitation levels of the ^{57}Fe Mössbauer nucleus. Therefore, this technique is sensitive to Mössbauer parameters like the quadrupole splitting energy (ΔE_Q),[113, 266] which was determined for the MnFe and FeFe cofactors.

Using density functional theory (DFT) and a combined quantum mechanics/ molecular mechanics (QM/MM) approach on cofactor and whole-protein model structures, theoretical ctv and vtc XAS/XES spectra, as well as NRVS spectra were calculated and quantitatively compared to the experimental data. This provided access to the differences in electronic structure, highlighted inter- and intra-molecular protein/cofactor interactions, and revealed vibrational marker bands of the FeFe and MnFe sites, facilitating assignment of the cofactor protonation state in R2lox. Refined cofactor structures are presented and possible relations of their differences to metalation specificity and redox chemistry are discussed.

7.2 Materials and Methods

7.2.1 Protein samples

The protein samples were prepared by Dr. Julia Griese at Stockholm University, Sweden (presently at Uppsala University). An N-terminally His-tagged full-length construct of the R2-like ligand-binding oxidase protein I (R2lox) from the thermophilic bacterium *Geobacillus kaustophilus* (accession number WP_011232245) was produced and purified in metal-free form as previously described.[84] MnFe or FeFe cofactors in their oxidized resting states were reconstituted by incubation of apo-protein with $MnCl_2$ and/or $(NH_4)_2Fe(SO_4)_2$ salts at molar ratios of protein monomer:Mn:Fe = 1:2:1 or 1:3 under aerobic conditions, and excess metal ions were removed by a desalting column step as described previously in detail.[83] Cofactor-

reconstituted protein was concentrated to 3-5 mM, loaded into acrylic-glass holders for X-ray spectroscopy, and frozen in liquid nitrogen. R2lox samples for NIS were prepared using $^{57}FeCl_2$ as the iron source during cofactor reconstitution.[131, 232] Protein concentrations were determined using extinction coefficients at 280 nm for the metal-free/bound states of R2lox of 47757/50563 $M^{-1}cm^{-1}$.[232]

7.2.2 Metal content

Elemental contents of R2lox were assayed by total reflection X-ray fluorescence analysis (TXRF) [116] using a PicoFox instrument (Bruker) on protein samples after addition of a gallium elemental standard (Sigma-Aldrich, 25 mg l^{-1}), and specific Mn/Fe contents were calculated using the routines of the spectrometer and the protein concentrations.

7.2.3 X-ray spectroscopy

X-ray spectroscopy experiments were performed at the bending-magnet SuperXAS beamline of the Swiss Light Source (SLS, Villigen, Switzerland) and at undulator beamlines ID26 and ID18 at the European Synchrotron Radiation facility (ESRF, Grenoble, France). XANES spectra at medium resolution (FWHM ~2 eV) and EXAFS spectra (scan duration ~15 min) were collected at the Mn and Fe K-edges at SLS using a Si[111] double-crystal monochromator and an energy-resolving 13-element Ge detector for monitoring of the total X-ray fluorescence in a standard XAS setup (spot size on sample ~1.0x0.25 mm^2 set by slits, ~10^{10} photons s^{-1} mm^{-2}). Up to 30 XAS scans on separate sample spots were averaged for the shown spectra. High-resolution (FWHM ~0.2 eV) Mn and Fe XANES spectra were collected at ID26 within ~1 s using the rapid-scan mode of the beamline, a Si[311] double-crystal monochromator, and a large-area scintillation fluorescence detector at ~1 m to the sample and shielded by 10 µm Cr (Mn K-edge) or Mn (Fe K-edge) foils against scattered incident X-rays for total Kα-fluorescence detection. Up to 200 XAS rapid-scans on separate sample spots were averaged for the shown spectra.[93] Kβ emission spectra were collected at ID26 using a vertical-plane Rowland-circle spectrometer. Energy bandwidths of ~0.9 eV or ~1.1 eV at the Mn or Fe $K\beta_{1,3}$ emission were achieved using the [111] or [620] Bragg reflections of five spherically-bent Ge wafers (R = 1000 mm). Monochromator energies of 7000 eV or 7800 eV were used for non-resonant excitation of the Mn or Fe Kβ emission (spot size on sample ~0.4x0.2 mm^2 set by slits, ~10^{12} photons s^{-1} mm^{-2}). The monochromator energy axis was calibrated using the energy of the pre-edge peak at 6543.3 eV of a $KMnO_4$ powder sample or the first inflection point at 7112.0 eV in the XANES of an iron foil as references and the emission energy was calibrated using the

elastic scattering peak of the incident X-rays and the $K\beta_{1,3}$ spectra of MnO or FeO powder samples (precision ±0.1 eV).[159] An avalanche photodiode (APD) was used for Kβ fluorescence detection shielded by a 1.5 mm slit against scattered X-rays. XES spectra were collected using a time-resolved energy-sampling approach to outrun rapid X-ray photoreduction of the Mn/Fe(III) ions.[92, 93, 289] A fluorescence time-scan trace (1 s) first was measured at each energy in the Kβ main- and satellite emission regions on fresh sample spots and the signal intensity, $I_F(E)/I_0(E)$, was calibrated to compensate for sample thickness and incident flux (<15%) variations by division by the summed reference fluorescence intensity, $I_{Fref}(E_{max})/I_0(E_{max})$, at the maximum of the $K\beta_{1,3}$ emission (6492 eV, Mn or 7059 eV, Fe) accumulated for 10 s in a second data collection round on the same sample spots.[289] Up to 15 data sets were averaged for the shown Kβ emission spectra. At both beamlines, samples were held in a liquid-helium cryostat (Cryovac, Germany) at 20 K. X-ray photoreduction kinetics at 20 K were determined using fluorescence time-scans at low K-edge energies.[83, 237] NRVS and NFS was performed at ID18 on ^{57}Fe-reconstituted R2lox using the previously described setup [30, 68, 113] including a heat-load monochromator, a high-resolution monochromator (FWHM ~0.75 meV), gated APD detectors for delayed inelastic and forward scattering detection with sub-nanosecond time resolution, and a cold-finger liquid-helium cryostat providing a sample temperature of about 50±7 K as determined from the amplitude ratios of the anti-Stokes and Stokes side lobes of the ^{57}Fe resonance.[37] The storage ring was operated in top-up 16-bunch mode (~90 mA) or hybrid mode (~200 mA). NRVS spectra were collected in a -10 meV to 100 meV energy region around the resonance (0.2 meV energy steps, 3 s per data point, spot size on sample ~1.5x0.5 mm^2, ~10^9 photons s^{-1} mm^{-2}) and up to 40 scans were averaged for the shown spectra (5 scans of ~30 min per sample spot). NFS traces were collected in a ~160 ns time window within ~30 min with the APD detectors at ~2 m to the sample. XAS/XES data were processed and evaluated using previously described procedures and in-house software for XANES normalization and extraction of EXAFS spectra.[49] EXAFS fit analysis was carried out with the in-house program SimX using full multiple-scattering phase functions calculated with FEFF9.[208] NRVS data were processed and the partial vibrational density of states (pDOS) of ^{57}Fe was calculated with the software package available at ID18.

7.2.4 DFT and QM/MM calculations

Quantum chemical and molecular mechanics calculations were carried out on truncated cofactor or whole-protein models (Figs. 7-2 and 7-3) initially derived from XRD structures of

R2lox containing the MnFe (PDB entry 5DCS, 2.0 Å resolution) or FeFe (PDB entry 4XB9, 1.8 Å resolution) cofactor.[83, 84] In truncated cofactor models, amino acids were saturated with protons and structures were geometry-optimized by DFT, fixing the outer C-atoms of the FA and amino acid ligands and the coordinates of non-H atoms of all non-metal bound amino acids to their XRD coordinates, in a COSMO solvation environment ($\varepsilon = 4$) including anti-ferromagnetic coupling (afc) of the metal ions by proper definition of molecular fragments using Gaussian09 [73] (broken-symmetry approach) and the BP86/TZVP or B3LYP/TZVP functional/basis set combinations. Geometry-optimized structures were used for calculation of ctv and vtc spectra with the ORCA program.[174] To facilitate direct comparison with experimental data, the energy axis of calculated ctv and vtc spectra were slightly stretched (factor of 1.15), accounting for an apparent slight underestimation of transition energy differences by the DFT approach.[140, 152] In addition, the amplitudes of calculated spectra were scaled using similar (empirical, but consistent) factors for Mn or Fe in the MnFe cofactor and two-times smaller factors for Fe in the FeFe cofactor for comparison to the normalized experimental absorption and emission spectra. Mulliken spin densities and CM5 charges from Hirshfeld population analysis [57] were calculated with Gaussian09. Molecular orbitals were visualized with Gview.[73] Wavefunction files of optimized structures were used for topological analysis of the electron density according to the atoms-in-molecules space-partitioning scheme using AIM2000.[22] Non-covalent interactions indicator (NCI) [40] analysis was conducted using NCIplot (grid step size = 0.1 bohr) and visualized with MolIso.[101] QM/MM calculations on whole-protein structures were carried out using the ONIOM [271] approach implemented in Gaussian09 and using afc or fc coupling of the Mn/Fe ions. The QM part (high-layer, B3LYP functional and TZVP or cep31g basis set) of the whole-protein models comprised all cofactor atoms up to Cβ of the histidine and glutamate residues and the forth C-atom of the FA ligand and for the MM part (low-layer) the universal force field was used. Normal mode analysis for calculation of vibrational frequencies was carried out with Gaussian09 and NISspec [185] was used for selection of modes with iron contributions and pDOS calculation. Stick spectra were broadened by Lorentzians (FWHM = 8 cm^{-1}) for comparison with experimental spectra. In-house software was used to extract transition energies and intensities and metal/ligand contributions to XAS/XES/NRVS spectra and atomic contributions to transitions and MOs from ORCA and Gaussian09 output files and this information was processed and visualized using in-house functionalized EXCEL spreadsheets to generate energy-aligned, scaled, and broadened calculated spectra. Representative input files

for DFT and QM/MM calculations and coordinates of model structures (Table A7-1) are given in the Appendix.

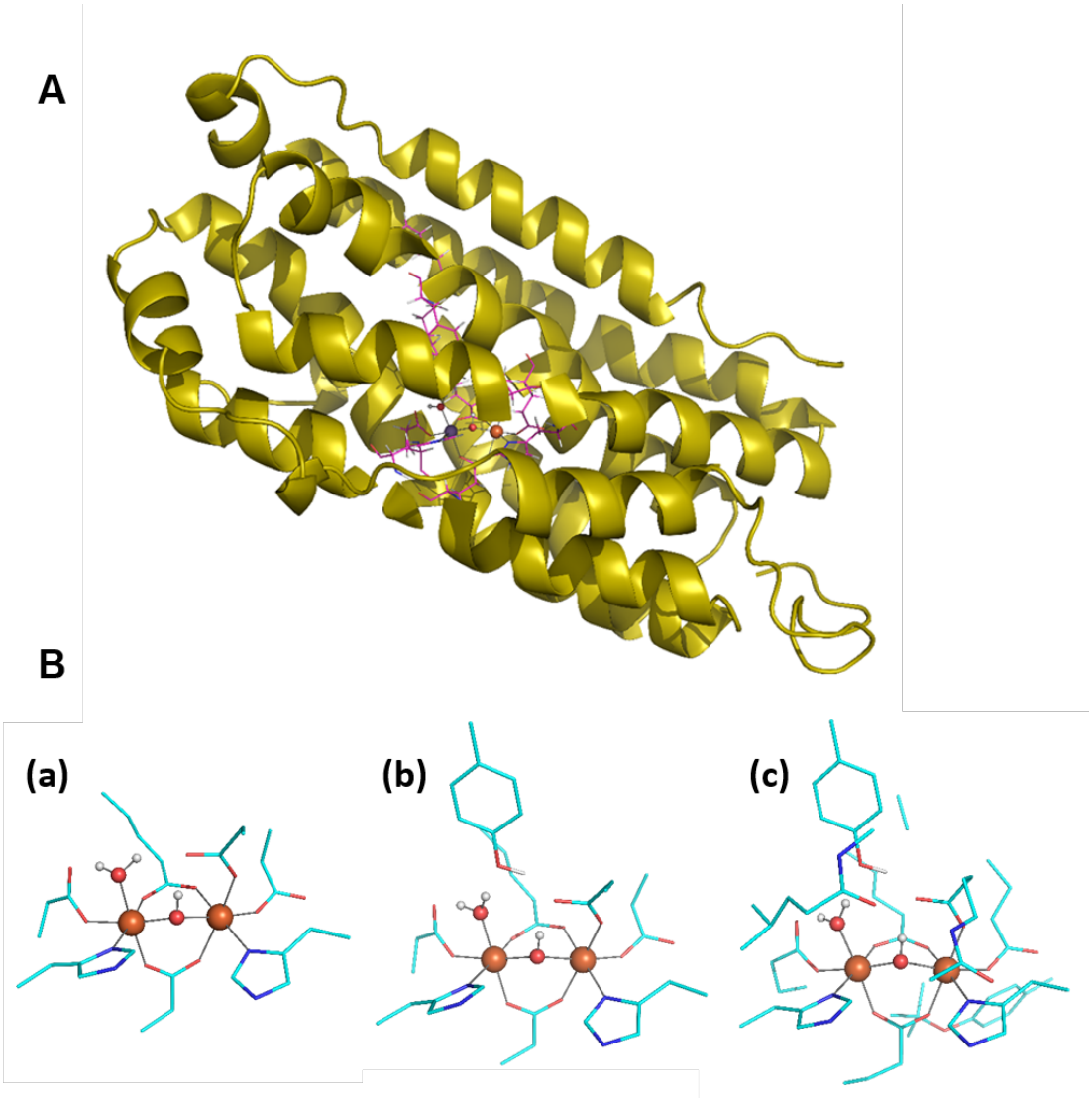

*Figure 7-2: R2lox model structures for QM/MM and DFT. (**A**) Whole-protein structure for QM/MM calculations using the ONIOM approach. The QM (DFT) "high-layer" core (ball-and-stick representation) comprised the cofactor and amino acids similar to structure (b) in (B) and the MM "low-layer" the protein crystal structure (ribbon representation) according to PDB entries 4XB9 (FeFe) or 5DCS (MnFe). (**B**) Cofactor structures for DFT calculations with increasing size (**a**, 93 atoms; **b**, 109 atoms; **c**, 188 atoms). The shown structures correspond to the FeFe cofactor in the H2O/μOH protonation state with Y175 being a hydrogen-bond donor to E202, similar models were used for the MnFe cofactor; alternative models comprised deprotonated water species at Mn/Fe1 and in the bridging position and alternative orientations of the phenolic group of Y175 (shown on top in (b) and (c), see Fig. 7-3).*

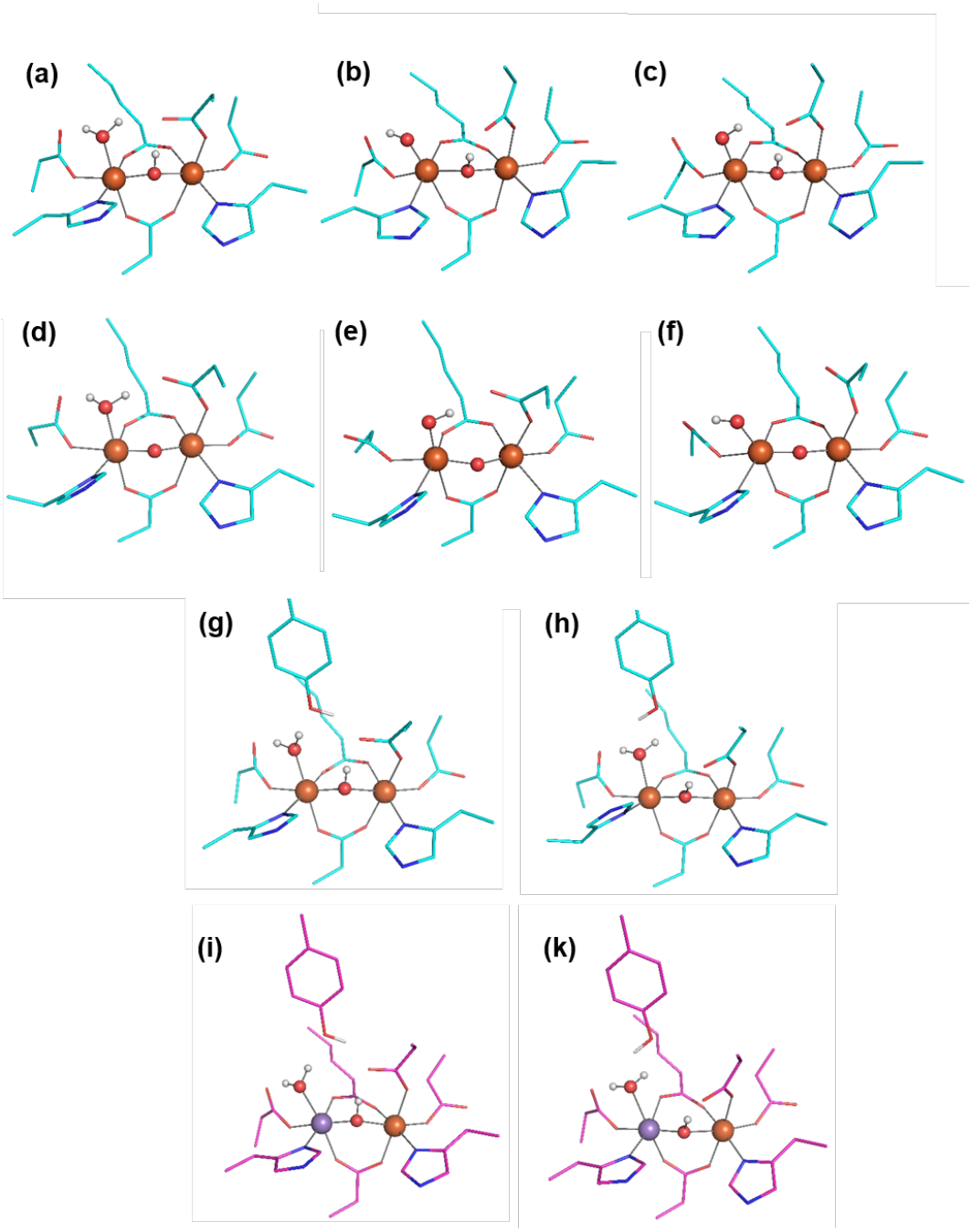

*Figure 7-3: Cofactor structures with protonation and hydrogen-bonding variations. Similar cofactor structures were used for DFT and QM/MM calculations. (**a-f**) Structures with different protonation states and proton orientations of the water species at Mn/Fe1 and of the bridging oxygen species; shown structures represent the FeFe cofactor, similar structures were used for the MnFe cofactor. (**g-k**) Structures with alternative orientations of the phenolic group of Y175; (g, h) FeFe cofactor, (i, k) MnFe cofactor.*

7.3 Results

7.3.1 Metal content quantification

Metal contents in R2lox protein samples were determined by TXRF analysis (Fig. 7-4). R2lox reconstituted only with iron contained on average 2.2 ± 0.2 Fe ions per protein, suggesting quantitative loading with the FeFe cofactor. For reconstitution with manganese and iron the observed 1.8 ± 0.2 metal ions per protein suggested slightly substoichimetric metal contents. The Fe per Mn ratio of 2.1 ± 0.2, under the assumption that all manganese was bound in MnFe sites, implied 60-70% MnFe sites and 40-30% FeFe sites. These attributions agreed with previous findings that MnMn sites or cofactors with Mn in site 2 and Fe in site 1 were not formed under our R2lox reconstitution conditions.[83, 84, 131] The iron X-ray spectra of the MnFe cofactor (below) accordingly were corrected for a 35% contribution of FeFe sites to yield pure spectra of the iron ion in site 2.

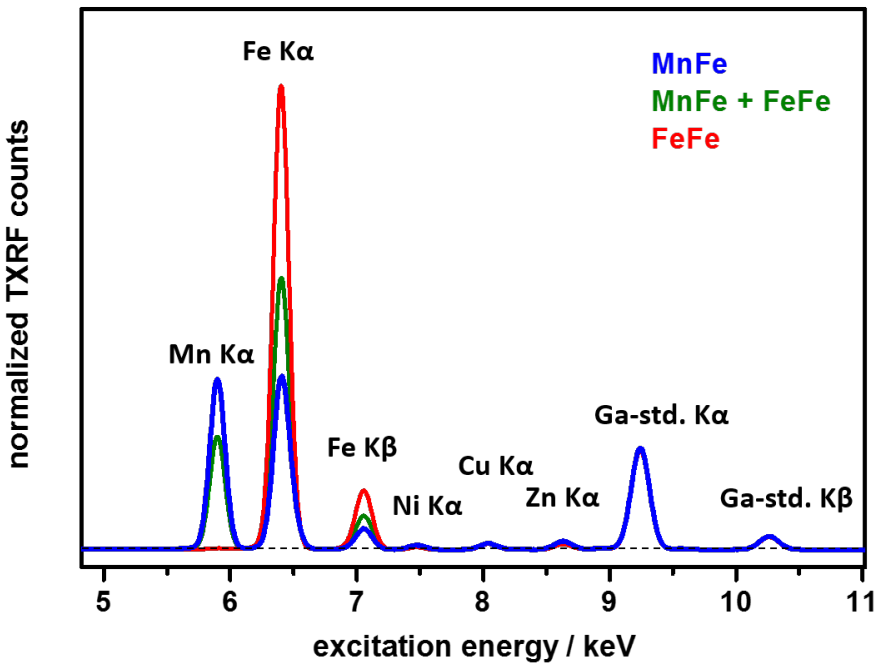

Figure 7-4: TXRF spectra of R2lox samples reconstituted with Fe only or Mn plus Fe. X-ray emission lines of elements are marked accordingly (Kα = 2p→1s or Kβ = 3p→1s decay); Ga-std. = gallium elemental standard added to the protein samples. The MnFe spectrum was derived by subtraction of 35% of the FeFe from the MnFe + FeFe spectrum. Spectra were normalized at the Ga Kα emission for comparison.

7.3.2 X-ray photoreduction

The rate of X-ray photoreduction (XPR) of metal ions in R2lox was determined by monitoring the total Kα X-ray fluorescence level increase due to shifts of the K-edge to lower energies upon Mn(II) and Fe(II) formation using excitation energies at the onset of absorption (Mn, 6549 eV; Fe, 7124 eV) (Fig. 7-5).[83, 237] Biphasic reduction of iron in the FeFe cofactor to the Fe(II) level occurred within halftimes ($t_{½}$) of ~52 s (50%) and ~347 s (50%), suggesting that initial reduction of the Fe(III)Fe(III) cofactor to the Fe(III)Fe(II) level was about 7-fold faster than subsequent reduction to the Fe(II)Fe(II) level. The MnFe cofactor showed monophasic Mn(II) formation with $t_{½}$ of ~17 s, whereas iron reduction was described by a dominant phase with $t_{½}$ of ~37 s (64%) and two phases with similar amplitudes (18 ± 3%) and the same $t_{½}$ values as for the FeFe cofactor, corroborating ~65% MnFe and ~35% FeFe cofactors in R2lox reconstituted with both metals. About 2-fold faster manganese than iron reduction in the MnFe cofactor mostly reflected the increased X-ray absorption of the protein sample at the lower Mn K-edge energy.[83] Mn(III) and Fe(III) reduction in the MnFe cofactor thus was similarly fast within uncertainty limits and ~3-fold faster than for the first Fe(III) ion in the FeFe cofactor. In

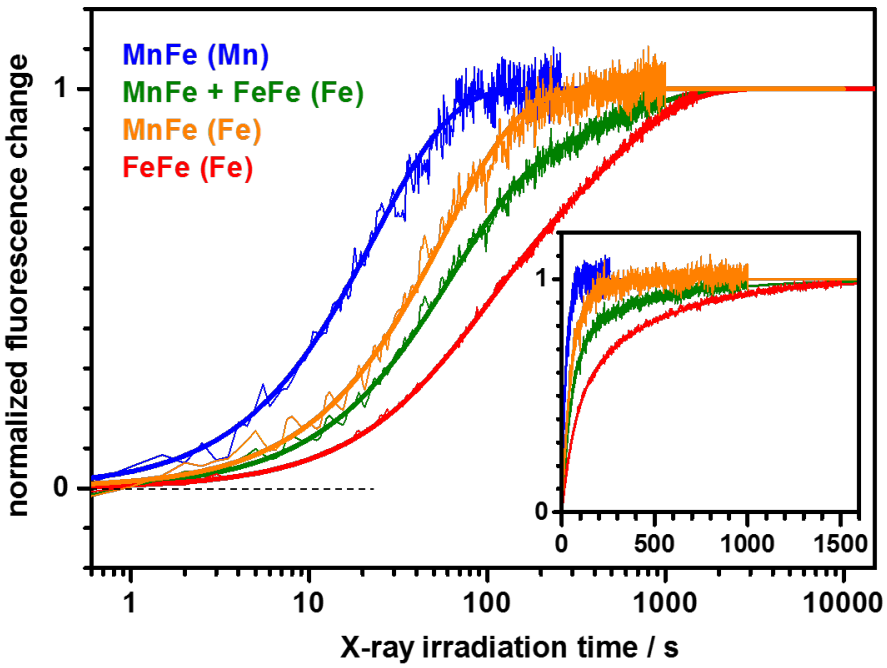

Figure 7-5: X-ray photoreduction of MnFe and FeFe cofactors. Timescan traces for increasing X-ray irradiation periods were measured at Mn or Fe K-edges (in parentheses) at 20 K. The inset shows the data on a linear time scale. The Fe trace for the MnFe cofactor (orange) was obtained by subtraction of 35% of the FeFe (red) from the MnFe + FeFe (green) trace. Smooth lines represent exponential fit curves with parameters given in the text.

the XAS/XES studies, XANES and Kβ emission spectra were collected in ~1 s using rapid monochromator/undulator scans or a time-resolved energy-sampling approach,[91, 92, 289] ensuring reduction of <5% of Mn/Fe(III) during data acquisition.

7.3.3 Metal oxidation state

K-edge X-ray absorption (XANES) spectra of the MnFe and FeFe cofactors are shown in Fig. 7-6. The Mn K-edge energy (~6549.0 eV) and the similar Fe K-edge energies (~7124.7 eV), in comparison to $Mn(III)_2O_3$ and $Fe(III)_2O_3$ and previous experiments on MnFe and FeFe cofactors in ribonucleotide reductases and Mn/Fe ions in other systems, indicated the dominating presence (>90%) of Mn(III) in the MnFe cofactor and of Fe(III) in both cofactor types.[49, 83, 141, 237, 289] We note that the (half-height) K-edge energies within series of (high-spin, near-octahedral) Mn or Fe sites with O/N ligands (and for series of compounds of other metals and/or different ligands) have been shown to be directly proportional to the metal

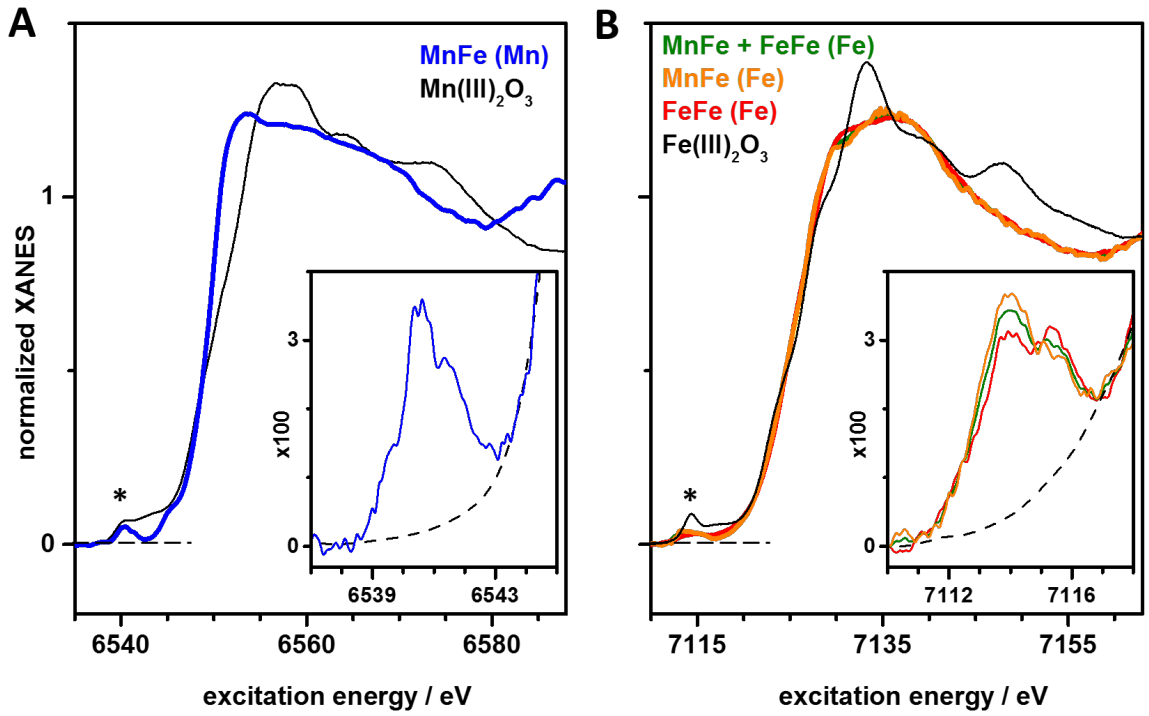

*Figure 7-6: XANES spectra of MnFe and FeFe cofactors. (**A**) Mn XANES of the MnFe cofactor and pre-edge feature (asterisk) in the inset compared to the spectrum of $Mn(III)_2O_3$. (**B**) Fe XANES spectra and pre-edge features (asterisk) in the inset compared to the spectrum of $Fe(III)_2O_3$; the Fe spectrum of the MnFe cofactor was obtained by subtraction of 35% of the FeFe spectrum from the MnFe + FeFe spectrum. High-resolution XANES spectra were collected in ~1 s using a rapid-scan approach; pre-edge spectra were measured separately at 0.1 eV per data point. Dashed lines in the insets show the main edge rise background, which was subtracted for extraction of ctv absorption spectra (Fig. 7-9).*

oxidation state (see, for example, refs.[49, 154, 165, 205, 218, 269]). A slightly larger primary edge maximum may suggest more regular octahedral symmetry around Fe2 in the FeFe compared to the MnFe cofactor.[50, 144] The pre-edge absorption features of the Mn and Fe K-edges showed two main maxima and a low-energy shoulder in the manganese spectrum (Fig. 7-6, inset). For the Mn1 and Fe2 pre-edges of the MnFe cofactor, the primary maxima were about 1.5-fold larger than the secondary ones. For the iron pre-edge of the FeFe cofactor, the two similar maxima differed from the ones of Fe2 in the MnFe cofactor. This suggested electronic structure differences of iron in the cofactors. Electronic transitions underlying the pre-edge features were analyzed using DFT further below.

7.3.4 Molecular structure differences

Interatomic distances in the cofactors were determined from EXAFS analysis (Fig. 7-7) and compared to XRD data and geometry-optimized structures from DFT (Tables 7-1, -2). Typical mean metal-ligand bond lengths (~2.1 Å) for Mn(III) and Fe(III) ions were obtained from EXAFS. Up to ~0.1 Å longer bond lengths are observed in crystal structures, which may be caused by metal reduction during diffraction data collection, but this difference is also within the range of the coordinate error of the crystal structures (0.2-0.3 Å).[83, 141, 237] The DFT approach (B3LYP/TZVP) yielded bond lengths and metal-metal distances, which deviated from the EXAFS data mostly by less than 0.05 Å. For the FeFe cofactor, the shortest distances (~2.0 Å) likely were dominated by Fe1-μO and Fe2-O(Glu167) interactions, whereas the longest bonds (~2.4 Å) reflected contributions from Fe1/2-N(His) and iron-water species interactions. For Fe2 in the MnFe cofactor, the shortest distances (~1.95 Å) were dominated by the Fe2-O(Glu167) bond opposed to the Fe2-μO bond, and the longest distance (~2.3 Å) corresponded to the Fe2-N(His205) bond. For Mn1 in the MnFe cofactor, the shortest distance (~1.9 Å) reflected mostly the Mn1-μO bond and the longest distance (2.25 Å) the manganese-water species interaction. The Jahn-Teller axis of Mn1(III) likely was oriented along the water species – Glu102 bonds. Consistent Mn/Fe-Fe distances (~3.5 Å) were obtained from EXAFS and XRD. DFT revealed a similar distance only for a protonated bridging oxygen (μOH) in the MnFe and FeFe cofactors, whereas a μO bridge yielded ~0.25 Å shorter metal-metal distances (Table 7-3). An axial OH^- at Mn/Fe1 diminished the metal-metal distance by <0.05 Å. For an OH^- at Mn/Fe1 and a μO(H) bridge, however, the calculated Mn/Fe1-OH bond lengths were significantly shorter than the EXAFS and XRD values, irrespective of the specific hydrogen bond orientations (Fig. 7-3, Table 7-3). These results suggested similar Fe2 geometries in both cofactors, but a Jahn-Teller distorted Mn1(III) ion with a weaker axial water ligand.

Table 7-1: Interatomic distances from EXAFS, XRD, and DFT in FeFe and MnFe cofactors.

cofactor	distance	EXAFS	XRD	DFT
FeFe	Fe-N/O_L	1.94(2)[d]	2.02(4)[e]	1.99(2)[e]
	Fe-N/O_L	2.08(2)	2.15(3)	2.07(1)
	Fe-N/O_L	2.45(9)[a,g]	2.43(9)[b]	2.25(2)[c]
	Fe-C_L	2.94(3)	3.08(1)	3.12(1)
	Fe-Fe	3.49(3)	3.51(1)	3.57(3)
MnFe	Fe-N/O_L	1.94(2)[d]	2.00(2)[f]	1.92(2)[f]
	Fe-N/O_L	2.08(3)	2.14(3)	2.06(3)
	Fe-N/O_L	2.29(4)[a]	2.34(2)[b]	2.25(2)[b]
	Fe-C_L	3.05(4)	3.14(1)	3.12(1)
	Mn-N/O_L	1.88(2)[d]	2.13(2)[f]	1.89(1)[e]
	Mn-N/O_L	2.09(3)	2.16(3)	2.04(1)
	Mn-N/O_L	2.24(3)[a]	2.33(2)[b]	2.25(3)[b]
	Mn-C_L	2.94(4)	3.05(1)	3.05(2)
	Mn-Fe	3.50(2)	3.51(2)	3.56(3)

Distances are given in Å. XRD values were taken from structures 4XB9/5DCO (FeFe, 1.8/2.3 Å resolution) and 5DCS/5DCR (MnFe, 2.0/2.1 Å resolution) (full range of bond lengths in parenthesis, unrealistically short Mn/Fe-FA bond lengths were neglected in the analysis). EXAFS values for the MnFe cofactor refer to analysis of data corrected for the minor FeFe contribution. DFT values give the full distance range for model size and theory level variations (Figs. 7-2 and -3) for the H2O/μOH protonation state; Tyr175 being H-bonded to H2O and Glu69 in the DFT models resulted in <0.1 Å shortened Mn/Fe1-OH2 bond lengths. L = amino acid or water ligand, [a]longest bond, [b]longest bond = Mn/Fe1-OH2, [c]longest bond = Fe2-N(His), [d]shortest bond, [e]shortest bond = Mn/Fe1-μO, [f]shortest bond = Mn/Fe1-O(Glu), [g]this heterogeneous bond length from EXAFS may be overestimated due to very minor contributions from (initially or XPR) reduced species with altered cofactor geometry (refs. [83, 84]).

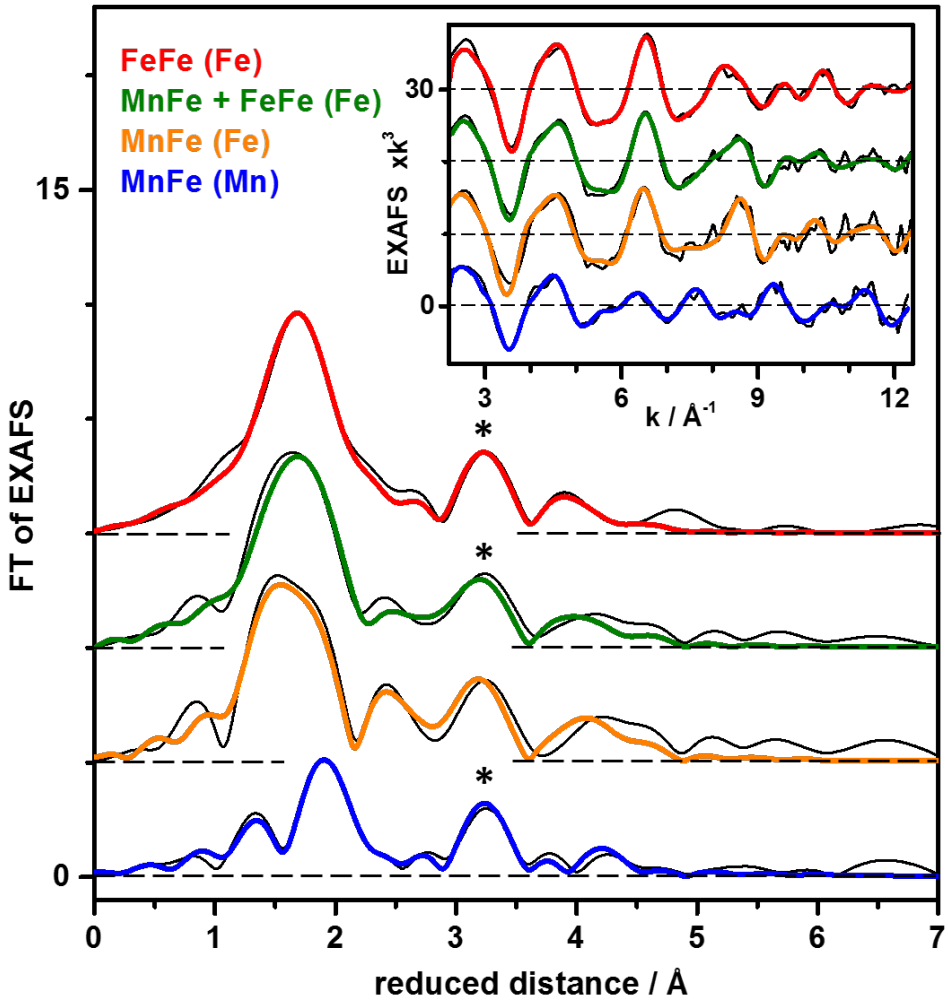

Figure 7-7: EXAFS analysis of MnFe and FeFe cofactors. Fourier-transforms (FTs) were calculated from a k-range of 3.4-12.2 $Å^{-1}$ of EXAFS oscillations in the inset to emphasize the Mn/Fe-Fe distances (asterisks). The Fe EXAFS of the MnFe cofactor was obtained by subtracting 35% of the FeFe spectrum from the MnFe + FeFe spectrum. FT and k-space spectra were vertically shifted for comparison (dashes show zero levels); black lines, experimental data; colored lines, fit curves with parameters in Tables 7-1 and -2.

Table 7-2: EXAFS simulation parameters.[a]

cofactor	N [per metal ion] / R [Å] / $2\sigma^2$ x10^3 [Å^2]			R_F [%]
Fe	Fe-N/O	Fe-C	Fe-Fe/Mn	
FeFe	2.2* / 1.94 / 5$^\#$ 2.8* / 2.09 / 5$^\#$ 1.0$^\&$ / 2.45 / 5$^\#$	2.0$^\&$ / 2.93 / 5$^\#$ 5.0$^\&$ / 4.43 / 5$^\#$	1.0$^\&$ / 3.49 / 8	11.1
MnFe + FeFe	2.4* / 1.96 / 12$^\#$ 2.6* / 2.10 / 12$^\#$ 1.0$^\&$ / 2.41 / 12$^\#$	2.0$^\&$ / 3.02 / 7$^\#$ 5.0$^\&$ / 4.48 / 7$^\#$	1.0$^\&$ / 3.49 / 11	15.5
MnFe	2.2* / 1.94 / 3$^\#$ 2.8* / 2.09 / 3$^\#$ 1.0$^\&$ / 2.31 / 3$^\#$	2.0$^\&$ / 3.05 / 4$^\#$ 5.0$^\&$ / 4.50 / 4$^\#$	1.0$^\&$ / 3.50 / 7	18.3
Mn	Mn-N/O	Mn-C	Mn-Fe	
MnFe	1.7* / 1.90 / 6$^\#$ 3.3* / 2.12 / 6$^\#$ 1.0$^\&$ / 2.26 / 6$^\#$	2.0$^\&$ / 2.94 / 8$^\#$ 5.0$^\&$ / 4.62 / 8$^\#$	1.0$^\&$ / 3.51 / 5	14.1

[a]Data correspond to EXAFS spectra at Mn or Fe K-edges in Fig. 7-7. N, coordination number; R = interatomic distance; $2\sigma^2$, Debye-Waller factor; RF, fit error sum calculated for reduced distances of 1-4 Å. *Coordination numbers were coupled to yield a sum of 5 for the first two N/O ligand shells (so that together with the third N/O shell a value of N = 6 resulted), $^\#2\sigma^2$ values were coupled to yield the same value for the indicated coordination shells, $^\&$N-values that were fixed in the fit procedure. The coupling of Debye-Waller factors for the N/O shells is justified by using N = 1 for the longest bond (for which a relatively larger $2\sigma^2$ value was expected) and N-values of about 2-3 for the shorter bonds (so that $2\sigma^2$ accounted for the expected bond length variations within a given shell). We note that only insignificant changes in fit qualities or bond lengths were observed for using integer N-values closest to the fitted fractional N-values for the first two coordination shells. S_0^2 was 0.85 for Mn and Fe.

Table 7-3: Calculated interatomic distances in FeFe and MnFe cofactors.[a]

protonation state	distance [Å] (FeFe / MnFe)			
	Fe/Mn1-OH_n	Fe/Mn1-μOH_n	Fe2-μOH_n	Fe/Mn1-Fe2
H_2O/μOH	2.13(8) / 2.29(12)	1.97(5) / 1.88(2)	2.07(3) / 2.13(2)	3.59(3) / 3.60(5)
OH/μOH	1.87(1) / 1.87(3)	2.03(3) / 1.90(5)	2.02(3) / 2.15(14)	3.61(4) / 3.62(9)
H_2O/μO	2.10(4) / 1.98(7)	1.84(2) / 1.82(4)	1.86(3) / 1.97(12)	3.33(4) / 3.43(10)
OH/μO	1.88(1) / 1.87(2)	1.89(3) / 1.80(4)	1.83(2) / 1.88(6)	3.36(5) / 3.37(8)

[a]Distances represent mean values from DFT and QM/MM calculations on model structures with complexity and configurational variations as shown in Figs. 7-1, -2, and -3; values in parenthesis give the full distance range (±) for the various models and theoretical approaches.

7.3.5 Spin state from Kß emission

Kβ main- and satellite emission lines due to radiative 3p→1s transitions or electronic decay from valence orbitals were recorded at the Mn and Fe K-edges (Fig. 7-8). The Mn $K\beta_{1,3}$ first-moment line energy (~6490.9 eV) was similar to octahedral Mn(III) sites[91, 92, 163, 267, 289, 290] and similar to $Mn(III)_2O_3$. The Fe $K\beta_{1,3}$ line energies (~7059.2 eV) and shapes of the MnFe and FeFe cofactors were almost identical and similar to $Fe(III)_2O_3$.[133, 159] These results were well compatible with near-quantitative Mn/Fe(III) contents in both cofactors. The Kβ' spin-polarization emission feature increases for increasing numbers of unpaired spins on the metal centers.[187, 198, 289] The pronounced relative amplitudes of the Mn (~6476 eV) and Fe (~7045 eV) Kβ' features were expected for ionic ligation environments [159, 196] and proved that the Mn(III) (d^4) and Fe(III) (d^5) ions were high-spin. This agrees with anti-ferromagnetic coupling in the FeFe cofactor, rendering it EPR-silent, whereas the S = ½ EPR signal of the MnFe cofactor is due to anti-ferromagnetic coupling of its Mn(III) and Fe(III) ions.[131, 232] Kβ satellite emission lines are displayed in Fig. 7-8 (inset). The Mn emission showed two main $K\beta_{2,5}$ maxima with an about 1.5-fold larger higher-energy peak and a weak Kβ'' feature. The Fe emission of the MnFe and FeFe cofactors also exhibited two main $K\beta_{2,5}$ maxima and a similar Kβ'' feature. For the MnFe cofactor, the lower-energy $K\beta_{2,5}$ peak of Fe2 showed a larger amplitude and the higher-energy peak a smaller amplitude compared to the FeFe cofactor. Kβ satellite emission spectra were analyzed in detail using DFT further below.

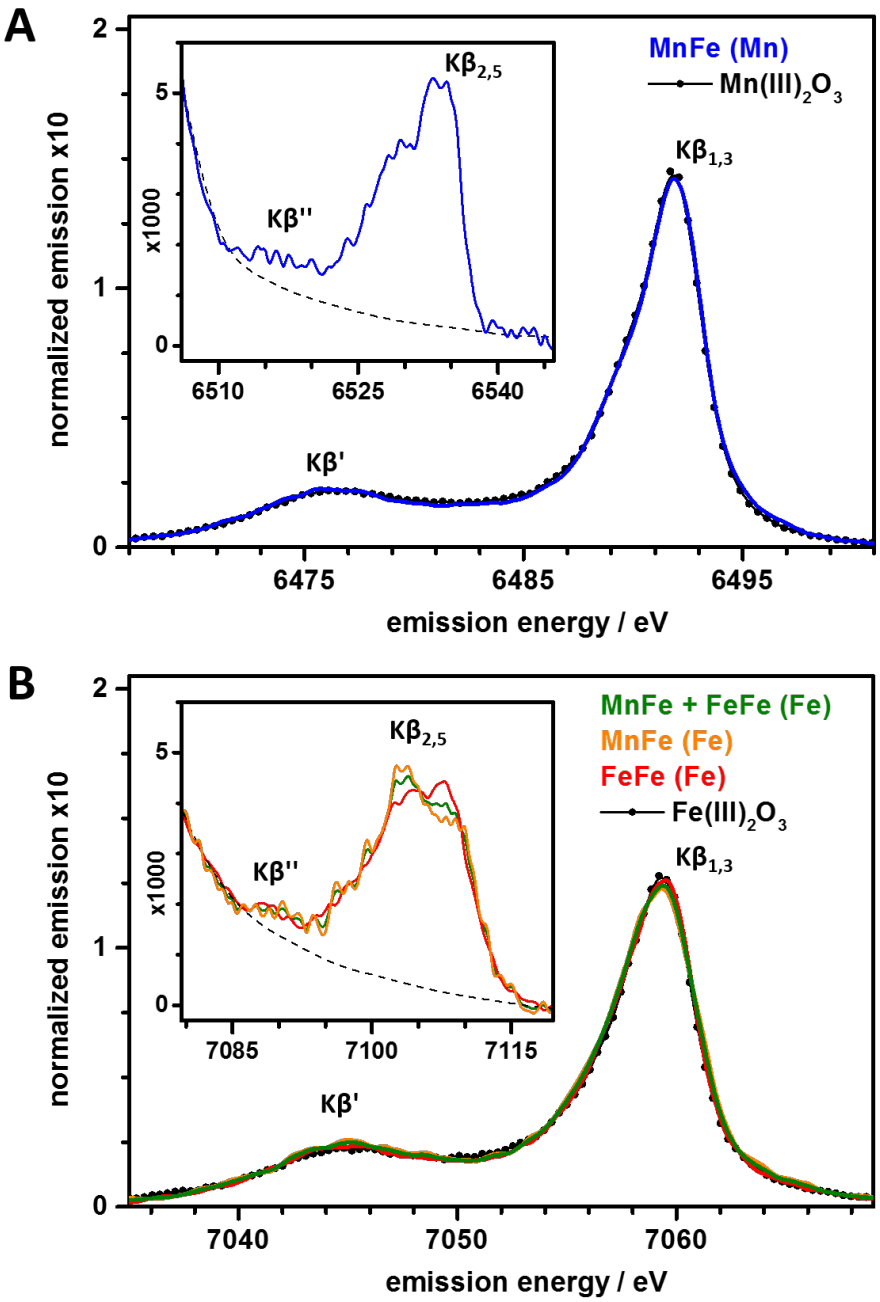

*Figure 7-8: Kβ X-ray emission spectra of MnFe and FeFe cofactors. (**A**) Mn emission and (**B**) Fe emission in the Kβ main-line and satellite line (inset) regions. Spectra of R2lox were obtained by a time-resolved energy-sampling approach within ~1 s and are compared to (continuous-scan) $Mn(III)_2O_3$ (A) and $Fe(III)_2O_3$ (B) spectra. Kβ satellite line spectra were collected on separate sample spots. The Fe spectrum of the MnFe cofactor in (B) was obtained by subtraction of 35% of the FeFe spectrum from the MnFe + FeFe spectrum. Dashed lines in the insets show $Kβ_{1,3}$ tail offsets, which were subtracted for vtc emission spectra extraction (Fig. 7-10).*

7.3.6 Cofactor protonation state

The pre-edge X-ray absorption reflects resonant 1s core electron excitation into unoccupied valence orbitals (core-to-valence transitions, ctv), whereas the Kβ satellite emission monitors radiative electronic decay from occupied valence orbitals to the core hole (valence-to-core transitions, vtc). Experimental ctv and vtc spectra were extracted from the XANES and Kβ satellite emission spectra (Figs. 7-6 and 7-8) and are shown in Figs. 7-9 and 7-10. We calculated Mn and Fe ctv and vtc spectra for four conceivable protonation states of the MnFe and FeFe cofactors in geometry-optimized model structures (Fig. 7-3), showing μOH or μO metal-bridging and terminal H_2O or OH^{-1} groups at Mn/Fe1, and compared them to the experimental spectra (Figs. 7-9 and 7-10). For the ctv spectra of the MnFe and FeFe cofactors, near-quantitative agreement between experimental and calculated spectra was observed only for the H_2O/μOH states, while the other protonation states yielded strongly deviating spectral shapes compared to the experimental data. For the vtc spectra, the spectral differences between protonation states were less pronounced, but in particular the calculated relative amplitudes of the two main $K\beta_{2,5}$ maxima and relatively small Kβ'' features matched the experimental data considerably better for the H_2O/μOH than for the other protonation states. The use of another DFT functional (BP86) or of increasing model sizes (Fig. 7-2) resulted in slightly altered energies and intensities (not shown), but in all cases, superior agreement between experimental and theoretical data was obtained for the H_2O/μOH state. Alternative hydrogen-bonding patterns at the H_2O ligand including Tyr175 did not improve agreement between calculated and experimental data (Fig. 7-11). Notably, while the Kβ satellite emission spectra were insensitive to spin orientations, i.e. anti-ferromagnetic (afc) or ferromagnetic (fc) coupling of Mn/Fe1 and Fe2 spins resulted in similar vtc spectra, the ctv spectra for the afc states of the H_2O/μOH species in particular for the MnFe cofactor described the experimental data considerably better (Fig. 7-12). These results suggested a bridging hydroxide and terminal water ligand at Mn/Fe1 in the MnFe and FeFe cofactors.

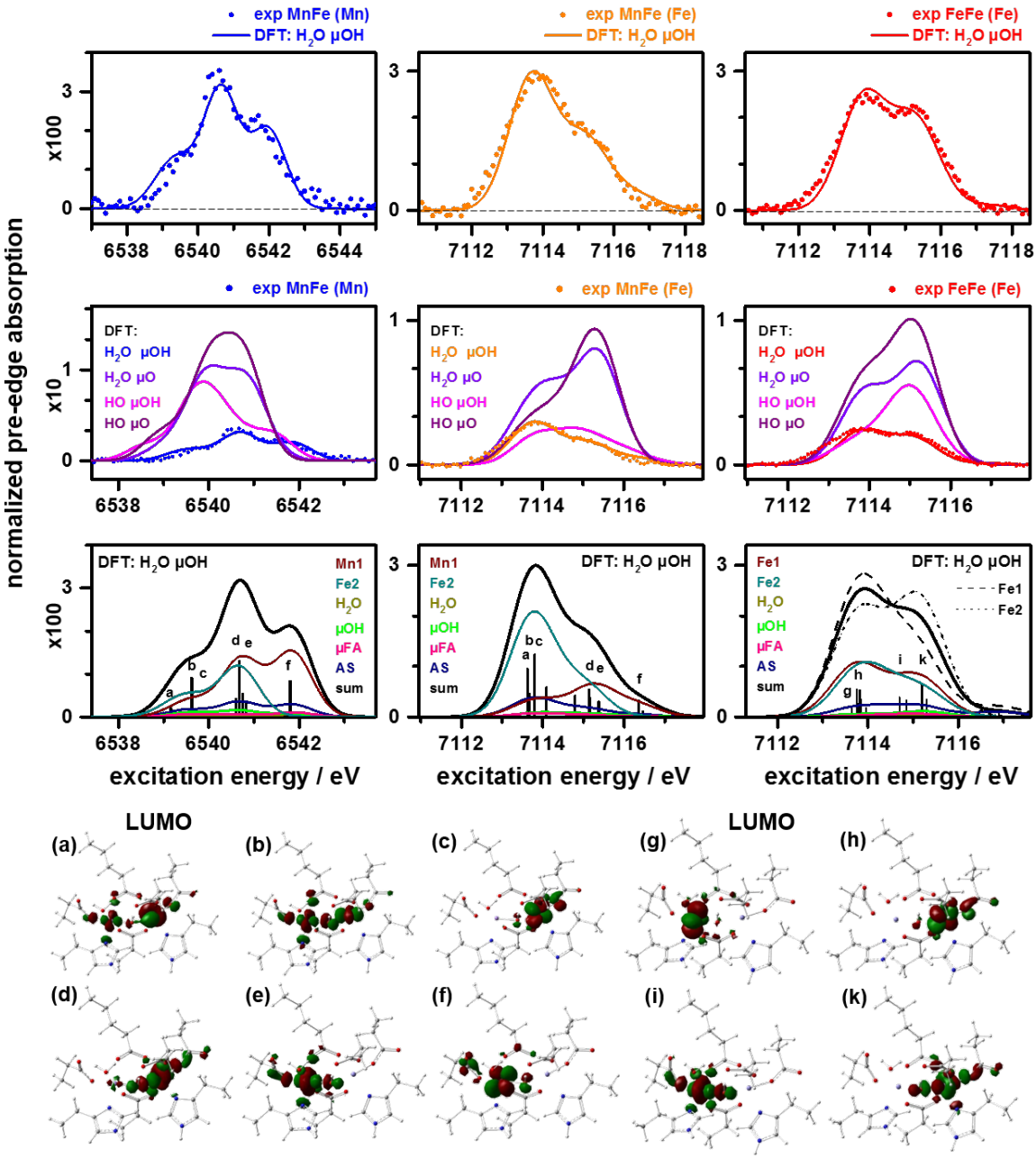

Figure 7-9: Core-to-valence (ctv) absorption spectra. ***Upper panel****, top: experimental ctv spectra (dots) at the Mn (left) and Fe (center) K-edges for the MnFe cofactor and at the Fe K-edge (right) for the FeFe cofactor compared to the DFT-calculated spectra (lines) for the H2O/μOH protonation states. Middle: calculated spectra for the indicated protonation states (lines) and experimental spectra (dots). Bottom: target molecular orbital characters of ctv excitation transitions for the H2O/μOH states (μFA = bridging fatty acid ligand, AS = amino acid ligands) and respective stick spectra (not drawn to scale); the individual sum spectra for Fe1 and Fe2 in the FeFe cofactor (right) were scaled by a factor of 2 for comparison.* ***Lower panel****: selected target MOs for ctv transitions (sticks marked in the bottom row) with predominant Mn/Fe-d character revealing, e.g., the z-axis ($d(z^2)$ orbital) orientation of the metal ions and MO delocalization. Stick spectra (11, Mn and Fe in MnFe; 20, FeFe) were broadened by Gaussians (FWHM = 1 eV, Mn or 1.25 eV, Fe) and shifted on the energy axis (134.2 eV, Mn; 145.9 eV, Fe) to derive theoretical spectra in the upper panel; calculated energy axes in the top row were stretched by a factor of 1.15, experimental energy axes in the middle row were compressed by a factor of 1.15, and calculated spectra were scaled by empirical factors of 1450 (Mn) or 1150/575 (Fe in MnFe/Fe in FeFe) for comparison. Experimental Fe spectra of the MnFe cofactor correspond to data corrected for the minor FeFe contribution.*

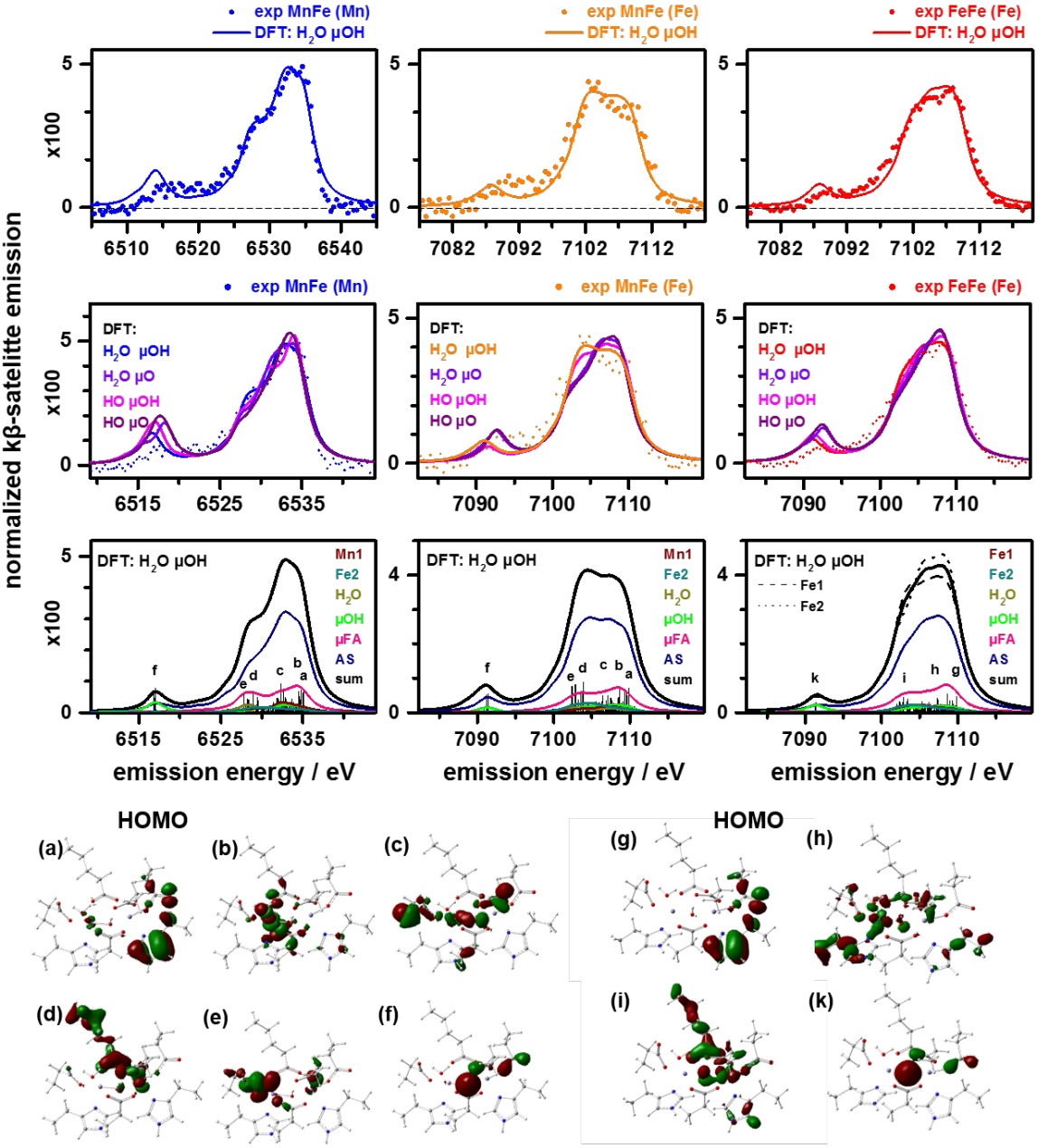

Figure 7-10: Valence-to-core (vtc) emission spectra. ***Upper panel****, top: experimental vtc spectra (dots) at the Mn (left) and Fe (center) K-edges for the MnFe cofactor and at the Fe K-edge (right) for the FeFe cofactor compared to the DFT-calculated spectra (lines) for the H2O/µOH protonation states. Middle: calculated spectra for the indicated protonation states (lines) and experimental spectra (dots). Bottom: source molecular orbital characters of vtc decay transitions for the H2O/µOH states (µFA = bridging fatty acid ligand, AS = amino acid ligands) and respective stick spectra (not drawn to scale); the individual sum spectra for Fe1 and Fe2 in the FeFe cofactor (right) were scaled by a factor of 2 for comparison.* ***Lower panel****: selected source MOs for vtc transitions (sticks marked in the bottom row) with predominant ligand characters revealing, e.g., ligand-s,p contributions and MO delocalization. Stick spectra (255, Mn and Fe in MnFe; 510, FeFe) were broadened by Lorentzians (FWHM = 2.5 eV, Mn or 3.0 eV, Fe) and shifted on the energy axis (133.5 eV, Mn; 146.2 eV, Fe) to derive theoretical spectra in the upper panel; calculated energy axes in the top row were stretched by a factor of 1.15, experimental energy axes in the middle row were compressed by a factor of 1.15, and calculated spectra were scaled by empirical factors of 120 (Mn) or 164/82 (Fe in MnFe/Fe in FeFe) for comparison. Experimental Fe spectra of the MnFe cofactor correspond to data corrected for the minor FeFe contribution.*

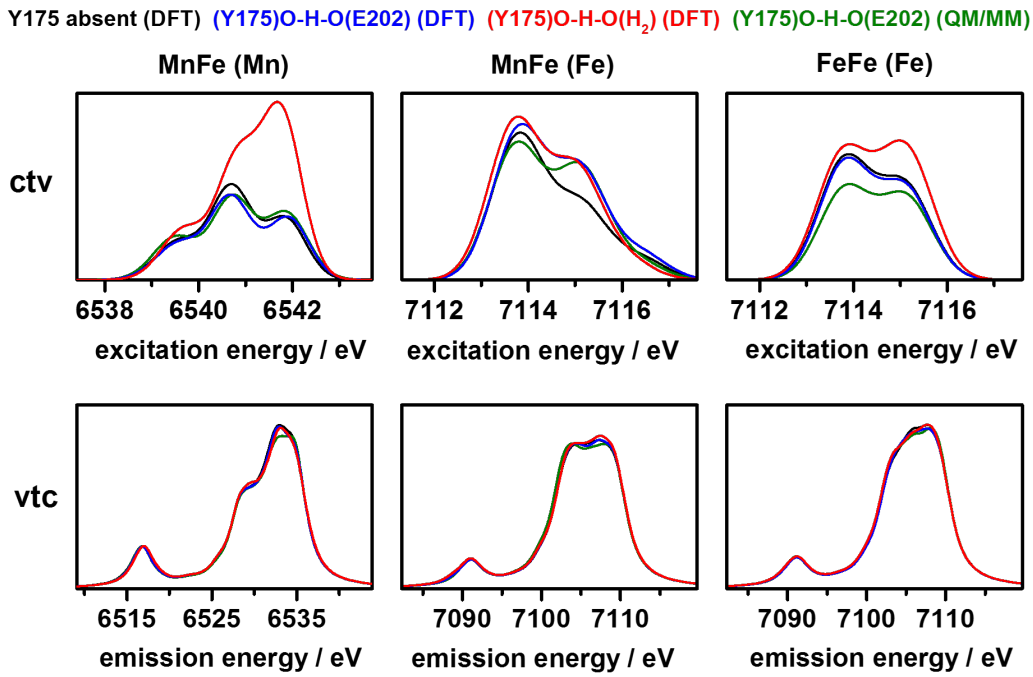

*Figure 7-11: ctv (pre-edge absorption) and vtc (Kß satellite emission) spectra for H-bonding variations. Shown are calculated Mn or Fe ctv (**top**) and vtc (**bottom**) spectra for the H2O/μOH protonation state of the MnFe and FeFe cofactors from the B3LYP/TZVP (DFT) and QM/MM (ONIOM) approaches (afc coupling) for the absence of Y175 in the model structures and for two orientations of hydrogen bonding of the Y175 phenolic proton (to the water ligand at Mn/Fe1 or the E202 carboxylic group) (see Figs. 7-2, -3 for respective structures). Spectra were shifted on the energy scale similar to data in Figs. A7-1 and -2 (given in the Appendix). Note the largely increased high-energy maximum in the ctv spectra for Y175 being a H-bond donor to the water ligand, which was not observed in the experimental data (Fig. 7-9), thereby favoring Y175 to function as a (weak) H-bond donor to E202 and a (weak) H-bond acceptor of the water ligand.*

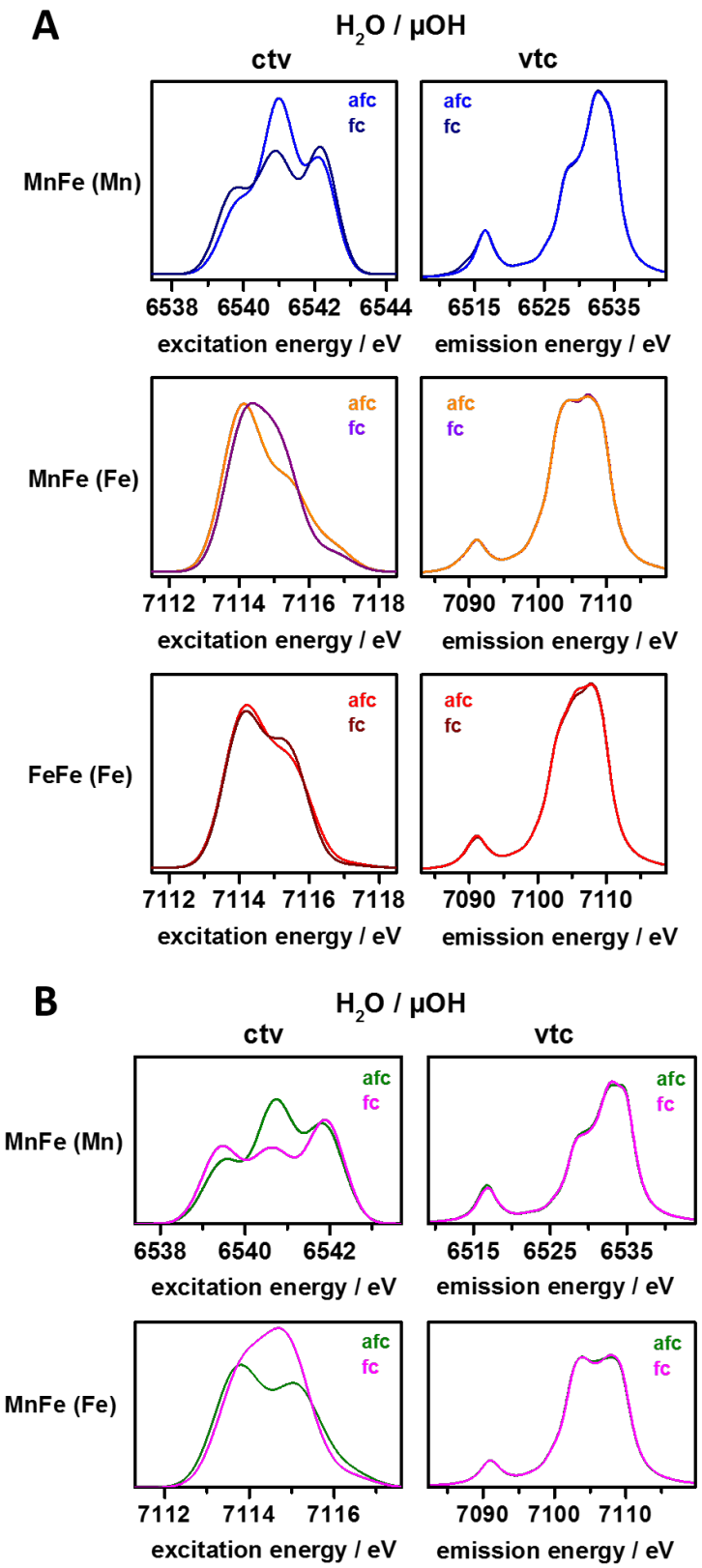

*Figure 7-12: ctv and vtc spectra for electronic coupling variations from DFT. Data are for the H2O/µOH protonation state (Y175 H-bond donor to E202) for ferromagnetic (fc) or anti-ferromagnetic (afc) coupling of the Mn/Fe1(III) and Fe2(III) ions. (**A**) Spectra from B3LYP/TZVP DFT calculations on MnFe and FeFe cofactor model structures (Fig. 7-2). (**B**) Spectra for the MnFe cofactor in the QM/MM whole-protein model (Fig. 7-2). Spectra in (B) were derived from single-point DFT calculations on the high-layer core of the QM/MM optimized model structure.*

7.3.7 Transitions underlying ctv and vtc spectra

Dissection of the calculated ctv transitions into target molecular orbital (MO) characters explained the features of the experimental pre-edge absorption spectra (Fig. 7-9). The Mn1/Fe2 ctv spectra of the MnFe cofactor were fully described by 11 transitions each, which reflected excitations of Mn1-$1s^{\alpha/\beta}$ (at Mn K-edge) or Fe2-$1s^{\alpha/\beta}$ (at Fe K-edge) electrons into unoccupied MOs with predominant Mn1-d (6 MOs) or Fe2-d (5 MOs) characters. The Fe1 + Fe2 ctv spectrum of the FeFe cofactor was described by 20 transitions, which reflected excitations of Fe1/2-$1s^{\beta}$ electrons into unoccupied MOs with predominant Fe1/2-d (10 MOs each) characters. For the Mn1/Fe2 ctv spectra, the low-energy-shoulder/first-maximum were due to Mn1/Fe2-$1s^{\beta}$ excitation into t_{2g} Fe2-d dominated MOs (e.g. β-LUMO) and $1s^{\alpha}$ excitation into the e_g Mn1-d(x^2-y^2) α-MO, the main-peak/second-maximum reflected $1s^{\beta}$ excitation into t_{2g} Mn1-d β-MOs (e.g. β-LUMO) and $1s^{\alpha}$ excitation into e_g Fe2-d(z^2, x^2-y^2) α-MOs, and the high-energy-peak/shoulder was attributable to $1s^{\alpha}$ excitations into e_g Mn1-d(z^2, x^2-y^2) α-MOs. For the Fe ctv spectrum of the FeFe cofactor, Fe1/2-$1s^{\alpha/\beta}$ excitation into t_{2g} Fe1/2-d α/β-MOs accounted for the first maximum and into e_g Fe1/2-d α/β-MOs for the second maximum. The calculated ctv spectra of Fe2 in the FeFe and MnFe cofactors were quite similar, e.g. showing a first maximum exceeding the second one due to intense low-energy transitions into Fe2-d MOs, whereas the increased second maximum of the Fe1 spectrum of the FeFe cofactor was explained by enhanced excitations into Fe1-d MOs with larger ligand contributions. Small admixtures of amino acid and FA ligand characters into Mn/Fe-d dominated MOs and admixtures of metal 4p orbitals in the whole ctv region accounted for the significant intensities of the formally dipole-forbidden 1s→3d transitions. Contributions of the H_2O or μOH ligands to the target MOs were negligible for the H_2O/μOH protonation states. In turn, the largely increased ctv intensities calculated for the gradually deprotonated species were due to enhanced delocalization of MOs with dominant Mn/Fe-d character over both metal ions and the ligands in response to shorter Mn/Fe1-OH/μO bonds and metal-metal distances, leading to enhanced OH/μO characters and metal 4p characters of the target MOs (Fig. A7-1, given in the Appendix). These findings explained the altered ctv spectra of the different protonation states of the two cofactors.

Dissection of the calculated vtc transitions into source MO characters explained the features of the experimental Kβ satellite emission spectra (Fig. 7-10). The $K\beta_{2,5}$ emission of both Mn and Fe vtc spectra was dominated by decay from ligand-based MOs contributing almost stoichiometrically to the spectra, as visible, e.g., for the contributions from MOs centered at the FA ligand. The increased first $K\beta_{2,5}$ maximum for Fe2 in the MnFe and FeFe cofactors could

thus be explained by the contribution of one more Glu ligand compared to the metal ion in site 1 having a water ligand instead. Accordingly, decay from MOs located at the H_2O or μOH groups contributed weakly to the $K\beta_{2,5}$ emission, but more prominently to the Kβ'' feature due to decay from MOs with large μO(H)-2s character. Contributions of decay from metal-d MOs were small in the entire spectral region. Similar overall $K\beta_{2,5}$ intensities for all protonation species were explained by similar delocalization of source MOs over the ligands. The vtc differences of iron thus reflected varying contributions from H_2O/OH or μO/O species to the Fe1/2 spectra (Fig. A7-2, given in the Appendix), emphasizing the sensitivity to the protonation state.

7.3.8 Electronic structure and bonding

Significant electronic structure differences of the MnFe and FeFe cofactors were revealed by the valence level energies (Fig. 7-13). For both cofactors, 5 unoccupied MOs each with predominant Fe1-d or Fe2-d character (60-89%) were identified, which were mostly lower in energy than the unoccupied Mn-d levels and showed almost octahedral degeneracy, similar energies, and separation (Δ) of t_{2g} and e_g levels by ~1.2 eV. The respective 5 occupied MOs assigned according to their largest iron character were at ~9 eV lower energies and showed much lower Fe-d characters (15-38%) and enhanced admixtures in particular of O-p and C-p levels compared to the unoccupied MOs, but also near-octahedral degeneracy with Δ-values of ~0.9 eV and ~0.2 eV for Fe1 and Fe2 in the FeFe cofactor and a doubled Δ of ~0.4 eV for Fe2 in the MnFe cofactor. The $d(z^2)$ orbital was oriented along the Fe1/2-μOH bond in both cofactors. For the Mn1 ion, the 5 unoccupied α-spin MOs identified by their largest Mn-d character (71-92%) showed energy separations approaching square-planar degeneracy with the $d(x^2-y^2)$ orbital at highest energy followed by the $d(z^2)$ orbital, due to a Jahn-Teller axis oriented along the H_2O-Mn1-O(Glu102) bonds, and a Δ of ~1.1 eV. For the occupied Mn-d levels, similar delocalization and O/C-p admixtures as for iron, almost square-planar degeneracy with the unoccupied $d(x^2-y^2)$ level at highest energy followed by the occupied $d(z^2)$ level, and a large Δ of ~5.6 eV were found. In both cofactors, the α/β HOMOs showed similar energies and exclusive ligand character and were located mostly on His205. In the FeFe cofactor, also the Fe1/2-d dominated α/β LUMOs showed similar energies so that a LUMO-HOMO energy gap of ~3.2 ± 0.1 eV was obtained. In the MnFe cofactor, the β-LUMO on Fe2 was ~1.4 eV lower in energy than the α-LUMO on Mn1 so that a larger mean energy gap of ~3.9 ± 0.7 eV was obtained. These results showed that the electronic structure of the Fe2 site was quite similar in

both cofactors, although slightly more distorted in the MnFe cofactor, but the octahedral Fe1 was replaced by a Mn1 ion with much decreased symmetry and d-level degeneracy and 90° reoriented z-axis in the MnFe cofactor.

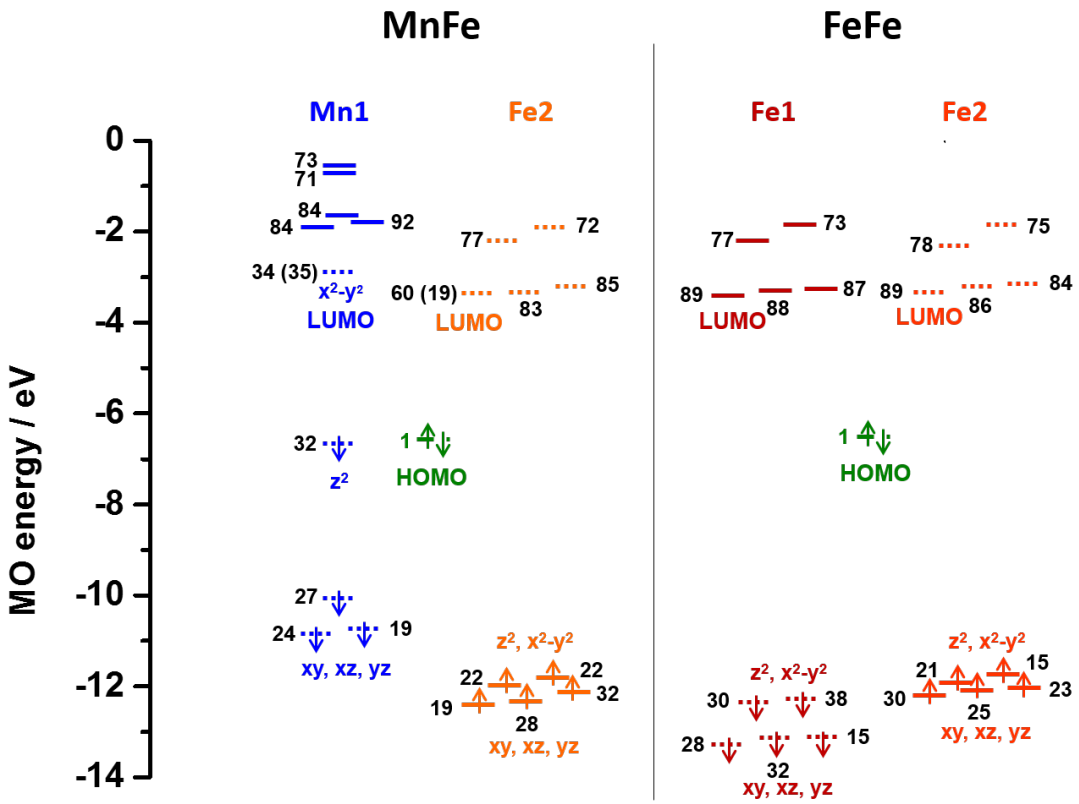

Figure 7-13: Valence level degeneracy in MnFe and FeFe cofactors. MO energies were obtained by DFT (B3LYP/TZVP) for the H2O/μOH protonation states; Mn/Fe-d characters (in %) of MOs are indicated (contributions >1% from the respective other metal site in parentheses). Dotted lines (downward arrows), α-spin (occupied) MOs; solid lines (upward arrows), β-spin (occupied) MOs. Note the Mn/Fe-centered LUMOs, but ligand-centered HOMOs.

Spin density and charge distributions in the cofactors are shown in Figs. 7-14 and 7-15. Overall quite similar charge distributions were observed for both types, with ~0.9 e on Mn and Fe and ~0.1 e less charge on Mn1 in the MnFe cofactor, about -1.6 e on the four Glu ligands in total, 0.2 e on each His ligand, -0.3 e on the fatty acid and μOH ligands, and negligible charge on H_2O. In the MnFe cofactor ~8 spins resided on metal, i.e. ~1 spin was delocalized mostly onto the Glu ligands. In the FeFe cofactor ~9 spins resided on metal, i.e. ~1 spin was delocalized mostly onto the Glu and H_2O/μOH ligands; about 50% of the surplus spin resided on Fe1 and the remainder mostly on its ligands. The spin density distribution at the FeFe cofactor thus was quite symmetric for Fe1 and Fe2 and showed low spin polarization. The MnFe cofactor showed axially distorted negative spin density and increased spin polarization with positive spin density

at the equatorial Mn-O/N bonds (Fig. 7-14). Real-space bonding indicator analysis revealed covalent and non-covalent interactions for the H_2O/μOH state of the MnFe and FeFe cofactors (Figs. 7-14 and A7-3). A specific hydrogen-bonding pattern was favored, with the H_2O at Mn/Fe1 serving as H-bond donor to Tyr175 and Glu69 and Tyr175 acting as H-bond donor to Glu202 (also H-bonded to μOH). Further weak interactions including C/N/O-H···O/N bonds and non-polar H-H contacts were identified for example to the water molecule. Non-covalent bonding aspects apparently are considerably stronger for the Mn-OH_2 (and Mn-μOH) than for the Fe-OH_2 (and Fe-μOH) species.

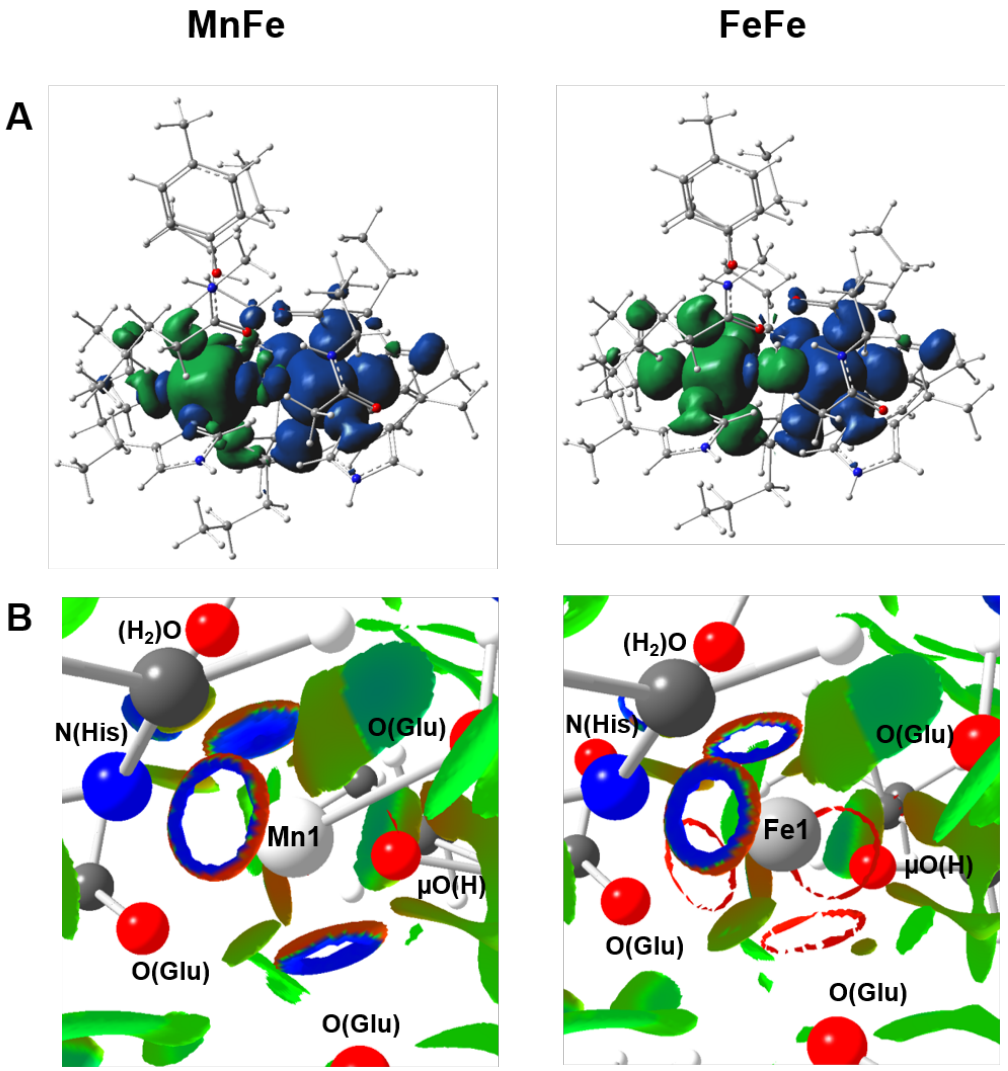

*Figure 7-14: Spin density distribution and bonding patterns. (**A**) Spin-densities in MnFe (left) and FeFe (right) cofactors (green, β-spin; blue, α-spin) from Hirshfeld population analysis. (**B**) non-covalent bonding patterns from NCI analysis. Ring-shaped basins indicate weak repulsive (red) or attractive (blue) forces, the disc-shaped basin for the Mn1-OH_2 bond shows predominance of non-covalent over covalent attractive forces, Van-der-Waals contacts are shown in green. Inter-molecular bonding contacts from AIM analysis are shown in Fig. A7-3.*

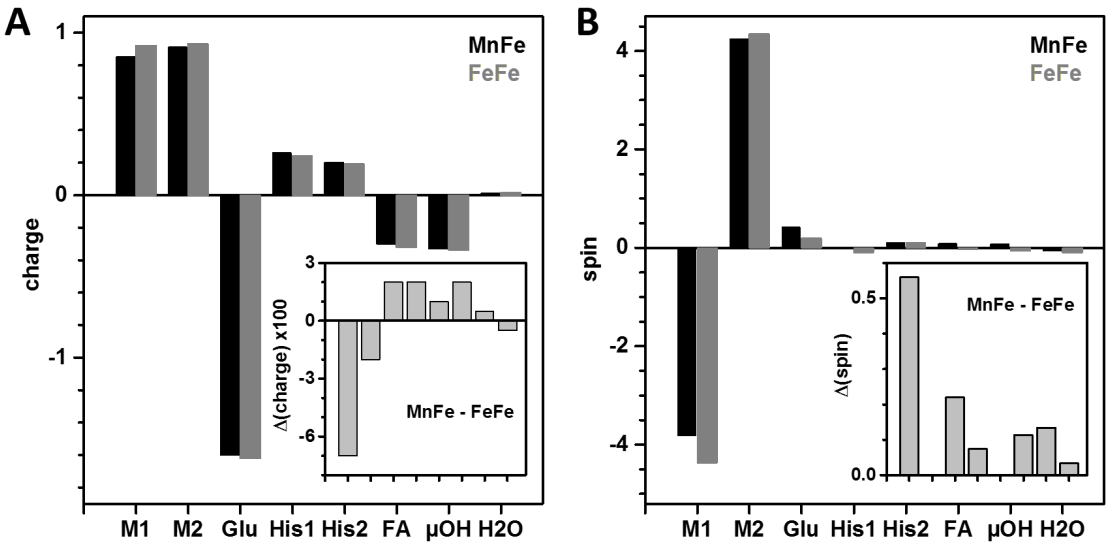

*Figure 7-15: Charge (**A**) and spin (**B**) distributions in MnFe and FeFe cofactors. MnFe, black; FeFe, grey. M1, M2 = metal ion in site 1 or 2, His1, His2 = histidine ligand at M1 or M2, FA = fatty acid ligand. The insets show the MnFe – FeFe difference values.*

7.3.9 Vibrational dynamics

NRVS spectra were collected for FeFe and MnFe R2lox reconstituted with ^{57}Fe. Respective partial vibrational density of states (pDOS) spectra are shown in Fig. 7-16. Prominent vibrational bands in the 50-550 cm^{-1} region were observed, which were superimposed on a broad and unresolved spectral background, whereas at higher frequencies the spectra approached the zero level for both cofactors. The spectra of the two cofactors showed significant band frequency and intensity differences, best visible in the MnFe - FeFe pDOS difference spectrum, which reflected different vibrational properties of the Fe2 ion in the MnFe cofactor and the Fe1 and Fe2 ions in the FeFe cofactor.

A QM/MM approach on whole-protein model structures, as well as DFT on smaller cofactor models, and normal mode analysis were employed to calculate pDOS spectra of iron for MnFe and FeFe cofactors. Comparison of pDOS spectra calculated by DFT on models with increasing size or by QM/MM on the whole protein showed that the broad spectral background in the 50-450 cm^{-1} region was largely due to a continuum of weak whole-cofactor/protein-matrix modes, i.e. the relative intensities of the more distinct bands in the (normalized) pDOS approached the QM/MM level for the largest DFT models (Figs. 7-17 and A7-4, given in the Appendix). The main bands were derived even from DFT models comprising only the cofactor, but their

experimental relative frequencies and intensities were best reproduced by QM/MM, including anti-ferromagnetic coupling of the Mn/Fe1 and Fe2 ions (Figs. 7-16 and 7-17).

PDOS spectra of the four protonation states of the cofactors were calculated (Fig. A7-4, given in the Appendix). For the FeFe cofactor, an OH^- instead of a H_2O ligand at Mn/Fe1 or a μO instead of a μOH bridge resulted in intense bands in the 450-650 cm^{-1} region for the QM/MM and DFT approaches, which were absent in the experimental spectrum. Only the H_2O/μOH state yielded a pDOS spectrum showing low intensities above ~450 cm^{-1} and major features around ~200 cm^{-1}, ~250 cm^{-1}, ~340 cm^{-1}, and ~420 cm^{-1}, as experimentally observed. The NRVS spectrum of the MnFe cofactor deviated from the FeFe spectrum for example by showing more narrow and intense bands at ~250 cm^{-1}, ~300 cm^{-1}, and ~350 cm^{-1} (Fig. 7-16). For the four protonation states, a terminal OH^- or bridging μO ligand caused the appearance of intense bands around ~470 cm^{-1} or even higher frequencies, which were not observed experimentally, whereas the H_2O/μOH state yielded relative spectral intensities in better agreement with the experimental MnFe spectrum (Figs. 7-16 and A7-4; given in the Appendix). The relative intensities and frequencies of the calculated NRVS spectra showed a moderate dependence on the used theory level (Fig. A7-5, given in the Appendix). However, the MnFe – FeFe difference spectra for the H_2O/μOH species reproduced the main features of the experimental spectra in particular at higher frequencies in all cases best. These results further supported a H_2O ligand at Mn/Fe1 and a μOH bridge in both cofactors.

A more quantitative understanding of the NRVS spectra was reached when evaluating individual metal-ligand vibrations from the calculations (Fig. 7-16). The observed most prominent bands corresponded to about 10 main vibrational modes in the 200-450 cm^{-1} region. These bands reflected modes with predominant contributions from Glu and FA oxygens (~220 cm^{-1}) or amino acid ligand and protein backbone atoms (~250 cm^{-1}) in the lower-frequency region. Large and varying contributions from the H_2O ligand and μOH bridge dominated bands around ~300 cm^{-1}, 350 cm^{-1}, and ~400 cm^{-1}. This explained the sensitivity of the high-frequency spectral region to changes in cofactor protonation. Notably, comparison of the NRVS spectra for two orientations of the Tyr175 phenolic group supported that this group functions as a hydrogen-bond donor to Glu202 (Fig. 7-17).

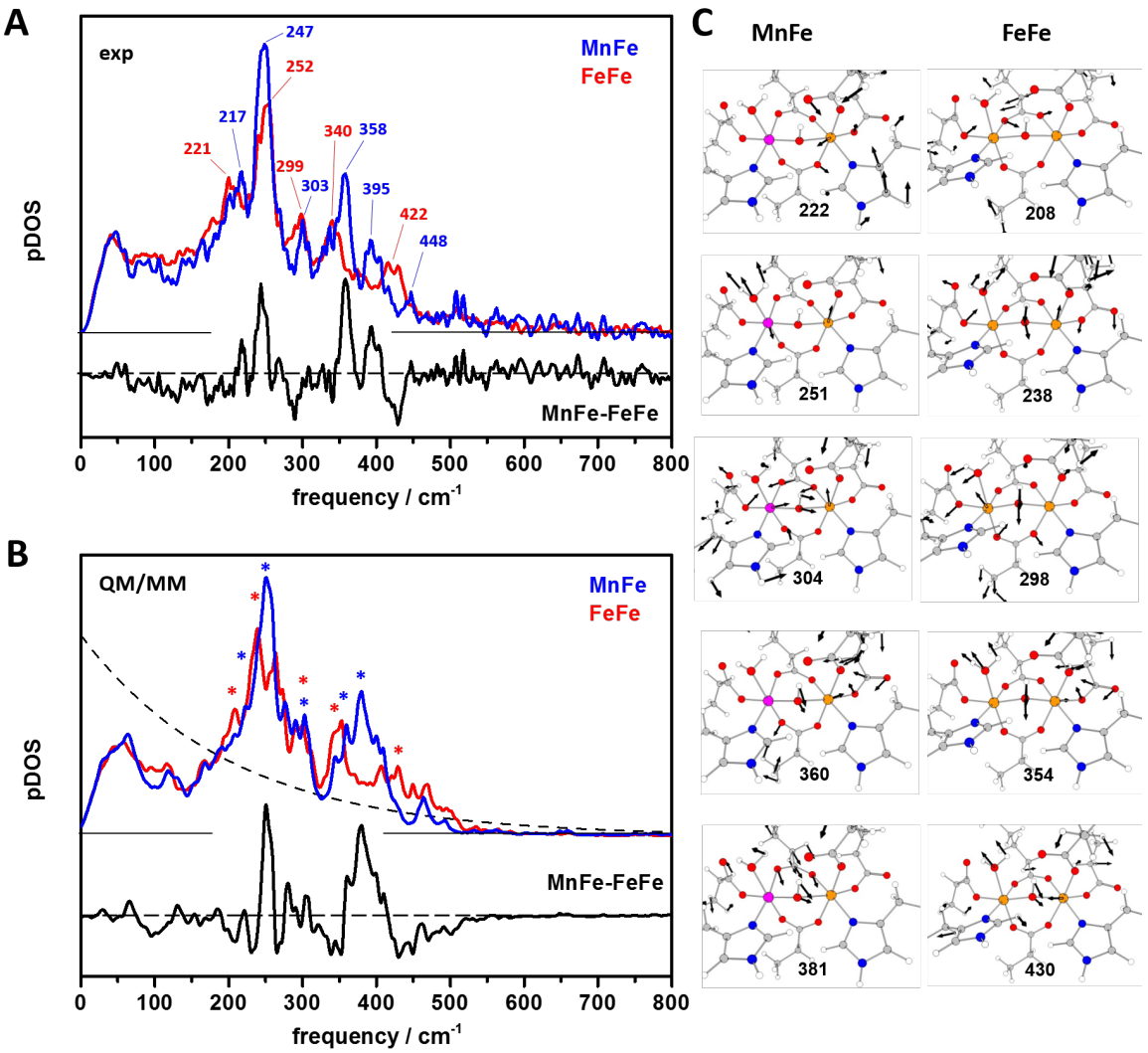

*Figure 7-16: Nuclear resonance vibrational spectroscopy on ^{57}Fe in MnFe and FeFe cofactors. **(A)** Experimental pDOS spectra (smoothed over 3 data points = 0.6 meV for display) with prominent vibrational bands marked and MnFe – FeFe difference spectrum (vertically displaced). The spectrum of Fe1 in the MnFe cofactor was derived by subtraction of 35% of the FeFe spectrum from the MnFe + FeFe spectrum (Fig. A7-6, given in the Appendix). **(B)** Spectra for ^{57}Fe in the two cofactor types from QM/MM (B3LYP/cep31g) calculations on whole-protein models including anti-ferromagnetic coupling of the Mn/Fe1 and Fe2 ions and MnFe – FeFe difference spectrum (vertically displaced) for the H2O/μOH protonation states (averaged spectra for slight "high layer" size variations in the ONIOM approach, for individual calculated spectra see Figs. 7-17, and A7-4, -5, given in the Appendix). The dashed line shows the relative Boltzmann population of excited vibrational modes at 293 K. **(C)** Selected calculated vibrational modes with contributions from the Fe ions and metal ligands (asterisks in B). Arrows show relative amplitudes and directions of vibrations of atoms (not drawn to scale), rounded mode frequencies are given in cm^{-1}.*

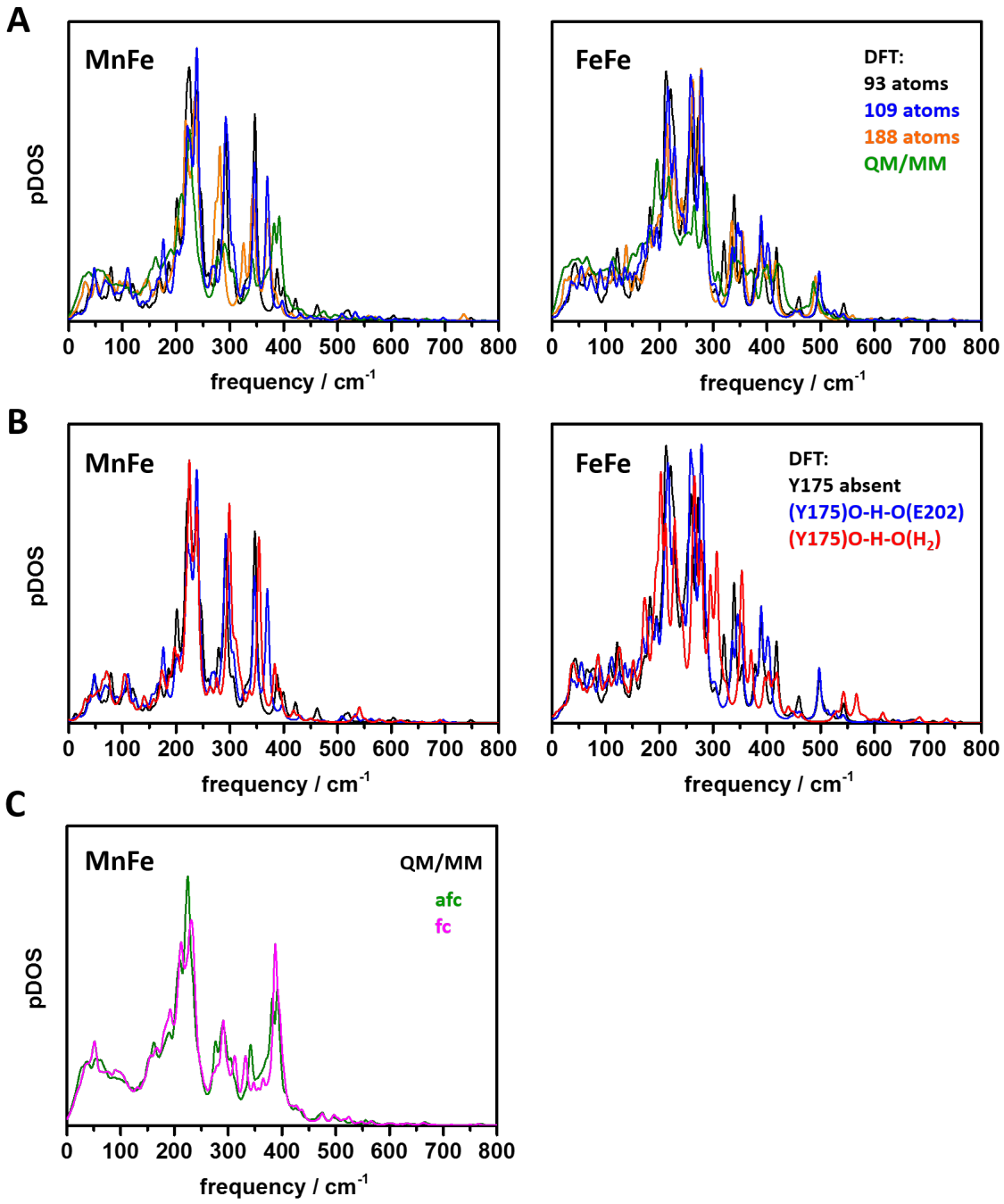

*Figure 7-17: Calculated NRVS spectra for model variations. (**A**) PDOS spectra for the H2O/μOH state from DFT for increasing model size compared to spectra from QM/MM (Fig. 7-2, B3LYP/TZVP in both approaches). (**B**) PDOS spectra for the H2O/μOH state for different hydrogen-bonding situations of Y175 (Fig. 7-3) from DFT. (**C**) PDOS spectra for the H2O/μOH state from QM/MM for ferromagnetic or anti-ferromagnetic coupling of the Mn1 and Fe2 ions.*

7.3.10 Nuclear forward scattering

NFS time-traces were collected for the MnFe and FeFe cofactors (Fig. 7-18). They showed rapid intensity (I) decrease related to the ^{57}Fe excited state lifetime (τ_0 = 141 ns) and superimposed oscillations due to interference of forward scattering from the I = 3/2 and I = 1/2 nuclear excitation levels, separated by the quadrupole splitting energy (ΔE_Q) as given by Eq. 21 (A = amplitude scaling factor, τ = effective decay lifetime, υ = modulation frequency, φ = phase shift due to experimental zero point shifts, B = detector count offset). Eq. 21 was used for $\Delta E_Q = h\upsilon$ ($h = 4.135 \times 10^{-6}$ neVs) determination.[38, 216, 266]

$$I_{NFS}(t) = A \exp\left(-\frac{t}{\tau}\right) cos^2(\pi\upsilon t + \varphi) + B \tag{21}$$

Fit analysis of the NFS traces revealed ΔE_Q values of 37(2) neV = 0.77(4) mms^{-1} for the FeFe and 41(3) neV = 0.84(6) mms^{-1} for the MnFe cofactors, i.e. a ΔE_Q difference of 4 neV = 0.08 mms^{-1}. The mean ΔE_Q (39 neV = 0.81 mms^{-1}) was identical to the value determined by

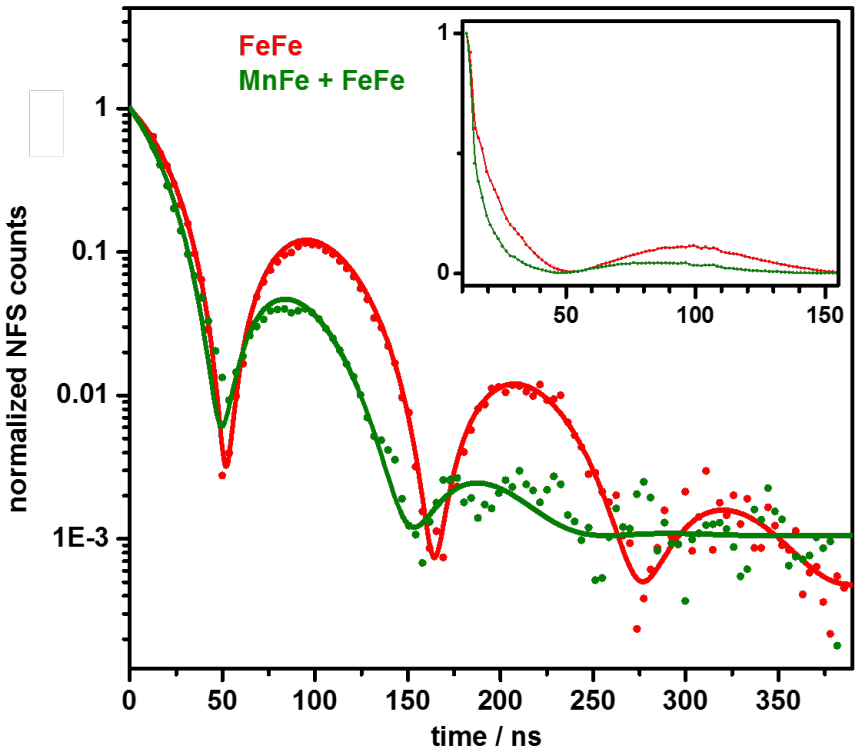

Figure 7-18: Nuclear forward scattering time traces for ^{57}Fe in MnFe and FeFe cofactors. Dots, experimental data; lines, simulations with Eq. 22 and the following parameters (B / τ / ν / φ): Fe in MnFe, 0.0010 / 29 ns / 0.0096 ns^{-1} / 0.11 ns; FeFe, 0.0005 / 47 ns / 0.0089 ns^{-1} / 0.12 ns. NFS count traces were normalized to unity amplitude at t = 0 according to the fit results for better comparison. The inset shows the first 150 ns of data on a linear amplitude scale.

Mössbauer spectroscopy (at 80 K) for both cofactors and is typical for high-spin Fe(III).[131, 232] The sensitive NFS interference method facilitated resolution of a slightly different ΔE_Q of the summed Fe1/2 sites in the FeFe and the Fe2 site in the MnFe cofactor. The apparent Mössbauer linewidth (Γ) may be calculated from τ using $\Gamma = h/2\pi(1/\tau_0 + 1/\tau)$, which yielded Γ–values of (τ = 47(3) ns) 18(2) neV = 0.38(4) mms^{-1} for the FeFe and (τ = 29(4) ns) 27(3) neV = 0.56(5) mms^{-1} for the MnFe cofactor. The Γ-value for FeFe was slightly smaller than the Mössbauer value (0.48 mms^{-1}), but Γ for the MnFe sample was similar to the Mössbauer value (0.55 cm^{-1}), showing that the larger linewidth was due to slightly different isomeric shifts of the Fe2 and Fe1/2 ions in the MnFe and FeFe cofactors.

7.4 Discussion

R2lox is a member of the growing class of DMC enzymes, which can carry a hetero-bimetallic MnFe cofactor instead of the classical FeFe cofactor.[5, 36, 84, 107, 128, 222, 268, 293] We show here that rapid-scan and energy-sampling, high-resolution XAS/XES/NRVS methods facilitate comprehensive determination of molecular, electronic, nuclear, and vibrational parameters of the high-valent dimetal cofactors. For R2lox, relative Mn and Fe contents, X-ray photoreduction kinetics, metal-ligand bond lengths and metal-metal distances, metal oxidation states, spin configurations, valence level degeneracies, molecular orbital compositions, vibrational normal modes, nuclear quadrupole splittings, and protonation states were determined for the EPR-visible Mn(III)Fe(III) and the EPR-silent Fe(III)Fe(III) cofactor. This was based on X-ray spectroscopic (and crystallographic) benchmark data, which were reproduced by DFT and QM/MM calculations. Combining advanced X-ray spectroscopy and quantum chemical methods is a powerful approach for DMC enzyme characterization.

Determination of unperturbed crystal structures of high-valent DMC sites by conventional XRD is precluded because divalent metal ions are formed by rapid X-ray photoreduction (XPR), leading to metal-ligand bond elongation.[82, 83, 141, 237, 288] Fast XPR is also problematic in continuous-scan XES experiments.[163] This is emphasized by Mn/Fe(II) formation by XPR within tens of seconds even under our X-ray spectroscopy conditions with at least two orders of magnitude smaller specific X-ray flux as in XRD.[83] Rapid XPR may be overcome in XRD and (dispersive) XES using femtosecond X-ray pulses of free electron lasers.[33, 114] We used an alternative approach, time-resolved energy-sampling XES, to obtain high-contrast Kβ emission spectra of R2lox. In particular the “two-color”[102] ctv and vtc experiments at Mn and Fe K-edges, which monitor direct and crossover transitions between Mn/Fe-1s core levels

and unoccupied or occupied Mn/Fe valence levels, have contributed to unambiguous structure assignment. Our results and XRD data [83, 84, 131, 232] suggest refined structures of the MnFe and FeFe cofactors with consistent geometries (Fig. 7-19).

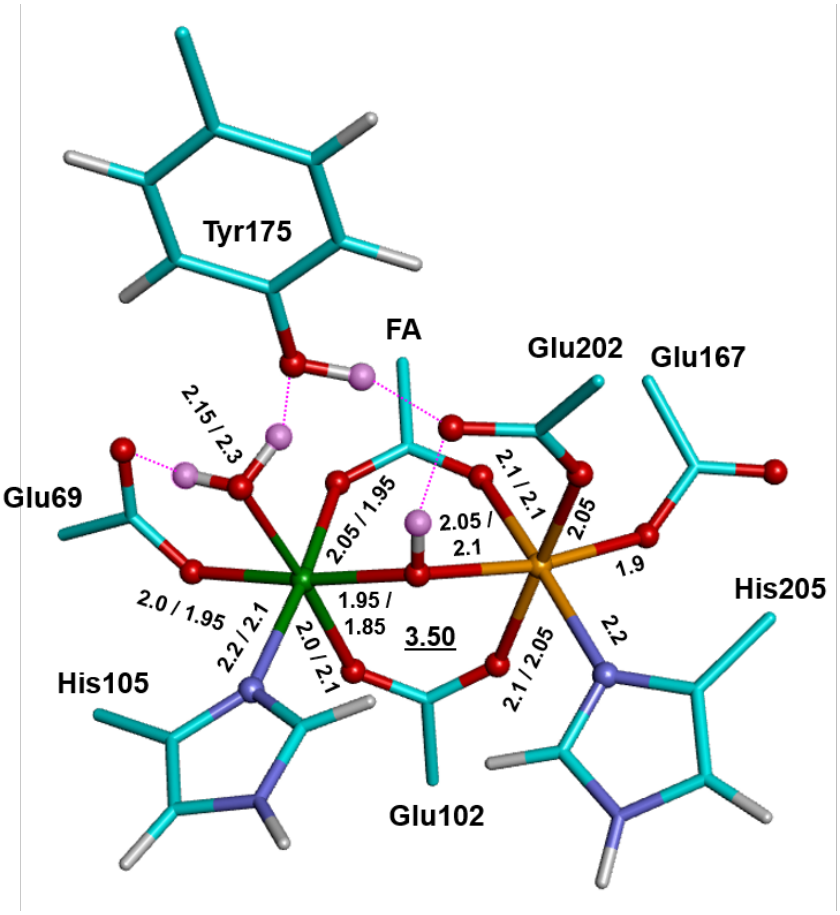

Figure 7-19: Refined model structures for Mn(III)Fe(III) and Fe(III)Fe(III) cofactors in R2lox. Bond lengths for FeFe / MnFe cofactors (from EXAFS and DFT) given in Å (rounded in the 2nd digit, the metal-metal distance is underlined), color code: green, Mn/Fe1; orange, Fe2; red, oxygen; blue, nitrogen; cyan, carbon; grey, hydrogen; magenta lines and shadings highlight protonation and hydrogen-bonding patterns suggested by the present study.

Rapid XPR is related to the highly oxidizing redox midpoint potential (E_m) of DMC sites, facilitating amino acid (tyrosine) oxidation by initially created Mn/Fe(IV) species.[16, 80, 203] This is highlighted by comparison to the Mn_4Ca complex of photosynthetic water oxidation, in which the reverse reaction occurs, Mn(IV) formation due to oxidation by a tyrosine radical ($E_m \approx 1.2$ eV).[51] For the FeFe cofactor, biphasic XPR suggested a Fe(III)Fe(III) → Fe(II)Fe(III) → Fe(II)Fe(II) reduction sequence. Reduction of the Fe1 and Fe2 sites according to their similar LUMO energies likely occurred at a similar E_m and was kinetically indistinguishable. This means that both iron ions were first reduced at equal probability to form the mixed-valence

cofactor with a lowered E_m, according to the following slower reduction to the $Fe(II)_2$ level. The apparent E_m drop suggests that mixed-valence state formation was not accompanied by protonation at the μOH group of the FeFe cofactor.[154] For the MnFe cofactor, similar XPR rates and LUMO energies of Mn1 and Fe2 implied that both sites have a comparable E_m. However, apparently monophasic reduction of both ions means that the two steps in the Mn(III)Fe(III) → Mn/Fe(II)Mn/Fe(III) → Mn(II)Fe(II) sequence were about equally fast. A significant E_m drop in the mixed-valence state thus did not occur, possibly due to μOH protonation. The mixed-valence states of the cofactors therefore may differ in proton affinity of the μOH group at least at cryogenic temperatures. Faster initial XPR further implies a more positive E_m of the Mn(III)Fe(III) cofactor. These results underpin the importance of protonation reactions in the redox chemistry at the dimetal cofactors.

The protonation state of metal ligands is difficult to assess by protein XRD.[23] While non-protein terminal and metal-bridging oxygen atoms have been resolved, respective protons remained invisible at 1.8 Å resolution or less of R2lox structures.[83, 84, 131, 232] We have compared our experimental X-ray spectroscopy data to calculations on model structures showing four conceivable protonation states of the MnFe and FeFe cofactors. This has revealed high sensitivity of ctv XAS, vtc XES, and NRVS spectra to cofactor protonation changes [35, 102, 129, 136] and consistently indicated a terminal water molecule at Mn/Fe1 and a metal-bridging hydroxide (μOH) in both cofactor types. This agrees with previous EPR data for the MnFe cofactor.[131, 232] The H_2O and μOH ligands are stabilized in a hydrogen-bonded network, with H_2O at Mn/Fe1 serving as H-bond donor to Tyr175 and Glu69, Glu202 as H-bond acceptor from Tyr175 and μOH, and H-bonding by Tyr175 tightening the Mn/Fe1-OH_2 bond. The H_2O and μOH ligands at the Mn/Fe(III) ions may correspond to the products of four-electron O_2 reduction and cleavage. However, a terminal oxygen at Mn/Fe1(II) is already observed in reduced R2lox, but not the bridging oxygen.[83, 84] The H-bonded network thus may guide at least one water product to the Mn/Fe(III) bridging position after Tyr-Val cross-link formation. Whether the latter process is equally efficient for both cofactors [83] or more efficient in MnFe R2lox,[213, 214] for example under (more O_2-limited) *in-vivo* conditions, remains to be clarified.

Electronic structure comparison of the two cofactors has revealed similar octahedral Fe2 ions with their z-axis directed along the Fe2-μOH bond and a more distorted Fe2 symmetry in the MnFe cofactor. Slight electronic structure differences at Fe2 were also reflected by minor variations in nuclear quadrupole splitting energies resolved by NFS, extending previous

Mössbauer data.[131, 232] The main difference between the two cofactors is the z-axis orientation along the Mn1-OH_2 bond in the MnFe, but along the Fe1-μOH bond in the FeFe cofactor. Accordingly, significant Jahn-Teller elongation of the (Glu102)O-Mn1(III)-OH_2 bonds and almost square-planar valence level degeneracy with the unoccupied Mn1-d(x^2-y^2) orbital at highest energy was found, compared to a near-octahedral Fe1(III) ion. Anti-ferromagnetic coupling of high-spin Mn/Fe1 and Fe2 ions was supported.[84, 131, 232] While the LUMO was Fe2-centered in the FeFe and more delocalized onto Mn1 in the MnFe cofactor, the HOMO largely resided on His205 at Fe2 in both cofactors. More delocalized unoccupied valence levels and significant spin polarization were found for the MnFe cofactor. These electronic structure differences may affect the catalytic performance of the cofactors.

Our site-selective NRVS experiments on ^{57}Fe-labeled R2lox have identified vibrational marker bands for the Fe2 site in the MnFe and Fe1/2 sites in the FeFe cofactor. The QM/MM calculations showed that in particular the high-frequency NRVS region reflects the water ligands and is sensitive to cofactor protonation, thereby supporting a H_2O/μOH state for both cofactors. Normal mode analysis further corroborated structural differences at the Fe2 site in the MnFe and FeFe cofactors, as imposed by the distorted Mn1 symmetry. Due to the Boltzmann population distribution, also modes above ~200 cm^{-1} (~25 meV) are expected to be (partially) excited at room temperature (kT ≈ 25 meV). Accordingly, besides low-frequency protein modes, the vibrations associated specifically with the H_2O and μOH groups may also contribute for example to guiding of O_2 cleavage products to their binding locations.

The R2lox cofactors were assembled *in-vitro* starting with divalent metal ions under aerobic conditions. Preferential Mn binding at site 1 was observed in XRD and previous spectroscopic studies [83, 84, 131, 232] and is confirmed here. Differential metalation of the two binding sites has been suggested to be due to facilitated Mn(II) binding at site 1 only in the presence of Fe(II) at site 2 and stabilization by subsequent metal oxidation by O_2.[131] Fewer available amino acid ligands compared to site 2 imply larger coordinative flexibility at site 1 and favor water binding at Mn(II), as found in reduced R2lox structures.[83, 84] Accommodation of a Mn(III) Jahn-Teller ion with its axis along the Mn-OH_2 bond thus is facilitated at site 1, whereas Mn(III) binding in site 2 would require larger amino acid rearrangements. Structural pre-adaptation of site 1 for Mn(III) binding thus may be an important thermodynamic (kinetic) factor for site-specific metalation in R2lox. O_2 reduction has been proposed to lead to Mn/Fe(IV)Fe(IV) species, which induce the Tyr162-Val72 cross-link by two-electron oxidation of the amino acids to form the Mn/Fe(III)Fe(III) cofactors.[84] Whether cross-link formation is an activation

reaction of the enzyme, an intermediate in actual catalysis, or related to binding of the redox-inert fatty acid instead of the (unknown) substrate is speculative. Elucidation of further high-valent cofactor species, which may be crucial in the O_2 and substrate chemistry of R2lox, is underway in our laboratories.

Conclusions

Besides the classical diiron site, the recently discovered group of dimetal-carboxylate cofactor proteins, called R2-like ligand-binding oxidase (R2lox), can contain a heterodinuclear manganese/iron cofactor. Both can be assembled *in-vitro* by aerobic reconstitution of the metal-free apo-protein with divalent metal ions. Although they are structurally related to the RNR class I proteins, R2lox proteins show a differing redox reaction pathway (1- versus 2-electron chemistry). To understand the site-specific metalation of R2lox proteins as well as their redox chemistry (O_2 reduction and cross-link formation in the protein scaffold), high-valent FeFe and MnFe cofactor sites of *Gk*R2lox were analyzed by advanced X-ray absorption, emission, and vibrational spectroscopy methods and quantum chemical calculations. The detailed study presented in this work provides the relative metal contents, X-ray photoreduction kinetics, metal oxidation states, metal site geometries and bond lengths, spin states, valence level degeneracies, molecular orbital compositions, nuclear quadrupole splitting energies, and vibrational dynamics for both cofactors. The protonation state of the cofactor in R2lox was determined (metal-bridging hydroxide (μOH) and terminal water ligand at site 1). The different orientation of the unique axis (z-axis along the Mn1-OH_2 bond in MnFe and along the Fe1-μOH bond in FeFe cofactor) provides an explanation for the more positive redox potential of the heterodinuclear cofactor and the higher proton affinity of the μOH group and thus relates the different metalation to the corresponding functionality. The results of this study were published in by Kositzki et al., *Inorg Chem* **2016**, 55, 9869–85 [123].

8 R2lox protein – effect of single-point mutations

Results reported in this chapter have been published in part in:
Y. Kutin, V. Srinivas, M. Fritz, R. Kositzki, H. S. Shafaat, J. Birrell, E. Bill, M. Haumann, W. Lubitz, M. Högbom, J. J. Griese, and N. Cox, **Divergent assembly mechanisms of the manganese/iron cofactors in R2lox and R2c proteins**, *J Inorg Biochem* **2016**, 162, 164-77 https://doi.org/10.1016/j.jinorgbio.2016.04.019 [131]

Parts of the results reported in this chapter are included in the following publications:
J. J. Griese, R. Kositzki, M. Haumann, and M. Högbom, **Assembly of a heterodinuclear Mn/Fe cofactor and formation of a tyrosine-valine ether cross-link are coupled in a R2-like ligand-binding oxidase**, to be published[4]
Y. Kutin, R. Kositzki, M. Haumann, N. Cox, M. Högbom, and J. J. Griese, **A single point mutation stabilizes an intermediate of the oxygen activation reaction of a heterodinuclear manganese/iron cofactor in a ligand-binding oxidase**, to be published[5]

8.1 Introduction

As shown in Chapter 7, the oxidized dinuclear metal cofactor of the wild-type (WT) R2lox protein from *Geobacillus kaustophilus* contains a single oxygen bridge (μ-hydroxo) and a long-chain fatty acid ligand which co-purifies with the protein and coordinates both metal ions [84]. So far, the physiological function of the R2lox protein is unknown [81]. Upon oxidation, R2lox catalyzes the formation of an ether cross-link between the Cβ of valine (V72) and the hydroxyl oxygen of tyrosine (Y162) in the vicinity of the active site in the protein scaffold (cf. Fig. 7-1 in Chapter 7). The protein can assemble both MnFe and FeFe cofactor sites, but not a dimanganese site. Further, site-specific metal loading with Mn in site 1 (N-terminal metal-binding site) and Fe in site 2 (C-terminal metal-binding site) in the mixed-metal cofactor was

[4] J. J. Griese, R. Kositzki, M. Haumann, and M. Högbom, **Assembly of a heterodinuclear Mn/Fe cofactor is coupled to tyrosine–valine ether cross-link formation in the R2-like ligand-binding oxidase**. *J Biol Inorg Chem* **2019**, 24, 211–21 (https://doi.org/10.1007/s00775-019-01639-4)

[5] Y. Kutin, R. Kositzki, R. M. M. Branca, V. Srinivas, D. Lundin, M. Haumann, M. Högbom, N. Cox, and J. J. Griese, **Chemical flexibility of heterobimetallic Mn/Fe cofactors: R2lox and R2c proteins**, *J Biol Chem* **2019**, 294(48), 18372-86. (https://doi.org/10.1074/jbc.RA119.010570)

observed. Both, MnFe and FeFe cofactors catalyze the cross-link formation [83, 131] but it was recently shown, that the reaction is more efficient in the heterodinuclear cofactor [81].

To clarify the role of amino acids around the cofactor and metal ligation in the O_2 activation and cross-link chemistry, several site-directed mutants of *Gk*R2lox containing either oxidized [FeFe] or [MnFe] sites were analyzed by XAS. In these single point mutants the fatty acid ligand and/or the cross-link are either present or absent (see Table 8.1). The XANES spectra at the Mn and Fe K-edges reveal oxidation states changes of the Mn and Fe ions for the R2lox variants. Analysis of the EXAFS spectra shows variations in metal-metal distances and metal-ligand bond lengths (first-sphere coordination). The well-known rapid X-ray photoreduction (XPR) of the metal centers (see Chapter 7) was monitored in time-resolved experiments at 20 K and this approach revealed different XPR kinetics for the mutant proteins. These results with respect to the presence and/or absence of cross-link formation and of the fatty acid ligand are related to potential functional aspects of the enzyme. To gather information how the single-point mutations affect the metal specificities of the variants, TXRF measurements on mutant variants of *Gk*R2lox were performed. The variants were produced by aerobic reconstitution with different amounts of Mn(II) and Fe(II) ions (Mn- and Fe titration series) and compared with the heterodinuclear cofactor assembly in R2c and R2lox under similar conditions.

Table 8.1 summarizes the characteristics of the R2lox variants with different mutations in the R2lox scaffold (see also Figure 8.1). The variants were analyzed in this work to determine their active site structure and metalation preference.

(i) Single-point mutations at the cross-link forming residues of R2lox, V72 and Y162. Both amino-acid residues are completely conserved in R2lox proteins but not in the R2 proteins of ribonucleotide reductase [96]. While in the variants **V72I**, **V72A**, and **Y162F** the cross-link formation does not occur, in **V72I-R2lox** the ether cross-link formation is observed [81].

(ii) Single-point mutations that block the binding of the fatty acid located in the ligand-binding tunnel of wild-type R2lox proteins. Both variants, **A171F** (this position is conserved as alanine in R2lox and in all groups of RNR R2 proteins as phenylalanine [96]) and **G68L** (this position is conserved as glycine in R2lox, in class Ib RNR this position contains leucine, and in the other R2 subclasses this position is not conserved [96]) prevent the binding of a fatty acid ligand at the active site and can create an R2c-like active site configuration with two instead of one oxo bridge between the metal ions. In **G68F-R2lox**, the ligand-binding tunnel is only blocked in the reduced state and harbors the bridging fatty acid ligand under aerobic reconstitution conditions.

(iii) Variant **E69D** is a single-point mutation in the first coordination sphere of the cofactor. The N-terminal carboxylate ligand to the metal in site 1 is conserved as glutamate in R2lox and R2c but as aspartate in R2 proteins. In *Gk*R2lox, this residue acts as hydrogen bonding partner to the water molecule bound to manganese in site 1 (see ref. [83] and Chapter 7). It is suggested from the crystal structure that in the E69D variant no enrichment of Mn in site 1 occurs in the oxidized resting state in contrast to WT.

(iv) Both, **Y175F** and **F109Y** are mutations in the R2lox protein scaffold. In R2lox proteins, phenylalanine Y175 forms a hydrogen bond with the water molecule bound to Mn at site 1 (see ref. [83] and Chapter 7). In RNR R2 proteins this position is conserved as tyrosine [96]. In **F109Y**, this position is conserved as tyrosine in standard R2 proteins (forming a tyrosyl radical during O_2 activation) and in R2lox and RNR class Ic it is phenylalanine [96].

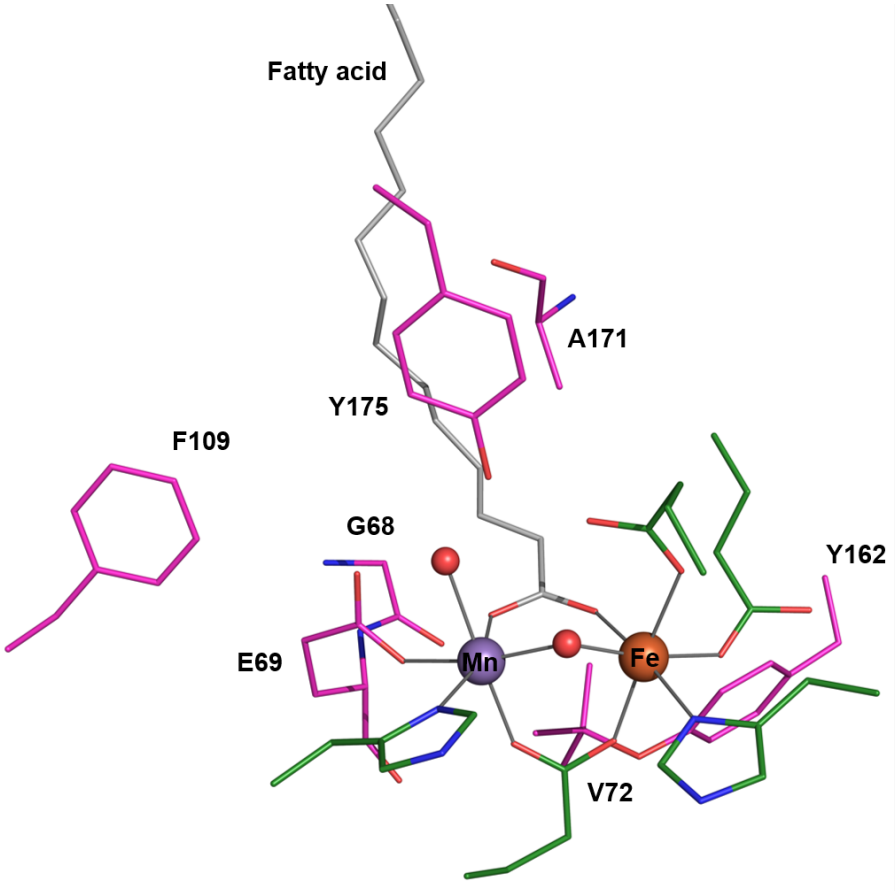

Figure 8-1: Positions of single-point mutations in the crystal structure of R2lox wild-type protein in the oxidized resting state (PDB entry 4HR0, ref. [84]). Color code: green, carbon atoms of wt-R2lox; magenta, carbon atoms of single-point mutation; red, oxygen atoms and blue, nitrogen atoms; grey, fatty acid ligand in wt-R2lox. Mn and Fe are shown as purple and orange spheres, respectively, and water/hydroxo ligands as red spheres.

Table 8-1: Characteristics of R2lox variants.

variant	mutation	function of mutated residue	cross-link formation	fatty acid ligand present
A171F[a]	alanine → phenylalanine	blocked ligand-binding pocket	yes	no
E69D[a]	glutamate → aspartate	N-terminal metal ligand (site 1)	very minor	yes
F109Y[b]	phenylalanine → tyrosine	residue in place of tyrosyl radical (in R2 proteins)	?	?
G68F[c]	glycine → phenylalanine	blocked ligand-binding tunnel only in reduced state	yes	yes
G68L[a]	glycine → leucine	blocked ligand-binding pocket	very minor	no
V72A[a] (PDB: 6F6C)	valine → alanine	cross-link residue prevents cross-link formation	no	yes
V72I[c] (PDB: 6F6F)	valine → isoleucine	cross-link residue cross-link formation	yes	yes
V72L[c] (PDB: 6F6H)	valine → leucine	cros-slink residue prevents cross-link formation	no	yes
Y162F[a]	tyrosine → phenylalanine	cross-link residue prevents cross-link formation	no	yes
Y175F[a]	tyrosine → phenylalanine	residue that might be involved in substrate reaction (tyrosyl radical intermediate)	+/-	yes

Information regarding the formation of the ether cross-link and the presence of the fatty acid ligand is accessible from crystal structures, except for F109Y (no crystal structure available).*
** data from Dr. Julia Griese (personal communication, published [81] and unpublished data)*
[a], XAS and TXRF titration, [b] only XAS and [c] only TXRF titration.

8.2 Sample preparation and characterization

8.2.1 Protein samples

The protein samples with single-point mutations were prepared by Dr. Julia Griese at Stockholm University, Sweden (presently at Uppsala University). The mutant variants of *Gk*R2loxI in metal-free form were produced and purified using the same protocol as for the wild-type R2lox (see Chapter 7 and ref. [84]). For the XAS experiments at the SLS and SOLEIL synchrotrons, two solution samples were prepared, which originated from different protein batches. The reconstitution protocol (see Chapter 7) was changed only slightly. Apo-protein of the point mutants was reconstituted aerobically with iron salt (molar ratios of protein monomer:Fe, for samples used at SOLEIL: 1:4, or at SLS: 1:3) to obtain the iron-only cofactor or with manganese and iron salts (molar ratios of protein monomer:Mn:Fe, SOLEIL: 1:2.4:1.2, SLS: 1:2:1) to reconstitute the Mn/Fe site, respectively. After removal of excess metal ions, the reconstituted proteins were concentrated to 1-3.5 mM and injected into Kapton-covered XAS sample holders (subsequently stored in liquid nitrogen until use at the synchrotron). For the TXRF titration series, the R2lox variants were aerobically reconstituted using different protein:Mn:Fe ratios. The final ratios of the Mn titration series are 1:2:2, 1:4:2, and 1:8:2 and of the Fe titration series 1:4:0.2, 1:4:0.6, and 1:4:1. Excess metal ions were removed and the samples concentrated to a protein concentration of ~ 0.4-0.9 mM (apo-protein: 0.7-1.4 mM) prior to the TRXF measurements. All samples were duplicated and in addition for E69D-R2lox, two sample preparations were made, which originated from different protein batches. The protein concentrations of the R2lox variants of the TRXF titration series were determined with a UV/VIS spectrometer using pre-defined extinction coefficients at 280 nm [232].

The preparation of the TRXF titration samples of R2c from *Saccharopolyspora erythraea* (*Se*) and R2lox from *Geobacillus kaustophilus* (*Gk*) was done by Dr. Julia Griese and is described in ref. [131]. The apo-proteins were titrated with Mn(II) and Fe(II) salts at different protein:Mn:Fe ratios under aerobic conditions. The protein concentrations were 0.10-0.14 mM (reconstituted samples) and ~1 mM (apo-protein samples) and 50% glycerol was added to these samples prior to storage in liquid nitrogen.

8.2.2 X-ray spectroscopy and metal content quantification

XAS experiments at the Mn and Fe K-edges were carried out at SuperXAS beamline of SLS (Villigen, Switzerland), at Samba beamline of SOLEIL (Paris, France), and at beamline KMC-

3 at BESSY (Helmholtz Center Berlin, Germany) in fluorescence detection mode using standard setups as previously described (Si[111] or Si[220] double-crystal monochromator, energy-resolving 5-element silicon-drift or energy-resolving Ge detector (13- or 36-element), liquid-helium cryostat for holding the samples at 20 K) [83, 123]. XANES and EXAFS spectra were collected with scan durations of about 2-15 min (BESSY, 30 min). For improving the signal-to-noise ratio up to 20 scans on separate sample spots were averaged and appropriate beam attenuation by Al filters was used to avoid X-ray photoreduction. XAS data evaluation and processing was performed as described in the previous chapters.

The iron and manganese contents (for XAS and TRXF titration series) were quantified by TXRF analysis (PicoFox spectrometer, Bruker) using a standard routine (see Chapter 7) i.e. a gallium metal standard was mixed with the protein sample (v/v 1:1 or 9:1) prior to the measurements. For practical reasons, the samples from SLS measurements were previously diluted 1:3 with deionized (Milli-Q) water. Four to eight TRXF measurements an each sample were conducted.

8.3 Formation of alternative cofactor species in *Gk*R2lox mutants

8.3.1 Metal contents

The determined metal concentrations of all analyzed single-point mutant variants of *Gk*R2lox protein, previously used in the XAS experiments, are shown in Figure 8-2 (values are summarized in Table A8-1, given in the Appendix). All iron-only reconstituted proteins contain almost no manganese and about 2.5-3.0 iron ions per protein monomer. This means that the iron content is slightly over-stoichiometric, suggesting quantitative loading with the FeFe cofactor. Most Mn/Fe-reconstituted proteins contain about one Fe and 0.5-0.9 Mn per protein on average. Overall, the metal content is slightly sub-stoichiometric and the Mn/Fe ratio is in the range of 0.5-0.8. However, the significantly higher ratio for the mutant **G68L** relative to the wild-type protein (WT) is presumably due to increased Mn and decreased Fe binding, which also suggests incorporation of manganese in site 2 of the cofactor in G68L-R2lox.

In **E69D** and **F109Y**, only a low amount of manganese was present (~0.2-0.3 Mn/protein), consequently suggesting relative small amounts of MnFe sites. Notably, the absolute Mn concentrations in the samples E69D (both batches) and F109Y were relatively low (~0.5 mM), which was problematic for measuring of Mn EXAFS spectra. There is no significant difference

in the metal contents between the two sample preparations used for XAS measurements at the SOLEIL and SLS. The concentration of other transition metals such as Co, Ni, Cu, and Zn were also determined and found to be negligibly small.

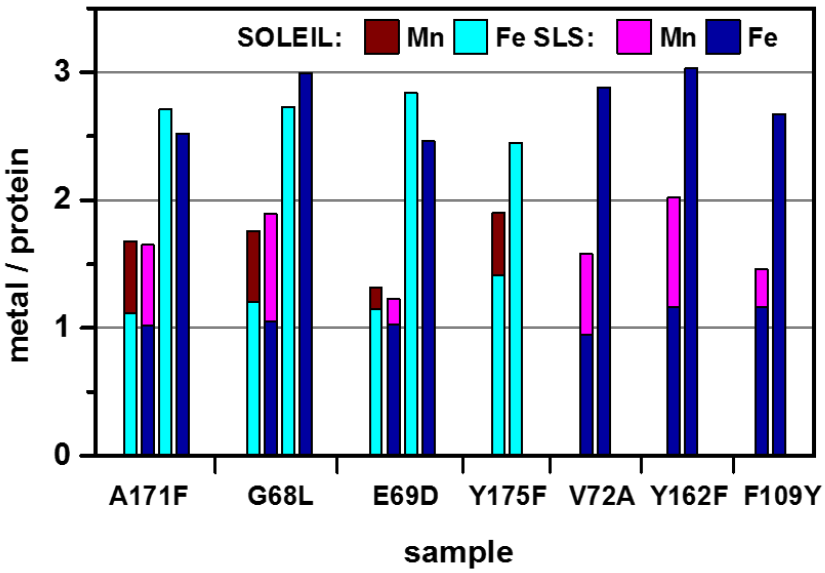

Figure 8-2: Mn and Fe contents of R2lox variants after aerobic reconstitution with Mn/Fe or only Fe in solution, from TXRF (Table A8-1, given in the Appendix). Shown is the average of six measurements on each variant. The error is ≤0.1 metals/protein. The amounts of other transition metals (Co, Ni, Zn and Cu) were also determined and were negligible in all variants.

8.3.2 Metal oxidation state and X-ray photoreduction

X-ray absorption near edge spectroscopy (XANES) was carried out on the R2lox variants to determine the metal oxidation state and compare it with the wild-type protein. XANES spectra at the Fe K-edge of the FeFe proteins and at the Mn K-edge of the MnFe proteins are shown in Fig. 8-3. Almost identical XANES spectra were obtained for the two preparation batches of the mutant variants A171F, E69D and G68L as well as for WT, measured at different beamlines. The initial Fe and Mn edge energies (at 50% level of the normalized XANES) are summarized in Table 8-2.

Comparison of the Fe XANES spectra of WT and the mutant variants reveals generally similar Fe K-edge shapes and energies, suggesting an overall similar near-octahedral coordination of the metal sites (Figure 8-3B). The initial Fe K-edge energies (Table 8-2) correspond approximately to the Fe(III) level (~7124.4 eV, see for example refs. [123, 141, 269]),

indicating that ferric iron is the dominant species in all samples. However, edge energies slightly (0.3-0.5 eV) above the Fe(III) level suggested a small fraction of Fe(IV) in some samples. It is concluded that the iron-only reconstitution with O_2 leads to mainly Fe(III)Fe(III) cofactors irrespective of the amino acid exchanges, similar to previous results on wild-type R2lox [83, 123].

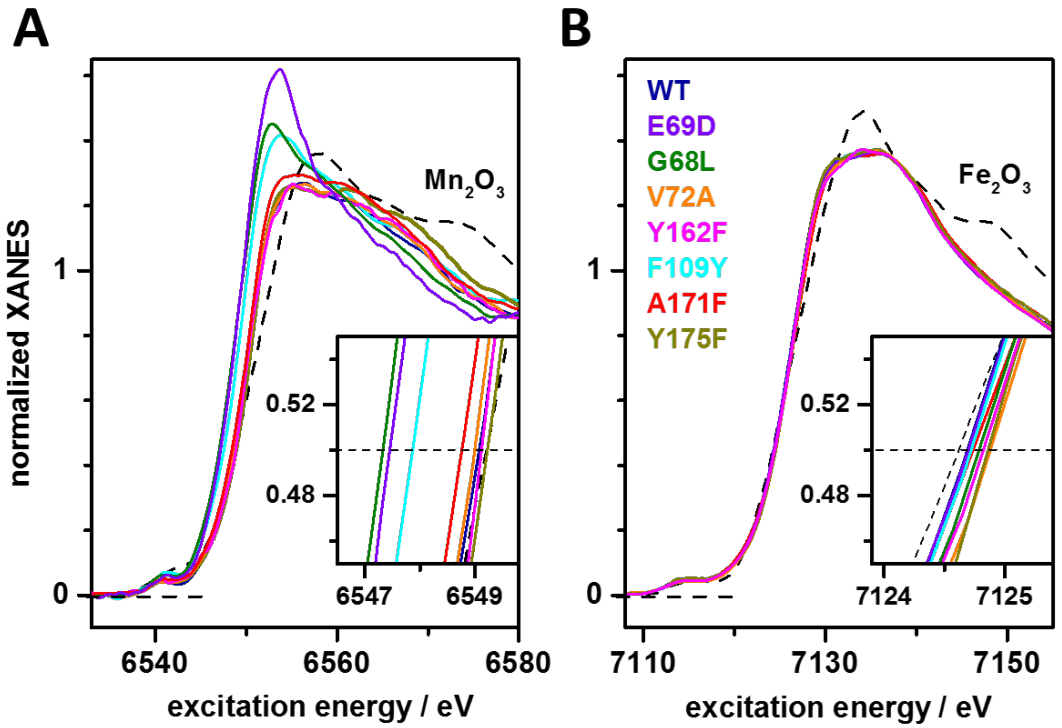

*Figure 8-3: XANES spectra of R2lox variants. (**A**) Mn K-edge spectra of Mn/Fe-reconstituted variants and (**B**) Fe K-edge spectra of Fe-only reconstituted variants. Spectra correspond to first scans on each sample spot reflecting the initial metal oxidation state. The color code is the same for the Fe-only and Mn/Fe-reconstituted samples. The spectra of solid Mn(III) and Fe(III) oxides are shown for comparison as black dashed lines.*

The Mn XANES spectra of the Mn/Fe-reconstituted samples reveal more pronounced differences (Figure 8-3A). The Mn K-edge energies of most mutant variants were close to the Mn(III) level (~6549.5 eV) [123, 141]. This finding as well as similar edge shapes compared to WT, suggests that mainly near-octahedral Mn(III) is present in the preferential cofactor species. Taking the results of metal content quantification into account and assuming that all manganese is bound in heteronuclear clusters implies that most samples contain at least 65% Mn(III)Fe(III) and not more than 35% Fe(III)Fe(III) cofactor sites, consistent with previous results for Mn/Fe-reconstituted WT [123]. However, significantly lower (by ~1.2-1.8 eV) Mn edge energies were found for **G68L**, **F109Y,** and **E69D** (Table 8-2). For G68L, the lower K-edge energy, larger edge maximum, and increased pre-edge feature suggests predominantly Mn(II) sites and thus

only a minor fraction (~20%) of Mn(III) ions in less symmetric sites. This indicates that the aerobically Mn/Fe-reconstituted **G68L** mutant also contains ~30% Mn(II)Mn(II) cofactors in addition to trivalent sites (~50% Fe(III)Fe(III) and ~20% Mn(III)Fe(III)). The variant **E69D** shows an altered edge shape and also a K-edge energy close to the Mn(II) level (~6546.7 eV) [48, 83]. This is in accordance with single-occupied Mn-sites of octahedral geometry being present in the solution sample in addition to the dominating diiron sites.

Table 8-2: Initial Fe and Mn K-edge energies.

	E (Mn-edge)* [eV]	E (Fe-edge)* [eV]
sample	MnFe	FeFe
WT	6549.1 / 6549.1	7124.7 / 7124.5
A171F	6548.8 / 6548.9	7124.7 / 7124.6
E69D	6547.5[#] / 6547.2	7124.7 / 7124.6
G68L	6547.3 / 6547.3	7124.8 / 7124.8
V72A	6549.0	7124.9
Y162F	6549.1	7124.8
F109Y	6547.9[#]	7124.7
Y175F	6549.2	7124.9

Initial Mn and Fe edge energies (± 0.1 eV) were derived at 50% level of the normalized XANES spectra in Fig. 8-3.
** Two values represent the edge energies for two preparation batches (measured at the beamlines of SLS and SOLEIL). [#] measured at the beamline of BESSY*

For the cross-link mutations (**V72A** and **Y162F**) very similar Mn and Fe K-edge shapes and almost identical K-edge energies were found in comparison to the WT, suggesting a conserved, near-octahedral metal coordination and the near-quantitative presence of Mn(III) and Fe(III) in these samples. The crystal structures of these variants are overall quite similar to the WT in the oxidized resting state (crystal structure data from Dr. Julia Griese, partly published [81], personal communication).

As previously shown, X-ray photoreduction (XRP) is an important issue for the dimetal cofactor in R2lox. Figure 8-4 shows changes in the Mn and Fe K-edge spectra caused by extended X-ray exposure (measured at the SOLEIL beamline). The respective K-edges shift to lower

energies (dashed lines) are due to the reduction of Mn(III) to Mn(II) and Fe(III) to Fe(II). XPR of Mn was about two-times faster than that of Fe. At both beamlines X-ray photoreduction of Fe ions in FeFe samples and Mn ions in MnFe samples was relatively rapid.

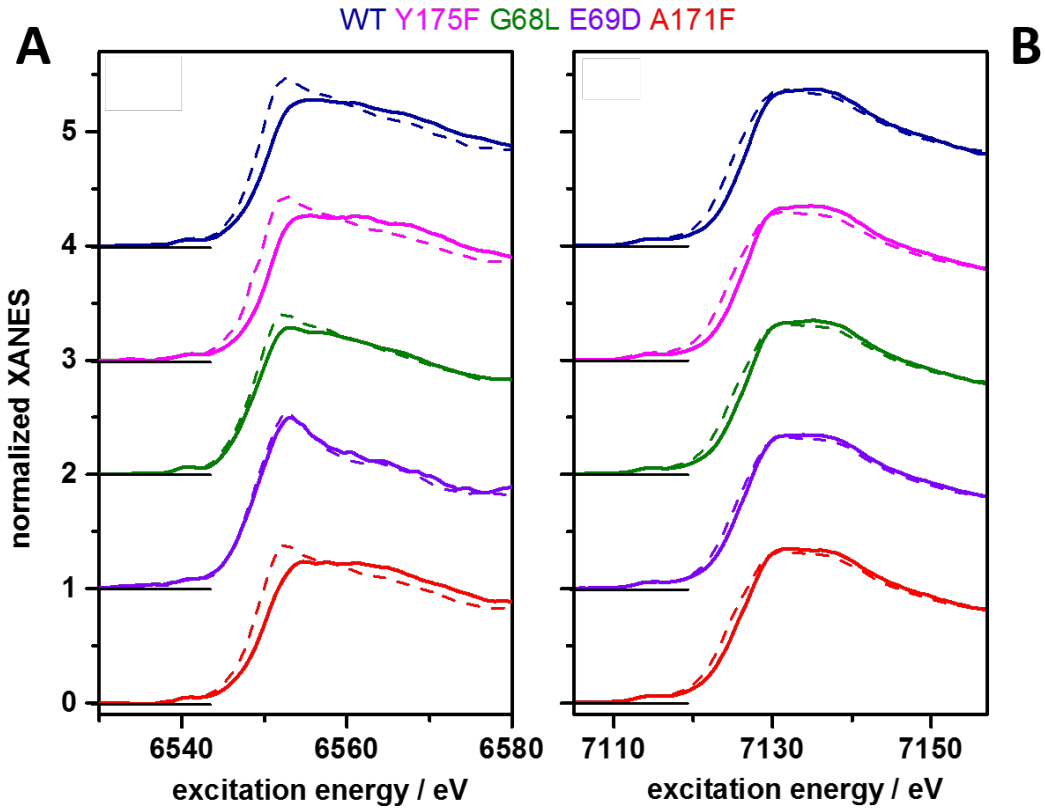

*Figure 8-4: XANES spectra of oxidized (initial spectra, solid lines) and X-ray photoreduced (after ~1h of X-ray exposure, dashed lines) proteins, measured at the SOLEIL beamline. (**A**) Mn K-edge spectra of Mn/Fe-reconstituted samples, (**B**) Fe K-edge spectra of Fe-only reconstituted samples.*

To quantify the X-ray induced photoreduction of the metal ions, successive monochromator scans on the same sample spot were performed. Different rates of XPR kinetics were obtained for the variants. In the following, the X-ray photoreduction kinetics (at 20 K) of the mutants **A171F** and **G68F** are compared to the WT (Fig. 8-5). For **G68L**, the much smaller Mn K-edge shift along with initially lower edge energy confirms the XANES results that only ~20% Mn(III) ions are present in the initial sample. The single-exponential fit reveals a slightly (~1.2-fold) slower reduction of Mn(III) and Fe(III) compared to WT, which presumably implies a slightly less positive redox potential for the trivalent cofactor sites. In contrast, the reduction of the metal(III) ions appears biphasic for **A171F**, i.e. it can better be described by a double-exponential fit, indicating the presence of a slow and a fast phase. The rate of the slower phase is similar to WT, whereas the rate of the faster phase is about 3-fold (Mn) or 2-fold (Fe) larger.

This biphasic reduction behavior indicates the presence of two different cofactor species in **A171F**, one of which is similar to the dominant species in the wild-type protein.

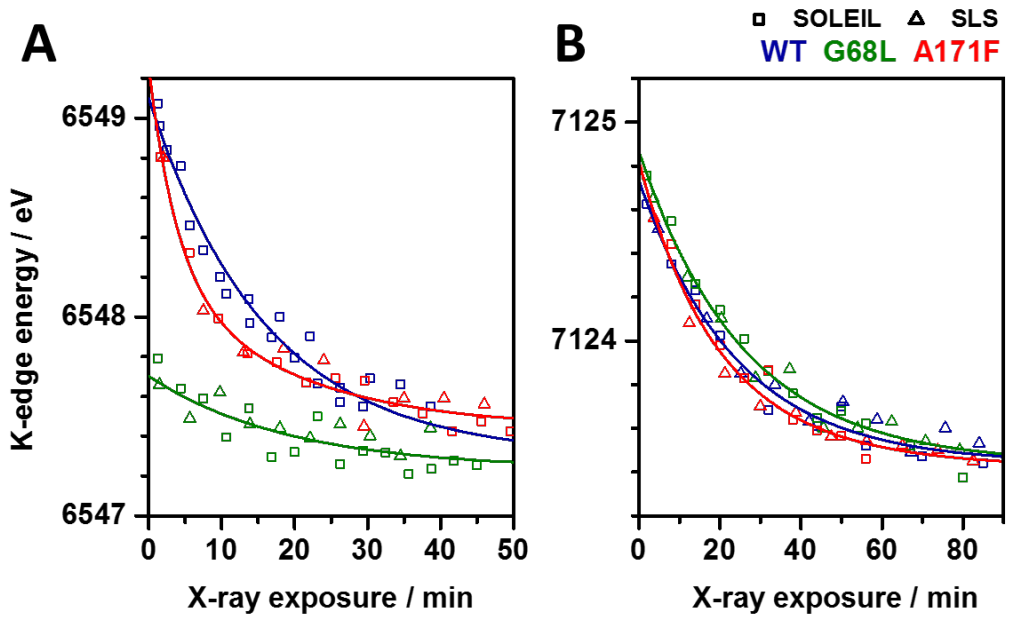

*Figure 8-5: XPR analysis of (**A**) Mn/Fe-reconstituted and (**B**) Fe-only reconstituted R2lox variants (shown are the experimental data for two preparations of each variant; squares and triangles, experimental data at SOLEIL and SLS, respectively). K-edge shifts due to X-ray photoreduction at 20 K with fit curves for merged data sets (time axes for data collected at Soleil were expanded by a factor of 1.2 vs. data collected at SLS for comparison).*

8.3.3 EXAFS analysis and metal cofactor structures

The results of the TXRF, XANES, and XPR analyses imply alternative cofactor species for the variants A171F and G68L that differ from the dominant species in the wild-type R2lox. The fatty acid (FA) ligand is absent in A171F and G68L, as shown by XRD. In WT, the FA ligand connects the two metal ions by a carboxylate bridge. How does the lack of this ligand affect the structure of the cofactor site? Extended X-ray absorption fine structure (EXAFS) analysis revealed metal-ligand bond lengths and metal-metal distances, providing a basis for cofactor structure analysis complementary to XRD data at lower inter-atomic distance-resolution.

In the following, the EXAFS data of **A171F** and **G68F** are compared to the WT (Figure 8-6, Table 8-3) and finally, possible cofactor structures of the mutants are derived (Figure 8-7). At first glance, the spectra reveal differences in the first-sphere metal coordination and metal-metal

distances, especially for the Mn/Fe reconstituted proteins. While the first FT peaks of the EXAFS spectra are roughly similar, the FT peaks due to metal-metal distances are altered, indicating changes in the metal-bridging mode. All EXAFS simulations involved for the first-sphere metal-coordination short metal-O bond(s), reflecting bridging oxygen motif(s) (~1.87-1.95 Å), longer metal-O/N bonds (~2.03-2.14 Å) as well as one particularly long (~2.24-2.62 Å) metal-O/N bond from the carboxylate, histidine, or terminal water ligands. Also a Fe-C distance (~2.88-3.09 Å) was included in the simulations, which presumably stems from C-atoms of carboxylate and histidine groups in the 2nd coordination sphere.

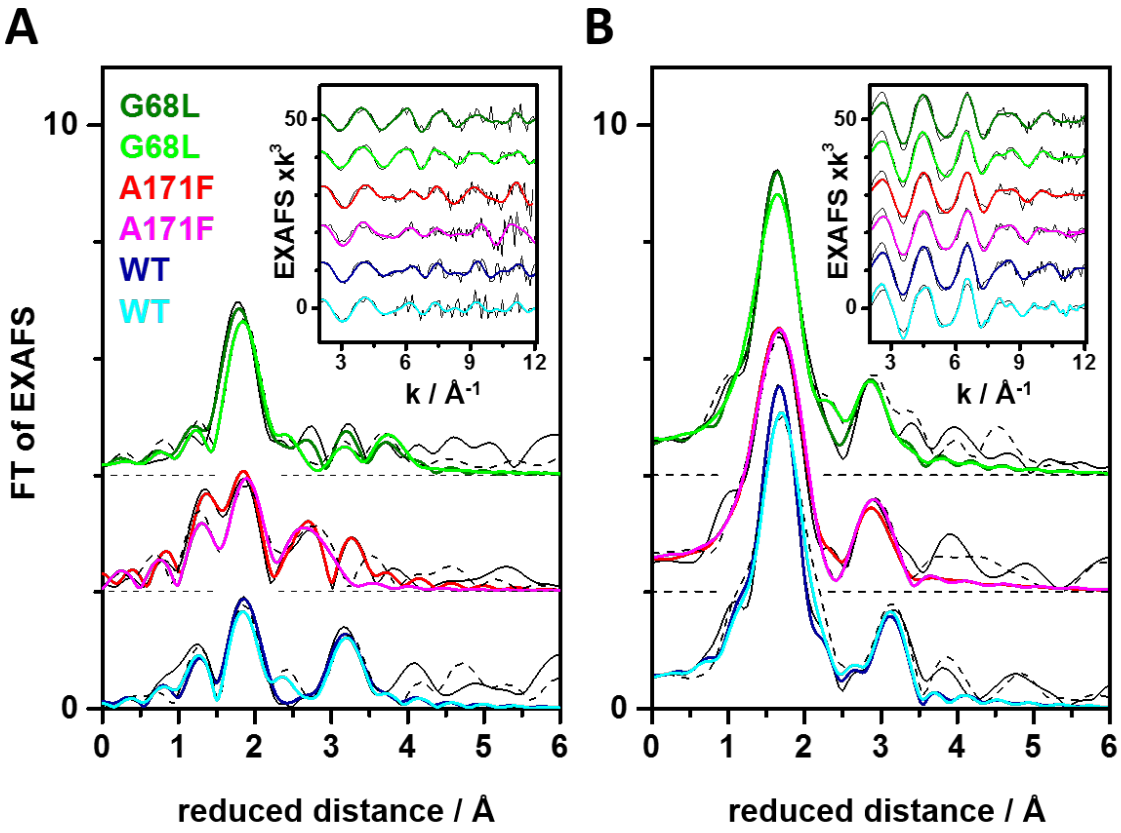

*Figure 8-6: EXAFS analysis of G68F- and A171F-R2lox in comparison to wild-type R2lox (FT and k-space spectra are vertically shifted for comparison). Shown are the data for two preparations of each variant (black lines, experimental data; colored lines, fit curves with parameters in Table 8-3). (**A**) Mn data of Mn/Fe-reconstituted and (**B**) Fe data of Fe-only reconstituted samples. Fourier transform (FTs) were calculated from a k-range of 3.8-12.3 Å^{-1} (cos-windows over 10% of both k-range ends) to emphasize metal-metal distances. The insets show the EXAFS oscillations.*

Table 8-3: EXAFS simulation parameters.[a]

variant	Fe/Mn-C/N/O	Fe/Mn-Fe/Mn	R_F
	N [per metal] / R [Å] / $2\sigma^2$ x10^3 [Å^2]		[%]
WT Fe/Fe (Fe)	0.9[&] / 1.88 / 11[#] 4.1[&] / 2.03 / 11[#] 1.0[*] / 2.53 / 5[*] 1.2 / 2.94 / 5[*]	0.3[§] / 3.03 / 5[*] 0.7[§] / 3.48 / 5[*]	11.6
	1.4[&] / 1.90 / 10[#] 3.6[&] / 2.04 / 10[#] 1.0[*] / 2.52 / 5[*] 1.1 / 2.96 / 5[*]	0.2[§] / 3.02 / 5[*] 0.8[§] / 3.47 / 5[*]	14.5
G68L Fe/Fe (Fe)	1.9[&] / 1.95 / 10[#] 3.1[&] / 2.05 / 10[#] 1.0[*] / 2.54 / 5[*] 1.2 / 2.88 / 5[*]	0.7[§] / 3.01 / 5[*] 0.3[§] / 3.46 / 5[*]	11.9
	2.2[&] / 1.93 / 7[#] 2.8[&] / 2.07 / 7[#] 1.0[*] / 2.59 / 5[*] 1.4 / 2.90 / 5[*]	0.8[§] / 3.03 / 5[*] 0.2[§] / 3.47 / 5[*]	13.8
A171F Fe/Fe (Fe)	2.1[&] / 1.93 / 4[#] 2.9[&] / 2.07 / 4[#] 1.0[*] / 2.55 / 5[*] 1.2 / 2.89 / 5[*]	0.6[§] / 3.01 / 5[*] 0.4[§] / 3.44 / 5[*]	13.5
	2.4[&] / 1.95 / 3[#] 2.6[&] / 2.06 / 3[#] 1.0[*] / 2.51 / 5[*] 1.4 / 2.92 / 5[*]	0.6[§] / 3.03 / 5[*] 0.4[§] / 3.43 / 5[*]	10.5
WT Mn/Fe (Mn)	1.3[&] / 1.87 / 12[#] 3.7[&] / 2.12 / 12[#] 1.0[*] / 2.43 / 5[*] 1.1 / 3.05 / 5[*]	0.1[§] / 3.24 / 5[*] 0.9[§] / 3.52 / 5[*]	18.6
	1.6[&] / 1.88 / 11[#] 3.4[&] / 2.10 / 11[#] 1.0[*] / 2.37 / 5[*] 1.5 / 3.09 / 5[*]	0.1[§] / 3.28 / 5[*] 0.9[§] / 3.53 / 5[*]	16.2
G68L Mn/Fe (Mn)	0.7[&] / 1.89 / 12[#] 4.3[&] / 2.12 / 12[#] 1.0[*] / 2.59 / 5* 1.5 / 3.03 / 5*	0.5[§] / 4.11 / 5[*] 0.5[§] / 3.55 / 5[*]	15.1
	1.1[&] / 1.91 / 11[#] 3.9[&] / 2.14 / 11[#] 1.0[*] / 2.62 / 5[*] 1.2 / 3.07 / 5[*]	0.7[§] / 4.06 / 5[*] 0.3[§] / 3.53 / 5[*]	13.6
A171F Mn/Fe (Mn)	2.2[&] / 1.87 / 12[#] 2.8[&] / 2.14 / 12[#] 1.0[*] / 2.24 / 5* 1.2 / 3.06 / 5*	0.6[§] / 2.99 / 5[*] 0.4[§] / 3.52 / 5[*]	14.9
	1.8[&] / 1.89 / 9[#] 3.2[&] / 2.12 / 9[#] 1.0[*] / 2.31 / 5[*] 1.4 / 2.97 / 5[*]	0.7[§] / 3.04 / 5[*] 0.3[§] / 3.47 / 5[*]	18.6

[a]Data correspond to spectra in Figure 8-6 of two preparations of each GkR2lox variant. Used abbreviations: N, coordination number; R, interatomic distance; $2\sigma^2$, Debye-Waller factor; R_F, fit error sum calculated for reduced distances of 1-3.5 Å. Fit restraints: [*]fixed parameters, [#]coupled to yield the same $2\sigma^2$ value, [&]coupled to yield a (coordination number) sum of 5, [§]coupled to yield a (coordination number) sum of 1.

As shown in Chapter 7 for WT, similar structures for the Mn(III)/Fe(III) and Fe(III)/Fe(III) cofactors were derived from the EXAFS analysis, including a metal-metal distance of ~3.5 Å, a single μOH bridge between the metal ions, a terminal water molecule at the metal ion in site 1 and a metal-bridging carboxylate ligand provided by the fatty acid.

The Fe EXAFS of **G68L** and **A171F** show increased numbers of short iron-ligand bonds at the expense of longer metal-ligand bonds compared to WT. This significant increase suggests an increase in the number of iron-bridging oxide species. Furthermore, in the absence of the fatty acid, a ~0.5 Å shorter Fe-Fe distance (~3.05 Å) becomes more prominent, especially in G68L-R2lox (Figure 8-8). This short metal-metal distance is also found in the Mn/Fe(III)/Fe(III) cofactors in *Chlamydia trachomatis* (*Ct*) R2c and *Mus musculus* (*Mm*, mouse) R2a proteins [141, 237], where the trivalent metal ions are linked by two oxygen bridges (μ-oxo and μ-hydroxo). This indicates that in the absence of the FA ligand an R2a/c-like μO, μOH-bridged Fe(III)/Fe(III) cofactor is preferably formed instead of the wild-type cofactor with a single μOH bridge (Figure 8-7).

The Mn EXAFS of **A171F** reveals two Mn/Fe-Fe distances of ~3.0 Å and ~3.5 Å. While the longer distance is related to the metal-metal distance in wt-R2lox, the dominating (~60% on average) shorter distance is similar to the main Fe(III)-Fe(III) distance in **G68L** (Figure 8-8). Consequently, these distances can be assigned to a cofactor with a single μOH bridge (wild-type) and to a μO,μOH bridged dimetal site in the mutant. The latter species represents the main cofactor in both Mn/Fe and Fe-only reconstituted A171F-R2lox. However, the dominant cofactor species in Mn/Fe-reconstituted **G68L** contains overall ~0.1 Å longer manganese-ligand bonds, which are typical for Mn(II) and a dominant long metal-metal distance (~4.1 Å). This large distance is similar to the distance in metal(II) cofactors in R2 proteins, which lack bridging oxides but hold a single carboxylate bridge (Figure 8-8) [269]. This distance together with the XANES results imply that in Mn/Fe G68L-R2lox the dominant species is a $Mn(II)_2$ cofactor lacking μO/μOH bridging motifs (Figure 8-7).

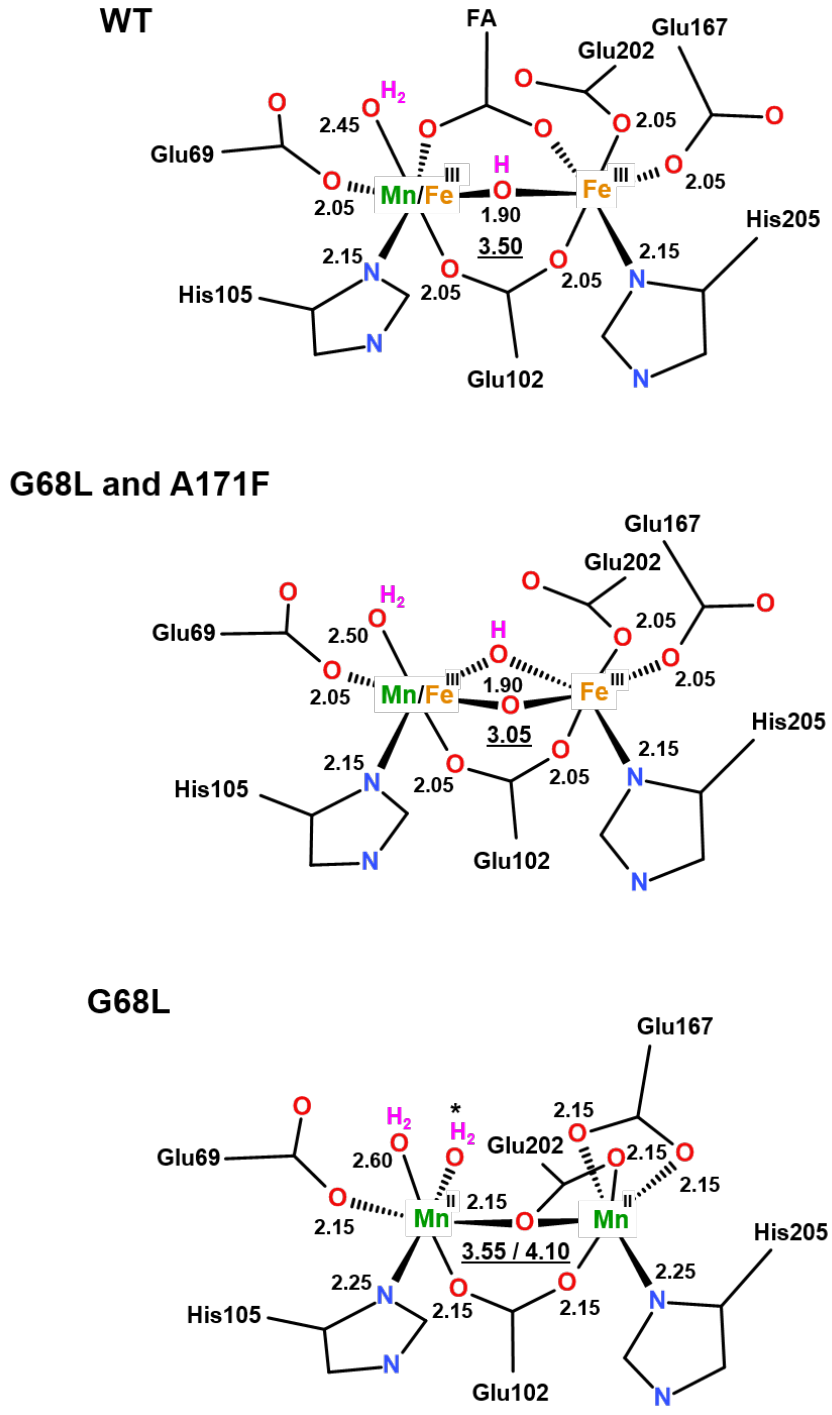

Figure 8-7: Cofactor structures in R2lox mutants combining crystallographic and XAS results. Shown are the mean bond lengths (in Å, the metal-metal distance is underlined) for Mn/Fe and Fe/Fe species as well as ligand protonation and metal redox state assignments. FA denotes the ligand modeled as a fatty acid in crystal structures. In the Mn(II)Mn(II) structure of G68L-R2lox (bottom), the water molecule marked by an asterisk was not observed in the crystal structure, but is suggested by the XAS data; a ~3.55 Å Mn-Mn distance may result from the semi-bridging carboxylate of E202 observed in crystals whereas E202 in a non-bridging position may result in the ~4.1 Å distance prevailing in the EXAFS of solution samples.

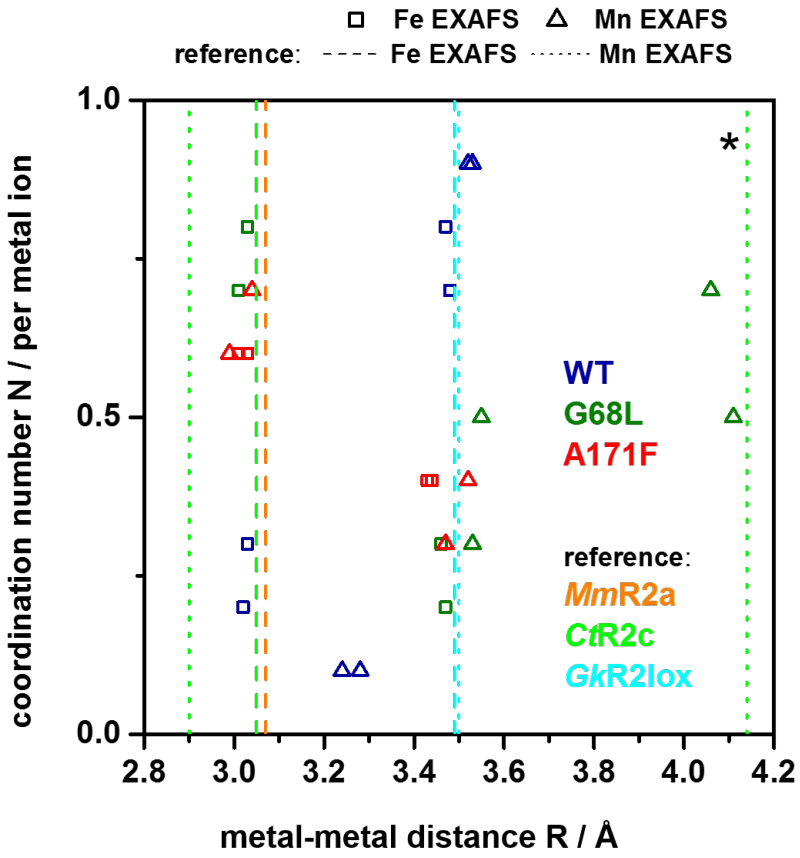

*Figure 8-8: Metal-metal distance versus coordination number in wild-type R2lox (blue) and the two mutant variants (G68L, green and A171F, red) from EXAFS analysis. Data correspond to parameters in Table 8-3. Squares, data from Fe-EXAFS, triangles, data from Mn-EXAFS. Vertical dashed and dotted lines mark main distances from Fe- and Mn-EXAFS analysis of two R2 proteins (class Ia and Ic) as well as previous R2lox analysis, respectively, see refs. [123, 141, 237, 269]. *Data correspond to reduced R2c protein.*

In summary, the exchange of the glycine residue by a leucine (**G68L**) leads to a manganese/iron cofactor of [MnFe] type and prevents fatty acid binding so that a R2c-like structure is formed. However, the dominant species is an inactive Mn(II)Mn(II) cofactor. In the variant **A171F**, in which also the binding of the fatty acid is prevented, a cofactor species different from wild-type R2lox is observed in the Mn/Fe-reconstituted as well as in iron-only reconstituted A171F-R2lox. In most R2lox variants the formation of trivalent dimetal sites is observed independently of the ether cross-link formation during the aerobic reconstitution.

8.4 Assembly mechanism of the heterodimeric Mn/Fe cofactor: Results from TXRF titration series

TXRF measurements were performed on different aerobic Mn/Fe-reconstituted (i.e. different protein:Mn:Fe ratios) R2lox and R2c samples as well as on nine R2lox mutant variants to compare the cofactor metal loading. This approach was intended to gain information on the heterometallic cofactor assembly in solution, i.e. under more physiological conditions compared to crystals.

8.4.1 Cofactor Assembly in R2lox versus R2c

Figure 8-9 illustrates the results of the metal content quantification of different Mn/Fe-reconstituted (Mn and Fe titration series) *Gk*R2lox and *Se*R2c samples as well as apo-protein preparations (results are also summarized in Table A8-2, given in the Appendix). The TXRF data show that the apo-protein preparations contain no manganese and small amounts (0.02-0.26) of iron per protein, suggesting up to 10% FeFe cofactor sites, depending on the used batch. The analysis of the Mn/Fe-reconstituted samples reveals that R2c generally binds more manganese than R2lox and can achieve nearly complete metalation. Assuming that all metals are bound in a dinuclear cluster and preferring the formation of heterometallic sites, a higher fraction of MnFe cofactor sites is assembled in R2c compared to R2lox under the same conditions (similar ratio of protein:Mn:Fe). Furthermore, when manganese is in excess and iron is substoichiometric (Fe titration), besides the preferred formation of heterodimer cofactor sites also homodimeric di-manganese sites are assembled in R2c, whereas in R2lox only diiron sites are formed. These findings confirm also previous results that no manganese-manganese sites are formed in R2lox [83]. Under these conditions, up to 0.6 Mn per protein can be accumulated in R2lox and even the highest relative amount of MnFe sites can be achieved, but also a significant fraction of apo-R2lox remains, i.e. uncomplete metalation occurs. However, when the iron amount is > 1 (Mn titration), more FeFe than MnFe clusters are formed in R2lox as opposed to R2c. It can be concluded, that excess Mn promotes heterometallic cofactor assembly in both proteins, but only in R2lox substoichiometric iron conditions are necessary. Additionally, the TXRF data shows, that the achievable hetero-binuclear assembly in R2lox depends also on the initial amount of iron in the used apo-protein batch (cf. Fe titration I and II in Figure 8-9, see also Figure 8-10). A higher initial iron content leads to a higher fraction of diiron sites.

The results of the TXRF measurements are in agreement with previous findings from other experiments (EPR, Mössbauer, XAD (X-ray anomalous dispersion) [131]). R2c from *Saccharopolyspora erythraea* and R2lox from *Geobacillus kaustophilus* assembled a heterobimetallic cofactor and are structurally similar, but perform chemically divergent oxidative reactions (one- or two-electron oxidation reaction) [131]. The comparison of the TRXF results suggests for both proteins different metalation processes or rather cofactor assembly mechanisms.

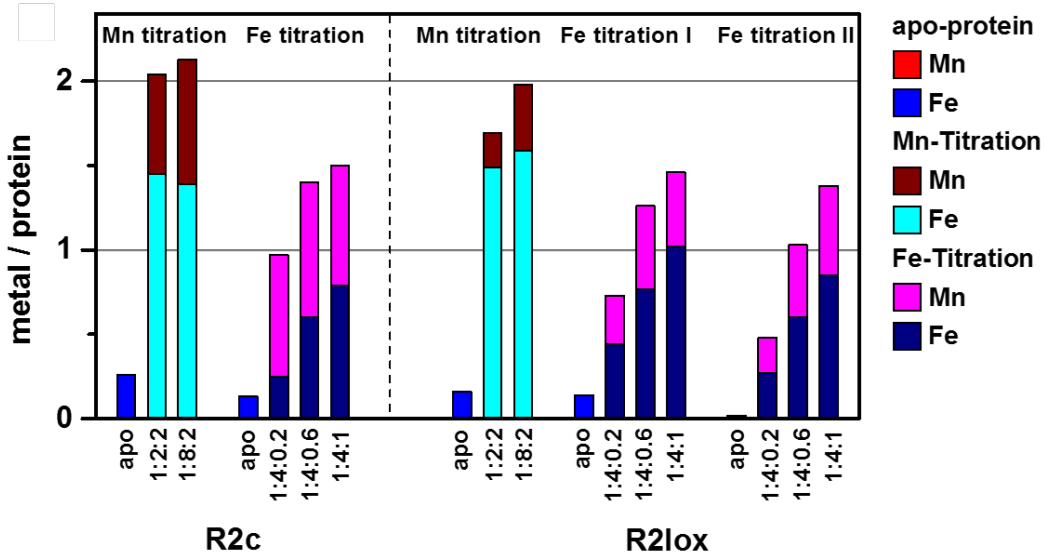

Figure 8-9: Mn and Fe contents of different aerobically reconstituted R2c and R2lox in solution as well as apo-protein batches, determined by TXRF (Table A8-2, given in the Appendix). Shown is the average of 4-8 measurements on each sample. The error is ≤0.1 metals/protein. The amounts of other transition metals (Co, Ni, Zn and Cu) were also determined and were negligible in all samples.

In summary, in R2c Mn(II) ions bind in both sites. Because the achieved dimanganese cofactor cannot be activated by O_2 [131] subsequent exchange of Mn(II) by Fe(II) at one cofactor site and activation by molecular oxygen lead to heterodinuclear cofactor assembly (see Figure B-8). Due to this assembly mechanism, no catalytic active protein with a diiron cofactor will be formed. In R2lox, the binding of Mn(II) ions initiates the cofactor assembly. The different metal-binding preferences lead to site-specific metal loading with Mn in site 1 in the mixed-metal cofactor in R2lox. It can be concluded that the metal selectivity in R2c exists prior to the oxygen activation [131] while in R2lox the specific metal loading occurs only upon O_2 activation. This is supported by TRXF results of anaerobically reconstituted R2lox samples (see Table A8-3, given in the Appendix) showing that the binding of both iron and manganese was highly sub-stoichiometric in the absence of molecular oxygen.[83] As mentioned above, the

assembled cofactors are similar in both proteins. However, the structures of the initial apo-proteins are different, which may have an effect on the different metal-binding preferences.

Figure 8-10 shows the TXRF results of three wt-R2lox preparations used for XAS measurements, which originate from different apo-protein batches. Although the reconstitution protocols differ only slightly, significant effects on formation of heterometallic cofactor sites were observed. When more than one iron was added to the apo-protein, more FeFe clusters are formed at the expense of MnFe clusters (cf. batch A and B in Figure 8-10). This result is consistent with previous XAD experiments, which showed that a small difference in protein:Fe ratio can have a major impact on the efficiency of the Mn/Fe cofactor assembly [131]. Also the effect of the initial iron content in the used apo-protein batch is visible in the data. More MnFe clusters are assembled at the expense of FeFe clusters with lower initial iron content under the same reconstitution conditions (batch to batch variability). These results prove that not only the availability of metal ions but also their concentration has an influence on the final cofactor configuration.

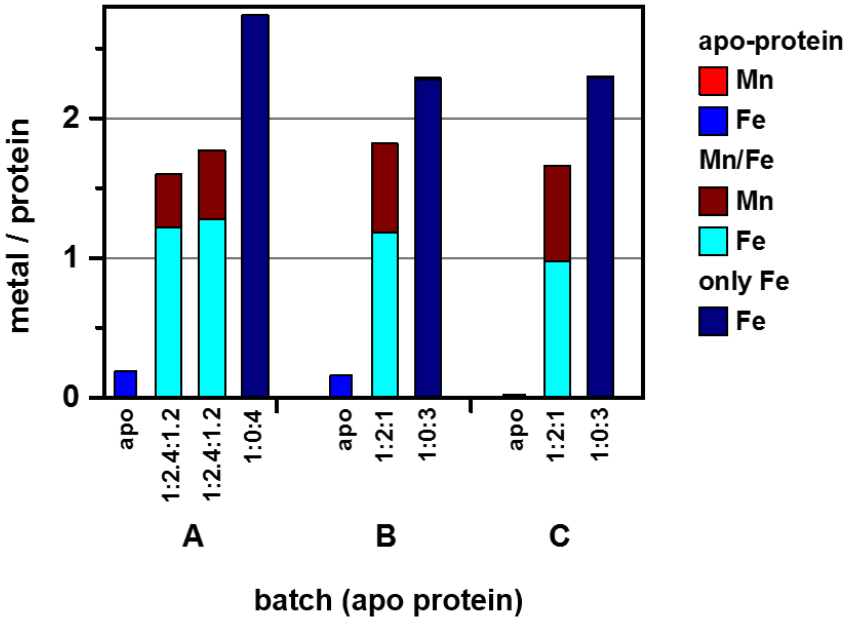

Figure 8-10: Metal content of R2lox samples before and after reconstitution, depending on different apo-protein batches and reconstitution protocol (Table A8-3, given in the Appendix).

8.4.2 Cofactor Assembly in R2lox mutant variants

To study the metalation behaviour of the R2lox variants, the corresponding apo-proteins were titrated with different amounts of manganese and iron (Mn and Fe titration series) under aerobic conditions. The metal content (i.e. cofactor content) of these samples was quantified using TRXF and compared to the results of wt-R2lox and R2c for similar metal reconstitution conditions (see previous section 8.4.1).

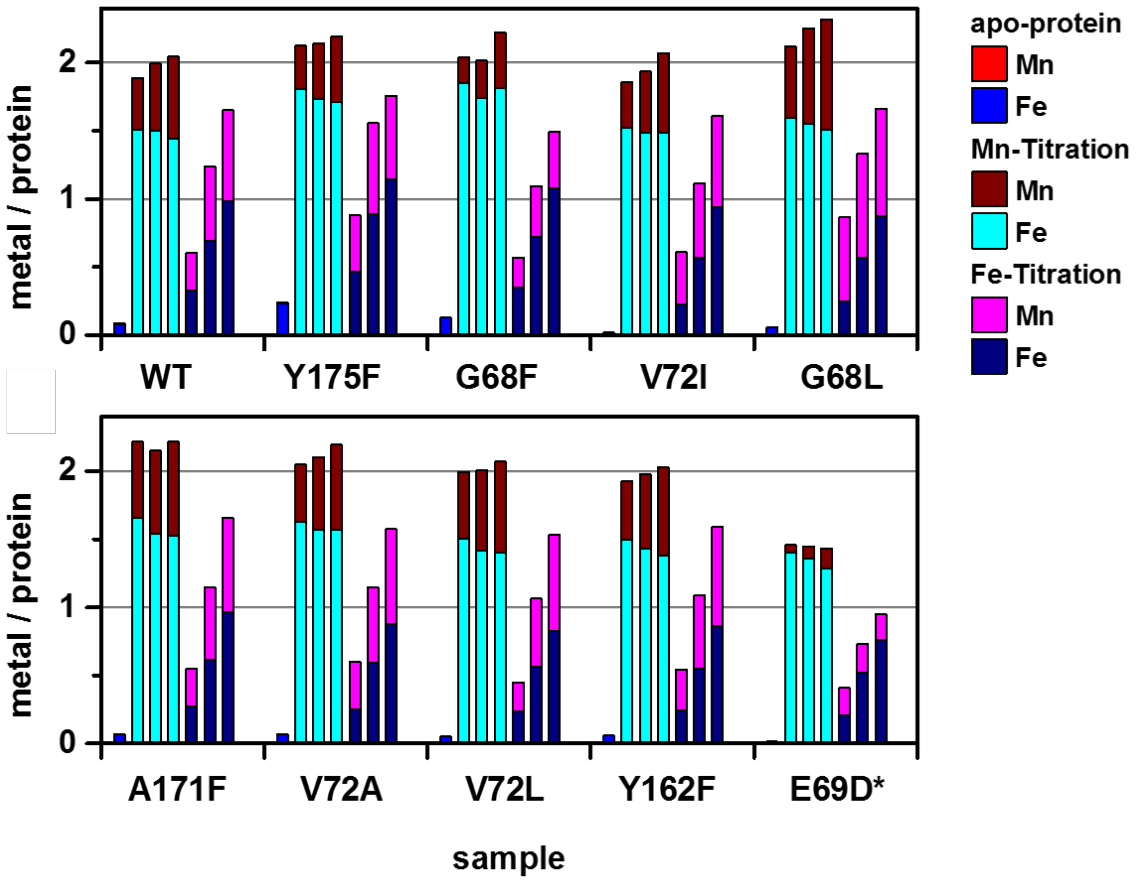

*Figure 8-11: Mn and Fe titration of R2lox variants. Mn and Fe contents in protein solution before and after aerobic reconstitution with Mn and Fe were determined by TXRF (Table A8-4, -5, given in the Appendix). Shown are the mean values of measurements of duplicate samples. The data are specified in the following order: apo-protein, Mn titration (1.2:2, 1:4:2, 1:8:2), Fe titration (1:4:0.2, 1:4:0.6, 1:4:1). The error is ≤0.1 metals/protein. The amounts of other transition metals (Co, Ni, Zn and Cu) were also determined and were negligible in all samples. *E69D- mean of two different preparation batches.*

In agreement with the TXRF results in section 8.4.1, the apo-protein preparations contain no significant amount of manganese and minor iron contents (≤0.1 Fe/protein). As mentioned above, this indicated up to 10% FeFe cofactor sites in the apo-proteins. The metal contents of R2lox variants after reconstitution in aerobic solution are shown in Figure 8-11. At first glance, almost complete metalation was achieved in the Mn titration series, whereas incomplete metalation was observed in the Fe titration series. Furthermore, the TRXF data revealed that most R2lox variants behave similar to the WT under the same conditions. The cofactor distributions were calculated assuming that all metals are bound in dimer sites and the heterometallic cofactor assembly is preferred (Figure 8-12).

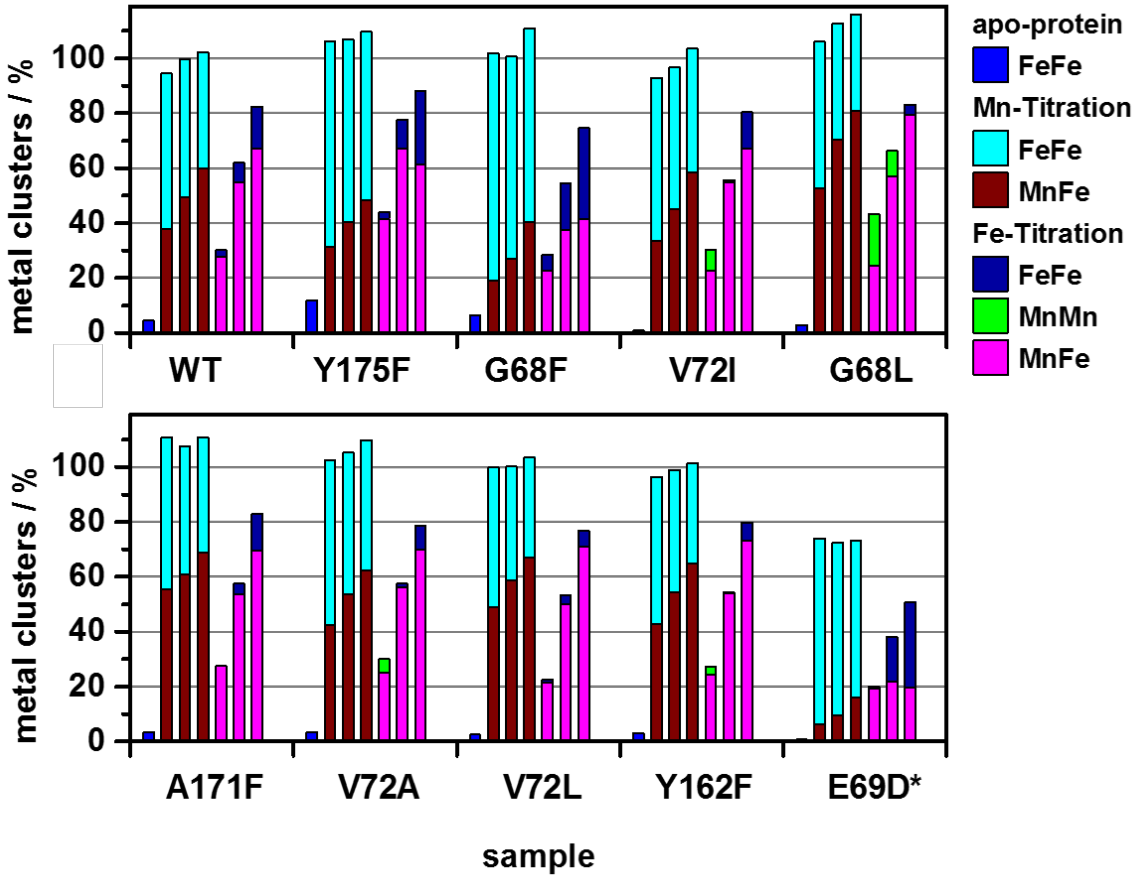

Figure 8-12: Percentage of binuclear cluster species in R2lox variants. The cofactor distributions are calculated under the assumption that all metals are bound in binuclear sites and that the formation of heterobinuclear cluster is preferred. The data is specified in the following order: apo-protein, Mn titration (1.2:2, 1:4:2, 1:8:2), Fe titration (1:4:0.2, 1:4:0.6, 1:4:1).

In the **Mn titration series** where both, Mn and Fe were added in excess, formation of maximal 60-70% heterobinuclear cluster was achieved with almost complete metalation, i.e. the proteins also contain significant amounts of diiron clusters. However, when 2 equivalents each of Mn and Fe were added to the apo-protein, more FeFe than MnFe clusters are formed in all variants of R2lox, in agreement with the results of WT (and in contrast to R2c).

When Mn was added to the apo-protein in excess and Fe is ≤ 1 (**Fe titration**), up to 0.7 Mn per protein are accumulated in almost all mutant samples. In addition, under the conditions of the Fe titration series, the stepwise incorporation of iron is found again in almost all data. However, the protein after reconstitution contains significant amounts of apo-protein, i.e. it is partially metal free. The data reveal that low Fe concentrations appear to favor heterometallic cofactor assembly in the variants as in WT (and also in R2c). Furthermore, in certain variants (**G68L**, **V72A**, **V72I**, and **Y162F)**, the assembly of MnMn cofactor sites can be proposed, when iron was added substoichiometrically (0.2 and 0.6 equivalents), most pronouncedly in G68L. However, apart from that, mutation at the cross-link residues (**V72A/I/L** and **Y162F**) does not significantly affect the metalation compared to WT.

The result for **G68L-R2lox** is in good agreement with the outcome of the XAS results (see section 8.3) and indicates that, in contrast to the WT, **G68L** allows manganese binding in both sites, reminiscent of the findings for R2c. Furthermore, the data shows that more MnFe clusters than in WT (80% versus 60%) are formed when Mn and Fe were added in excess to the apo-protein, which is also in agreement with the results for R2c. Finally, it is suggested that G68L-R2lox adopts an R2c-like metalation process.

Interestingly, although the mutation occurs at the same amino acid residue as in G68L, **G68F** does not show the same effect on metalation behavior, i.e. formation of dimanganese sites is not observed. Comparison of crystal structures reveals that in **G68F-R2lox** the fatty acid ligand is present and the active site geometry in the oxidized state is similar to the WT. However, the TXRF data shows that more iron and less manganese ions than in the WT are assembled under the same conditions. Does the G68F mutation affect the metalation preferentially at site 1? The data suggests that the metalation of another second-sphere mutation **A171F** is very similar to WT. Thus, it follows that the absence of the fatty acid does not cause the increased Mn binding in site 2 in G68L-R2lox. In **E69D**, only a small amount of Mn is accumulated, suggesting that this first-sphere mutation prevents the assembly of manganese in the protein.

8.5 Discussion

Seven different *Gk*R2lox variants with amino acid exchanges were investigated by X-ray absorption spectroscopy in order to obtain insight in the role of the fatty acid ligand, the ether cross-link formation, as well as the metalation specificity. TXRF measurements were performed on nine different variants of *Gk*R2lox, which were aerobically reconstituted with different ratios of Mn(II) and Fe(II) ions to compare the assembly of heterodinuclear cofactor sites and to gain information on the metal binding behavior in solution.

The Fe XANES spectra of the R2lox variants are overall similar to the WT in both edge shape and energy. Pronounced differences are observed in the Mn XANES spectra of the Mn/Fe-reconstituted samples. The analysis of the X-ray photoreduction kinetics suggests that cofactor species different from wild-type R2lox are present in the Mn/Fe-reconstituted G68L- and A171F-R2lox as well as in iron-only reconstituted A171F-R2lox.

EXAFS analysis reveals that in the absence of the fatty acid ligand, a R2a/c-like μO,μOH-bridged Fe(III)/Fe(III) cofactor is preferably formed in Fe-only protein (Figure 8-6). In contrast to WT, in the Mn/Fe-reconstituted G68L only a minor amount of Mn(III)Fe(III) cofactors are formed and the Mn(II)Mn(II) cofactor is the dominate species (Figure 8-6).

In A171F, the mutation in the second coordination sphere blocks the binding of the fatty acid ligand. WT-like Mn/Fe(III)-Fe(III) cofactors (containing a μOH bridge) and R2(c)-like μO,μOH bridged Mn/Fe(III)-Fe(III) cofactors are found, the latter being the major cofactor species. Accordingly, in the absence of the fatty acid ligand, aerobic reconstitution of A171F-R2lox leads to the assembly of a Mn/Fe(III)-Fe(III) cofactor and Tyr-Val ether cross-link formation procedes, but these processes result in an R2c-like cofactor structure (Figure 8-6). The faster phase of the biphasic X-ray photoreduction behavior can be assigned to the μO,μOH bridged cofactor, which has a more positive redox potential compared to the μOH bridged cofactor.

Assembly of both metal ions in the trivalent state appears to be independent of the metal ligation motif and the ability to form the ether cross-link in most R2lox variants prepared in solution under aerobic conditions (i.e. in the presence of O_2). Consequently, in almost all aerobically Mn/Fe-reconstituted variants, a similar specificity for binding manganese in site 1 compared to WT is concluded. However, the mutations in E69D-, F109Y-, and G68L-R2lox lead either to incorporation of only a small amount of manganese (E69D and F109Y) or to incorporation of manganese also at site 2 of the cofactor.

TXRF analysis of the Fe and Mn titration series confirms the XAS results. It is concluded that in solution, almost all of the single-point mutations in the R2lox scaffold have no significant influence on the metal content and thus a similar metalation behaviour as for WT is found (at least ~ 60-70% of the Mn/Fe-reconstituted protein contains heterodimetallic cofactors, in agreement with earlier results for WT, see Chapter 7). Exceptions are mutations at positions directly or very close to the N-terminal metal-binding site (site 1) in the mixed-metal cofactor. Mutation of the glycine residue, G68, to a leucine (G68L) promotes the formation of MnMn dimers, in agreement with the results from the XAS experiments. When the glycine residue is mutated to a phenylalanine (G68F) the metal loading is slightly affected and more iron and less manganese than in WT are assembled under the same conditions. Although the geometry of the active site in G68F-R2lox in the oxidized state is similar to the WT, this mutation seems to affect the Mn specificity in site 1. Mutation of the N-terminal glutamate ligand (E69D) apparently prevents manganese binding in site 1, i.e. the amount of manganese in this variant is low and the XAS results suggest mostly Mn(II). Interestingly, mutations at the cross-link residues do not affect the metal binding behavior, no matter whether cross-link formation still occurs (V72I) or is prevented (V72A, V72L, and Y162F). However, single-point mutations in the R2lox scaffold, which prevent the binding of a fatty acid ligand between the metal ions (G68L and A171F), convert the *Gk*R2lox-type cofactor to a R2-type cofactor.

Conclusions

The ligand-binding oxidase from *Geobacillus kaustophilus* (*Gk*R2lox) contains bimetallic cofactors of [FeFe] and [MnFe] type, which are able to catalyze the formation of an ether cross-link in the protein scaffold. The two metal ions are coordinated by a fatty acid ligand. So far, the influence of the fatty acid (FA) ligand on the active site and the cross-link formation remained unclear. Single-point mutant proteins were investigated using X-ray absorption spectroscopy and TXRF titration series (XAS on seven and TRXF on nine *Gk*R2lox variants) to obtain insight in the role of the fatty acid ligand, the ether cross-link formation, as well as the metalation specificity. In proteins with mutations that prevent binding of the FA ligand, R2(c)-like μO,μOH bridged Mn/Fe(III)-Fe(III) cofactors are formed and the bridging FA is replaced by μO(H)s species. Further, most variants show trivalent cofactor sites after aerobic reconstitution, regardless of the presence or absence of cross-link formation. It can be concluded that the O_2 activation leads to high-valent metal(IV)species, which are either reduced by the formation of an ether cross-link in the protein scaffold or partially reduced by external electron sources in the absence of cross-linking. In addition, mutations in the first- and second sphere can also affect the incorporation of manganese in the cofactor sites and thus the intrinsic metal specificity of the wild-type R2lox protein. The results of this study were compiled in two forthcoming publications (Griese et al., to be published; Kutin et al., to be published).

III Summary and Outlook

In this thesis, a variety of X-ray methods (XAS, XES, NRVS, and TXRF) was employed to provide element specific information on geometric, electronic and vibrational properties of metal centers in metalloproteins as well as biomimetic model compounds.

X-ray absorption spectroscopy (XAS): Transition metal K-edges provided electronic and structural information. While the edge energy is sensitive to the metal oxidation state, the edge shape shows a strong dependence on coordination number and ligand type. The weak, low-energy pre-edge features (core-to-valence, ctv) are sensitive to the symmetry of the metal site and provide further information on metal oxidation and spin state as well as ligand environment. EXAFS analysis provides information about the surrounding ligands of the specific absorber atom within about 6 Å. The amplitude reveals the number and type of neighboring ligands. Metal-ligand distances can be determined with an error of ~ 1%, i.e. with an accuracy of 0.02 Å, which is much better than the distance resolution of protein X-ray diffraction (XRD).

X-ray emission spectroscopy (XES) was employed to investigate the local and electronic structure of first-row transition metals. Whereas the Kβ main-line emission (energy and shape of the spectra) is a "marker" for the metal spin state, the Kβ satellite lines show higher sensitivity to the chemical environment and thus valence-to-core (vtc) spectra can be used to determine ligation state (e.g. identity and number of ligands, ligand protonation state). Furthermore, the vtc region is sensitive to the metal spin and valence state.

The combination of XAS and XES (**XAES**) has provided additional insights and facilitates spin-, valence- and site-selective X-ray absorption measurements.

Nuclear resonance vibrational spectroscopy (NRVS) was used for the investigation of vibrational dynamics of Fe in metalloproteins. This technique provides frequencies, amplitudes and directions of iron vibrational modes in ^{57}Fe labeled materials.

Total reflection X-ray fluorescence (TXRF) was employed to determine the amount of metal or other elements in the samples and can was for metal quantification in metalloproteins.

Quantum chemistry calculations based on **density functional theory** (DFT) were performed for assignment of the observed spectroscopic features in the experimental ctv (XAS), vtc (XES) and pDOS (NRVS) spectra. Combination of theoretical with experimental methods facilitated access to molecular geometries, electronic configurations, and vibrational properties of the

metal sites thus providing necessary information for understanding the catalytic reactivity of metalloenzymes.

In the following, the central results of the thesis are summarized:

I. High-resolution X-ray absorption / emission spectroscopy and density functional theory calculations were applied to study a large series of synthetic diiron complexes mimicking the [FeFe]-hydrogenase active site (**Chapter 4**). The effects of ligand substitution at the iron ions (dithiolate bridge and terminal ligand variation) on the structural, electronic, and spectroscopic properties were examined. This has provided insight in the correlation between molecular structure (terminal and bridging ligand variation) and electronic configuration (charge density distribution, valence localization, bond covalency) [124].

II. The molecular and electronic properties of *in-vitro* maturated HydA1 [FeFe]-hydrogenase proteins were analyzed by X-ray absorption and emission spectroscopy (**Chapter 5**). The bridgehead group of the dithiolate ligand in the synthetic diiron complexes used for maturation was varied. Comparison of the semi-synthetic and native [FeFe]-hydrogenases proved successful H-cluster generation with the *in-vitro* maturation approach.

III. Protein lyophilization prevents the oxygen induced degeneration of the H-cluster of [FeFe]-hydrogenase *Cr*HydA1 (**Chapter 6)**. X-ray absorption spectroscopy on lyophilized [FeFe]-hydrogenases revealed that freeze-drying did not affected the structure of the H-cluster i.e. an intact H-cluster was revealed. This method can be used to transform [FeFe]-hydrogenases into O_2-resistant enzymes [180] and thus may be relevant for biotechnological applications.

IV. Advanced X-ray absorption, emission, and vibrational spectroscopy methods, supported by density functional theory calculations, were applied to study the geometric structure, redox changes as well as the electronic and vibrational properties of homo- and hetero-bimetallic cofactors (FeFe, MnFe) in wild-type *Gk*R2lox protein (**Chapter 7**). The cofactor protonation state was revealed and insights into the effect of the different metalations on the cofactor structure were provided. Parameters from XAS were used to improve the cofactor models from crystallographic data which are typically affected by X-ray photoreduction (XPR) of the initially high-valent metal centers.[83] This comprehensive X-ray spectroscopy study has established general procedures for characterization of metal cofactors in proteins.

V. To clarify the role of amino acids around the cofactor and metal ligation in the O_2 activation and cross-link chemistry as well as to gain further insight into the basics for metal specificity of the cofactor assembly, 10 single point mutation variants of *Gk*R2lox were studied

by XAS and TXRF (**Chapter 8**). In these mutants the fatty acid ligand and/or the cross-link are either present or absent. The study has revealed correlations between specific mutation and metal binding behavior in solution as well as formation of alternative cofactor structures suggesting different possible pathways for the O_2 activation reaction in, e.g., ribonucleotide reductases and ligand-binding oxidases.

In summary, the work in this thesis has established procedures for application of advanced X-ray spectroscopy methods in combination with quantum chemical calculations to metal cofactors and model compounds. This has contributed to better understanding of cofactor structures and functions in biological hydrogen conversion and oxygen activation. The developed experimental and computational approach can be generally applied for in-depth characterization of active sites under functional conditions in bioinorganic chemistry.

IV List of publications

Hydrogenases and Models

15 Ramona Kositzki, Stefan Mebs, Nils Schuth, Nils Leidel, Lennart Schwartz, Michael Karnahl, Florian Wittkamp, Daniel Daunke, Andreas Grohmann, Ulf-Peter Apfel, Frédéric Gloaguen, Sascha Ott, and Michael Haumann
Electronic and molecular structure relations in diiron compounds mimicking the [FeFe]-hydrogenase active site studied by X-ray spectroscopy and quantum chemistry
Dalton Trans, **2017**, 46, 12544-57 (DOI: 10.1039/c7dt02720f)

14 Stefan Mebs, Ramona Kositzki, Jifu Duan, Moritz Senger, Florian Wittkamp, Ulf-Peter Apfel, Thomas Happe, Sven T. Stripp, Martin Winkler, and Michael Haumann
Hydrogen and oxygen trapping at the H-cluster of [FeFe]-hydrogenase revealed by site-selective spectroscopy and QM/MM calculations
Biochim Biophys Acta, **2017**, 1859, 28-41 (DOI: 10.1016/j.bbabio.2017.09.003)

13 Jens Noth, Ramona Kositzki, Kathrin Klein, Martin Winkler, Michael Haumann, and Thomas Happe
Lyophilization protects [FeFe]-hydrogenases against O_2-induced H-cluster degradation
Scientific Reports, **2015**, 5, 13978 (DOI: 10.1038/srep13978)

12 Petko Chernev. Camilla Lambertz, Annika Brünje, Nils Leidel, Kajsa G.V. Sigfridsson, Ramona Kositzki, Chung-Hung Hsieh, Shenglai Yao, Rafael Schiwon, Matthias Driess, Christian Limberg, Thomas Happe, and Michael Haumann
Hydride Binding to the Active Site of [FeFe]-Hydrogenase
Inorg Chem **2014**, 53, 12164-77 (DOI: 10.1021/ic502047q)

Oxidases

11 Ramona Kositzki, Stefan Mebs, Jennifer Marx, Julia J. Griese, Nils Schuth, Martin Högbom, Volker Schünemann, and Michael Haumann
Protonation State of MnFe and FeFe Cofactors in a Ligand-Binding Oxidase Revealed by X-ray Absorption, Emission, and Vibrational Spectroscopy and QM/MM Calculations
Inorg Chem, **2016**, 55, 9869-85 (DOI: 10.1021/acs.inorgchem.6b01752)

10 Julia J. Griese, Ramona Kositzki, Michael Haumann, and Martin Högbom
Assembly of a heterodinuclear Mn/Fe cofactor and formation of a tyrosine-valine ether cross-link are coupled in a R2-like ligand-binding oxidase
To be published[6]

9 Yuri Kutin, Ramona Kositzki, Michael Haumann, Nicholas Cox, Martin Högbom, and Julia J. Griese
A single point mutation stabilizes an intermediate of the oxygen activation reaction of a heterodinuclear manganese/iron cofactor in a ligand-binding oxidase
To be published[7]

8 Yuri Kutin, Vivek Srinivas, Matthieu Fritz, Ramona Kositzki, Hannah S. Shafaat, James Birrell, Eckhard Bill, Michael Haumann, Wolfgang Lubitz, Martin Högbom, Julia J. Griese, and Nicholas Cox
Divergent assembly mechanisms of the manganese/iron cofactors in R2lox and R2c proteins
J Inorg Biochem, **2016**, 162, 164-77 (DOI: 10.1016/j.jinorgbio.2016.04.019)

7 Julia J. Griese, Ramona Kositzki, Peer Schrapers, Rui M. M. Branca, Anders Nordström, Janne Lehtiö, Michael Haumann, and Martin Högbom
Structural Basis for Oxygen Activation at a Heterodinuclear Manganese/Iron Cofactor
J Biol Chem, **2015**, 290, 25254-72 (DOI 10.1074/jbc.M115.675223)

Further publications

6 Stefan Reschke, Stefan Mebs, Kajsa G. V. Sigfridsson, Ramona Kositzki, Silke Leimkühler, and Michael Haumann
Protonation and Sulfido versus Oxo Ligation Changes at the Molybdenum Cofactor in Xanthine Dehydrogenase (XDH) Variants Studied by X-ray Absorption Spectroscopy
Inorg Chem, **2017**, 56, 2165-76 (DOI: 10.1021/acs.inorgchem.6b02846)

---

[6] J. J. Griese, R. Kositzki, M. Haumann, and M. Högbom, **Assembly of a heterodinuclear Mn/Fe cofactor is coupled to tyrosine–valine ether cross-link formation in the R2-like ligand-binding oxidase**. *J Biol Inorg Chem* **2019**, 24, 211–21 (https://doi.org/10.1007/s00775-019-01639-4)

[7] Y. Kutin, R. Kositzki, R. M. M. Branca, V. Srinivas, D. Lundin, M. Haumann, M. Högbom, N. Cox, and J. J. Griese, **Chemical flexibility of heterobimetallic Mn/Fe cofactors: R2lox and R2c proteins**, *J Biol Chem* **2019**, 294(48), 18372-86. (DOI: 10.1074/jbc.RA119.010570)

5 Nils Schuth, Stefan Mebs, Henrike Gehring, Bettina Horn, Patrick Holze, Ramona Kositzki, Peer Schrapers, Christian Limberg, and Michael Haumann
Biomimetic mono- and dinuclear Ni(I) and Ni(II) complexes studied by X-ray absorption and emission spectroscopy and quantum chemical calculations
J Phys Conf Ser, **2015**, 712, 1-012134

4 Peer Schrapers, Stefan Mebs, Julia Ilina, Dana. S. Warner, Christina Wörmann, Nils Schuth, Ramona Kositzki, Holger Dau, Christian Limberg, Holger Dobbek, and Michael Haumann
The binuclear nickel center in the A-cluster of acetyl-CoA synthase (ACS) and two biomimetic dinickel complexes studied by X-ray absorption and emission spectroscopy
J Phys Conf Ser **2015**, 712, 1-012029

3 Stefan Mebs, Beatrice Braun, Ramona Kositzki, Christian Limberg, and Michael Haumann
Abrupt versus Gradual Spin-Crossover in $Fe^{II}(phen)_2(NCS)_2$ and $Fe^{III}(dedtc)_3$ Compared by X‑ray Absorption and Emission Spectroscopy and Quantum-Chemical Calculations
Inorg Chem, **2015**, *54*, 11606-24 (DOI: 10.1021/acs.inorgchem.5b01822)

2 Dennis Huwald, Peer Schrapers, Ramona Kositzki, Michael Haumann, and Anja Hemschemeier
Characterization of unusual truncated hemoglobins of *Chlamydomonas reinhardtii* suggests specialized functions
Planta, **2015**, *242*, 167-85 (DOI 10.1007/s00425-015-2294-4)

1 Peer Schrapers, Tobias Hartmann, Ramona Kositzki, Holger Dau, Stefan Reschke, Carola Schulzke, Silke Leimkühler, and Michael Haumann
Sulfido and Cysteine Ligation Changes at the Molybdenum Cofactor during Substrate Conversion by Formate Dehydrogenase (FDH) from *Rhodobacter capsulatus*
Inorg Chem, **2015**, *54*, 3260-71 (DOI: 10.1021/ic502880y)

V References

1. Adamska-Venkatesh, A., et al., *New redox states observed in [FeFe] hydrogenases reveal redox coupling within the H-cluster.* J Am Chem Soc, **2014**. 136(32): p. 11339-46.
2. Adamska-Venkatesh, A., et al., *Artificially maturated [FeFe] hydrogenase from Chlamydomonas reinhardtii: a HYSCORE and ENDOR study of a non-natural H-cluster.* Phys Chem Chem Phys, **2015**. 17(7): p. 5421-30.
3. Adamska, A., et al., *Identification and Characterization of the "Super-Reduced" State of the H-Cluster in [FeFe] Hydrogenase: A New Building Block for the Catalytic Cycle?* Angew Chem Int Edit, **2012**. 51(46): p. 11458-62.
4. Alp, E.E., et al., *Vibrational dynamics studies by nuclear resonant inelastic X-ray scattering.* Hyperfine Interact, **2002**. 144(1): p. 3-20.
5. Andersson, C.S. and M. Hogbom, *A Mycobacterium tuberculosis ligand-binding Mn/Fe protein reveals a new cofactor in a remodeled R2-protein scaffold.* Proc Natl Acad Sci U S A, **2009**. 106(14): p. 5633-8.
6. Apfel, U.P., et al., *Models for the Active Site in [FeFe] Hydrogenase with Iron-Bound Ligands Derived from Bis-, Tris-, and Tetrakis(mercaptomethyl)silanes.* Inorg Chem, **2010**. 49(21): p. 10117-32.
7. Armstrong, F.A., et al., *Dynamic electrochemical investigations of hydrogen oxidation and production by enzymes and implications for future technology.* Chem Soc Rev, **2009**. 38(1): p. 36-51.
8. Artero, V., et al., *From Enzyme Maturation to Synthetic Chemistry: The Case of Hydrogenases.* Acc Chem Res, **2015**. 48(8): p. 2380-7.
9. Bachmeier, A. and F. Armstrong, *Solar-driven proton and carbon dioxide reduction to fuels-lessons from metalloenzymes.* Curr Opin Chem Biol, **2015**. 25: p. 141-51.
10. Barreto, L., A. Makihira, and K. Riahi, *The hydrogen economy in the 21st century: a sustainable development scenario.* Int J Hydrogen Energ, **2003**. 28(3): p. 267-84.
11. Barton, B.E. and T.B. Rauchfuss, *Terminal hydride in [FeFe]-hydrogenase model has lower potential for H2 production than the isomeric bridging hydride.* Inorg Chem, **2008**. 47(7): p. 2261-3.
12. Barton, B.E., et al., *Isomerization of the hydride complexes [HFe2(SR)(2)(PR3)(x)(CO)(6-x)](+) (x=2, 3, 4) relevant to the active site models for the [FeFe]-hydrogenases.* Dalton Trans, **2010**. 39(12): p. 3011-9.
13. Becke, A.D., *Density-Functional Exchange-Energy Approximation with Correct Asymptotic-Behavior.* Phys Rev A, **1988**. 38(6): p. 3098-100.
14. Becke, A.D., *Density-Functional Thermochemistry .3. The Role of Exact Exchange.* J Chem Phys, **1993**. 98(7): p. 5648-52.
15. Beneze, K.Z., K.C. Kondapalli, and T.L. Stemmler, *X-ray Absorption Spectroscopy*, in *Applications of Physical Methods to Inorganic and Bioinorganic Chemistry*, R.A. Scott and C.M. Lukehart, Editors. 2007, Wiley. p. 513-28.
16. Bennati, M., et al., *Spectroscopic and theoretical approaches for studying radical reactions in class I ribonucleotide reductase.* Biol Chem, **2005**. 386(10): p. 1007-22.
17. Berggren, G., et al., *Biomimetic assembly and activation of [FeFe]-hydrogenases.* Nature, **2013**. 499(7456): p. 66-70.
18. Bergmann, U. and P. Glatzel, *X-ray emission spectroscopy.* Photosynth Res, **2009**. 102(2-3): p. 255-66.
19. Bergmann, U., et al., *High-resolution X-ray spectroscopy of rare events: a different look at local structure and chemistry.* J Synchrotron Radiat, **2001**. 8: p. 199-203.

20. Bergmann, U., et al., *Chemical dependence of interatomic X-ray transition energies and intensities - a study of Mn K beta '' and K beta(2,5) spectra.* Chem Phys Lett, **1999**. 302(1-2): p. 119-24.
21. Bethel, R.D. and M.Y. Darensbourg, *The bioorganometallic chemistry of hydrogenase*, in *Bioorganometallic Chemistry: Applications in Drug Discovery Biocatalysis, and Imaging*, G. Jaouen and M. Salmain, Editors. 2014, Wiley-VCH: Weinheim.
22. Biegler-Konig, F., J. Schonbohm, and D. Bayles, *Software news and updates - AIM2000 - A program to analyze and visualize atoms in molecules.* J Comput Chem, **2001**. 22(5): p. 545-59.
23. Blakeley, M.P., S.S. Hasnain, and S.V. Antonyuk, *Sub-atomic resolution X-ray crystallography and neutron crystallography: promise, challenges and potential.* IUCrJ, **2015**. 2(Pt 4): p. 464-74.
24. Blomberg, M.R., et al., *Quantum chemical studies of mechanisms for metalloenzymes.* Chem Rev, **2014**. 114(7): p. 3601-58.
25. Boal, A.K., et al., *Structural basis for activation of class Ib ribonucleotide reductase.* Science, **2010**. 329(5998): p. 1526-30.
26. Bollinger, J.M., Jr., et al., *The manganese(IV)/iron(III) cofactor of Chlamydia trachomatis ribonucleotide reductase: structure, assembly, radical initiation, and evolution.* Curr Opin Struct Biol, **2008**. 18(6): p. 650-7.
27. Bossel, U., B. Eliasson, and G. Taylor, *The future of the hydrogen economy: bright or bleak?* Cogeneration and Competitive Power Journal, **2003**. 18(3): p. 29-70.
28. Bowman, S.E., J. Bridwell-Rabb, and C.L. Drennan, *Metalloprotein Crystallography: More than a Structure.* Acc Chem Res, **2016**. 49(4): p. 695-702.
29. Bunker, G., *A Practical Guide to X-ray Absorption Fine Structure Spectroscopy*. 2010: Cambridge University Press, New York.
30. Bykova, E., et al., *Structural complexity of simple Fe2O3 at high pressures and temperatures.* Nat Commun, **2016**. 7: p. 1-6.
31. Cabeza, J.A., et al., *Binuclear iron(I), ruthenium(I), and osmium(I) hexacarbonyl complexes containing a bridging benzene-1,2-dithiolate ligand. Synthesis, X-ray structures, protonation reactions, and EHMO calculations.* Organometallics, **1998**. 17(8): p. 1471-7.
32. Cammack, R., *Hydrogenase sophistication.* Nature, **1999**. 397(6716): p. 214-5.
33. Chapman, H.N., et al., *Femtosecond X-ray protein nanocrystallography.* Nature, **2011**. 470(7332): p. 73-7.
34. Charreteur, K., et al., *Effect of electron-withdrawing dithiolate bridge on the electron-transfer steps in diiron molecules related to [2Fe](H) subsite of the [FeFe]-hydrogenases.* Inorg Chem, **2010**. 49(5): p. 2496-501.
35. Chernev, P., et al., *Hydride binding to the active site of [FeFe]-hydrogenase.* Inorg Chem, **2014**. 53(22): p. 12164-77.
36. Choi, Y.S., et al., *In vitro reconstitution and crystal structure of p-aminobenzoate N-oxygenase (AurF) involved in aureothin biosynthesis.* Proc Natl Acad Sci U S A, **2008**. 105(19): p. 6858-63.
37. Chumakov, A. and R. Ruffer, *Nuclear inelastic scattering.* Hyperfine Interact, **1998**. 113(1-4): p. 59-79.
38. Chumakov, A.I., et al., *Nuclear resonance energy analysis of inelastic x-ray scattering.* Phys Rev Lett, **1996**. 76(22): p. 4258-61.
39. Colomban, C., et al., *X-ray Absorption and Emission Spectroscopies of X-Bridged Diiron Phthalocyanine Complexes (FePc)(2)X (X = C, N, O) Combined with DFT Study of (FePc)(2)X and Their High-Valent Diiron Oxo Complexes.* Inorg Chem, **2014**. 53(21): p. 11517-30.
40. Contreras-Garcia, J., et al., *NCIPLOT: A Program for Plotting Noncovalent Interaction Regions.* J Chem Theory Comput, **2011**. 7(3): p. 625-32.
41. Cotruvo, J.A. and J. Stubbe, *Class I ribonucleotide reductases: metallocofactor assembly and repair in vitro and in vivo.* Annu Rev Biochem, **2011**. 80: p. 733-67.

42. Cox, N., et al., *A tyrosyl-dimanganese coupled spin system is the native metalloradical cofactor of the R2F subunit of the ribonucleotide reductase of Corynebacterium ammoniagenes.* J Am Chem Soc, **2010**. 132(32): p. 11197-213.
43. Cramer, C.J., *Essentials of Computational Chemistry: Theories and Models*. 2005: Wiley.
44. Czech, I., et al., *The [FeFe]-hydrogenase maturation protein HydF contains a H-cluster like [4Fe4S]-2Fe site.* FEBS Lett, **2011**. 585(1): p. 225-30.
45. Darensbourg, M.Y., *Synthetic chemistry: making a natural fuel cell.* Nature, **2005**. 433(7026): p. 589-91.
46. Darensbourg, M.Y. and R.D. Bethel, *BIOMIMETIC CHEMISTRY Merging the old with the new.* Nat Chem, **2012**. 4(1): p. 11-13.
47. Darensbourg, M.Y., E.J. Lyon, and J.J. Smee, *The bio-organometallic chemistry of active site iron in hydrogenases.* Coordin Chem Rev, **2000**. 206: p. 533-61.
48. Dau, H. and M. Haumann, *The manganese complex of photosystem II in its reaction cycle - Basic framework and possible realization at the atomic level.* Coordin Chem Rev, **2008**. 252(3-4): p. 273-95.
49. Dau, H., P. Liebisch, and M. Haumann, *X-ray absorption spectroscopy to analyze nuclear geometry and electronic structure of biological metal centers--potential and questions examined with special focus on the tetra-nuclear manganese complex of oxygenic photosynthesis.* Anal Bioanal Chem, **2003**. 376(5): p. 562-83.
50. Dau, H., P. Liebisch, and M. Haumann, *The manganese complex of oxygenic photosynthesis: Conversion of five-coordinated Mn(III) to six-coordinated Mn(IV) in the S-2-S-3 transition is implied by XANES simulations.* Phys Scripta, **2005**. T115: p. 844-6.
51. Dau, H., I. Zaharieva, and M. Haumann, *Recent developments in research on water oxidation by photosystem II.* Curr Opin Chem Biol, **2012**. 16(1-2): p. 3-10.
52. Daunke, D., *Metallkomplexe polypodaler Thiolatliganden als Modellsysteme für FeFe- und FeNi-Hydrogenasen*. Ph.D. Thesis. 2014, Berlin: Technische Universität Berlin.
53. de Groot, F., *High-resolution X-ray emission and X-ray absorption spectroscopy.* Chem Rev, **2001**. 101(6): p. 1779-808.
54. De Groot, F. and A. Kotani, *Core Level Spectroscopy of Solids*. 2008, Boca Raton, FL, USA: Taylor & Francis CRC press.
55. de Groot, F.M.F., et al., *1s2p resonant inelastic X-ray scattering of iron oxides.* J Phys Chem B, **2005**. 109(44): p. 20751-62.
56. De Lacey, A.L., et al., *FTIR characterization of the active site of the Fe-hydrogenase from Desulfovibrio desulfuricans.* J Am Chem Soc, **2000**. 122(45): p. 11232-3.
57. De Proft, F., et al., *Atomic charges, dipole moments, and Fukui functions using the Hirshfeld partitioning of the electron density.* J Comput Chem, **2002**. 23(12): p. 1198-209.
58. DeBeer-George, S.D., T. Petrenko, and F. Neese, *Prediction of Iron K-Edge Absorption Spectra Using Time-Dependent Density Functional Theory.* J Phys Chem A, **2008**. 112(50): p. 12936-43.
59. Doedens, R.J., *Structural Studies of Organonitrogen Compounds of the Transition Elements. IV. The Crystal and Molecular Structure of Benzo [c] cinnolinebis(tricarbonyliron), C12H8N2Fe2(CO)(6).* Inorg Chem, **1970**. 9(3): p. 429-36.
60. Du Bois, J., T.J. Mizoguchi, and S.J. Lippard, *Understanding the dioxygen reaction chemistry of diiron proteins through synthetic modeling studies.* Coordination Chemistry Reviews, **2000**. 200: p. 443-85.
61. Erdem, O.F., et al., *A Model of the [FeFe] Hydrogenase Active Site with a Biologically Relevant Azadithiolate Bridge: A Spectroscopic and Theoretical Investigation.* Angew Chem Int Edit, **2011**. 50(6): p. 1439-43.
62. Eremenko, I.L., et al., *Formation of Antiferromagnetic Heteronuclear Thiolate and Sulfide Bridged Complexes .2. Synthesis, Magnetic-Properties, and Molecular-Structures of the Clusters Cp2cr2(Mu-Scme3)2(Mu-4-S)W2(Mu-I)2(Co)4(No)2 and Cp2cr2(Mu-3-S)2(Mu-Scme3)2w(Scme3)(No).* J Organomet Chem, **1994**. 471(1-2): p. 123-32.

63. Esselborn, J., et al., *Spontaneous activation of [FeFe]-hydrogenases by an inorganic [2Fe] active site mimic.* Nat Chem Biol, **2013**. 9(10): p. 607-9.
64. Esselborn, J., et al., *A structural view of synthetic cofactor integration into [FeFe]-hydrogenases.* Chem Sci, **2016**. 7(2): p. 959-68.
65. Evans, D.J. and C.J. Pickett, *Chemistry and the hydrogenases.* Chem Soc Rev, **2003**. 32(5): p. 268-75.
66. Ezzaher, S., et al., *Evidence for the formation of terminal hydrides by protonation of an asymmetric iron hydrogenase active site mimic.* Inorg Chem, **2007**. 46(9): p. 3426-8.
67. Ezzaher, S., et al., *Directing protonation in [FeFe] hydrogenase active site models by modifications in their second coordination sphere.* Chem Commun, **2010**. 46(31): p. 5775-7.
68. Faus, I., et al., *Isoprenoid Biosynthesis in Pathogenic Bacteria: Nuclear Resonance Vibrational Spectroscopy Provides Insight into the Unusual [4Fe-4S] Cluster of the E. coli LytB/IspH Protein.* Angew Chem Int Edit, **2015**. 54(43): p. 12584-7.
69. Felton, G.A.N., et al., *Review of electrochemical studies of complexes containing the Fe2S2 core characteristic of [FeFe]-hydrogenases including catalysis by these complexes of the reduction of acids to form dihydrogen.* J Organomet Chem, **2009**. 694(17): p. 2681-99.
70. Filippi, G., et al., *DFT Dissection of the Reduction Step in H-2 Catalytic Production by [FeFe]-Hydrogenase-Inspired Models: Can the Bridging Hydride Become More Reactive Than the Terminal Isomer?* Inorg Chem, **2015**. 54(19): p. 9529-42.
71. Finkelmann, A.R., M.T. Stiebritz, and M. Reiher, *Inaccessibility of the μ-hydride species in [FeFe] hydrogenases.* Chem Sci, **2013**. DOI: 10.1039/c3sc51700d.
72. Fourmond, V., et al., *The oxidative inactivation of FeFe hydrogenase reveals the flexibility of the H-cluster.* Nat Chem, **2014**. 6(4): p. 336-42.
73. Frisch, M.J.T., G. W.; Schlegel, H. B.; Scuseria, G. E.; Robb, M. A.; Cheeseman, J. R.; Scalmani, G.; Barone, V.; Mennucci, B.; Petersson, G. A.; Nakatsuji, H.; Caricato, M.; Li, X.; Hratchian, H. P.; Izmaylov, A. F.; Bloino, J.; Zheng, G.; Sonnenberg, J. L.; Hada, M.; Ehara, M.; Toyota, K.; Fukuda, R.; Hasegawa, J.; Ishida, M.; Nakajima, T.; Honda, Y.; Kitao, O.; Nakai, H.; Vreven, T.; Montgomery, J. A., Jr.; Peralta, J. E.; Ogliaro, F.; Bearpark, M.; Heyd, J. J.; Brothers, E.; Kudin, K. N.; Staroverov, V. N.; Kobayashi, R.; Normand, J.; Raghavachari, K.; Rendell, A.; Burant, J. C.; Iyengar, S. S.; Tomasi, J.; Cossi, M.; Rega, N.; Millam, J. M.; Klene, M.; Knox, J. E.; Cross, J. B.; Bakken, V.; Adamo, C.; Jaramillo, J.; Gomperts, R.; Stratmann, R. E.; Yazyev, O.; Austin, A. J.; Cammi, R.; Pomelli, C.; Ochterski, J. W.; Martin, R. L.; Morokuma, K.; Zakrzewski, V. G.; Voth, G. A.; Salvador, P.; Dannenberg, J. J.; Dapprich, S.; Daniels, A. D.; Farkas, Ö.; Foresman, J. B.; Ortiz, J. V.; Cioslowski, J.; Fox, D. J. , *Gaussian 09, Revision D.01.* Gaussian, Inc., Wallingford CT., **2009**.
74. George, G.N., B. Hedman, and K.O. Hodgson, *An edge with XAS.* Nat Struct Biol, **1998**. 5: p. 645-7.
75. Gilbert-Wilson, R., et al., *Spectroscopic Investigations of [FeFe] Hydrogenase Maturated with [(57)Fe2(adt)(CN)2(CO)4](2-).* J Am Chem Soc, **2015**. 137(28): p. 8998-9005.
76. Glatzel, P. and U. Bergmann, *High resolution 1s core hole X-ray spectroscopy in 3d transition metal complexes - electronic and structural information.* Coordin Chem Rev, **2005**. 249(1-2): p. 65-95.
77. Glatzel, P., et al., *Site-selective EXAFS in mixed-valence compounds using high-resolution fluorescence detection: a study of iron in Prussian Blue.* Inorg Chem, **2002**. 41(12): p. 3121-7.
78. Gloaguen, F., *Electrochemistry of Simple Organometallic Models of Iron-Iron Hydrogenases in Organic Solvent and Water.* Inorg Chem, **2016**. 55(2): p. 390-8.
79. Gloaguen, F. and T.B. Rauchfuss, *Small molecule mimics of hydrogenases: hydrides and redox.* Chem Soc Rev, **2009**. 38(1): p. 100-8.
80. Graslund, A. and M. Sahlin, *Electron paramagnetic resonance and nuclear magnetic resonance studies of class I ribonucleotide reductase.* Annu Rev Biophys Biomol Struct, **1996**. 25: p. 259-86.

81. Griese, J.J., et al., *Ether cross-link formation in the R2-like ligand-binding oxidase.* J Biol Inorg Chem, **2018**. 23(6): p. 879-86.
82. Griese, J.J. and M. Hogbom, *X-ray reduction correlates with soaking accessibility as judged from four non-crystallographically related diiron sites.* Metallomics, **2012**. 4(9): p. 894-8.
83. Griese, J.J., et al., *Structural Basis for Oxygen Activation at a Heterodinuclear Manganese/Iron Cofactor.* J Biol Chem, **2015**. 290(42): p. 25254-72.
84. Griese, J.J., et al., *Direct observation of structurally encoded metal discrimination and ether bond formation in a heterodinuclear metalloprotein.* Proc Natl Acad Sci U S A, **2013**. 110(43): p. 17189-94.
85. Griese, J.J., V. Srinivas, and M. Hogbom, *Assembly of nonheme Mn/Fe active sites in heterodinuclear metalloproteins.* J Biol Inorg Chem, **2014**. 19(6): p. 759-74.
86. Groom, C.R., et al., *The Cambridge Structural Database.* Acta Crystallogr B, **2016**. 72: p. 171-9.
87. Guo, M.Y., et al., *Simulations of iron K pre-edge X-ray absorption spectra using the restricted active space method.* Phys Chem Chem Phys, **2016**. 18(4): p. 3250-9.
88. Hammes-Schiffer, S., *Proton-Coupled Electron Transfer: Moving Together and Charging Forward.* J Am Chem Soc, **2015**. 137(28): p. 8860-71.
89. Happe, T. and A. Hemschemeier, *Metalloprotein mimics - old tools in a new light.* Trends Biotechnol, **2014**. 32(4): p. 170-6.
90. Haumann, M., *Metal centers in hydrogenase enzymes studied by X-ray spectroscopy*, in *Biohydrogen*, M. Rögner, Editor. 2015, DeGruyter: Berlin. p. 97-116.
91. Haumann, M., et al., *Photosynthetic water oxidation at elevated dioxygen partial pressure monitored by time-resolved X-ray absorption measurements.* Proc Natl Acad Sci U S A, **2008**. 105(45): p. 17384-9.
92. Haumann, M., et al., *Photosynthetic O2 formation tracked by time-resolved x-ray experiments.* Science, **2005**. 310(5750): p. 1019-21.
93. Haumann, M., et al., *Structural and oxidation state changes of the photosystem II manganese complex in four transitions of the water oxidation cycle (S0 --> S1, S1 --> S2, S2 --> S3, and S3,4 --> S0) characterized by X-ray absorption spectroscopy at 20 K and room temperature.* Biochemistry, **2005**. 44(6): p. 1894-908.
94. Haumann, M. and S.T. Stripp, *The Molecular Proceedings of Biological Hydrogen Turnover.* Acc Chem Res, **2018**. 51(8): p. 1755-63.
95. Heinekey, D.M., *Hydrogenase enzymes: Recent structural studies and active site models.* J Organomet Chem, **2009**. 694(17): p. 2671-80.
96. Hogbom, M., *The manganese/iron-carboxylate proteins: what is what, where are they, and what can the sequences tell us?* J Biol Inorg Chem, **2010**. 15(3): p. 339-49.
97. Hogbom, M., *Metal use in ribonucleotide reductase R2, di-iron, di-manganese and heterodinuclear-an intricate bioinorganic workaround to use different metals for the same reaction.* Metallomics, **2011**. 3(2): p. 110-20.
98. Hogbom, M., et al., *Displacement of the tyrosyl radical cofactor in ribonucleotide reductase obtained by single-crystal high-field EPR and 1.4-A x-ray data.* Proc Natl Acad Sci U S A, **2003**. 100(6): p. 3209-14.
99. Hogbom, M., et al., *The radical site in chlamydial ribonucleotide reductase defines a new R2 subclass.* Science, **2004**. 305(5681): p. 245-8.
100. Hohenberg, P. and W. Kohn, *Inhomogeneous Electron Gas.* Phys Rev B, **1964**. 136(3b): p. B864-71.
101. Hubschle, C.B. and P. Luger, *MolIso - a program for colour-mapped iso-surfaces.* J Appl Crystallogr, **2006**. 39: p. 901-4.
102. Hugenbruch, S., et al., *In search of metal hydrides: an X-ray absorption and emission study of [NiFe] hydrogenase model complexes.* Phys Chem Chem Phys, **2016**. 18(16): p. 10688-99.
103. Jensen, F., *Introduction to Computational Chemistry*. 2007: Wiley.
104. Jensen, F., *Introduction to Computational Chemistry*. 2013: Wiley.

105. Jensen, K.P., *Bioinorganic Chemistry Modeled with the TPSSh Density Functional.* Inorg Chem, **2008**. 47(22): p. 10357-65.
106. Jiang, W., et al., *Branched activation- and catalysis-specific pathways for electron relay to the manganese/iron cofactor in ribonucleotide reductase from Chlamydia trachomatis.* Biochemistry, **2008**. 47(33): p. 8477-84.
107. Jiang, W., et al., *A manganese(IV)/iron(III) cofactor in Chlamydia trachomatis ribonucleotide reductase.* Science, **2007**. 316(5828): p. 1188-91.
108. Jiang, W., et al., *Formation and function of the Manganese(IV)/Iron(III) cofactor in Chlamydia trachomatis ribonucleotide reductase.* Biochemistry, **2008**. 47(52): p. 13736-44.
109. Justice, A.K., et al., *Redox and structural properties of mixed-valence models for the active site of the [FeFe]-hydrogenase: Progress and challenges.* Inorg Chem, **2008**. 47(16): p. 7405-14.
110. Justice, A.K., T.B. Rauchfuss, and S.R. Wilson, *Unsaturated, mixed-valence diiron dithiolate model for the H-ox state of the [FeFe] hydrogenase.* Angew Chem Int Edit, **2007**. 46(32): p. 6152-4.
111. Karlin, K.D., *Metalloenzymes, structural motifs, and inorganic models.* Science, **1993**. 261(5122): p. 701-8.
112. Karnahl, M., et al., *Mixed-valence [(FeFeII)-Fe-I] hydrogenase active site model complexes stabilized by a bidentate carborane bis-phosphine ligand.* Dalton Trans, **2012**. 41(40): p. 12468-77.
113. Keppler, C., et al., *Nuclear forward scattering of synchrotron radiation by deoxymyoglobin.* Eur Biophys J Biophy, **2000**. 29(2): p. 146-52.
114. Kern, J., et al., *Simultaneous femtosecond X-ray spectroscopy and diffraction of photosystem II at room temperature.* Science, **2013**. 340(6131): p. 491-5.
115. Kirchner, B., et al., *Theoretical bioinorganic chemistry: the electronic structure makes a difference.* Curr Opin Chem Biol, **2007**. 11(2): p. 134-41.
116. Klockenkämper, R., *Total Reflection X-ray Fluorescence Analysis*. 1996, London, UK: Wiley-VCH.
117. Klockenkamper, R., et al., *Total-Reflection X-Ray-Fluorescence Spectroscopy.* Anal Chem, **1992**. 64(23): p. A1115-23.
118. Knorzer, P., et al., *Importance of the protein framework for catalytic activity of [FeFe]-hydrogenases.* J Biol Chem, **2012**. 287(2): p. 1489-99.
119. Koch, W. and M.C. Holthausen, *A Chemist's Guide to Density Functional Theory*. 2001: Wiley-VCH.
120. Kohn, W. and L.J. Sham, *Self-Consistent Equations Including Exchange and Correlation Effects.* Phys Rev, **1965**. 140(4a): p. 1133-8.
121. Kolberg, M., et al., *Structure, function, and mechanism of ribonucleotide reductases.* Biochim Biophys Acta, **2004**. 1699(1-2): p. 1-34.
122. Kopp, D.A. and S.J. Lippard, *Soluble methane monooxygenase: activation of dioxygen and methane.* Curr Opin Chem Biol, **2002**. 6(5): p. 568-76.
123. Kositzki, R., et al., *Protonation State of MnFe and FeFe Cofactors in a Ligand-Binding Oxidase Revealed by X-ray Absorption, Emission, and Vibrational Spectroscopy and QM/MM Calculations.* Inorg Chem, **2016**. 55(19): p. 9869-85.
124. Kositzki, R., et al., *Electronic and molecular structure relations in diiron compounds mimicking the [FeFe]-hydrogenase active site studied by X-ray spectroscopy and quantum chemistry.* Dalton Trans, **2017**. 46(37): p. 12544-57.
125. Kovaleva, E.G. and J.D. Lipscomb, *Versatility of biological non-heme Fe(II) centers in oxygen activation reactions.* Nat Chem Biol, **2008**. 4(3): p. 186-93.
126. Kowalska, J. and S. DeBeer, *The role of X-ray spectroscopy in understanding the geometric and electronic structure of nitrogenase.* BBA-Mol Cell Res, **2015**. 1853(6): p. 1406-15.

127. Kowalska, J.K., et al., *X-ray Absorption and Emission Spectroscopic Studies of [L2Fe2S2](n) Model Complexes: Implications for the Experimental Evaluation of Redox States in Iron-Sulfur Clusters.* Inorg Chem, **2016**. 55(9): p. 4485-97.
128. Krebs, C., et al., *AurF from Streptomyces thioluteus and a possible new family of manganese/iron oxygenases.* Biochemistry, **2007**. 46(37): p. 10413-8.
129. Krewald, V., et al., *The protonation states of oxo-bridged Mn(IV) dimers resolved by experimental and computational Mn K pre-edge X-ray absorption spectroscopy.* Inorg Chem, **2013**. 52(22): p. 12904-14.
130. Kuchenreuther, J.M., et al., *Nuclear Resonance Vibrational Spectroscopy and Electron Paramagnetic Resonance Spectroscopy of Fe-57-Enriched [FeFe] Hydrogenase Indicate Stepwise Assembly of the H-Cluster.* Biochemistry, **2013**. 52(5): p. 818-26.
131. Kutin, Y., et al., *Divergent assembly mechanisms of the manganese/iron cofactors in R2lox and R2c proteins.* J Inorg Biochem, **2016**. 162: p. 164-77.
132. Kwak, Y., et al., *Geometric and Electronic Structure of the Mn(IV)Fe(III) Cofactor in Class Ic Ribonucleotide Reductase: Correlation to the Class Ia Binuclear Non-Heme Iron Enzyme.* J Am Chem Soc, **2013**. 135(46): p. 17573-84.
133. Lambertz, C., et al., *Electronic and molecular structures of the active-site H-cluster in [FeFe]-hydrogenase determined by site-selective X-ray spectroscopy and quantum chemical calculations.* Chem Sci, **2014**. 5(3): p. 1187-203.
134. Lambertz, C., et al., *O-2 Reactions at the Six-iron Active Site (H-cluster) in [FeFe]-Hydrogenase.* J Biol Chem, **2011**. 286(47): p. 40614-23.
135. Lansing, J.C., et al., *Hydrogen Production Catalyzed by Bidirectional, Biomimetic Models of the [FeFe]-Hydrogenase Active Site.* Organometallics, **2014**. 33(20): p. 5897-906.
136. Lassalle-Kaiser, B., et al., *Experimental and computational X-ray emission spectroscopy as a direct probe of protonation states in oxo-bridged Mn(IV) dimers relevant to redox-active metalloproteins.* Inorg Chem, **2013**. 52(22): p. 12915-22.
137. Lee, N., et al., *Probing valence orbital composition with iron Kbeta X-ray emission spectroscopy.* J Am Chem Soc, **2010**. 132(28): p. 9715-27.
138. Leidel, N., et al., *Site-selective X-ray spectroscopy on an asymmetric model complex of the [FeFe] hydrogenase active site.* Inorg Chem, **2012**. 51(8): p. 4546-59.
139. Leidel, N., et al., *Electronic structure of an [FeFe] hydrogenase model complex in solution revealed by X-ray absorption spectroscopy using narrow-band emission detection.* J Am Chem Soc, **2012**. 134(34): p. 14142-57.
140. Leidel, N., et al., *Bridging-hydride influence on the electronic structure of an [FeFe] hydrogenase active-site model complex revealed by XAES-DFT.* Dalton Trans, **2013**. 42(21): p. 7539-54.
141. Leidel, N., et al., *High-valent [MnFe] and [FeFe] cofactors in ribonucleotide reductases.* Biochim Biophys Acta, **2012**. 1817(3): p. 430-44.
142. Li, H.X. and T.B. Rauchfuss, *Iron carbonyl sulfides, formaldehyde, and amines condense to give the proposed azadithiolate cofactor of the Fe-only hydrogenases.* J Am Chem Soc, **2002**. 124(5): p. 726-7.
143. Li, Y.L. and T.B. Rauchfuss, *Synthesis of Diiron(I) Dithiolato Carbonyl Complexes.* Chem Rev, **2016**. 116(12): p. 7043-77.
144. Lima, F.A., et al., *Probing the electronic and geometric structure of ferric and ferrous myoglobins in physiological solutions by Fe K-edge absorption spectroscopy.* Phys Chem Chem Phys, **2014**. 16(4): p. 1617-31.
145. Lippard, S.J. and J.M. Berg, *Bioanorganische Chemie.* 1995, Heidelberg: Spektrum Akademischer Verlag.
146. Liu, Z.P. and P. Hu, *A density functional theory study on the active center of Fe-only hydrogenase: Characterization and electronic structure of the redox states.* J Am Chem Soc, **2002**. 124(18): p. 5175-82.

147. Loscher, S., et al., *Facilitated hydride binding in an Fe-Fe hydrogenase active-site biomimic revealed by X-ray absorption spectroscopy and DFT calculations.* Inorg Chem, **2007**. 46(26): p. 11094-105.
148. Lubitz, W., et al., *Hydrogenases.* Chem Rev, **2014**. 114(8): p. 4081-148.
149. Lubitz, W. and W. Tumas, *Hydrogen: an overview.* Chem Rev, **2007**. 107(10): p. 3900-3.
150. Lundin, D., et al., *Use of structural phylogenetic networks for classification of the ferritin-like superfamily.* J Biol Chem, **2012**. 287(24): p. 20565-75.
151. Lyon, E.J., et al., *Carbon monoxide and cyanide ligands in a classical organometallic complex model for Fe-only hydrogenase.* Angew Chem Int Edit, **1999**. 38(21): p. 3178-80.
152. MacMillan, S.N., et al., *Ligand-Sensitive But Not Ligand-Diagnostic: Evaluating Cr Valence-to-Core X-ray Emission Spectroscopy as a Probe of Inner-Sphere Coordination.* Inorg Chem, **2015**. 54(1): p. 205-14.
153. Magnuson, A., et al., *Biomimetic and Microbial Approaches to Solar Fuel Generation.* Acc Chem Res, **2009**. 42(12): p. 1899-909.
154. Magnuson, A., et al., *Bridging-type changes facilitate successive oxidation steps at about 1 V in two binuclear manganese complexes--implications for photosynthetic water-oxidation.* J Inorg Biochem, **2006**. 100(7): p. 1234-43.
155. Manor, B.C., M.R. Ringenberg, and T.B. Rauchfuss, *Borane-Protected Cyanides as Surrogates of H-Bonded Cyanides in [FeFe]-Hydrogenase Active Site Models.* Inorg Chem, **2014**. 53(14): p. 7241-7.
156. Martinie, R.J., et al., *Evidence for a Di-mu-oxo Diamond Core in the Mn(IV)/Fe(IV) Activation Intermediate of Ribonucleotide Reductase from Chlamydia trachomatis.* J Am Chem Soc, **2017**. 139(5): p. 1950-7.
157. Marx, J., et al., *Nuclear inelastic scattering at the diiron center of ribonucleotide reductase from Escherichia coli.* Hyperfine Interact, **2017**. 238.
158. Matthews, S.L. and D.M. Heinekey, *A Carbonyl-Rich Bridging Hydride Complex Relevant to the Fe-Fe Hydrogenase Active Site.* Inorg Chem, **2010**. 49(21): p. 9746-8.
159. Mebs, S., et al., *Abrupt versus Gradual Spin-Crossover in Fe(II)(phen)2(NCS)2 and Fe(III)(dedtc)3 Compared by X-ray Absorption and Emission Spectroscopy and Quantum-Chemical Calculations.* Inorg Chem, **2015**. 54(24): p. 11606-24.
160. Mebs, S., et al., *Hydrogen and oxygen trapping at the H-cluster of [FeFe]-hydrogenase revealed by site-selective spectroscopy and QM/MM calculations.* Biochim Biophys Acta, **2018**. 1859(1): p. 28-41.
161. Mebs, S., et al., *Bridging Hydride at Reduced H-Cluster Species in [FeFe]-Hydrogenases Revealed by Infrared Spectroscopy, Isotope Editing, and Quantum Chemistry.* J Am Chem Soc, **2017**. 139(35): p. 12157-60.
162. Megarity, C.F., et al., *Electrochemical Investigations of the Mechanism of Assembly of the Active-Site H-Cluster of [FeFe]-Hydrogenases.* J Am Chem Soc, **2016**. 138(46): p. 15227-33.
163. Messinger, J., et al., *Absence of Mn-centered oxidation in the S(2) --> S(3) transition: implications for the mechanism of photosynthetic water oxidation.* J Am Chem Soc, **2001**. 123(32): p. 7804-20.
164. Miller, E.K., et al., *Time-Resolved Investigations of Heterobimetallic Cofactor Assembly in R2lox Reveal Distinct Mn/Fe Intermediates.* Biochemistry, **2017**. 56(26): p. 3369-79.
165. Milsmann, C., et al., *Stabilization of High-Valent (FeS6)-S-IV-Cores by Dithiocarbamate(1-) and 1,2-Dithiolate(2-) Ligands in Octahedral [Fe-IV(Et(2)dtc)(3-n)(mnt)(n)]((n-1)-) Complexes (n=0, 1, 2, 3): A Spectroscopic and Density Functional Theory Computational Study.* Chem-Eur J, **2010**. 16(12): p. 3628-45.
166. Mitschler, A., B. Rees, and M.S. Lehmann, *Electron-Density in Bis(Dicarbonyl-Pi-Cyclopentadienyliron) at Liquid-Nitrogen Temperature by X-Ray and Neutron-Diffraction.* J Am Chem Soc, **1978**. 100(11): p. 3390-7.

167. Moeser, B., et al., *Nuclear inelastic scattering and Mossbauer spectroscopy as local probes for ligand binding modes and electronic properties in proteins: vibrational behavior of a ferriheme center inside a beta-barrel protein.* J Am Chem Soc, **2012**. 134(9): p. 4216-28.
168. Moller, F., et al., *From Enzymes to Functional Materials-Towards Activation of Small Molecules.* Chem-Eur J, **2018**. 24(7): p. 1471-93.
169. Mulder, D.W., et al., *Stepwise [FeFe]-hydrogenase H-cluster assembly revealed in the structure of HydA(DeltaEFG).* Nature, **2010**. 465(7295): p. 248-51.
170. Mulder, D.W., et al., *Identification of a Catalytic Iron-Hydride at the H-Cluster of [FeFe]-Hydrogenase.* J Am Chem Soc, **2017**. 139(1): p. 83-6.
171. Mulder, D.W., et al., *EPR and FTIR Analysis of the Mechanism of H-2 Activation by [FeFe]-Hydrogenase HydA1 from Chlamydomonas reinhardtii.* J Am Chem Soc, **2013**. 135(18): p. 6921-9.
172. Mulder, D.W., et al., *Insights into [FeFe]-hydrogenase structure, mechanism, and maturation.* Structure, **2011**. 19(8): p. 1038-52.
173. Neese, F., *Prediction of molecular properties and molecular spectroscopy with density functional theory: From fundamental theory to exchange-coupling.* Coordin Chem Rev, **2009**. 253(5-6): p. 526-63.
174. Neese, F., *The ORCA program system.* Wiley Interdisciplinary Reviews-Computational Molecular Science, **2012**. 2(1): p. 73-8.
175. Newville, M., *Fundamentals of XAFS.* Rev Mineral Geochem, **2014**. 78: p. 33-74.
176. Nicolet, Y., et al., *Crystallographic and FTIR spectroscopic evidence of changes in Fe coordination upon reduction of the active site of the Fe-only hydrogenase from Desulfovibrio desulfuricans.* J Am Chem Soc, **2001**. 123(8): p. 1596-601.
177. Nicolet, Y., et al., *A novel FeS cluster in Fe-only hydrogenases.* Trends Biochem Sci, **2000**. 25(3): p. 138-43.
178. Nicolet, Y., et al., *Desulfovibrio desulfuricans iron hydrogenase: the structure shows unusual coordination to an active site Fe binuclear center.* Structure, **1999**. 7(1): p. 13-23.
179. Noth, J., et al., *[FeFe]-Hydrogenase with Chalcogenide Substitutions at the H-Cluster Maintains Full H2 Evolution Activity.* Angew Chem Int Edit, **2016**. 55(29): p. 8396-400.
180. Noth, J., et al., *Lyophilization protects [FeFe]-hydrogenases against O2-induced H-cluster degradation.* Sci Rep, **2015**. 5: p. 13978.
181. Olsen, M.T., et al., *New Nitrosyl Derivatives of Diiron Dithiolates Related to the Active Site of the [FeFe]-Hydrogenases.* Inorg Chem, **2008**. 47(24): p. 11816-24.
182. Orio, M., D.A. Pantazis, and F. Neese, *Density functional theory.* Photosynth Res, **2009**. 102(2-3): p. 443-53.
183. Pandey, A.S., et al., *Dithiomethylether as a ligand in the hydrogenase H-cluster.* J Am Chem Soc, **2008**. 130(13): p. 4533-40.
184. Paulsen, H., et al., *Dynamics of metal centers monitored by nuclear inelastic scattering.* Hyperfine Interact, **2005**. 165(1-4): p. 17-24.
185. Paulsen, H., et al., *Measurement and simulation of nuclear inelastic-scattering spectra of molecular crystals.* Phys Rev B, **1999**. 59(2): p. 975-84.
186. Pelmenschikov, V., et al., *Reaction Coordinate Leading to H-2 Production in [FeFe]-Hydrogenase Identified by Nuclear Resonance Vibrational Spectroscopy and Density Functional Theory.* J Am Chem Soc, **2017**. 139(46): p. 16894-902.
187. Peng, G., et al., *High-Resolution Manganese X-Ray-Fluorescence Spectroscopy - Oxidation-State and Spin-State Sensitivity.* J Am Chem Soc, **1994**. 116(7): p. 2914-20.
188. Penner-Hahn, J.E., *2.13 - X-ray Absorption Spectroscopy A2 - McCleverty, Jon A*, in *Comprehensive Coordination Chemistry II*, T.J. Meyer, Editor. 2003, Pergamon: Oxford. p. 159-86.
189. Perdew, J.P., *Density-Functional Approximation for the Correlation-Energy of the Inhomogeneous Electron-Gas.* Phys Rev B, **1986**. 33(12): p. 8822-4.

190. Peters, J.W., et al., *X-ray crystal structure of the Fe-only hydrogenase (CpI) from Clostridium pasteurianum to 1.8 angstrom resolution.* Science, **1998**. 282(5395): p. 1853-8.
191. Peters, J.W., et al., *[FeFe]- and [NiFe]-hydrogenase diversity, mechanism, and maturation.* Biochim Biophys Acta, **2015**. 1853(6): p. 1350-69.
192. Petuker, A., et al., *Spontaneous Si-C bond cleavage in (TriphosSi)-nickel complexes.* Dalton Trans, **2017**. 46(3): p. 907-17.
193. Pierik, A.J., et al., *A low-spin iron with CN and CO as intrinsic ligands forms the core of the active site in [Fe]-hydrogenases.* Eur J Biochem, **1998**. 258(2): p. 572-8.
194. Pollock, C.J. and S. DeBeer, *Valence-to-core X-ray emission spectroscopy: a sensitive probe of the nature of a bound ligand.* J Am Chem Soc, **2011**. 133(14): p. 5594-601.
195. Pollock, C.J. and S. DeBeer, *Insights into the Geometric and Electronic Structure of Transition Metal Centers from Valence-to-Core X-ray Emission Spectroscopy.* Acc Chem Res, **2015**. 48(11): p. 2967-75.
196. Pollock, C.J., et al., *K beta Mainline X-ray Emission Spectroscopy as an Experimental Probe of Metal-Ligand Covalency.* J Am Chem Soc, **2014**. 136(26): p. 9453-63.
197. Posewitz, M.C., et al., *Identification of genes required for hydrogenase activity in Chlamydomonas reinhardtii.* Biochem Soc Trans, **2005**. 33(Pt 1): p. 102-4.
198. Qian, Q., et al., *Valence measurement of Mn oxides using Mn K-beta emission spectroscopy.* J Phys Chem Solids, **2000**. 61(3): p. 457-60.
199. Ragsdale, S.W., *Metals and their scaffolds to promote difficult enzymatic reactions.* Chem Rev, **2006**. 106(8): p. 3317-37.
200. Rao, P.V. and R.H. Holm, *Synthetic analogues of the active sites of iron-sulfur proteins.* Chem Rev, **2004**. 104(2): p. 527-59.
201. Rauchfuss, T.B., *Chemistry - A promising mimic of hydrogenase activity.* Science, **2007**. 316(5824): p. 553-4.
202. Rauchfuss, T.B., *Diiron azadithiolates as models for the [FeFe]-hydrogenase active site and paradigm for the role of the second coordination sphere.* Acc Chem Res, **2015**. 48(7): p. 2107-16.
203. Reece, S.Y., et al., *Proton-coupled electron transfer: the mechanistic underpinning for radical transport and catalysis in biology.* Philos Trans R Soc Lond B Biol Sci, **2006**. 361(1472): p. 1351-64.
204. Reece, S.Y. and D.G. Nocera, *Proton-coupled electron transfer in biology: results from synergistic studies in natural and model systems.* Annu Rev Biochem, **2009**. 78: p. 673-99.
205. Rees, J.A., et al., *Experimental and theoretical correlations between vanadium K-edge X-ray absorption and K[Formula: see text] emission spectra.* J Biol Inorg Chem, **2016**. 21(5-6): p. 793-805.
206. Rehr, J.J. and A.L. Ankudinov, *Progress in the theory and interpretation of XANES.* Coordin Chem Rev, **2005**. 249(1-2): p. 131-140.
207. Rehr, J.J., et al., *Theoretical X-Ray Absorption Fine-Structure Standards.* J Am Chem Soc, **1991**. 113(14): p. 5135-40.
208. Rehr, J.J., et al., *Parameter-free calculations of X-ray spectra with FEFF9.* Phys Chem Chem Phys, **2010**. 12(21): p. 5503-13.
209. Reijerse, E.J., et al., *Direct Observation of an Iron-Bound Terminal Hydride in [FeFe]-Hydrogenase by Nuclear Resonance Vibrational Spectroscopy.* J Am Chem Soc, **2017**. 139(12): p. 4306-9.
210. Rifkin, J., *The Hydrogen Economy*. 2002, New York: Tarcher Penguin.
211. Rittle, J., C.C.L. McCrory, and J.C. Peters, *A 10(6)-Fold Enhancement in N-2-Binding Affinity of an Fe-2(mu-H)(2) Core upon Reduction to a Mixed-Valence (FeFeI)-Fe-II State.* J Am Chem Soc, **2014**. 136(39): p. 13853-62.
212. Roos, K. and P.E. Siegbahn, *Density functional theory study of the manganese-containing ribonucleotide reductase from Chlamydia trachomatis: why manganese is needed in the active complex.* Biochemistry, **2009**. 48(9): p. 1878-87.

213. Roos, K. and P.E. Siegbahn, *Oxygen cleavage with manganese and iron in ribonucleotide reductase from Chlamydia trachomatis.* J Biol Inorg Chem, **2011**. 16(4): p. 553-65.
214. Roos, K. and P.E. Siegbahn, *A comparison of two-electron chemistry performed by the manganese and iron heterodimer and homodimers.* J Biol Inorg Chem, **2012**. 17(3): p. 363-73.
215. Rose, H.R., et al., *Structural Basis for Superoxide Activation of Flavobacterium johnsoniae Class I Ribonucleotide Reductase and for Radical Initiation by Its Dimanganese Cofactor.* Biochemistry, **2018**. 57(18): p. 2679-93.
216. Rüffer, R., *Nuclear Resonance Scattering*, in *Reference Module in Materials Science and Materials Engineering*, H. Saleem, Editor. 2016, Elsevier: Amsterdam. p. 1-13.
217. Sage, J.T., et al., *Nuclear resonance vibrational spectroscopy of a protein active-site mimic.* J Phys-Condens Mat, **2001**. 13(34): p. 7707-22.
218. Salomone-Stagni, M., et al., *The iron-site structure of [Fe]-hydrogenase and model systems: an X-ray absorption near edge spectroscopy study.* Dalton Trans, **2010**. 39(12): p. 3057-64.
219. Schafer, A., C. Huber, and R. Ahlrichs, *Fully Optimized Contracted Gaussian-Basis Sets of Triple Zeta Valence Quality for Atoms Li to Kr.* J Chem Phys, **1994**. 100(8): p. 5829-35.
220. Scheidt, W.R., S.M. Durbin, and J.T. Sage, *Nuclear resonance vibrational spectroscopy--NRVS.* J Inorg Biochem, **2005**. 99(1): p. 60-71.
221. Scheidt, W.R., J.F. Li, and J.T. Sage, *What Can Be Learned from Nuclear Resonance Vibrational Spectroscopy: Vibrational Dynamics and Hemes.* Chem Rev, **2017**. 117(19): p. 12532-63.
222. Schenk, G., et al., *A purple acid phosphatase from sweet potato contains an antiferromagnetically coupled binuclear Fe-Mn center.* J Biol Chem, **2001**. 276(22): p. 19084-8.
223. Schilter, D., et al., *Hydrogenase Enzymes and Their Synthetic Models: The Role of Metal Hydrides.* Chem Rev, **2016**. 116(15): p. 8693-749.
224. Schmidt, M., S.M. Contakes, and T.B. Rauchfuss, *First generation analogues of the binuclear site in the Fe-only hydrogenases: Fe-2(mu-SR)(2)(CO)(4)(CN)(2)(2-).* J Am Chem Soc, **1999**. 121(41): p. 9736-7.
225. Schünemann, V., *Biophysik: Eine Einführung*. 2004: Springer Berlin Heidelberg.
226. Schwartz, L., et al., *Iron hydrogenase active site mimic holding a proton and a hydride.* Chem Commun, **2006**(5): p. 520-2.
227. Schwartz, L., et al., *Dynamic ligation at the first amine-coordinated iron hydrogenase active site mimic.* Chem Commun, **2006**(40): p. 4206-8.
228. Schwartz, L., et al., *Tuning the electronic properties of Fe-2(mu-arenedithiolate) (CO)(6-n)(PMe3)(n) (n=0, 2) complexes related to the [Fe-Fe]-hydrogenase active site.* CR Chim, **2008**. 11(8): p. 875-89.
229. Senger, M., et al., *Proton-Coupled Reduction of the Catalytic [4Fe-4S] Cluster in [FeFe]-Hydrogenases.* Angew Chem Int Edit, **2017**. 56(52): p. 16503-6.
230. Senger, M., et al., *Protonation/reduction dynamics at the [4Fe-4S] cluster of the hydrogen-forming cofactor in [FeFe]-hydrogenases.* Phys Chem Chem Phys, **2017**.
231. Senger, M., et al., *Stepwise isotope editing of [FeFe]-hydrogenases exposes cofactor dynamics.* Proc Natl Acad Sci U S A, **2016**. 113(30): p. 8454-9.
232. Shafaat, H.S., et al., *Electronic structural flexibility of heterobimetallic Mn/Fe cofactors: R2lox and R2c proteins.* J Am Chem Soc, **2014**. 136(38): p. 13399-409.
233. Shulman, R.G., et al., *Observation and Interpretation of X-Ray Absorption Edges in Iron Compounds and Proteins.* Proc Natl Acad Sci U S A, **1976**. 73(5): p. 1384-8.
234. Si, G., et al., *Facile synthesis and functionality-dependent electrochemistry of Fe-only hydrogenase mimics.* Inorg Chem, **2008**. 47(18): p. 8101-11.
235. Siebel, J.F., et al., *Hybrid [FeFe]-Hydrogenases with Modified Active Sites Show Remarkable Residual Enzymatic Activity.* Biochemistry, **2015**. 54(7): p. 1474-83.
236. Siegbahn, P.E.M., J.W. Tye, and M.B. Hall, *Computational studies of [NiFe] and [FeFe] hydrogenases.* Chem Rev, **2007**. 107(10): p. 4414-35.

237. Sigfridsson, K.G., et al., *Rapid X-ray photoreduction of dimetal-oxygen cofactors in ribonucleotide reductase.* J Biol Chem, **2013**. 288(14): p. 9648-61.
238. Silakov, A., et al., *Spectroelectrochemical characterization of the active site of the [FeFe] hydrogenase HydA1 from Chlamydomonas reinhardtii.* Biochemistry, **2009**. 48(33): p. 7780-6.
239. Silakov, A., et al., *The electronic structure of the H-cluster in the [FeFe]-hydrogenase from Desulfovibrio desulfuricans: A Q-band Fe-57-ENDOR and HYSCORE study.* J Am Chem Soc, **2007**. 129(37): p. 11447-58.
240. Silakov, A., et al., *Spin distribution of the H-cluster in the H-ox-CO state of the [FeFe] hydrogenase from Desulfovibrio desulfuricans: HYSCORE and ENDOR study of N-14 and C-13 nuclear interactions.* J Biol Inorg Chem, **2009**. 14(2): p. 301-13.
241. Silakov, A., et al., *(14)N HYSCORE investigation of the H-cluster of [FeFe] hydrogenase: evidence for a nitrogen in the dithiol bridge.* Phys Chem Chem Phys, **2009**. 11(31): p. 6592-9.
242. Simmons, T.R., et al., *Mimicking hydrogenases: From biomimetics to artificial enzymes.* Coordin Chem Rev, **2014**. 270: p. 127-50.
243. Singh, P.S., et al., *(I,0) Mixed-Valence State of a Diiron Complex with Pertinence to the [FeFe]-Hydrogenase Active Site: An IR, EPR, and Computational Study.* Inorg Chem, **2009**. 48(23): p. 10883-5.
244. Singleton, M.L., et al., *Synthetic Support of De Novo Design: Sterically Bulky [FeFe]-Hydrogenase Models.* Angew Chem Int Edit, **2008**. 47(49): p. 9492-5.
245. Singleton, M.L., et al., *The effect of bridgehead steric bulk on the ground state and intramolecular exchange processes of (mu-SCH2CR2CH2S)[Fe(CO)(3)][Fe(CO)(2)L] complexes.* CR Chim, **2008**. 11(8): p. 861-74.
246. Sintchak, M.D., et al., *The crystal structure of class II ribonucleotide reductase reveals how an allosterically regulated monomer mimics a dimer.* Nat Struct Biol, **2002**. 9(4): p. 293-300.
247. Smith, S.E., et al., *Reversible Electrocatalytic Production and Oxidation of Hydrogen at Low Overpotentials by a Functional Hydrogenase Mimic.* Angew Chem Int Edit, **2012**. 51(13): p. 3152-5.
248. Sommer, C., et al., *Proton Coupled Electronic Rearrangement within the H-Cluster as an Essential Step in the Catalytic Cycle of [FeFe] Hydrogenases.* J Am Chem Soc, **2017**. 139(4): p. 1440-3.
249. Song, L.C., et al., *Novel single and double diiron oxadithiolates as models for the active site of [Fe]-Only hydrogenases.* Organometallics, **2004**. 23(13): p. 3082-4.
250. Stiebritz, M.T. and M. Reiher, *Hydrogenases and oxygen.* Chem Sci, **2012**. 3(6): p. 1739-51.
251. Stowasser, R. and R. Hoffmann, *What do the Kohn-Sham orbitals and eigenvalues mean?* J Am Chem Soc, **1999**. 121(14): p. 3414-20.
252. Stripp, S., et al., *The Structure of the Active Site H-Cluster of [FeFe] Hydrogenase from the Green Alga Chlamydomonas reinhardtii Studied by X-ray Absorption Spectroscopy.* Biochemistry, **2009**. 48(22): p. 5042-9.
253. Stripp, S.T., et al., *How oxygen attacks [FeFe] hydrogenases from photosynthetic organisms.* Proc Natl Acad Sci U S A, **2009**. 106(41): p. 17331-6.
254. Stripp, S.T. and T. Happe, *How algae produce hydrogen-news from the photosynthetic hydrogenase.* Dalton Trans, **2009**(45): p. 9960-9.
255. Sturhahn, W., *Nuclear resonant spectroscopy.* J Phys-Condens Mat, **2004**. 16(5): p. S497-S530.
256. Sturhahn, W., et al., *Phonon Density-of-States Measured by Inelastic Nuclear Resonant Scattering.* Phys Rev Lett, **1995**. 74(19): p. 3832-5.
257. Sun, L.C., B. Akermark, and S. Ott, *Iron hydrogenase active site mimics in supramolecular systems aiming for light-driven hydrogen production.* Coordin Chem Rev, **2005**. 249(15-16): p. 1653-63.
258. Swanson, K.D., et al., *[FeFe]-hydrogenase oxygen inactivation is initiated at the H cluster 2Fe subcluster.* J Am Chem Soc, **2015**. 137(5): p. 1809-16.

259. Tard, C., et al., *Synthesis of the H-cluster framework of iron-only hydrogenase.* Nature, **2005**. 433(7026): p. 610-3.
260. Tard, C. and C.J. Pickett, *Structural and Functional Analogues of the Active Sites of the [Fe]-, [NiFe]-, and [FeFe]-Hydrogenases.* Chem Rev, **2009**. 109(6): p. 2245-74.
261. Teo, B.K., *EXAFS: Baisc Principles and Data Analysis*. 1986: Springer-Verlag.
262. Theil, E.C., T. Tosha, and R.K. Beherat, *Solving Biology's Iron Chemistry Problem with Ferritin Protein Nanocages.* Acc Chem Res, **2016**. 49(5): p. 784-91.
263. Tschierlei, S., S. Ott, and R. Lomoth, *Spectroscopically characterized intermediates of catalytic H-2 formation by [FeFe] hydrogenase models.* Energ Environ Sci, **2011**. 4(7): p. 2340-52.
264. Valentine, A.M. and S.J. Lippard, *Principles of small molecule activation by metalloenzymes as exemplified by the soluble methane monooxygenase from Methylococcus capsulatus (Bath).* J Chem Soc Dalton, **1997**(21): p. 3925-31.
265. van Bokhoven, J.A. and C. Lamberti, *X-Ray Absorption and X-Ray Emission Spectroscopy*. 2016, New York: Wiley.
266. Vanburck, U., et al., *Nuclear Forward Scattering of Synchrotron Radiation.* Phys Rev B, **1992**. 46(10): p. 6207-11.
267. Visser, H., et al., *Mn K-edge XANES and Kbeta XES studies of two Mn-oxo binuclear complexes: investigation of three different oxidation states relevant to the oxygen-evolving complex of photosystem II.* J Am Chem Soc, **2001**. 123(29): p. 7031-9.
268. Voevodskaya, N., et al., *High catalytic activity achieved with a mixed manganese-iron site in protein R2 of Chlamydia ribonucleotide reductase.* FEBS Lett, **2007**. 581(18): p. 3351-5.
269. Voevodskaya, N., et al., *Redox intermediates of the Mn-Fe Site in subunit R2 of Chlamydia trachomatis ribonucleotide reductase: an X-ray absorption and EPR study.* J Biol Chem, **2009**. 284(7): p. 4555-66.
270. Vollmers, N.J., et al., *Experimental and Theoretical High-Energy-Resolution X-ray Absorption Spectroscopy: Implications for the Investigation of the Entatic State.* Inorg Chem, **2016**. 55(22): p. 11694-706.
271. Vreven, T., et al., *Geometry optimization with QM/MM, ONIOM, and other combined methods. I. Microiterations and constraints.* J Comput Chem, **2003**. 24(6): p. 760-9.
272. Wang, H., et al., *A practical guide for nuclear resonance vibrational spectroscopy (NRVS) of biochemical samples and model compounds.* Methods Mol Biol, **2014**. 1122: p. 125-37.
273. Wang, M., et al., *Approaches to efficient molecular catalyst systems for photochemical H-2 production using [FeFe]-hydrogenase active site mimics.* Dalton Trans, **2011**. 40(48): p. 12793-800.
274. Wang, N., et al., *Reactions of [FeFe]-hydrogenase models involving the formation of hydrides related to proton reduction and hydrogen oxidation.* Dalton Trans, **2013**. 42(34): p. 12059-71.
275. Wang, N., et al., *Preparation, Facile Deprotonation, and Rapid H/D Exchange of the mu-Hydride Diiron Model Complexes of the [FeFe]-Hydrogenase Containing a Pendant Amine in a Chelating Diphosphine Ligand.* Inorg Chem, **2009**. 48(24): p. 11551-8.
276. Wang, N., et al., *Catalytic Activation of H-2 under Mild Conditions by an [FeFe]-Hydrogenase Model via an Active mu-Hydride Species.* J Am Chem Soc, **2013**. 135(37): p. 13688-91.
277. Wang, W., et al., *Isolation of a mixed valence diiron hydride: evidence for a spectator hydride in hydrogen evolution catalysis.* J Am Chem Soc, **2013**. 135(9): p. 3633-9.
278. Wang, X., F.M.F. deGroot, and S.P. Cramer, *Spin-polarized x-ray emission of 3d transition-metal ions: A comparison via K alpha and K beta detection.* Phys Rev B, **1997**. 56(8): p. 4553-64.
279. Westre, T.E., et al., *A multiplet analysis of Fe K-edge 1s->3d pre-edge features of iron complexes.* J Am Chem Soc, **1997**. 119(27): p. 6297-314.
280. Whittington, D.A. and S.J. Lippard, *Crystal structures of the soluble methane monooxygenase hydroxylase from Methylococcus capsulatus (Bath) demonstrating geometrical variability at the dinuclear iron active site.* J Am Chem Soc, **2001**. 123(5): p. 827-38.

281. Winkler, M., J. Esselborn, and T. Happe, *Molecular basis of [FeFe]-hydrogenase function An insight into the complex interplay between protein and catalytic cofactor.* BBA-Bioenergetics, **2013**. 1827(8-9): p. 974-85.
282. Winkler, M., et al., *Accumulating the hydride state in the catalytic cycle of [FeFe]-hydrogenases.* Nat Commun, **2017**. 8.
283. Wobrauschek, P., *Total reflection x-ray fluorescence analysis - a review.* X-Ray Spectrom, **2007**. 36(5): p. 289-300.
284. Yang, D.W., et al., *Synthesis and Electrocatalytic Property of Diiron Hydride Complexes Derived from a Thiolate-Bridged Diiron Complex.* Inorg Chem, **2015**. 54(21): p. 10243-9.
285. Yano, J. and V.K. Yachandra, *X-ray absorption spectroscopy.* Photosynth Res, **2009**. 102(2-3): p. 241-54.
286. Yao, S.L., et al., *Biomimetic [2Fe-2S] Clusters with Extensively Delocalized Mixed-Valence Iron Centers.* Angew Chem Int Edit, **2015**. 54(42): p. 12506-10.
287. Young, N.A., *The application of synchrotron radiation and in particular X-ray absorption spectroscopy to matrix isolated species.* Coordin Chem Rev, **2014**. 277: p. 224-74.
288. Younker, J.M., et al., *Structural analysis of the Mn(IV)/Fe(III) cofactor of Chlamydia trachomatis ribonucleotide reductase by extended X-ray absorption fine structure spectroscopy and density functional theory calculations.* J Am Chem Soc, **2008**. 130(45): p. 15022-7.
289. Zaharieva, I., et al., *Room-Temperature Energy-Sampling Kbeta X-ray Emission Spectroscopy of the Mn4Ca Complex of Photosynthesis Reveals Three Manganese-Centered Oxidation Steps and Suggests a Coordination Change Prior to O2 Formation.* Biochemistry, **2016**. 55(30): p. 4197-211.
290. Zaharieva, I., et al., *Towards a comprehensive X-ray approach for studying the photosynthetic manganese complex—XANES, K-alpha/K-beta/K-beta-satellite emission lines, RIXS, and comparative computational approaches for selected model complexes.* J Phys Conf Ser, **2009**. 190: p. 012142, 1-6.
291. Zeng, W., et al., *Nuclear Resonance Vibrational Spectroscopy (NRVS)*, in *Applications of Physical Methods to Inorganic and Bioinorganic Chemistry*, R.A. Scott and C.M. Lukehart, Editors. 2007, Wiley. p. 401-21.
292. Zhao, X., et al., *H/D exchange reaction in dinuclear iron thiolates as activity assay models of Fe-H(2)ase.* J Am Chem Soc, **2001**. 123(39): p. 9710-1.
293. Zocher, G., et al., *Structure and action of the N-oxygenase AurF from Streptomyces thioluteus.* J Mol Biol, **2007**. 373(1): p. 65-74.

VI Appendix

Appendix Chapter 4

Table A4-1: Bond lengths in diiron compounds.[a]

compound	mean bond length [Å]				
	Fe-Fe distance	Fe-ligand distance	terminal CO ligands	other terminal ligands	bridging ligands
1	2.539 (2.541)	2.032 (2.046)	1.763 (1.746)	2.128 (2.155)	1.925 (1.922)
2	2.556 (2.578)	1.972 (1.979)	1.796 (1.782)	-	2.234 (2.275)
3	2.510 (2.543)	1.981 (1.990)	1.800 (1.786)	-	2.252 (2.295)
4	2.494 (2.530)	1.985 (1.992)	1.800 (1.786)	-	2.263 (2.301)
5	2.480 (2.513)	1.982 (1.995)	1.792 (1.786)	-	2.268 (2.307)
6	2.512 (2.535)	1.988 (1.996)	1.799 (1.791)	-	2.272 (2.304)
7	2.508 (2.535)	1.826 (1.851)	1.768 (1.791)	-	1.914 (1.940)
8	2.555 (2.622)	2.051 (2.071)	1.758 (1.758)	2.237 (2.272)	2.252 (2.285)
9	2.569 (2.599)	2.047 (2.074)	1.755 (1.754)	2.222 (2.271)	2.252 (2.295)
10	2.546 (2.583)	2.050 (2.071)	1.758 (1.758)	2.221 (2.252)	2.256 (2.294)
11	2.552 (2.569)	2.002 (2.010)	1.790 (1.774)	2.064 (2.081)	2.251 (2.288)
12	2.519 (2.546)	2.017 (2.027)	1.787 (1.776)	2.203 (2.222)	2.258 (2.292)
13	2.531 (2.571)	2.073 (2.081)	1.779 (1.772)	2.217 (2.243)	2.296 (2.308)
14	2.544 (2.595)	2.059 (2.078)	1.781 (1.775)	2.206 (2.245)	2.263 (2.299)
15	2.497 (2.559)	2.061 (2.082)	1.771 (1.775)	2.197 (2.230)	2.284 (2.314)
16	2.518 (2.582)	1.991 (2.008)	1.737 (1.754)	1.926 (1.913)	2.276 (2.309)
17	2.509 (2.563)	2.000 (2.010)	1.746 (1.750)	1.942 (1.916)	2.283 (2.316)
18	2.518 (2.584)	1.991 (2.007)	1.737 (1.754)	1.926 (1.912)	2.276 (2.308)

[a]*Bond lengths refer to crystal structures or to geometry-optimized structures (BP86/TZVP, COSMO solvation model, ε = 4; in parenthesis).*

Table A4-2: Normalized iron parameters.[a]

observable	compound															
	2	**3**	**5**	**4**	**6**	**8**	**11**	**9**	**10**	**12**	**14**	**13**	**15**	**18**	**16**	**17**
	normalized parameter															
Fe-Fe distance	89	33	0	11	33	78	78	100	78	44	67	56	22	44	44	33
Fe charge	100	82	83	80	78	9	86	14	8	43	2	0	2	11	13	6
HOMO energy	95	75	86	76	100	25	47	24	24	50	58	60	67	0	5	5
vtc energy	89	81	79	100	86	93	36	44	46	69	51	88	46	41	36	0
$K\beta_{1,3}$ energy	43	32	21	36	25	86	76	96	100	79	54	50	57	14	7	0
LUMO energy	100	85	91	84	90	30	42	22	22	46	44	30	44	0	5	14
ctv energy	47	100	92	35	26	93	13	51	78	21	70	19	29	7	0	3
K-edge energy	67	84	94	82	100	54	56	53	35	45	2	17	0	61	62	56
Fed degeneracy	100	24	64	31	39	50	31	35	47	29	27	0	17	39	39	67
Fed localization	80	75	46	76	14	64	100	63	27	30	0	17	12	47	44	32
mean	81	67	66	61	59	58	57	50	47	46	37	34	30	27	26	22

[a]*Normalized parameter values (P^{norm}, rounded to integer values) for each observable (O) and compound (i) were calculated according to (O^{min} and O^{max} = minimal or maximal observable values in the series of compounds): $P_i^{norm} = (O_i - O^{min}) / (O^{max} - O^{min})$ x100.*

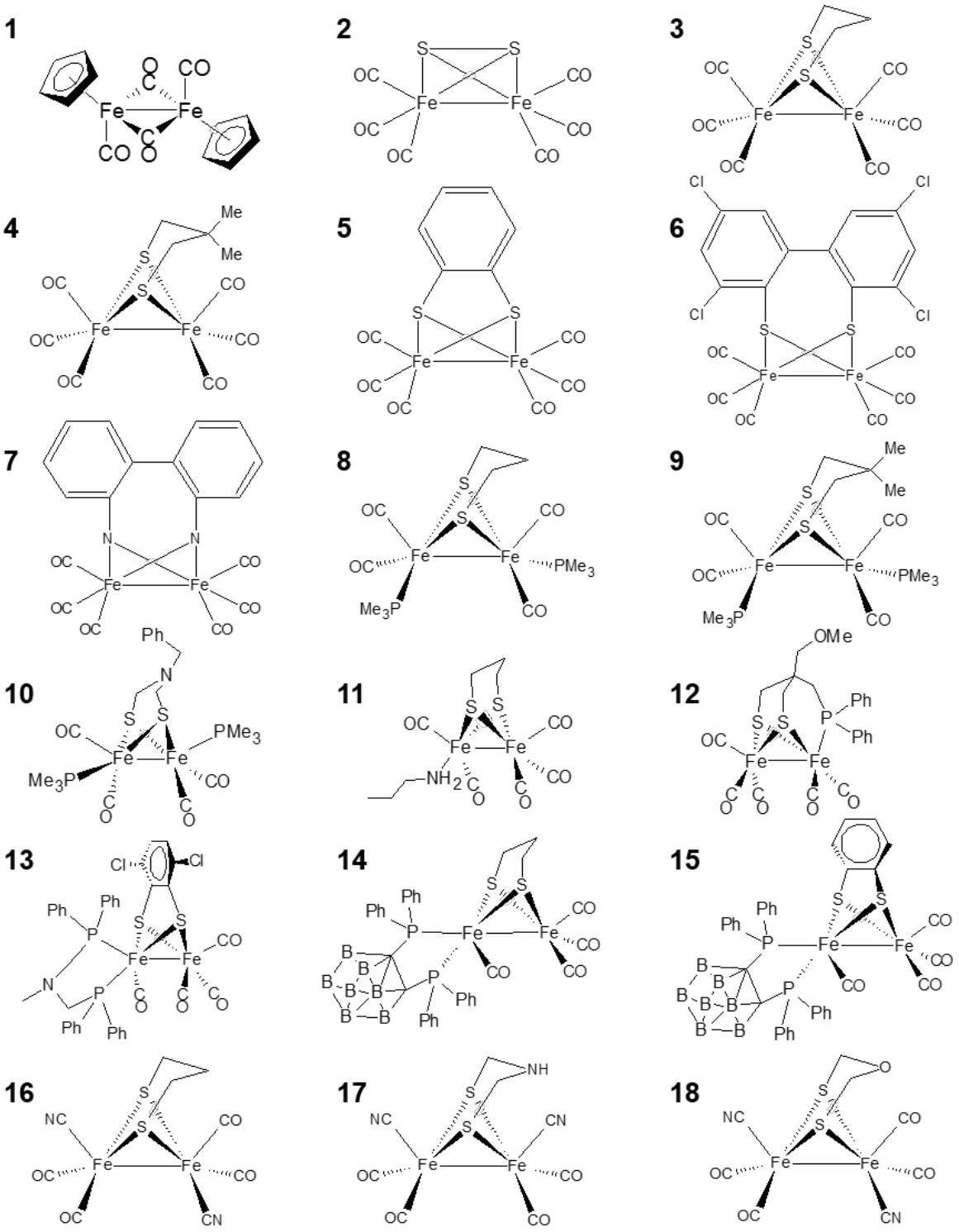

Figure A4-1: Schematic drawing of the structures of the diiron compounds. For crystal structures see Fig. 4-2.

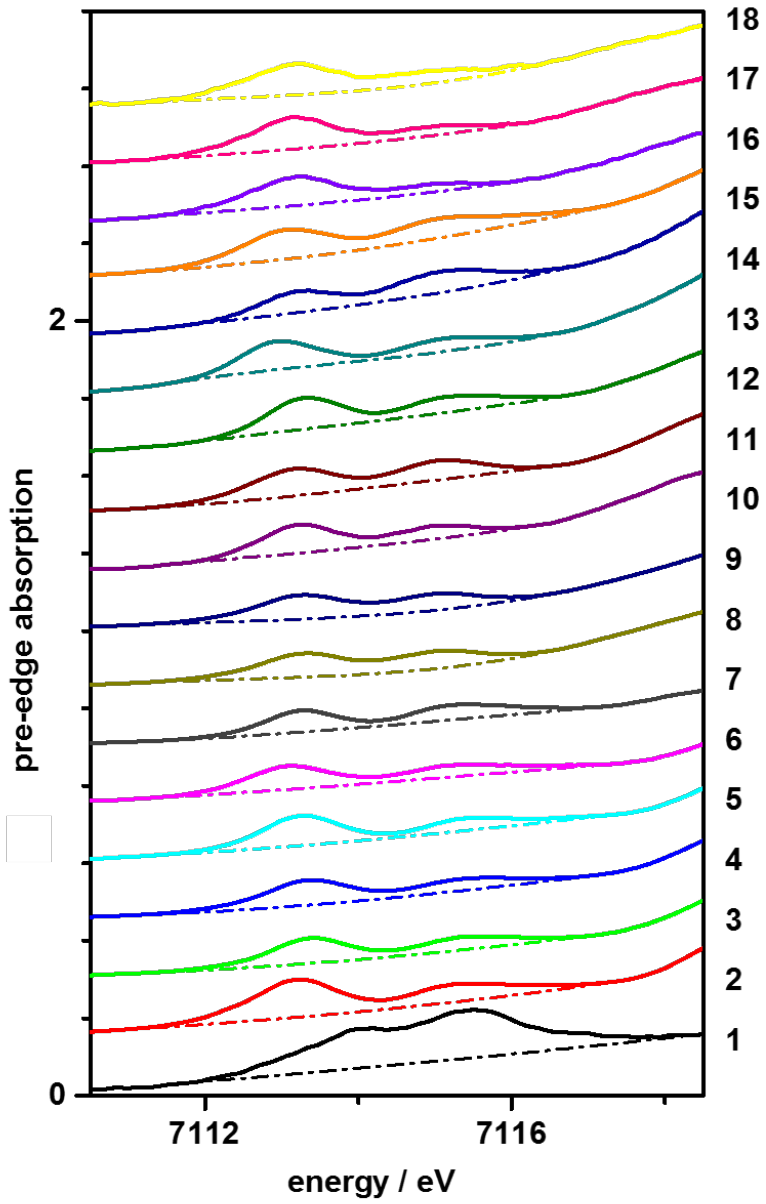

Figure A4-2: Pre-edge absorption features in the XANES. Spectra correspond to data of the 18 compounds in Fig. 4-3A with the pre-edge absorption region shown in magnification (spectra vertically shifted for comparison). Subtraction of smooth background curves (dash-dotted lines) from the spectra yielded the experimental ctv spectra shown in Fig. 4-4A.

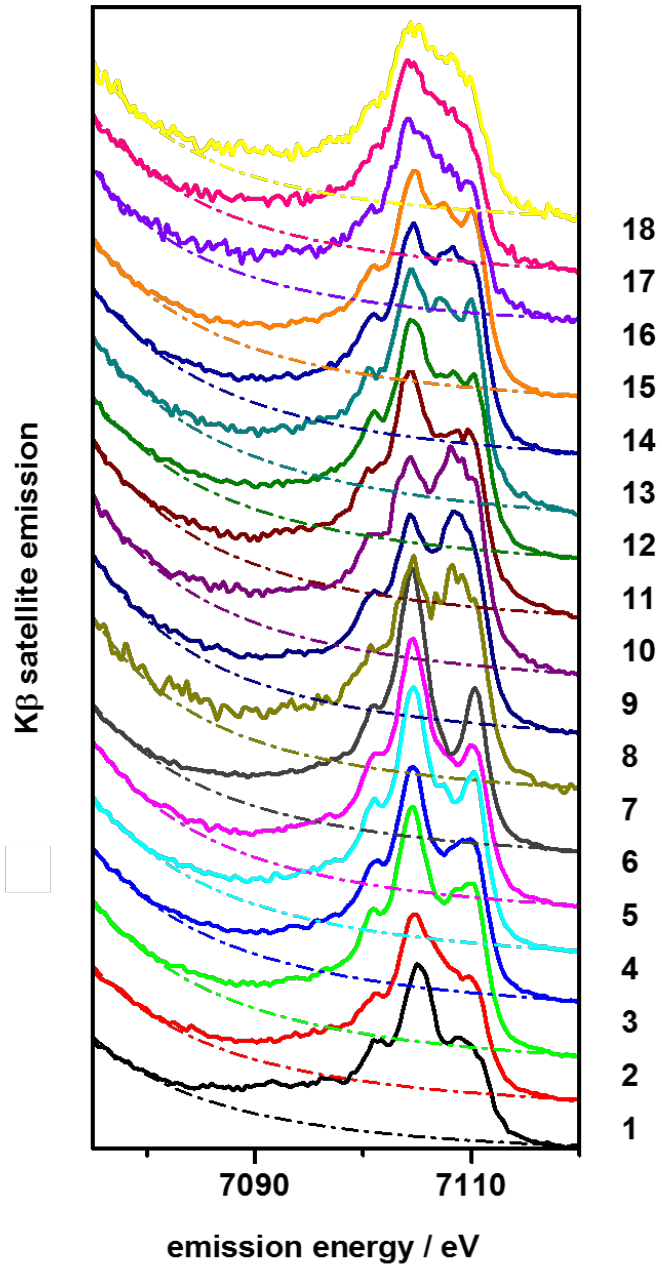

Figure A4-3: Experimental Kβ satellite emission spectra. Non-normalized spectra in the Kβ satellite emission region of the 18 compounds indicated on the right were vertically shifted for comparison. Subtraction of background curves (dash-dotted lines) and normalization of the resulting spectra to unity area yielded the experimental vtc spectra shown in Fig. 4-5A.

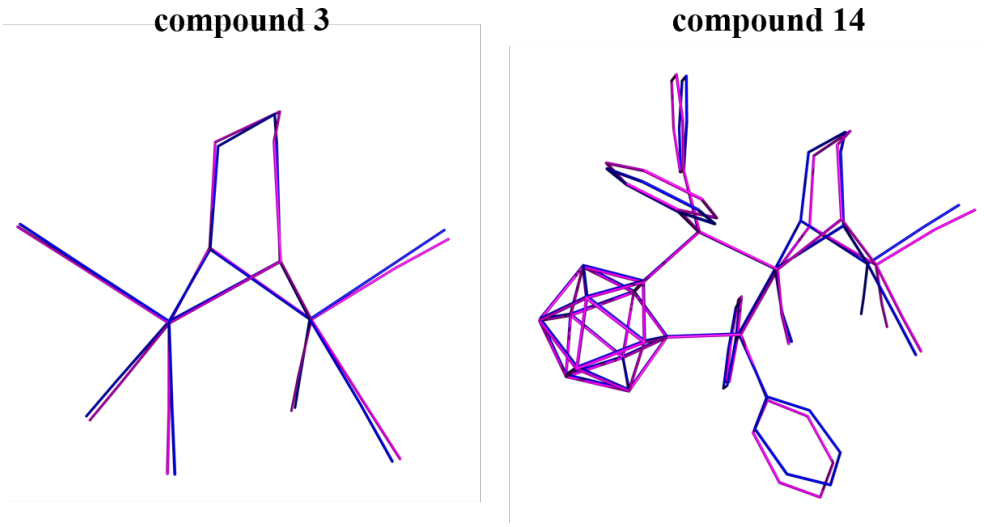

*Figure A4-4: Crystal structures and geometry-optimized structures. Colours: blue lines = crystal structures; magenta lines, geometry-optimized structures (Table A4-1). Protons were omitted for clarity. Note small coordinate deviations between crystal and relaxed structures for the symmetric (**3**) and asymmetric (**14**) compounds, which were also found for the remaining compounds (Table A4-1, Fig. A4-5). Relaxed structures were only used for calculation of CM5 charges (Fig. 4-9) whereas crystal structures were used for calculation of ctv/vtc spectra (Figs. 4-4 - 8) and electronic parameters (Figs. 4-10 and -11, Table 4-2).*

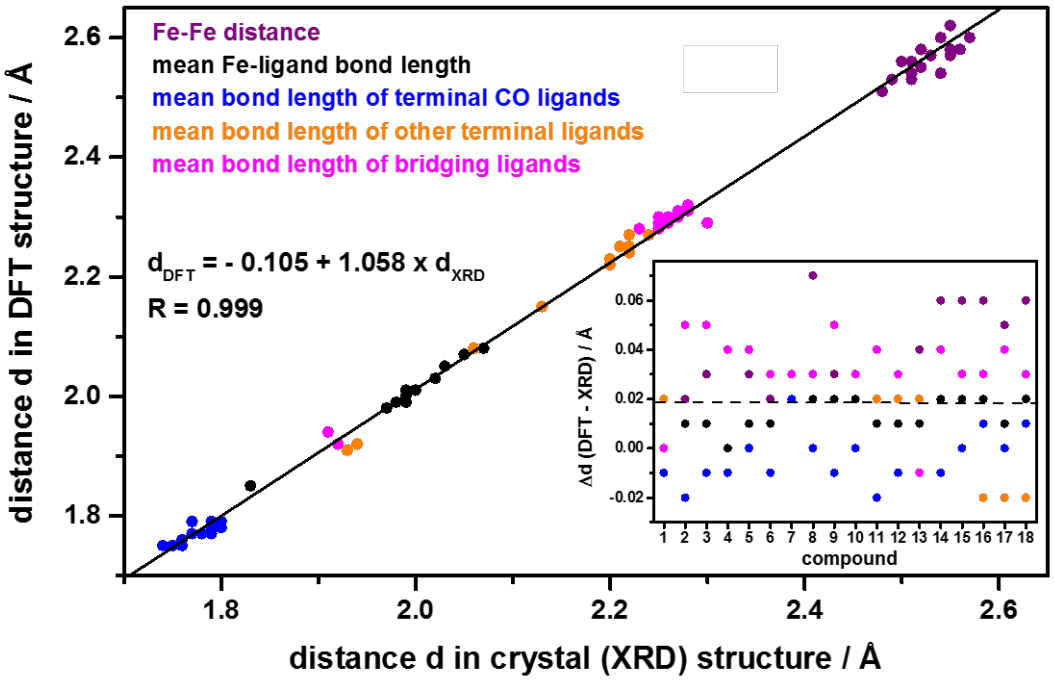

*Figure A4-5: Interatomic distances in **1-18** from crystal and relaxed structures. For individual bond lengths in the compounds in crystal structures and geometry-optimized structures from DFT see Table A4-1. Note good correlation of distances in DFT and XRD structures and overall small overestimation of distances (mean of ~0.02 Å, inset) by the DFT approach.*

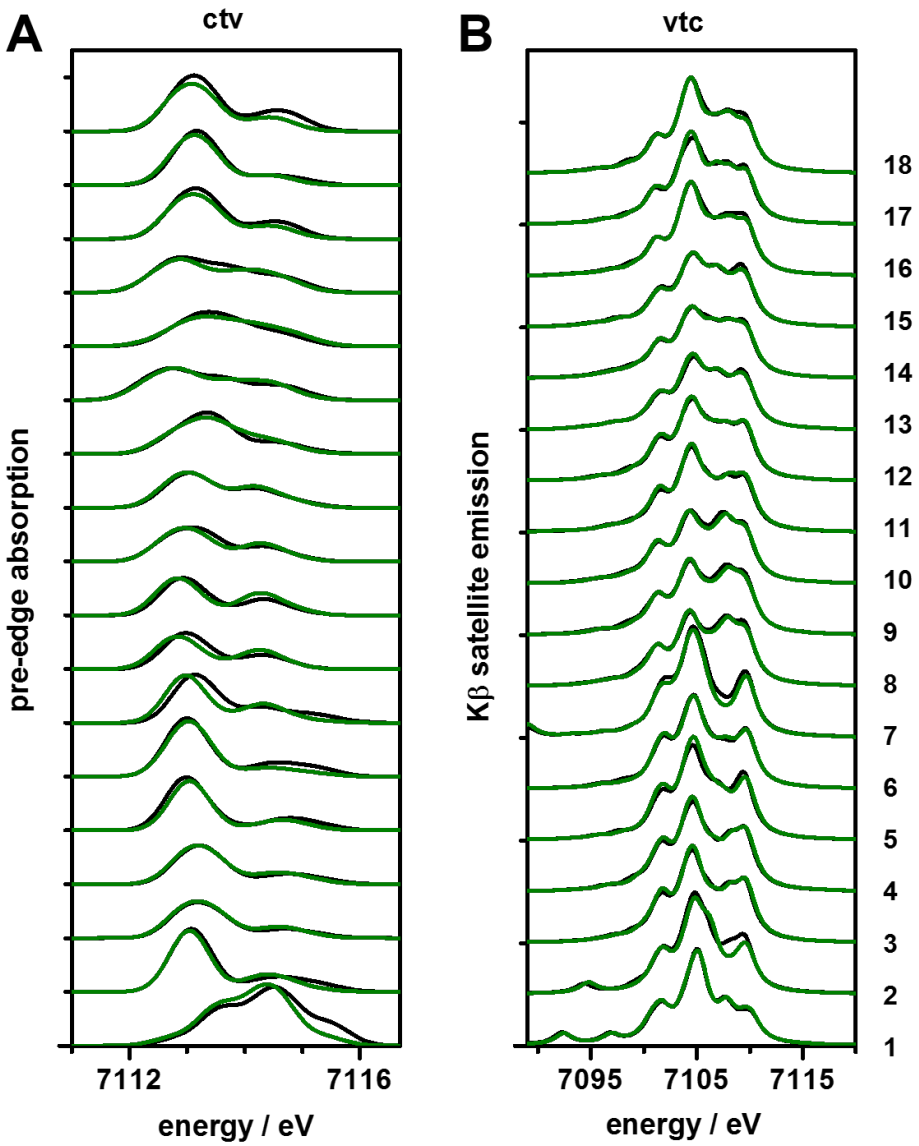

Figure A4-6: Calculated ctv and vtc spectra for crystal and relaxed structures. Left: ctv spectra. Right: vtc spectra. Black lines, spectra from single-point DFT calculations on crystal structures; green lines, calculations on DFT geometry-optimized structures (Table A4-1) for compounds indicated on the right. Note high similarity of ctv/vtc spectra from both computational approaches.

Appendix Chapter 7

Examples of input-files for calculations on model structures.

(A) DFT approach for geometry optimization and frequency analysis (Gaussian09)
(i) Assignment of anti-ferromagnetic coupling

```
%chk=/path/FeFe_OH_H2O_Y_a_afc_bt.chk
%mem=2000MB
%nprocshared=4
#p UB3LYP/TZVP guess=(only,Fragment=12) output=wfn

FeFe_OH_H2O_Y_a_afc_bt

0 1 3 -6 3 6 -1 1 -1 1 -1 1 0 1 -1 1 -1 1 0 1 0 1 -1 1 0 1
 Fe(Fragment=1)         -0.62220700   -1.75928200    0.04993700
 Fe(Fragment=2)          2.34601700    0.17200400   -0.49241900
…
```

(ii) Geometry optimization

```
%chk=/path/FeFe_OH_H2O_Y_b_optf_bt.chk
%mem=35000MB
%nprocshared=8
#p UB3LYP/TZVP scf=(conver=7,nosymm) guess=read geom=(check,modredundant)
#scrf=(solvent=diethylether) opt=(modredundant,tight) freq output=wfn

FeFe_OH_H2O_Y_b_optf_bt

0 1

X 9 F
X 23 F
X 33 F
X 45 F
X 58 F
X 68 F
X 80 F
X 90 F
X 91 F
X 92 F
X 93 F
X 94 F
X 95 F
X 96 F

/path/FeFe_OH_H2O_Y_b_optf_bt.wfn
```

(B) QM/MM approach for geometry optimization and frequency analysis (Gaussian09)
(i) Generation of input-file for assignment of anti-ferromagnetic coupling

```
%chk=/path/4HR0_FeFe_OH-H2O_Y_a_afc-ini.chk
%mem=10GB
%nprocshared=16
#oniom(ub3lyp/tzvp:uff)=OnlyInputFiles geom=connectivity

4HR0_FeFe_OH-H2O_Y_a_afc-ini

0 11 0 11 0 11
 N-N_3-0.057700(PDBName=N,ResName=VAL,ResNum=2_B)    0   26.15229700   -
3.61747300    6.79259600 L
 C-C_3--0.005400(PDBName=CA,ResName=VAL,ResNum=2_B)  0   26.23746400   -
2.98342500    5.46066900 L
…
```

(ii) Assignment of anti-ferromagnetic coupling

```
%chk=/path/4HR0_FeFe_OH-H2O_Y_b_afc-fix.chk
%mem=40GB
%nprocshared=16
# ub3lyp/tzvp geom=connectivity guess=(only,Fragment=12) IOp(2/15=1,5/32=2,5/38=1)

4HR0_FeFe_OH-H2O_Y_b_afc-fix

0 1 0 1 3 6 3 -6 -1 1 0 1 0 1 0 1 -1 1 -1 1 -1 1 -1 1 -1 1
  Bq-#1-
0.057700(Iso=14.00307401,Spin=2,ZNuc=7.,QMom=2.044,GFac=0.403761,PDBName=N,R
esName=VAL,ResNum=2_B)         26.152296996445     -3.617472989030
6.792596003100
  Bq-#1--0.005400(Iso=12,ZNuc=6.,PDBName=CA,ResName=VAL,ResNum=2_B)
26.237463996386     -2.983424989022      5.460669003100
…
```

(iii) Geometry optimization

```
%chk=/path/4HR0_FeFe_OH-H2O_Y_c_afc-opt.chk
%mem=50GB
%nprocshared=16
#opt=tight oniom(ub3lyp/tzvp:uff) guess=read geom=connectivity
#scf=(nosymm,maxcycles=1024,conver=5) int=grid=ultrafine

4HR0_FeFe_OH-H2O_Y_c_afc-opt

0 1 0 1 0 1
 N-N_3-0.057700(PDBName=N,ResName=VAL,ResNum=2_B)    0   26.15229700   -
3.61747300    6.79259600 L
 C-C_3--0.005400(PDBName=CA,ResName=VAL,ResNum=2_B)  0   26.23746400   -
2.98342500    5.46066900 L
…
```

(C) Calculation of XAS/XES spectra (ORCA).
(i) Single point calculation

```
!uks b3lyp tzvp PAL4 tightscf
%cosmo epsilon 4 end
%output Print[P_ReducedOrbPopMO_M] 1 end

 %scf
       #GuessMode CMatrix
        FlipSpin 0
        FinalMs 0.0
   DirectResetFreq 0
   TCut   1e-14
   Thresh 1e-12
   MaxCore 2000
   MaxIntMem 2000
   CNVZerner true
   maxiter 10000
   DIIS Start 0.0005  end
   DampErr    0.0005
   DIISMaxIt 1000
   ShiftErr 0.0 # do NOT turn off level shift! Please!
   LevelShift 0.4
   DampFac 0.8
   DampMax 0.8
   DampMin 0.0
 end

* xyzfile 0 11 FeFe_OH_H2O_Y_afcM1_b3lyp.xyz
```

(ii) Calculations of XAS/XES spectra

```
!uks b3lyp tzvp PAL4 tightscf moread noiter
%moinp "FeFe_OH_H2O_Y_afcM1_b3lyp.gbw"
%cosmo epsilon 4 end

* xyzfile 0 1 FeFe_OH_H2O_Y_afcM1_b3lyp.xyz

%xes
  MaxNVirt 800 # Number of empty MOs that accept electrons
  DoQuad true  # Switch for the calculation of magnetic dipole and electric quadrupole
transition moments
  DoXAS  true  # Do absorbtion
  CoreOrb 0,1,0,1 # List of core orbitals in which a hole is generated
  OrbOp   0,0,1,1 # The operators for each CoreOrb (0: spin up, 1: spin down)
  Normalize false # if set to true, most intensive feature will be set to 1 (default true)

End
```

Table A7-1: Representative cofactor coordinates from DFT and QM/MM.[a]

(A) DFT: FeFe (μOH/H_2O)

Fe	-0.622207	-1.759282	0.049937	C	0.934835	2.748031	0.430696
Fe	2.346017	0.172004	-0.492419	C	1.110041	4.194592	0.844348
O	-0.294842	-1.537935	-1.952142	C	0.844470	4.349513	2.345505
O	1.180089	0.126042	-2.205729	H	2.113781	4.527319	0.584307
C	0.250766	-0.613023	-2.620683	H	0.398985	4.798456	0.273480
C	-0.291381	-0.383182	-4.015634	H	1.557634	3.764487	2.930245
C	-1.761412	0.050370	-3.948185	H	0.944736	5.393732	2.646813
C	-2.435846	0.163591	-5.312059	H	-0.159248	4.014523	2.604707
C	-3.916981	0.502339	-5.168605	O	3.781529	0.753127	-1.642390
H	0.320258	0.360448	-4.526308	O	5.253975	2.245287	-2.376142
H	-0.213206	-1.327042	-4.563018	C	4.137183	1.745064	-2.431304
H	-1.830229	1.011644	-3.428359	C	3.125857	2.221879	-3.475588
H	-2.309740	-0.669958	-3.338284	C	2.793112	3.720345	-3.395247
H	-1.934092	0.925774	-5.917560	H	3.583491	2.008869	-4.447138
H	-2.324533	-0.783082	-5.851855	H	2.221149	1.628188	-3.396251
H	-4.053887	1.453990	-4.648295	H	2.119689	3.997492	-4.208677
H	-4.407533	0.583539	-6.141622	H	2.301287	3.960989	-2.451330
H	-4.440389	-0.265165	-4.593358	H	3.694933	4.329342	-3.475580
O	0.902528	-3.077892	0.134492	N	3.607856	0.234240	1.342098
O	2.697549	-1.902553	-0.541721	N	4.235129	-0.493622	3.313892
C	2.118514	-2.976015	-0.204896	C	3.370854	-0.648766	2.296927
C	2.943570	-4.256347	-0.204192	C	5.078215	0.552024	2.997916
C	2.254978	-5.491914	0.386942	C	4.689937	1.012144	1.769623
H	3.878409	-4.034553	0.316883	C	5.273096	2.149156	0.985145
H	3.228301	-4.434423	-1.245965	C	6.484846	2.833624	1.641682
H	2.927396	-6.349961	0.331746	H	2.592135	-1.390834	2.282396
H	1.988317	-5.335540	1.433023	H	4.266226	-1.052516	4.152040
H	1.343107	-5.735227	-0.157638	H	5.862963	0.868319	3.660449
O	-2.012293	-3.059217	-0.618174	H	5.545936	1.793576	-0.009463
O	-3.820711	-1.901226	-1.243122	H	4.483269	2.885359	0.811003
C	-3.118092	-2.932877	-1.257912	H	6.234187	3.261287	2.615717
C	-3.582009	-4.111217	-2.097707	H	7.312699	2.134466	1.780388
C	-2.902573	-5.442018	-1.806188	H	6.837437	3.642951	1.001713
H	-4.666155	-4.181685	-1.986674	O	-2.742355	2.198841	0.997066
H	-3.408872	-3.817358	-3.138642	C	-3.628452	3.240974	1.098663
H	-3.275664	-6.213251	-2.483474	C	-3.211341	4.536270	1.234799
H	-3.095884	-5.773219	-0.784552	C	-4.142273	5.542899	1.363621
H	-1.822637	-5.369441	-1.932823	C	-5.509141	5.259858	1.368010
N	-1.095838	-2.240951	2.153282	C	-5.902332	3.942571	1.226227
N	-1.164437	-1.812005	4.301079	C	-4.977386	2.938005	1.093826
C	-0.720217	-1.398635	3.102175	C	-6.528084	6.369541	1.490165
C	-1.866098	-2.984919	4.115730	H	-1.801439	2.489790	0.936991
C	-1.825245	-3.252540	2.775332	H	-2.153210	4.769460	1.240842

C	-2.440438	-4.396783	2.032760	H	-3.807765	6.568374	1.473113
C	-3.134747	-5.431458	2.914346	H	-6.958538	3.695522	1.225472
H	-0.142270	-0.504623	2.946871	H	-5.284307	1.904682	0.987665
H	-1.021278	-1.335171	5.177578	H	-6.122703	7.223827	2.034848
H	-2.322562	-3.510064	4.934837	H	-6.843926	6.730252	0.506283
H	-1.669853	-4.876502	1.425486	H	-7.424087	6.030307	2.013394
H	-3.159289	-3.995089	1.319356	O	0.627248	-0.322987	0.547663
H	-2.443029	-5.891933	3.624030	H	0.172968	0.553764	0.631337
H	-3.956407	-4.989392	3.482697	O	-2.199002	-0.368262	0.006908
H	-3.552626	-6.226996	2.295984	H	-2.434358	0.514671	0.349310
O	1.923583	2.157780	-0.108463	H	-2.978704	-0.803663	-0.457797
O	-0.160580	2.186285	0.680292				

(B) DFT: MnFe (μOH/H_2O)

Mn	-0.210446	-1.811921	0.073623	C	0.195053	2.734145	0.597589
Fe	2.266468	0.685542	-0.518181	C	-0.032393	4.191719	0.941602
O	-0.717471	-0.926988	-1.603554	C	-0.268507	4.356320	2.445339
O	1.116108	0.219442	-2.191253	H	0.821697	4.779463	0.608517
C	-0.031337	-0.235150	-2.414213	H	-0.908954	4.535321	0.384273
C	-0.660602	0.036820	-3.765438	H	0.604258	4.030278	3.015321
C	-2.171007	-0.159409	-3.783875	H	-0.454385	5.403239	2.691890
C	-2.810931	0.081858	-5.145961	H	-1.124312	3.770111	2.778533
C	-4.312810	-0.174215	-5.088671	O	3.331543	1.756086	-1.718214
H	-0.377309	1.046036	-4.070413	O	4.119082	3.632096	-2.603257
H	-0.171820	-0.641953	-4.474127	C	3.198838	2.838855	-2.455194
H	-2.629482	0.507194	-3.047119	C	1.862199	3.027690	-3.169609
H	-2.404924	-1.172837	-3.453212	C	1.488226	4.474971	-3.478452
H	-2.619122	1.108485	-5.475770	H	1.082728	2.547586	-2.588050
H	-2.350330	-0.573917	-5.893012	H	1.940638	2.451572	-4.098272
H	-4.796510	0.488382	-4.366252	H	1.360410	5.052902	-2.560631
H	-4.789771	-0.011528	-6.058269	H	2.256409	4.967350	-4.075728
H	-4.523022	-1.202304	-4.782935	H	0.547771	4.510541	-4.032570
O	1.648050	-2.681602	-0.606103	N	3.606113	1.029887	1.211235
O	3.229786	-1.093504	-0.671535	N	4.716007	0.429573	3.004102
C	2.839189	-2.309892	-0.673742	C	3.820227	0.053590	2.076329
C	3.923112	-3.374093	-0.777720	C	5.107643	1.720606	2.717292
C	3.545007	-4.718023	-0.149674	C	4.416649	2.097845	1.598416
H	4.838558	-2.969881	-0.343003	C	4.490988	3.398838	0.862876
H	4.127336	-3.500628	-1.846484	C	5.532364	4.373400	1.423227
H	4.356181	-5.436277	-0.283306	H	3.367909	-0.920935	2.046238
H	3.358732	-4.615969	0.921315	H	5.058863	-0.143798	3.758683
H	2.644331	-5.125308	-0.607160	H	5.832435	2.240506	3.316405
O	-1.069625	-3.363129	-0.719584	H	4.704710	3.196083	-0.187551
O	-3.275366	-2.946094	-0.777484	H	3.501135	3.863561	0.870381
C	-2.269458	-3.552091	-1.169714	H	5.320597	4.646627	2.460146

C	-2.394607	-4.596299	-2.267885	H	6.538106	3.949122	1.382822
C	-1.510813	-5.829938	-2.097584	H	5.536213	5.290069	0.832501
H	-3.447679	-4.868498	-2.342613	O	-3.274850	1.444299	1.080875
H	-2.133457	-4.082589	-3.199877	C	-4.373473	2.227754	1.321444
H	-1.641721	-6.507037	-2.943927	C	-4.287926	3.577967	1.521558
H	-1.768597	-6.380046	-1.190080	C	-5.433099	4.307532	1.751436
H	-0.458516	-5.554220	-2.038970	C	-6.682738	3.687019	1.793972
N	0.015678	-2.679197	1.997298	C	-6.739950	2.321969	1.585843
N	0.528310	-2.686431	4.123346	C	-5.601295	1.593070	1.352763
C	0.600020	-2.000230	2.972452	C	-7.939181	4.494165	2.027299
C	-0.144195	-3.865779	3.880877	H	-2.413976	1.920156	1.093332
C	-0.469901	-3.859178	2.553659	H	-3.323856	4.072547	1.495184
C	-1.237132	-4.875318	1.774876	H	-5.361222	5.377392	1.911358
C	-1.618847	-6.115733	2.566286	H	-7.698627	1.814998	1.612618
H	1.046207	-1.028489	2.863909	H	-5.643733	0.522893	1.192070
H	0.885997	-2.377587	5.013689	H	-7.715293	5.445626	2.511931
H	-0.332365	-4.584268	4.657340	H	-8.449598	4.718399	1.085507
H	-0.657085	-5.156921	0.896405	H	-8.648387	3.953924	2.657917
H	-2.144099	-4.400812	1.395595	O	0.772912	-0.288369	0.643524
H	-0.739491	-6.644940	2.941821	H	0.125968	0.444267	0.834711
H	-2.256567	-5.873659	3.419938	O	-2.250480	-1.177184	0.902835
H	-2.172856	-6.808071	1.930714	H	-2.638435	-0.282985	0.909686
O	1.273708	2.427845	-0.003330	H	-2.823672	-1.742244	0.324908
O	-0.671357	1.895285	0.949523				

(C) QM/MM (ONIOM high layer): FeFe (μOH/H_2O)

Fe	-1.783154	4.830755	1.969057	C	-0.191656	3.225756	-2.195505
Fe	1.272637	3.797602	0.438166	C	-0.095072	2.864408	-3.669845
O	-1.522818	2.883647	2.423910	C	-0.408466	4.124996	-4.517089
O	0.196125	2.179898	1.178412	H	0.879621	2.430791	-3.883565
C	-0.821879	1.979815	1.886527	H	-0.851274	2.101873	-3.874405
C	-1.241226	0.545469	2.143845	H	0.440716	4.775986	-4.515476
C	-2.749734	0.319415	2.033629	H	-0.632038	3.832888	-5.521872
C	-3.163683	-1.131277	2.295947	H	-1.250301	4.635852	-4.098472
C	-4.616051	-1.363925	1.870204	O	2.824611	2.725575	0.557438
H	-0.701851	-0.094179	1.445572	O	4.539419	1.554292	-0.226601
H	-0.893761	0.293160	3.151340	C	3.391020	1.595580	0.174445
H	-3.080094	0.611460	1.031799	C	2.535843	0.343574	0.247704
H	-3.269881	0.984740	2.725602	C	2.571071	-0.412122	-1.095789
H	-2.499362	-1.805333	1.745079	H	1.527198	0.622731	0.532830
H	-3.034525	-1.353782	3.357353	H	2.948456	-0.268928	1.053882
H	-4.715778	-1.171416	0.822399	H	2.342123	0.265024	-1.892002
H	-4.889403	-2.378125	2.074108	H	3.546713	-0.824389	-1.247637
H	-5.257845	-0.704801	2.416608	H	1.848824	-1.201434	-1.080075
O	-0.300286	5.460952	3.181357	N	2.452044	5.503487	-0.494156
O	1.607767	4.776198	2.224598	N	3.207267	7.559209	-0.595224

C	0.958894	5.453172	3.066155	C	2.256376	6.744102	-0.095230
C	1.788303	6.320705	4.008344	C	4.059642	6.791823	-1.359656
C	1.047118	7.113781	5.097057	C	3.588392	5.506456	-1.306219
H	2.406937	6.959285	3.370361	C	4.101014	4.245960	-1.942121
H	2.501869	5.639671	4.480686	H	1.464128	7.076758	0.552309
H	1.758066	7.546370	5.769604	H	3.286872	8.550481	-0.452940
H	0.468879	7.890271	4.641422	H	4.909465	7.222854	-1.859163
H	0.398561	6.456665	5.637864	H	4.368993	3.545109	-1.179301
O	-3.150751	4.701746	3.461581	H	3.338248	3.823687	-2.562423
O	-5.077357	4.148709	2.474390	H	4.960985	4.471127	-2.537646
C	-4.356737	4.271035	3.486092	O	-3.881260	3.342677	-1.863984
C	-4.983331	3.876524	4.809797	C	-4.805174	3.142767	-2.845896
C	-4.262027	4.244477	6.114128	C	-4.457225	2.923335	-4.176260
H	-5.987487	4.307705	4.799532	C	-5.451217	2.653205	-5.110882
H	-5.138751	2.803186	4.698627	C	-6.802273	2.591601	-4.763572
H	-4.955446	4.206397	6.928143	C	-7.129094	2.883735	-3.435628
H	-3.860934	5.233152	6.033222	C	-6.151964	3.153840	-2.491183
H	-3.466980	3.550331	6.290088	C	-7.812658	2.197270	-5.830890
N	-2.353568	6.970883	1.512561	H	-2.950218	3.425230	-2.177866
N	-2.445749	8.751114	0.238529	H	-3.415361	2.941668	-4.472083
C	-1.844068	7.562282	0.449773	H	-5.164642	2.466876	-6.139969
C	-3.400729	8.921279	1.220086	H	-8.158668	2.876180	-3.099699
C	-3.345839	7.806876	2.012449	H	-6.430363	3.354462	-1.465451
C	-4.161835	7.396835	3.205967	H	-7.314120	1.667673	-6.615675
H	-1.076663	7.143657	-0.178523	H	-8.562733	1.569325	-5.397331
H	-2.253465	9.387223	-0.517217	H	-8.271589	3.077532	-6.230166
H	-4.021816	9.797010	1.269404	O	-0.518614	4.846755	0.449989
H	-3.514545	7.007710	3.963923	H	-0.964645	4.496102	-0.361475
H	-4.864507	6.643813	2.915949	O	-3.341625	4.369370	0.673695
H	-4.687437	8.247035	3.587807	H	-3.484155	3.958986	-0.198768
O	0.862967	3.167365	-1.489543	H	-4.158408	4.234694	1.262808
O	-1.300689	3.639001	-1.774534				

(D) QM/MM (ONIOM high layer): MnFe (μOH/H_2O)

Mn	-1.827283	4.875001	1.908909	C	-0.209612	3.227758	-2.099071
Fe	1.304877	3.826303	0.528473	C	-0.098443	2.853185	-3.569970
O	-1.788337	2.900473	2.087212	C	-0.415347	4.101843	-4.433913
O	0.243170	2.261685	1.392677	H	0.880023	2.422238	-3.772195
C	-0.909997	2.029391	1.830251	H	-0.848291	2.083435	-3.771819
C	-1.292103	0.585719	2.106367	H	0.432945	4.753932	-4.442969
C	-2.791892	0.312093	2.029509	H	-0.640570	3.795693	-5.434136
C	-3.172665	-1.148665	2.286342	H	-1.257024	4.617259	-4.020602
C	-4.627441	-1.392573	1.873805	O	2.843702	2.735468	0.600543
H	-0.740403	-0.040874	1.403964	O	4.510276	1.533148	-0.235751
H	-0.901330	0.350106	3.102285	C	3.368843	1.598294	0.180635

H	-3.151863	0.606929	1.039371	C	2.478831	0.369715	0.237519
H	-3.317886	0.956960	2.736130	C	2.523223	-0.394699	-1.099671
H	-2.507444	-1.808813	1.720113	H	1.472570	0.675001	0.505646
H	-3.027383	-1.379433	3.343689	H	2.858233	-0.248043	1.056714
H	-4.738048	-1.201750	0.826784	H	2.294770	0.275856	-1.901585
H	-4.891373	-2.408598	2.081007	H	3.501326	-0.803683	-1.244404
H	-5.269177	-0.737760	2.425434	H	1.804399	-1.187078	-1.081568
O	-0.246225	5.391377	3.264525	N	2.450070	5.514915	-0.480162
O	1.662207	4.849764	2.221676	N	3.205877	7.568930	-0.608998
C	0.993745	5.463989	3.113045	C	2.260439	6.759571	-0.090543
C	1.830531	6.336776	4.046291	C	4.050368	6.793513	-1.373619
C	1.086150	7.135037	5.127462	C	3.578736	5.509085	-1.302934
H	2.451528	6.970722	3.406597	C	4.088388	4.242731	-1.930441
H	2.542695	5.657847	4.524846	H	1.480804	7.097763	0.569014
H	1.795126	7.578347	5.795092	H	3.288955	8.561127	-0.475368
H	0.502684	7.903603	4.665106	H	4.895791	7.219227	-1.884984
H	0.442199	6.479128	5.675195	H	4.355297	3.546662	-1.162881
O	-3.059839	4.728293	3.415351	H	3.324347	3.817777	-2.547333
O	-5.021852	4.222198	2.446971	H	4.948495	4.461856	-2.528020
C	-4.279540	4.300800	3.435244	O	-3.904621	3.221210	-1.892936
C	-4.868862	3.866724	4.765655	C	-4.825903	3.062882	-2.884594
C	-4.160653	4.258544	6.071821	C	-4.481651	2.863768	-4.218617
H	-5.892626	4.247197	4.762474	C	-5.479892	2.613545	-5.154879
H	-4.969483	2.786454	4.644947	C	-6.830064	2.553041	-4.804789
H	-4.863930	4.240850	6.878040	C	-7.153305	2.830339	-3.473081
H	-3.753499	5.243327	5.975239	C	-6.172392	3.078767	-2.528182
H	-3.371376	3.564295	6.271721	C	-7.845202	2.165747	-5.868809
N	-2.312562	6.984081	1.536350	H	-2.977217	3.357117	-2.192545
N	-2.429613	8.752274	0.251315	H	-3.440001	2.877251	-4.515784
C	-1.811804	7.575006	0.468484	H	-5.196985	2.437492	-6.186756
C	-3.386915	8.916087	1.230943	H	-8.182155	2.824247	-3.134350
C	-3.317020	7.809709	2.032235	H	-6.448862	3.263853	-1.499861
C	-4.132211	7.403531	3.227286	H	-7.350327	1.642864	-6.660385
H	-1.045760	7.158402	-0.161971	H	-8.592015	1.533466	-5.435922
H	-2.244608	9.386452	-0.507754	H	-8.307521	3.048408	-6.258771
H	-4.017851	9.784734	1.277135	O	-0.555986	4.902318	0.504787
H	-3.484115	7.020372	3.987589	H	-0.996472	4.515664	-0.299501
H	-4.832439	6.646855	2.940893	O	-3.477529	4.667596	0.448514
H	-4.660593	8.254118	3.604398	H	-3.598019	4.086850	-0.323806
O	0.833088	3.160456	-1.376606	H	-4.210469	4.455655	1.091310
O	-1.320778	3.652915	-1.695369				

[a]*Coordinates represent geometry-optimized structures. Respective structures for other protonation states were derived by removal of one or two protons (and respective charge adjustment), followed by geometry optimization.*

Table A7-2: Calculated interatomic distances in FeFe and MnFe cofactors with different basis set and functional.[a]

proto-nation state	Functional / basis set	distance [Å] (**FeFe/MnFe**)					
		Fe/Mn^{site1}-Fe^{site2}	Fe/Mn^{site1}-OH_n	Fe/Mn^{site1}-μOH_n	Fe^{site2}-μOH_n	Fe/Mn^{site1}-L^{site1}	Fe^{site2}-L^{site2}
$H_2O/\mu OH$	bp86 / tzvp	3.55 / 3.54	2.15 / 2.28	1.96 / 1.88	2.03 / 2.10	2.07 / 2.05	2.08 / 2.09
	tpssh / tzvp	3.55 / 3.53	2.13 / 2.28	1.96 / 1.88	2.03 / 2.09	2.05 / 2.05	2.07 / 2.07
	b3lyp / tzvp	3.57 / 3.56	2.15 / 2.30	1.97 / 1.89	2.04 / 2.11	2.06 / 2.06	2.08 / 2.08
	b3lyp / cep-31g	3.60 / 3.62	2.07 / 2.19	1.97 / 1.90	2.04 / 2.10	2.04 / 2.04	2.06 / 2.06
$OH/\mu OH$	bp86 / tzvp	3.52 / 3.47	1.86 / 1.82	1.96 / 1.90	2.01 / 2.01	2.08 / 2.03	2.09 / 2.11
	tpssh / tzvp	3.54 / 3.47	1.86 / 1.82	1.99 / 1.93	2.00 / 1.99	2.07 / 2.07	2.07 / 2.07
	b3lyp / tzvp	3.58 / 3.51	1.87 / 1.83	2.00 / 1.94	2.01 / 2.01	2.08 / 2.09	2.08 / 2.08
	b3lyp / cep-31g	3.62 / 3.55	1.87 / 1.84	2.00 / 1.93	2.02 / 2.00	2.06 / 2.06	2.06 / 2.05
$H_2O/\mu O$	bp86 / tzvp	3.22 / 3.26	2.11 / 2.01	1.81 / 1.76	1.81 / 1.85	2.08 / 2.06	2.10 / 2.13
	tpssh / tzvp	3.26 / 3.25	2.12 / 2.02	1.82 / 1.77	1.83 / 1.84	2.07 / 2.06	2.09 / 2.11
	b3lyp / tzvp	3.29 / 3.28	2.15 / 2.06	1.82 / 1.78	1.83 / 1.85	2.08 / 2.07	2.10 / 2.09
	b3lyp / cep-31g	3.34 / 3.33	2.07 / 2.01	1.83 / 1.79	1.85 / 1.87	2.06 / 2.05	2.07 / 2.10
$OH/\mu O$	bp86 / tzvp	3.20 / 3.25	1.88 / 1.85	1.82 / 1.79	1.81 / 1.83	2.09 / 2.09	2.11 / 2.12
	tpssh / tzvp	3.28 / 3.24	1.89 / 1.85	1.86 / 1.82	1.80 / 1.82	2.08 / 2.09	2.09 / 2.10
	b3lyp / tzvp	3.31 / 3.27	1.89 / 1.85	1.87 / 1.83	1.81 / 1.82	2.10 / 2.11	2.10 / 2.12
	b3lyp / cep-31g	3.39 / 3.35	1.89 / 1.85	1.89 / 1.84	1.82 / 1.84	2.08 / 2.09	2.08 / 2.08

[a]*Distances represent values from DFT calculations on model structures (shown in Figs. 7-3a, b, d, and e) with different theoretical levels (used functional and basis set) for geometry optimization.*

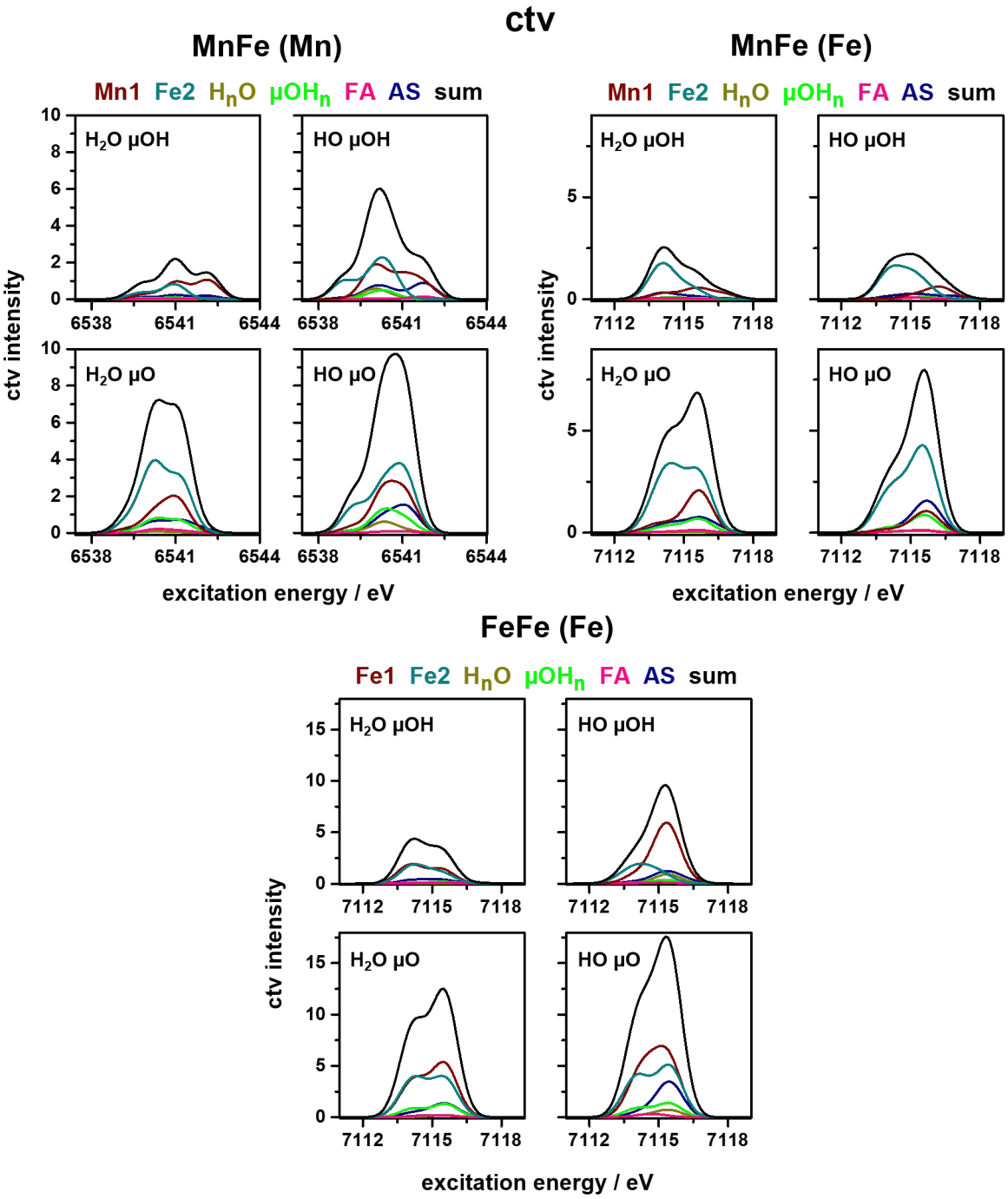

Figure A7-1: Metal and ligand contributions to target MOs for ctv transitions for four cofactor protonation states at Mn and Fe K-edges. Protonation states and ligand species are defined as in Fig. 7-9.

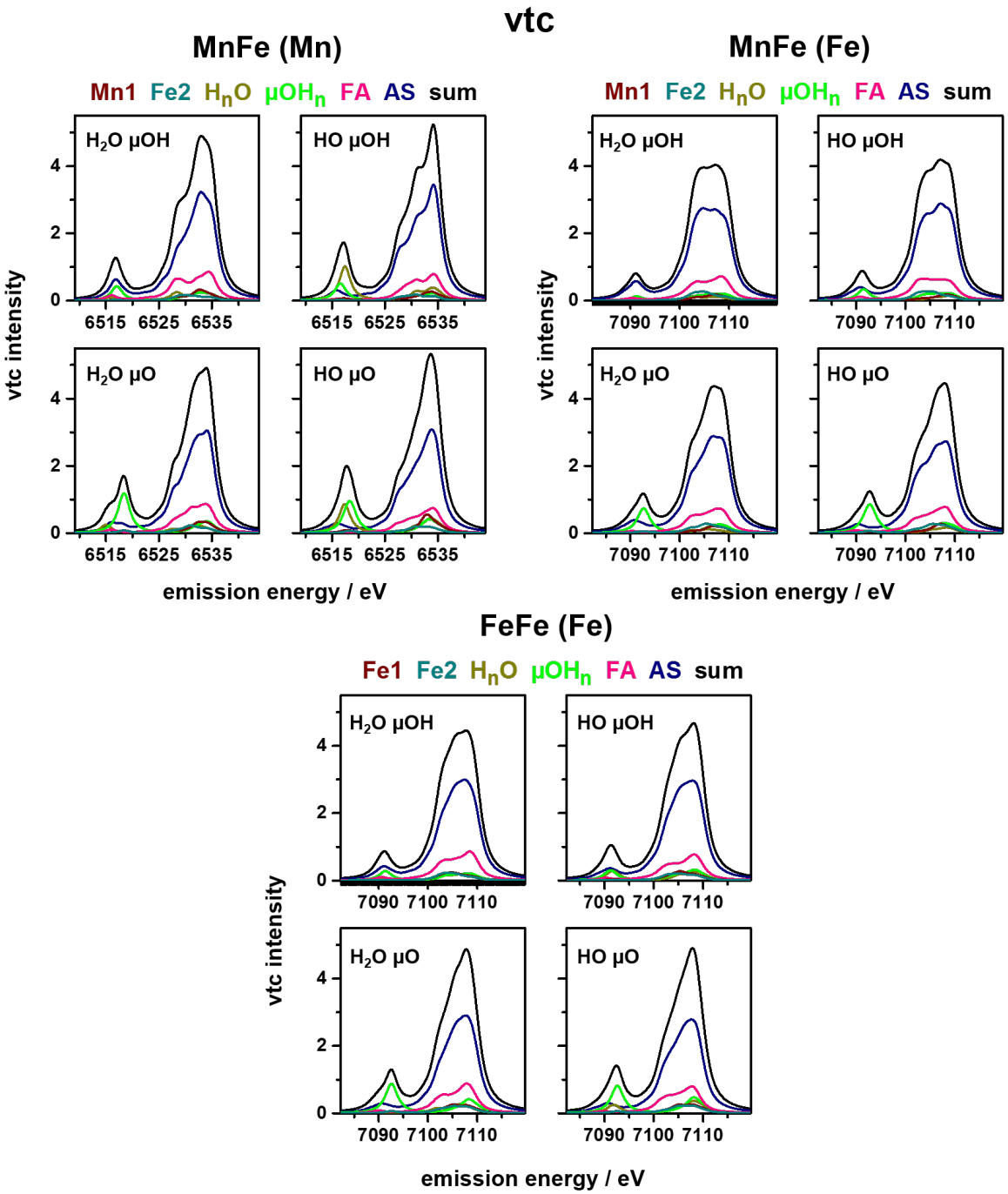

Figure A7-2: Metal and ligand contributions to source MOs for vtc transitions for four cofactor protonation states. Protonation states and ligand species are defined as in Fig. 7-10.

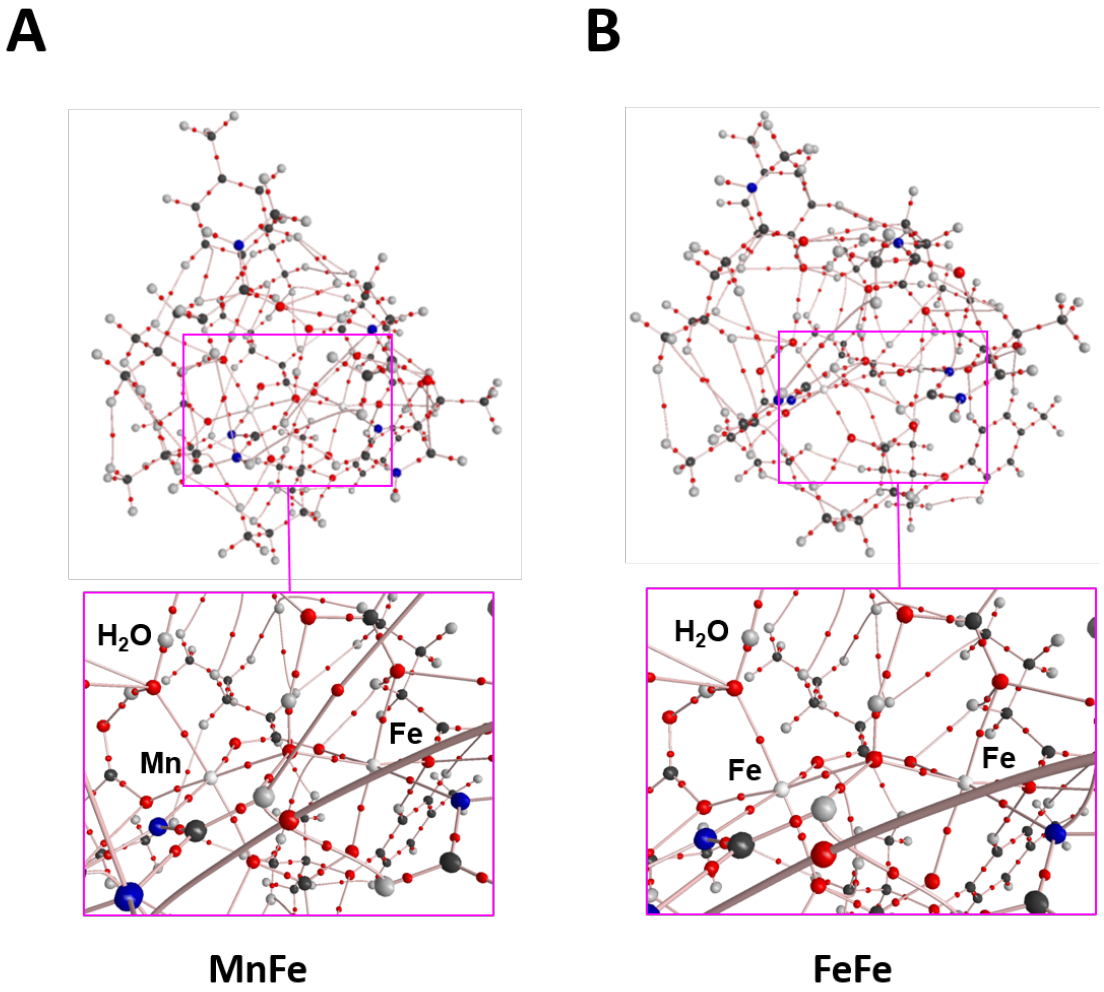

*Figure A7-3: Inter-molecular contacts in (**A**), MnFe and (**B**), FeFe structures from DFT. Data correspond to model size (c) in Fig. 7-2B. Shown bonding patterns and secondary inter-molecular contacts stem from atoms-in-molecules (AIM) topology analysis; small red dots denote bond-critical-points. Color code: white, Mn and Fe; blue, N; black, C; grey, H; red, O. Note weak H-bonding interactions between backbone C-H groups and the water ligand at Mn/Fe1.*

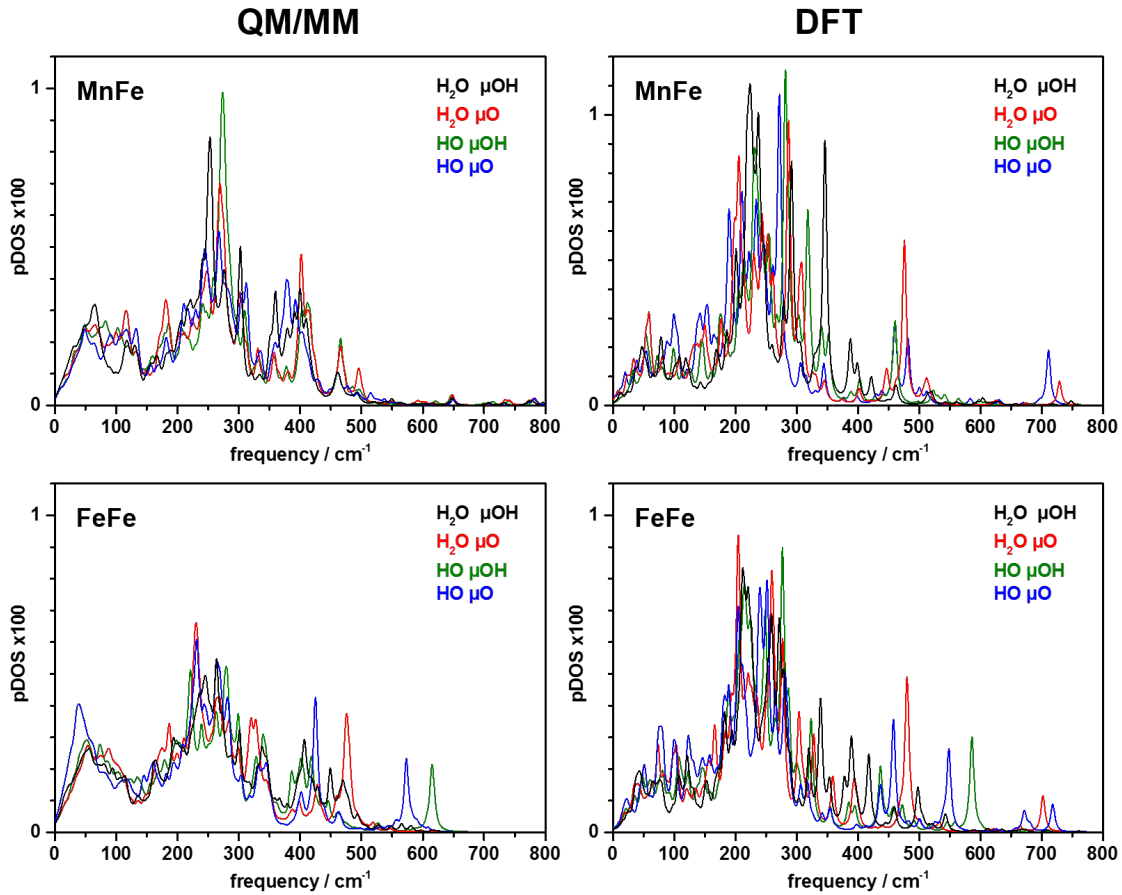

Figure A7-4: Calculated NRVS spectra for four cofactor protonation states. QM/MM: ONIOM approach on the whole-protein structure (Fig. 7-2A and –B, b) using the B3LYP/cep31g functional/basis set combination and ferromagnetic coupling of the Mn/Fe1 and Fe2 ions. DFT: DFT approach on the cofactor structure with Y175 being a hydrogen-bond donor to E202 (Fig. 7-3, a, b, d, e) using the B3LYP/TZVP functional/basis set combination and anti-ferromagnetic coupling of the Mn/Fe1 and Fe2 ions. Note similar intense high-frequency vibrational bands for both theory levels for the three less protonated MnFe and FeFe cofactor structures, which are absent or show lower intensities in the calculated spectra of the H2O/µOH state and in the experimental spectra (Fig. 7-16).

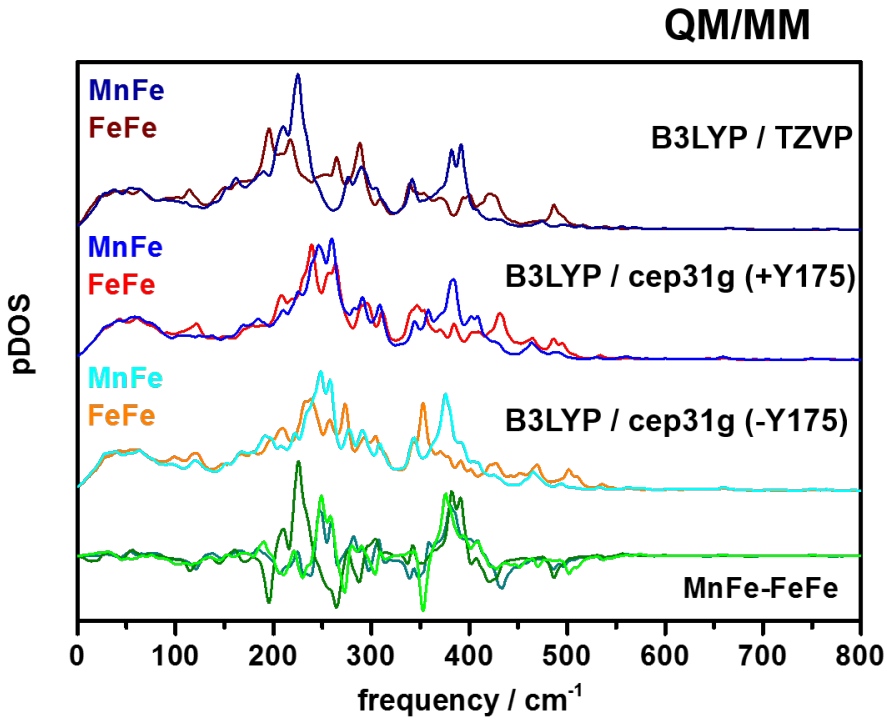

Figure A7-5: Calculated NRVS spectra for theory level variations. pDOS spectra were calculated using the QM/MM approach and the indicated functional/basis set combinations. Respective difference spectra are shown on the bottom. (+/-Y175, Tyr175 was included or not in the DFT "high-layer" in the ONIOM calculations).

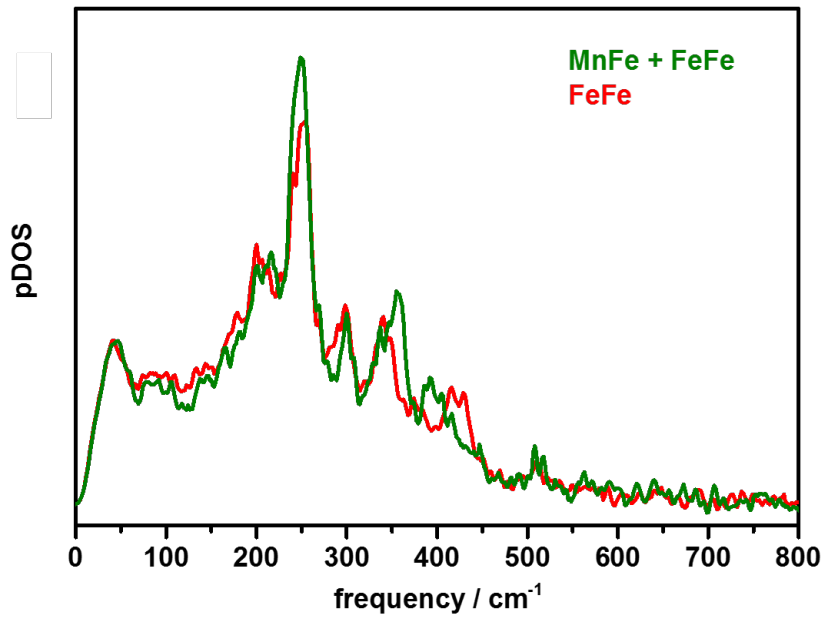

Figure A7-6: Experimental NRVS spectra for Mn/Fe loaded R2lox. The MnFe + FeFe spectrum represents a mixture of FeFe and MnFe cofactor sites (see Fig. 7-4). Subtraction of 35% of the FeFe spectrum (Fig. 7-16) from the MnFe + FeFe spectrum yielded the pure Fe spectrum of the MnFe cofactor shown in Fig. 7-16.

Appendix Chapter 8

Table A8-1: Metal contents from TXRF.

	concentration		ratios		metal clusters [%]		
protein:Mn:Fe loading ratio	**protein [mM]**	**Mn: protein**	**Fe: protein**	**Mn/Fe**	**Mn/Fe**	**Fe/Fe**	**total**
A171F-R2lox							
1:2.4:1.2	1.03	0.56	1.12	0.5	56.5	27.5	84
1:2:1	2.82	0.63	1.02	0.6	64	19	83
1:0:4	0.98	<0.01	2.71	<0.01	0	136	136
1:0:3	1.27	<0.01	2.52	<0.01	0	127	127
E69D-R2lox							
1:2.4:1.2	1.25	0.17	1.15	0.2	17	49	66
1:2:1	2.44	0.20	1.03	0.5	19.5	42	61.5
1:0:4	1.27	<0.01	2.84	<0.01	0	140	140
1:0:3	2.70	<0.01	2.46	<0.01	0	123	123
G68L-R2lox							
1:2.4:1.2	1.38	0.56	1.20	0.5	56	32	88
1:2:1	2.92	0.84	1.05	0.8	83.5	10.5	94
1:0:4	1.24	<0.01	2.73	<0.01	0	136.5	136.5
1:0:3	2.26	<0.02	2.99	<0.01	0	150	150
Y175F-R2lox							
1:2.4:1.2	1.07	0.49	1.41	0.3	48.5	46.5	95
1:0:4	1.22	<0.01	2.45	<0.01	0	122.5	122.5
F109Y-R2lox							
1:2:1	1.23	0.30	1.16	0.3	29	44	73
1:0:3	1.35	<0.02	2.67	<0.01	0	133	133
V72A-R2lox							
1:2:1	3.03	0.63	0.95	0.7	63	16	79
1:0:3	2.57	<0.02	2.88	<0.01	0	144	144
Y162F-R2lox							
1:2:1	1.13	0.86	1.16	0.7	85	16	101
1:0:3	1.24	<0.02	3.03	<0.01	0	152	152

The amounts of metal cluster species were calculated assuming that all metals are bound in dimer sites and the heterometallic cofactor assembly is preferred.

Table A8-2: Metal contents of R2c and R2lox samples before and after reconstitution with Mn(II) and Fe(II) in solution, as determined by TXRF.

		concentration	ratios		metal clusters [%]		
protein (batch)	**protein:Mn:Fe loading ratio**	**protein [mM]**	**Mn: protein**	**Fe: protein**	**Mn/Fe**	**Fe/Fe *Mn/Mn**	**total**
R2c							
Mn titration	apo	1.00	0.01	0.26	1	12.5	13.5
	1:2:2	0.12	0.59	1.44	59	42	101
	1:8:2	0.12	0.76	1.36	76	30	106
Fe titration	apo	1.10	0.00	0.13	0	6.5	6.5
	1:4:0.2	0.14	0.72	0.22	22	25*	47
	1:4:0.6	0.14	0.73	0.58	58	7*	65
	1:4:1	0.15	0.74	0.81	74	3	77
R2lox							
Mn titration	apo	0.93	0.00	0.16	0	8	8
	1:2:2	0.14	0.21	1.50	21	64	85
	1:8:2	0.12	0.43	1.62	43	60	103
Fe titration A	apo	0.28	0.00	0.14	0	7	7
	1:4:0.2	0.11	0.26	0.44	26	9	35
	1:4:0.6	0.11	0.53	0.80	53	13	66
	1:4:1	0.09	0.44	1.00	44	28	72
Fe titration B	apo	1.30	0.00	0.02	0	1	1
	1:4:0.2	0.14	0.22	0.29	22	3	25
	1:4:0.6	0.14	0.42	0.63	42	10	52
	1:4:1	0.14	0.49	0.85	49	18	67

The amounts of metal cluster species were calculated assuming that all metals are bound in dimer sites and the heterometallic cofactor assembly is preferred.

Table A8-3: Metal contents of R2lox samples before and after reconstitution with Mn(II) and Fe(II) in solution, as determined by TXRF.

		concentration	ratios		metal clusters [%]		
protein (batch)	**protein:Mn:Fe loading ratio**	**protein [mM]**	**Mn: protein**	**Fe: protein**	**Mn/Fe**	**Fe/Fe**	**total**
R2lox – apo protein							
apo A		1.18	0.00	0.19	0	10	10
apo B		0.93	0.00	0.16	0	8	8
apo C		1.30	0.00	0.02	0	1	1
apo D		0.99	0.00	0.03	0	1.5	1.5
apo E		0.28	0.00	0.14	0	7	7
R2lox - ox[a]							
(apo A)	1:0:4	1.16	0.00	2.74	0	137	137
(apo B)	1:0:3	4.00	0.02	2.28	2	113	115
(apo C)	1:0:3	3.42	0.01	2.29	1	114	115
(apo A)	1:2.4:1.2	1.29	0.38	1.22	38	42	80
(apo A)	1:2.4:1.2	2.10	0.49	1.28	49	40	88
(apo B)	1:2:1	3.82	0.64	1.18	64	27	91
(apo C)	1:2:1	3.44	0.68	0.98	68	15	83
R2lox - red[a]							
	1:0:4	1.78	0.00	0.59	0	29.5	29.5
	1:2.4:1.2	2.23	0.10	0.22	10	6	16

[a]ox, oxidized samples; red, reduced samples.
The amounts of metal cluster species were calculated assuming that all metals are bound in dimer sites and the heterometallic cofactor assembly is preferred.

Table A8-4: Metal contents of R2lox variants before and after reconstitution with Mn(II) and Fe(II) in solution, as determined by TXRF.

		ratios		metal clusters [%]		
protein	**protein:Mn:Fe loading ratio**	**Mn: protein**	**Fe: protein**	**Mn/Fe**	**Fe/Fe *Mn/Mn**	**total**
wt-R2lox	apo	0.01	0.08	1	3.5	4.5
Mn titration	1:2:2	0.38	1.51	38	56.5	94.5
	1:4:2	0.50	1.50	50	50	100
	1:8:2	0.60	1.44	60	42	102
Fe titration	1:4:0.2	0.28	0.32	28	2	30
	1:4:0.6	0.55	0.69	55	7	62
	1:4:1	0.67	0.98	67	15.5	82.5
A171F-R2lox	apo	0.00	0.07	0	3.5	3.5
Mn titration	1:2:2	0.56	1.66	55.5	55.5	111
	1:4:2	0.61	1.54	61	46.5	107.5
	1:8:2	0.69	1.52	69	42	111
Fe titration	1:4:0.2	0.28	0.28	27.5	0	27.5
	1:4:0.6	0.54	0.61	53.5	4	57.5
	1:4:1	0.69	0.96	69.5	13.5	83
E69D-R2lox[#]	apo	0.00	0.02	0	1	1
Mn titration	1:2:2	0.06	1.40	6	68	74
	1:4:2	0.09	1.36	10	63	73
	1:8:2	0.15	1.29	16	57	73
Fe titration	1:4:0.2	0.20	0.21	19	1	20
	1:4:0.6	0.21	0.52	22	16	38
	1:4:1	0.19	0.77	20	31	51
G68F-R2lox	apo	0.00	0.13	0	6.5	6.5
Mn titration	1:2:2	0.19	1.85	19	83	102
	1:4:2	0.27	1.75	27	74	101
	1:8:2	0.41	1.81	40.5	70.5	111
Fe titration	1:4:0.2	0.23	0.34	22.5	6	28.5
	1:4:0.6	0.38	0.72	37.5	17.5	55
	1:4:1	0.41	1.08	41.5	33.5	75
G68L-R2lox	apo	0.00	0.06	0	3	3
Mn titration	1:2:2	0.53	1.60	52.5	53.5	106
	1:4:2	0.71	1.55	70.5	42.5	113
	1:8:2	0.81	1.51	81	35	116
Fe titration	1:4:0.2	0.62	0.25	24.5	19*	43.5
	1:4:0.6	0.76	0.57	57	9.5*	66.5
	1:4:1	0.80	0.87	79.5	4	83.5

The amounts of metal cluster species were calculated assuming that all metals are bound in dimer sites and the heterometallic cofactor assembly is preferred.

Table A8-5: Metal contents of R2lox variants before and after reconstitution with Mn(II) and Fe(II) in solution, as determined by TXRF

		ratios		metal clusters [%]		
protein	**protein:Mn:Fe loading ratio**	**Mn: protein**	**Fe: protein**	**Mn/Fe**	**Fe/Fe *Mn/Mn**	**total**
V72A-R2lox	apo	0.00	0.07	0	3.5	3.5
Mn titration	1:2:2	0.42	1.63	42.5	60	102.5
	1:4:2	0.54	1.57	53.5	52	105.5
	1:8:2	0.63	1.57	63	47	110
Fe titration	1:4:0.2	0.35	0.25	25	5*	30
	1:4:0.6	0.56	0.59	56	1.5	57.5
	1:4:1	0.70	0.88	70	9	79
V72I-R2lox	apo	0.00	0.02	0	1	1
Mn titration	1:2:2	0.34	1.52	33.5	59.5	93
	1:4:2	0.45	1.48	45	52	97
	1:8:2	0.58	1.48	58.5	45	103.5
Fe titration	1:4:0.2	0.39	0.23	22.5	8*	30.5
	1:4:0.6	0.55	0.56	55	1	56
	1:4:1	0.67	0.94	67	13.5	80.5
V72L-R2lox	apo	0.00	0.05	0	2.5	2.5
Mn titration	1:2:2	0.49	1.50	49	51	100
	1:4:2	0.58	1.42	58.5	42	100.5
	1:8:2	0.67	1.40	67	36.5	103.5
Fe titration	1:4:0.2	0.22	0.23	21.5	1	22.5
	1:4:0.6	0.50	0.56	50	3.5	53.5
	1:4:1	0.71	0.82	71	6	77
Y162F-R2lox	apo	0.00	0.06	0	3	3
Mn titration	1:2:2	0.43	1.50	43	53.5	96.5
	1:4:2	0.55	1.44	54.5	44.5	99
	1:8:2	0.65	1.38	65	36.5	101.5
Fe titration	1:4:0.2	0.30	0.25	24.5	3*	27.5
	1:4:0.6	0.54	0.55	54	0.5	54.5
	1:4:1	0.73	0.86	73	7	80
Y175F-R2lox	apo	0.01	0.23	1	11	12
Mn titration	1:2:2	0.32	1.81	31.5	75	106.5
	1:4:2	0.41	1.73	40.5	66.5	107
	1:8:2	0.48	1.71	48.5	61.5	110
Fe titration	1:4:0.2	0.41	0.46	41.5	2.5	44
	1:4:0.6	0.67	0.89	67	11	78
	1:4:1	0.61	1.15	61.5	26.5	88

The amounts of metal cluster species were calculated assuming that all metals are bound in dimer sites and the heterometallic cofactor assembly is preferred.

Zusammenfassung

Die Aktivierung von kleinen Molekülen wie H_2O, H_2, O_2, und CO_2 wird durch zahlreiche metallische Kofaktoren in biologischen Enzymen (Metalloproteine) katalysiert. Die Bestimmung der molekularen und elektronischen Eigenschaften der aktiven Zentren, sowie das Verständnis der katalytischen Reaktionsmechanismen sind von großem wissenschaftlichem Interesse. Der Schwerpunkt dieser Arbeit liegt in der Untersuchung von zwei verschiedenen biologischen Systemen. [FeFe]-Hydrogenasen katalysieren die reversible Wasserstoff-produktion, während sogenannte Ligandenbindende Oxidasen Sauerstoff aktivieren. Hier wurde eine umfangreiche Untersuchung an einer Reihe von synthetischen Verbindungen, die das Zweieisen-Zentrum von [FeFe]-Hydrogenasen modellieren, mittels Röntgen-Absorption und Emission Spektroskopie und DFT Methoden durchgeführt. Der Effekt der Variationen der Liganden auf die elektronischen Eigenschaften der Zweieisenkomplexe wurde herausgearbeitet. Prinzipiell wurde eine gute Übereinstimmung zwischen den experimentellen und berechneten Ergebnissen erzielt. Die Studie trägt bei zur Entwicklung verbesserter Katalysatoren für die Wasserstoffgewinnung. Durch XAS/XES-Studien konnte belegt werden, dass bei der Rekonstitution von *Cr*HydA1 [FeFe]-Hydrogenasen mit synthetischen Zweieisenkomplexen erfolgreich der katalytische H-Cluster assembliert wird. Der Vergleich von XAS-Daten von gefriergetrockneten und in Lösung befindlichen [FeFe]-Hydrogenasen hat dazu beigetragen, die Lyophilisierung als eine geeignete Methode zur Verhinderung des durch Sauerstoff induzierten Abbaus des H-Clusters zu etablieren. Binukleare Metall-Kofaktoren der Ligandenbindenden Oxidase *Gk*R2lox wurden mit einer Vielzahl von Röntgenspektrosko-pischen Methoden (XAS, XES, und NRVS) an Synchrotronstrahlungsquellen und DFT Rechnungen charakterisiert. Die molekulare Struktur und die elektronische Konfiguration, sowie der Protonierungszustand der aktiven Zentren (FeFe, MnFe) konnte entschlüsselt werden. Die Beschreibung der Kofaktoren auf atomarer Ebene wurde in Kombination mit XRD-Daten signifikant verbessert. Die Durchführung von NRVS-Experimenten an ^{57}Fe markierten *Gk*R2lox, sowie die Zuordnung der Schwingungsbanden mit Hilfe von DFT-Rechnungen konnte etabliert werden. Detaillierte XAS und TRXF Untersuchungen an mutierten Varianten von *Gk*R2lox wurden durchgeführt und zeigen den Einfluss der Aminosäureliganden auf Kofaktormetallierung sowie Metallspezifität (Mn versus Fe). Neue Zusammenhänge zwischen dem Mechanismus der O_2-Aktivierung und der Kofaktor-Struktur konnten gezeigt werden. Die Kombination von fortgeschrittenen Röntgenmethoden mit quantenchemischen Rechnungen wurde in dieser Arbeit weiterentwickelt. Dieser Ansatz ist gut für die Aufklärung von molekularer Strukturen und elektronischer Konfigurationen von aktiven Zentren in Metalloproteinen und synthetischen Modellverbindungen. Es konnten neue Einblicke in die Eigenschaften der Metallzentren von Hydrogenasen und Oxidasen gewonnen werden und die vorgestellten Ergebnisse haben zu mehreren Publikationen beigetragen.

Selbstständigkeitserklärung

Ich erkläre gegenüber der Freien Universität Berlin, dass ich die vorliegende Doktorarbeit selbstständig und ohne Benutzung anderer als der angegebenen Quellen und Hilfsmittel angefertigt habe. Die vorliegende Arbeit ist frei von Plagiaten. Alle Ausführungen, die wörtlich oder inhaltlich aus anderen Schriften entnommen sind, habe ich als solche kenntlich gemacht. Diese Arbeit wurde in gleicher oder ähnlicher Form noch bei keiner anderen Universität als Prüfungsleistung eingereicht und ist auch noch nicht veröffentlicht.

Berlin, den ……..

……

Ramona Kositzki